DUCTED MAGNETOACOUSTIC WAVES IN THE SOLAR CORONA

Jason M. Smith

A Thesis Submitted for the Degree of PhD
at the
University of St Andrews

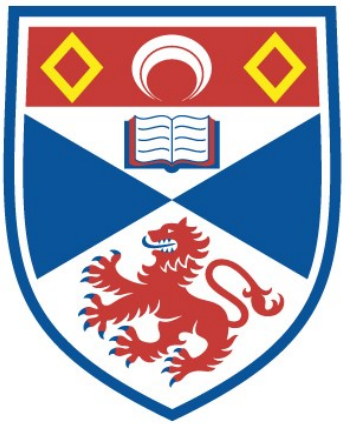

1997

Ducted Magnetoacoustic Waves in the Solar Corona

Jason M. Smith

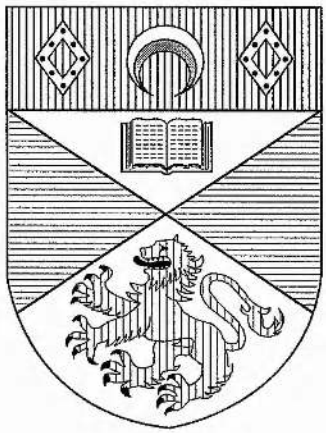

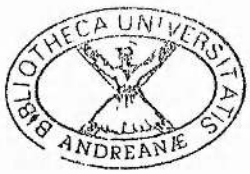

Thesis submitted for the degree of Doctor of Philosophy
of the University of St Andrews

September 23, 1997

In memory of Dan Lawrence

"You'll never walk alone"

Declaration

1. I, Jason Mark Smith, hereby certify that this thesis, which is approximately 55 000 words in length, has been written by me, that it is a record of work carried out by me and that it has not been submitted in any previous application for a higher degree.
   date 4 August 1997 signature of candidate .

2. I was admitted as a research student in October 1994 and as a candidate for the degree of PhD in October 1995; the higher study for which was carried out in the University of St Andrews between 1994 and 1997.
   date 4 August 1997 signature of candidate ..

3. I hereby certify that the candidate has fulfilled the conditions of the Resolution and Regulations appropriate to the degree of PhD in the University of St Andrews and that the candidate is qualified to submit the thesis in application for that degree.
   date 4 August 1997 signature of supervisor ..

4. In submitting this thesis to the University of St Andrews I understand that I am giving permission for it to be made available for use in accordance with the regulations of the University Library for the time being in force, subject to any copyright vested in the work not being affected thereby. I also understand that the title and abstract will be published and that a copy of the work may be made and supplied to any bona fide library or research worker.
   date 4 August 1997 signature of candidate ...

Abstract

This thesis investigates the ducting of magnetoacoustic waves in coronal structures. The propagation of waves in current sheets and coronal loops has been examined in order to understand wave ducting in structured plasmas, and to provide an explanation of the observed oscillatory behaviour in the solar corona.

Firstly a comprehensive review of the observations of loops and oscillations in the corona is given. An investigation into how the curvature of the loop alters the ducting of magnetoacoustic waves is then presented by studying the effect of the length, width and the density enhancement of the loop and also the frequency of oscillation. The effect of the curvature is to generate wave leakage from the loop.

The guiding of magnetoacoustic waves by a current sheet is also considered. An investigation into the type of modes which may propagate and the time scales of oscillation is performed. Impulsively generated waves exhibit similar temporal signatures to observations of X-ray and radio emission. Periods of oscillation for all the ducted wave models are in good agreement with reported observations.

The effect of a random boundary motion on a magnetospheric cavity is examined through numerical simulations. A broadband driving spectrum excites the quasi-monochromatic fast modes whose frequencies lie within the driving spectrum. These fast modes couple to an Alfvén mode if the frequency lies within the Alfvén continuum. The position of the resonant field lines and the Alfvén mode eigenfunction may be accurately calculated by assuming a periodic boundary motion.

To conclude the work in this thesis the three-dimensional magnetic topologies surrounding neutral points are studied. The local linear magnetic structure about the null is found to depend only on a 3×3 matrix containing four parameters. The type of topology is dependent upon the nature of the eigenvalues and eigenvectors of this matrix.

Publications

The contents of Chapters 2 and 3 have been published in *Astronomy and Astrophysics* (Smith, Roberts and Oliver 1997a,b). In addition to the publications in *Astronomy and Astrophysics*, poster presentations of the research in these two chapters have been given during the 1996 Summer School on Reconnection and the 1997 Cormack Bequest meeting, both held in St Andrews. The work described in Chapter 6 has been published in *Physics of Plasmas* and *Geophysical and Astrophysical Fluid Dynamics* (Parnell, Smith, Neukirch and Priest 1996; Parnell, Neukirch, Smith and Priest 1997). The research undertaken in Chapters 4 and 5 is currently in preparation (Smith, Roberts and Murawski 1997; Smith, Wright and Rickard 1997).

Oral presentations of the work contained in this thesis have been given at the: Department of Physics, University of the Balearic Islands, 1995 and 1996; the National Astronomy Meeting, Liverpool, 1996; UK MHD Meeting, University of London, 1996; UK Solar Physics meeting, University of Central Lancashire, 1997.

Acknowledgements

I would like to thank:

- my supervisor Professor Bernard Roberts for his guidance, advice and encouragement during the past three years.

- Drs Ramon Oliver and Jose-Luis Ballester of the Department of Physics, University of the Balearic Islands for accommodating my two visits to Palma; and especially to Ramon Oliver for the collaboration on the ducted wave models described in this thesis.

- Dr Kris Murawski of the Technical University of Lublin for helpful advice with the time dependent simulations undertaken in this thesis.

- the EPSRC for financial support.

- the staff at the Department of Physics, University of Wales, Swansea for the excellent grounding in physics and magnetohydrodynamics.

- past and present members of the Solar Theory Group at St Andrews. In particular Dr Andrew Wright and Professor Eric Priest for their help with Chapters 5 and 6 respectively. Also Dr Tricia Heggie for her unfailing help with computational problems and Clare Martin for proof reading this thesis.

Finally, I would like to thank my Mum and Dad for their encouragement and support during my university career.

Contents

Chapter 1

Introduction

"Nature has a great simplicity and therefore a great beauty."

Richard Feynman

1.1 Introduction to the Sun

The Sun, our nearest star, is situated 1.5×10^8 km away from the Earth. It is 4.5×10^9 years old, with a mass ($M_\odot$) of 1.99×10^{30} kg (330 000 times greater than the mass of the Earth). The Sun is composed mainly of hydrogen (90 %), with a helium abundance of 10 % and also traces of heavier elements. The solar radius ($R_\odot$) is 696 000 km, 109 times larger than the Earth's radius. The Sun is a plasma held together by gravitational forces. The Sun does not rotate uniformly, the equator and poles revolving once about every 25 and 30 days respectively. The total electromagnetic energy radiated per unit time from the Sun (the "luminosity") is 3.86×10^{26} W. The mean density of the Sun is 1.4×10^3 kg m^{-3} (compared with 5.5×10^3 kg m^{-3} for the Earth). The gravitational acceleration at the solar surface is 274 m s^{-2} (compared with 9.81 m s^{-2} for the Earth).

We give a brief description of the different regions of the Sun. We begin with an overview of the solar interior (Section 1.1.1) and then proceed to the three layers that make up the solar atmosphere, namely the *photosphere* (Section 1.1.2), the *chromosphere* (Section 1.1.3) and the *corona* (Section 1.1.4). Each of these regions is characterised by different physical properties, such as temperature and density. Comprehensive reviews of the observations may be found in Zirin (1988). Observations and theory are discussed in Priest (1982) and Phillips (1992). In our review we concentrate mainly on the corona, since the work contained in this thesis is predominately concerned with this region.

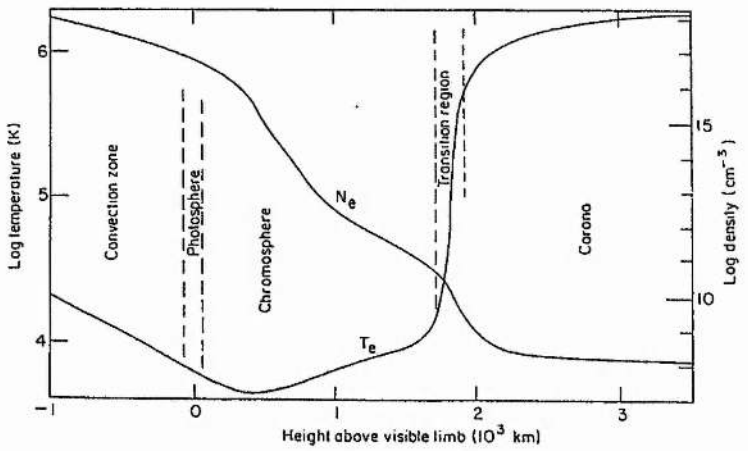

Figure 1.1: The variation of the electron density (N_e) and temperature (T_e) from the convection zone to the corona. Note the dramatic rise in temperature in the transition region (Mason 1994).

1.1.1 The Solar Interior

The interior of the Sun cannot be observed. However the study of helioseismology (the global oscillations of the Sun) has recently begun to give important information about the solar interior. The solar *core* produces 99 % of the Sun's energy. The temperature within this region is 1.6×10^7 K, with a density of 1.6×10^5 kg m^{-3}. The core, which extends over a region of $0.3\mathrm{R}_\odot$, is a fusion reactor where hydrogen is burned to generate energy. Approximately half of the Sun's mass is contained within the core. The area surrounding the core, between 0.3 and $0.7\mathrm{R}_\odot$, is called the *radiative zone*; the primary energy transport mechanism is radiation. The density and temperature decrease rapidly as we move away from the Sun's centre. At a radius $R = 0.3\mathrm{R}_\odot$ the temperature has fallen to half its value at the centre of the core, whilst the density has decreased to 10 % of its maximum value. The density and temperature continue to decrease throughout the radiative zone, until at $R = 0.7\mathrm{R}_\odot$ the temperature is 2×10^6 K, with the density reaching a value of 200 kg m^{-3}. This is the beginning of the convective zone where, as the name suggests, the dominant energy transfer process is convection. The convection is generated by the steep temperature gradient (the temperature decreases from 2×10^6 K to 6400 K across this zone). The density also decreases dramatically in this region, declining from 200 kg m^{-3} at $R = 0.7\mathrm{R}_\odot$ to 3×10^{-4} kg m^{-3} at $R = \mathrm{R}_\odot$. On top of this zone is the solar atmosphere which may be split into three layers. A sketch of the electron temperature and density profiles from the convection zone to the corona is depicted in Figure 1.1.

1.1.2 The Photosphere

The photosphere is a thin layer, 0.5 Mm (1 Mm = 1 Megametre $\equiv 10^6$ m) thick, which emits most of the Sun's light. The density and temperature decrease with increasing height throughout the photosphere. The temperature at the base of the photosphere is 6400 K, falling to a minimum value of 4400 K at the top of the layer. The density declines from 3×10^{-4} kg m^{-3} at the top of the convective zone to 8×10^{-5} kg m^{-3} at the temperature minimum.

The top of the convective cells are observed in the photosphere as granules. The granule cells typically have diameters of between 0.7 and 1.5 Mm, with lifetimes of 8 minutes. The average distance between the cell centres is 1.8 Mm. An upflow of 0.4 to 0.8 km s^{-1} is observed in the centre of each granule, with a flow of 0.25 km s^{-1} towards the boundary. Supergranules are cells with diameters 20 to 54 Mm (mean diameter 32 Mm). Material rises at the centre of the cell with a velocity of 0.1 km s^{-1} and moves outwards at 0.3 to 0.4 km s^{-1}. The lifetime of a supergranule is a day. The boundaries of the supergranule cells are associated with intense magnetic flux tubes with field strengths of 1000 to 2000 G (1 G = 1 Gauss $\equiv 10^{-4}$ Tesla).

The largest magnetic field strengths in the photosphere occur in sunspots and may reach 4000 G. Sunspots consist of two main components. The inner part is the umbra, with diameters of 10 to 20 Mm and field strengths of several thousand gauss. The surrounding outer region is called the penumbra, with widths lying between 15 and 30 Mm and a field strength lower than that found in the umbra (typically 1000 G).

1.1.3 The Chromosphere

The chromosphere is the region situated between the temperature minimum and the corona. An interesting characteristic of the chromosphere is the increase of temperature with height. The temperature increases from 4400 K at the base of the chromosphere to 50 000 K at a height of 2 Mm above the photospheric base. The temperature increase in the transition region is much more dramatic, rising from 50 000 K to 500 000 K in a narrow region of just 0.5 Mm (Figure 1.1).

It is natural to believe that the temperature of the solar atmosphere should decrease away from the core. Evidently this is not the case. The physical processes underlying an explanation of this interesting phenomenon continues to be an active area of research in solar physics (see Section 1.5). The density falls from several times 10^{-5} kg m^{-3} in the low chromosphere to 10^{-10} kg m^{-3} in the high chromosphere.

At the granular boundaries plasma jets called spicules are observed at the limb. These have a diameter of 0.5 to 1.2 Mm and a lifetime of 15 minutes. The spicule temperature is 1–2 $\times 10^4$ K, with a velocity of 20–30 km s^{-1}. Spicules attain a height of 9 Mm before fading away.

1.1.4 The Corona

Brief Overview of the Corona

The solar corona is the hot, tenuous, magnetically dominated, outermost region of the Sun's atmosphere. The temperature of the corona is several million degrees kelvin, with a density of several times 10^{-12} kg m^{-3}. In this region hydrogen is fully ionised and therefore the corona may be observed in a wide range of wavelengths.

The X-ray and Extreme Ultraviolet (EUV) images made by the Skylab mission in 1973 have shown that the corona is highly structured and dominated by the magnetic field. This has been confirmed by recent Yohkoh observations (Acton et al. 1992) and by white light images taken during the 1991 eclipse (November and Koutchmy 1996). Instruments onboard the recently launched SoHO (Solar and Heliospheric Observatory) satellite have, once more, revealed the complex nature of this region by using a variety of emission lines; see also Section 1.6. An X-ray image of the corona is shown in Figure 1.2 during a peak in the activity cycle. The image, taken on the 12 November 1991 by the Yohkoh satellite, reveals the corona at a temperature of 2×10^6 K. It is dominated by loops, revealing the complexity and inhomogeneity present in the active region corona. The EUV image of the Sun, taken using the EIT instrument onboard SoHO during a quieter part of the cycle, shows loop structures on the limb (Figure 1.3). Finally, the white light images recorded by November and Koutchmy (1996), shown in Figure 1.4, again clearly illustrate the inhomogeneities present in the coronal plasma.

Many different structures are found in the solar corona. These include prominences which are large, almost vertical sheets of dense cool plasma located in the much hotter and more rarefied corona. The prominence temperature is 100 times less than coronal values and the density is 100 times greater. On the disc these structures are called filaments, forming along polarity inversion lines.

There are two types of prominence: *quiescent* and *active* (Priest 1982). Quiescent prominences are stable and they may exist for several months. Typical electron densities are 10^{11} cm^{-3}, with a temperature of 7000 K and a field strength of between 5 and 10 G. Spatial dimensions for the length, height and width are typically 200 Mm, 50 Mm and 6 Mm respectively. Active region prominences are usually associated with flares and have lifetimes of only minutes or hours. They are three or four times smaller than quiescent prominences, with larger densities and similar temperatures, and their height is at most 20 Mm.

Figure 1.2: The X-ray corona on 12 November 1991 taken by the Yohkoh satellite.

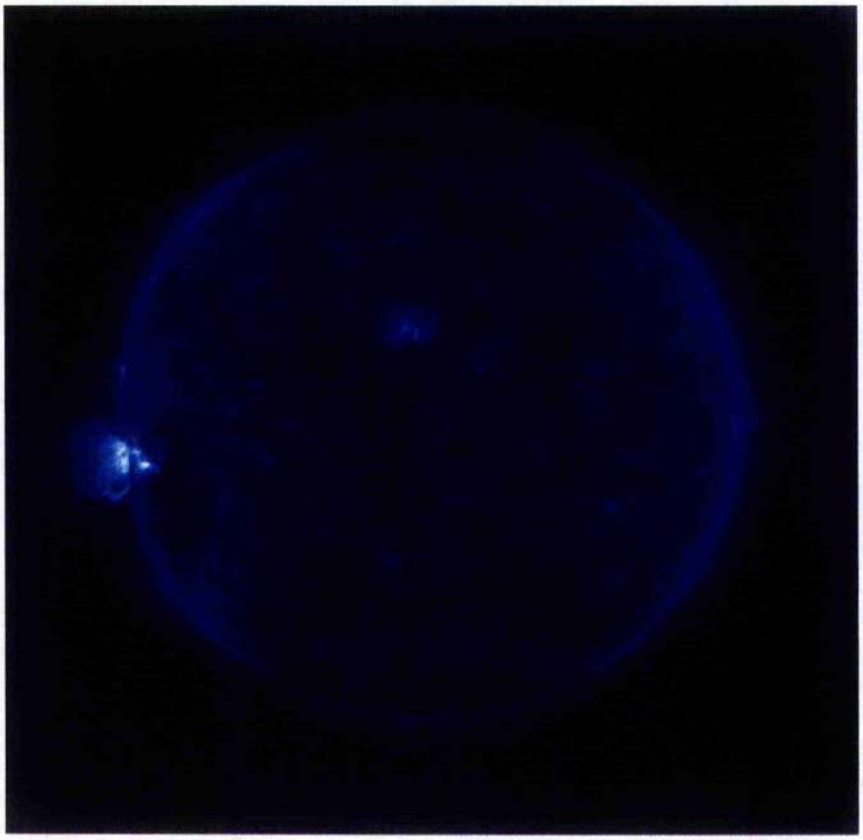

Figure 1.3: The solar corona at 1×10^6 K. The image was taken with the Extreme ultraviolet Imaging Telescope (EIT) onboard SoHO in the Fe IX/X emission lines at 171 Å on 22 August at 20:15. Notice an active region (enhanced emission) on the east limb containing coronal loops, and coronal holes (reduced emission) at the poles.

X-ray bright points are also observed in the corona. Diameters are typically 22 Mm, with a bright core ranging from 4 to 7 Mm in size. They consist of several loops, with a characteristic width and length of 2.5 Mm and 12 Mm respectively. Approximately 1500 bright points appear every day and they have a mean lifetime of 8 hours. Bright points are formed from bipolar areas of emerging flux. A review of the observations of bright points may be found in Parnell (1994).

Other important structures in the corona are holes and loops, corresponding to regions of open and closed magnetic field respectively.

In coronal holes the plasma flows outward, giving rise to the solar wind. In X-ray and EUV images (Figures 1.2 and 1.3 respectively) coronal holes appear as dark regions representing very low emission. The density of a coronal hole is depleted by a factor of approximately 3 compared with

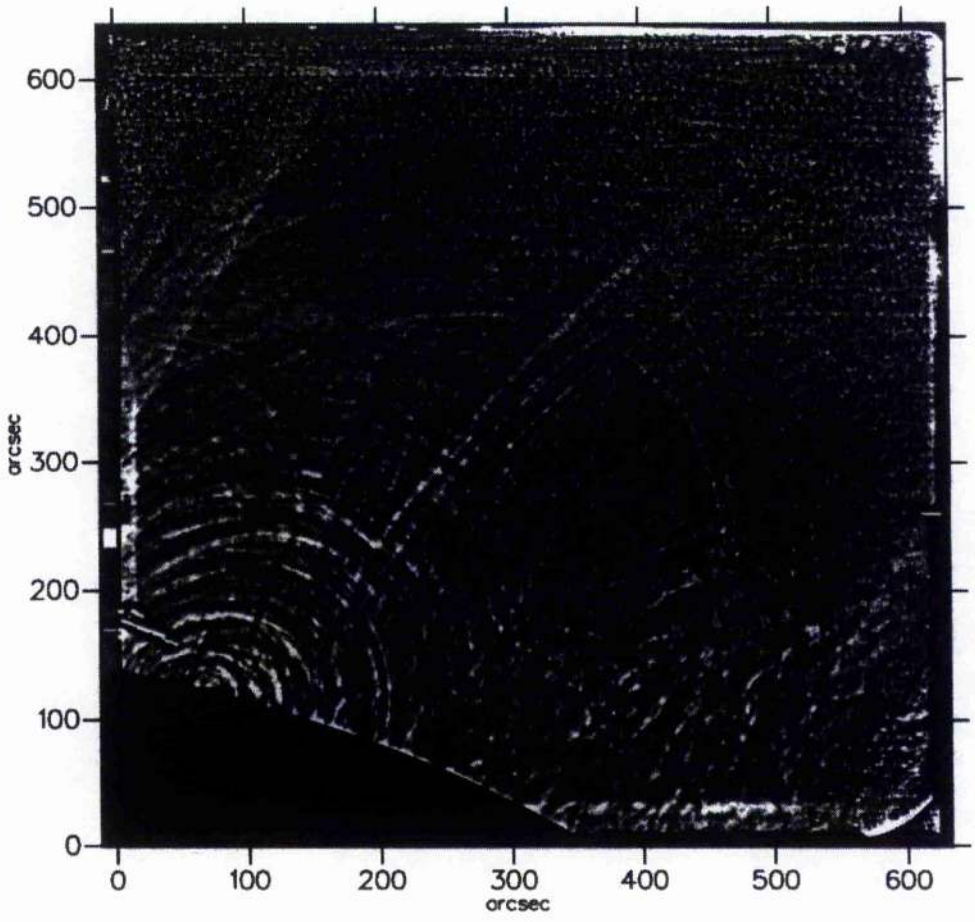

Figure 1.4: White light images of the solar corona taken during the eclipse of 11 July 1991 (November and Koutchmy 1996). An arcade of dense loops is present, clearly showing the importance of the density inhomogeneity and the curvature of the structures in this region of the solar atmosphere. The loops have a density twice that of the ambient corona.

quiet regions. The lifetime of a coronal hole is several months, with a temperature of $1\text{–}1.5\times10^6$ K and a magnetic field strength of 1 to 10 G. Inside coronal holes bright points and plumes may be found. Coronal plumes are observed in white light images as rays of enhanced density; the density being 3 to 5 times greater than the background value (Koutchmy 1977). In EUV images they appear as shorter spikes on the solar limb and have a characteristic lifetime of several hours. The width of a plume at the limb is typically 60–70 Mm. Electron densities are characteristically between 10^8 and 10^9 cm^{-3}, with a temperature of 10^6 K.

Coronal Loops and Active Regions

The active region corona consists mainly of *coronal loops*. In this section we review in detail the observations of the structure and physical characteristics of loops. A comprehensive review of coronal loops and prominences is given in Bray, Cram, Durrant and Loughhead (1991). Observations are obtained by examining a range of wavelengths such as the green and red coronal lines, EUV lines, X-ray emission, radio emission and white light.

(i) Spatial Sizes of Coronal Loops

We begin by reviewing the observations of the spatial parameters (width, height and distance between footpoints) associated with loops. We summarise the typical observations of coronal loops. A comprehensive listing of the observations of coronal loops is presented in Appendix A.

Kleczek (1963), using the green coronal line, reports that the typical height of a small coronal loop lies between 50 and 100 Mm. The width of a loop lies between 3 and 8 Mm, although values between 5 and 6 Mm are more typical. The aspect ratio ($a/L \equiv$ ratio of radius a to length L) is approximately 0.05. Large loops, however, may extend over substantial distances, connecting different active regions. They may reach heights of half a solar radius (348 Mm). The width of these larger loops is typically between 8 and 12 Mm, but may be as low as 3 Mm. Sheeley et al. (1975) show that loops observed in EUV lines may arch across the disk for distances of the order of 100 Mm to link two or more active regions and form large magnetic complexes. Such loops are not confined to active regions lying in the same hemisphere but may involve regions lying on both sides of the equator. Upon restoring the three-dimensional shape of coronal loops from Skylab EUV images, Berton and Sakurai (1985) studied two loops. The maximum heights of the two loops were 120 and 130 Mm respectively, with the inclination to the vertical being 25 and 7 degrees. The shape of the loop was asymmetric, but the authors illustrated that the observed asymmetry was consistent with a potential magnetic field between two active regions.

X-ray loops may be classified into three types (see, for example, Davis and Krieger 1982; Bray, Cram, Durrant and Loughhead 1991). Class I loops are those which occur in the core of an active region, joining areas of opposite polarity either side of a neutral line. Loops of Class II are larger in size than those of Class I and occupy the area surrounding the core of the active region.

Parameter	Class I	Class II	Class III
Width (Mm)	0.7–5	5–15	10–30
Length (Mm)	7–20	10–100	50–500
Aspect ratio	0.2	0.18	0.09

Table 1.1: Classification of X-ray loop sizes from Davis and Krieger (1982).

Loops of Class III may link adjacent active regions or just terminate outside an active region. Davis and Krieger (1982), observing loops in the X-ray spectral region, give values for the lengths, widths and aspect ratios for the various types of loop (Table 1.1).

Additional Class II observations have been undertaken by Howard and Švestka (1977). Their X-ray observations showed loop heights of 200 Mm, with one particular loop reaching 260 Mm. For Class III loops Krieger, de Freiter and Vaiana (1976), using Skylab measurements, observed X-ray loops up to heights of 100 Mm, although a value of 50 Mm is more typical. Haisch, Strong, Harrison and Gary (1988), studying two prominent X-ray loops in an active region, found the length of a loop was 130 Mm, with heights of 40 and 60 Mm and an aspect ratio of 0.1. From the Yohkoh satellite Acton et al. (1992) observe X-ray loops. In particular, one small loop has width 4 Mm, height 10 Mm and length 18 Mm. A larger loop was also observed which was 27 Mm wide, 190 Mm long and 82 Mm high. A large X-ray loop (height 350 Mm, length 400 Mm) was also reported.

McConnell and Kundu (1983), observing 20 cm radio emission (1.4 GHz), report a loop with length 70 Mm, whereas Lang, Willson and Rayrole (1982) find lengths ranging from 40 to 400 Mm. Studying the microwave structure of the quiet Sun at 8.5 GHz, Gary, Zirin and Wang (1990) reported a loop length of 22 Mm. Widths of 10 Mm and 30 Mm have been quoted by Kundu, Schmahl and Gerassimenko (1980). Finally, using white light observations during a solar eclipse Koutchmy, Bouchard, Mouette and Koutchmy (1993) and November and Koutchmy (1996) studied coronal loops with sub-arcsecond resolution. Their results show coronal loops that are thin and irregular with widths lying between 1 and 2 arcseconds (0.726–1.452 Mm) and with an aspect ratio of 0.01 (Figure 1.4).

The width of a coronal loop is approximately constant along its length. Golub (1991), analysing results from the Normal Incidence X-ray Telescope (NIXT), gives lengths of loops from 1.5 Mm to 90 Mm. The loop widths were several megametres and Golub gives an aspect ratio of between 0.025 and 0.25. The loops were found to maintain a relatively uniform cross-section for most of their length, with a sharp decrease at the footpoints. This is in agreement with Klimchuk, Lemen, Feldman, Tsuneta and Uchida (1992) who conclude, from Yohkoh X-ray measurements, that loops have an almost uniform width along their length; the loop width decreased near the footpoints. A loop of length 82 Mm was observed with a mean half width lying between 7.26 and 9.1 Mm. This was also found by Porter and Klimchuk (1995) who measured the lengths of 47 non-flaring loops. Loops with lengths from 4.7 to 33 Mm were observed and the loop width was constant (to within 7

%) along the length.

Typically the widths of loops lie between 3 and 10 Mm. However observers suggest that due to relatively poor spatial resolution there is a difficulty in distinguishing between individual loops (see, for example, Foukal 1975; Kilmchuk et al. 1992). Aschwanden (1994), in a review article, suggests the inhomogeneity in the solar corona is evident in the highest resolution images (one arcsecond). Therefore it is likely that active region loops consist of unresolved fine structures.

(ii) Density and Temperature of Active Regions

We now give an overview of the observations of the electron density and temperature found in active regions. A detailed listing is given in Appendix B. Temperatures in active region coronal loops lie in the range $1\text{–}6\times10^6$ K, with a characteristic value of 2×10^6 K. These values are observed in a range of wavelengths. In particular Krucker, Benz, Aschwanden and Bastian (1995) report temperatures of $2.1 \pm 0.1 \times 10^6$ K using X-rays. Using the green and red coronal lines temperatures of $2\text{–}3\times10^6$ K are observed by Hanaoka, Kurokawa and Saito (1988). In the EUV regime temperatures of $2.0\text{–}2.2\times10^6$ K are routinely observed (Cheng 1980). Electron densities lie between 1×10^9 cm^{-3} and 1×10^{10} cm^{-3}. Specifically, in X-rays, Parkinson (1973) reports electron densities ranging from 2 to 10×10^9 cm^{-3}. Electron densities inferred from radio observations range from 1 to 10×10^9 cm^{-3} (Kundu and Lang 1985). Hanaoka, Kurokawa and Saito (1988), using the red and green coronal lines, give values between 0.4 and 7.2×10^9 cm^{-3}.

There are conflicting reports that cool loops may exist in much hotter loops. Hanaoka, Kurokawa and Saito (1988), using the green and red coronal lines, examined the density and temperature in a loop during an eclipse. Comparing the position of the cool loop (red line, $T = 1\times10^6$ K) with that of the hot loop (green line, $T = 2 \times 10^6$ K) they concluded that the two loops were coaxial. The average density in the hot loop was 1.2×10^9 cm^{-3}, whereas the cool loop was at least five times denser. The authors suggested that the cool loops may consist of many small "threads" of diameter 1 Mm which are unresolved in the observations. Hanaoka et al. (1988) suggested that cool dense threads of material exist in hot coronal loops. The fact that hot loops may have a cool core was observed from Skylab measurements (see, for example, Foukal et al. 1974; Foukal 1975, 1976; Levine and Withbroe 1977). However other observations suggest that hot and cool loops may exist independently (Cheng 1980; Cheng, Smith and Tandberg-Hanssen 1980; Sheeley 1980; Dere 1982). Koutchmy et al. (1993) and November and Koutchmy (1996), using high resolution (sub-arcsecond) white light observations, suggest that a coronal loop with a cool core and hot surroundings is too simple a model. They observe coronal loops with temperature and density inhomogeneities along the loop. Recent Yohkoh observations (Matthews 1997, private communication) have shown cool loops (Oxygen V, $T = 2 \times 10^5$ K) are co-spatial with X-ray loops ($T = 3 \times 10^6$ K). This is in agreement with recent SoHO observations. Recent results from the SoHO CDS instrument have once again shown the existence of 10^5 K plasma next to 10^6 K plasma (Phillips 1997, private communication).

(iii) Density Enhancements in the Solar Corona

An important observational result is that active regions (including loops) are *denser* than the surrounding plasma. This simple fact is of paramount importance when investigating the guiding of magnetoacoustic waves in the corona. Until now, no thorough review has been given on the density enhancements in the corona. Therefore in Table 1.2 we give a comprehensive summary of measured density enhancements (the ratio of the plasma density in an active region to the density in the background plasma). Table 1.2 gives the paper where the results were published, the reported density enhancement and the wavelength used in the measurement. We summarise the main results, which have been confirmed in a range of wavelengths. We begin by examining the observations that use the green coronal line and the continuum. Fisher (1971a) quotes a density enhancement of 2 by calculating the density at the loop summit and in the surrounding plasma. The electron density was 7.8×10^9 cm^{-3} at the top of the loop and 3.9×10^9 cm^{-3} outside. A slightly lower density excess of 1.8 was measured at the sides of the loop. In addition Fisher (1971b), measuring the density inside a loop and just below using the green line and the continuum, gives density enhancements of 4.8 and 3 respectively. Using a white light coronagraph on Skylab, Pick, Trottet and MacQueen (1979) found an electron density 10 times that of the background corona. The density varied by a factor of 2 over several hours.

The magnitude of the density enhancement has also been measured using the EUV emission lines. Observations of active regions by Noyes, Withbroe and Kirshner (1970) and Noyes (1971) in the temperature range 10^4 to 3.5×10^5 K have shown a density enhancement between two and six times the background value. Fisher (1971b), using the FeXV line, measures a density excess 6.5 times that of the surrounding plasma. These results were obtained from 26 measurements across 14 loops in 4 active regions during the Skylab mission. Stewart and Vorpahl (1977), using the soft X-ray telescope onboard Skylab, suggest the density ratio of an active region over a quiet region lies between 4 and 16. Using X-ray measurements Davis and Krieger (1982) find the material outside the loop to be ten times less dense; the density outside the loop was 1×10^8 cm^{-3} and that inside was 1×10^9 cm^{-3}.

We conclude our review by looking at the radio observations. Malitson and Erickson (1966), using a compilation of several results, found that the electron density in coronal streamers over active regions was ten times that of the surrounding plasma. The results were obtained from radio observations in the range 1.5 to 200 MHz. Also, using radio observations at 169 MHz, Leblanc (1970) found the electron density of an active region was three times that of the background corona.

Aschwanden (1996, private communication), analysing Yohkoh, EUV and radio data, suggests for flare loops that the density lies in the range from a few times 10^{10} cm $^{-3}$ to several times 10^{12} cm $^{-3}$ (see also Doschek, Strong and Tsuneta 1995). Aschwanden (1994) quotes density enhancements of greater than 100 for flare loops. A similar figure of between 30 and 150 is given by Švestka (1995) using X-ray measurements.

Paper	Year	Density Enhancement	Observations
Malitson and Erickson	1966	10	Radio
Newkirk	1967	2–5	Radio
Leblanc	1970	3	Radio
Noyes et al. Noyes	1970 1971	2–6	EUV lines
Fisher	1971a	1.8–2	Green Line
Fisher	1971b	6.5 4.8 3.0	EUV line Green line Continuum
Dupree et al.	1973	7	EUV line
Parkinson	1973	10	X-Ray
Mercier and Rosenberg	1974	10.5	Radio
Stewart	1974	4	Radio
Reeves et al.	1974	≈ 10	EUV
Allen	1975	5	EUV
Foukal	1975	4	EUV
Stewart	1976	8–10	Radio
Stewart and Vorpahl	1977	4–16	Soft X-ray
Foukal	1978	1.4–12	EUV
Pick et al.	1979	10	White light
Cheng	1980	1.5	EUV
Davis and Krieger	1982	10	X-ray
Stewart et al.	1986	≈ 10	EUV
Hanaoka et al.	1988	2	Green Line
Švestka et al.	1995	30–150	X-Ray (Flare Loop)
Brosius et al.	1996	2–8	EUV
Brosius et al.	1997	2	EUV / X-ray
November and Koutchmy	1997*	2	White light

Table 1.2: A comprehensive summary of density enhancements (the ratio of the density in the active region corona to the surrounding plasma) in the solar corona. The asterisk denotes a private communication.

Paper	Year	Magnetic Field (G)	Plasma Beta	Wavelength
Fisher	1971a,b	5	-	Green Line
Parkinson	1973	5.5–16	-	X-ray
Neupert et al.	1975	100	-	X-ray / EUV
Kundu et al.	1980	300	0.01	X-ray / EUV
McConnell and Kundu	1983	130–170	3×10^{-4}	Radio
Dulk and Gary	1983	20–70	-	X-ray
Hiei	1994	10–100	-	X-ray
McKenzie	1997	-	0.001–0.045	X-ray

Table 1.3: Summary of the observations of the magnetic field and plasma beta in coronal loops and active regions.

In general, these results show that the active region corona is 3 to 10 times denser than the background plasma.

(iv) Magnetic Field Strength and Plasma Beta

Table 1.3 summarises the measurements of the magnetic field and plasma beta (the ratio of plasma pressure p to the magnetic pressure $B^2/2\mu_0$; $\beta = 2\mu_0 p/B^2$) in active regions. Here B is the magnetic field strength and μ_0 is the permeability of free space. We find that typical magnetic field strengths lie in the range 5 to 100 G, with a plasma beta much less than unity. Therefore the corona is magnetically dominated and the effects of plasma pressure are generally negligible.

(v) Lifetimes of Coronal Loops

Picat, Fort, Dantel and Leroy (1973), analysing loops in both the green and red coronal lines, show that smaller loops may only appear for periods of a few hours, whereas larger loops may exist for several days. This is in agreement with Kleczek (1963) who, using the green line, suggested larger loops are more stable. Stewart, Brueckner and Dere (1986), examining EUV and soft X-ray loops, found the lifetime to be about a day. Loops which existed for longer than 31 days (the observation time) were reported by Berton and Sakurai (1985). The lifetime of loops has also been studied by Sheeley (1980). For cool loops (NeVII, T = 0.5×10^6 K) the lifetime of the loop was only 30 minutes. Hotter loops (MgIX, T = 1.0×10^6 K and FeXV, T = 2.0×10^6 K) existed for 1.5 hours (MgIX) and 6 hours (FeXV). Acton et al. (1992) give the lifetime of an X-ray loop as days to weeks. Cheng, Smith and Tandberg-Hanssen (1980) find that the lifetime of the loop is dependent upon the aspect ratio of the loop. From EUV observations they find a small aspect ratio (a/L) loop changes more rapidly than a loop with a large aspect ratio.

(vi) Characteristic Speeds

Consider a typical coronal magnetic field strength of $B = 50$ G and a plasma density of $\rho = 4 \times 10^{-12}$ kg m^{-3}. The Alfvén speed $v_A \left(= B/\sqrt{\mu_0 \rho}\right)$ equals 2230 km s^{-1}. A characteristic sound speed $c_s \left(= \sqrt{\gamma p/\rho}\right)$ in the corona, assuming a temperature of 1.5×10^6 K, is 204 km s^{-1}. In our work we adopt typical values for the Alfvén and sound speeds of several thousand and several hundred kilometres per second respectively. A typical tube speed $c_T \left(= c_s v_A / \left(c_s^2 + v_A^2\right)^{\frac{1}{2}}\right)$ with $c_s = 200$ km s^{-1} and $v_A = 2000$ km s^{-1} is $c_T = 199$ km s^{-1}. Therefore in the corona the sound speed and tube speed attain similar values.

Typical coronal loop parameters are summarised in Table 1.4. The very recent X-ray observations from Yohkoh (McKenzie 1997) confirm these values. McKenzie finds loops with lengths ranging from 42 to 150 Mm, whilst the electron temperature and density are found to be 2.3–4.7$\times 10^6$ K and 1.6–5.6$\times 10^{10}$ cm^{-3} respectively. The plasma beta inferred from the measurements lies between 0.001 and 0.045. Finally, the average Alfvén and sound speeds are estimated to be 4000 km s^{-1} and 240 km s^{-1} respectively. A summary of X-ray loops has also been given by Beaufumé, Coppi and Golub (1992), with conclusions in agreement with our review. Using results from Skylab, SMM (Solar Maximum Mission) and NIXT (Normal Incidence X-ray Telescope) observations, typical parameters for X-ray loops are presented. Beaufumé et al. (1992) state that the characteristic parameters for coronal loops may take a wide range of values. The aspect ratio is quoted to lie between 0.01 and 0.04. A typical coronal loop has a half-width of 0.5 to 4 Mm and a length of 20 to 200 Mm. The loops are mainly isothermal with a characteristic temperature of 2–3$\times 10^6$ K. Loops with temperatures in excess of 2×10^6 K were reported to have a lifetime of several days. Cooler loops were found to be thinner and less stable, with shorter lifetimes than hotter loops. Typical coronal magnetic fields, obtained by extrapolating from the photosphere, lie in the range from 30 to 200 G. Electron densities were given as 1–10$\times 10^9$ cm^{-3}.

1.2 Oscillations in the Corona

1.2.1 Introduction

Observations suggest that periodic and quasi-periodic oscillations commonly occur in the corona. Oscillations are detected by measuring the temporal variation in intensity, line width and Doppler velocity of coronal emission lines. A summary, together with prominence oscillations, is given by Tsubaki (1988). Further information about oscillations of the coronal plasma comes from radio and X-ray emission, with periods ranging from sub-second to several minutes. Short (one second) periods of oscillation are frequently reported. These observations are reviewed by Edwin (1984) and Aschwanden (1987). In this section we comprehensively review the observations, updating earlier work. We begin in Section 1.2.2 by briefly describing the oscillations reported throughout the

Parameter	Value
Footpoint Separation	1.5–500 Mm (100)
Width	0.7–30 Mm (3–10)
Height	40–560 Mm (50–100)
Densities	$0.2–20\times10^{9}$ cm^{-3} (2)
Density Enhancement	1.5–16 (3–10)
Temperature	$1.4–6\times10^{6}$ K (2)
Magnetic Field	5–300 G (100)
Aspect Ratio	0.01–0.25
Plasma Beta	0.003–0.01
Alfvén Speed	2000 km s^{-1}
Sound Speed	200 km s^{-1}

Table 1.4: Summary of observed coronal loops parameters. Figures in brackets denote "typical" values.

Sun. Coronal oscillations are then summarised in detail. In Section 1.2.3 we review the oscillations detected in coronal emission lines, and then proceed to oscillations in radio and X-ray emission in Section 1.2.4.

1.2.2 Solar Oscillations

The Sun can sustain oscillations. Wave-like motions have been detected throughout the different regions of the Sun. Here we give a brief summary of the reported oscillations, concentrating on the corona; see Roberts (1991a) for a review of observations and theory.

We begin our review by briefly summarising the reported oscillations in the solar interior. Leighton, Noyes and Simon (1962) reported oscillations in the photosphere with a 5 minute period. These oscillations are now known to be acoustic waves trapped within a cavity formed by the increasing sound speed in the solar interior (see, for example, Ulrich 1970). The investigation of these oscillations has led to the subject of helioseismology. The properties of the solar interior, such as the density and temperature, are inferred from such a study.

Sunspot oscillations have also been reported. The umbra oscillates with 3 and 5 minute periods (Moore and Rabin 1985). The region surrounding the umbra, the penumbra, oscillates with periods of 4 to 5 minutes; see Roberts (1991a, 1992) for a review.

Wave motions in the chromosphere, with periods lying between 40 seconds and several minutes have been reported. Specifically, Endler and Deubner (1983) and White and Athay (1979) have reported oscillations between 40 and 140 seconds and from 170 to 500 seconds respectively.

Prominence oscillations are reviewed in Tsubaki (1988), with typical periods lying in the range from 5 to 90 minutes; see also Joarder and Roberts (1992, 1993), Roberts and Joarder (1994) and Joarder, Nakariakov and Roberts (1997).

1.2.3 Coronal Emission Line Observations

A comprehensive summary of the reported coronal oscillations obtained from emission lines is given in Table 1.5. This table has been adapted and updated from Tsubaki (1988), incorporating the latest observations. The table shows the paper where the results were published and the wavelength of the observations. The period of oscillation is given and also the physical parameter measured. We now summarise the main results.

The first report of a coronal oscillation was made in 1959 by Billings. Using the FeXIV, 5303 Å green coronal line, Billings found an oscillatory pattern in the half-width of the line. However the period of oscillation was undetermined. Periods from 2 to 6 minutes have been routinely observed in coronal emission lines. However in recent years, short period oscillations (of the order of a few seconds) have also been reported. In particular, during the 1983 total eclipse Pasachoff and Landman (1984) and Pasachoff and Ladd (1987) reported periodic oscillations in the intensity of the green coronal line between 0.5 and 4 seconds. Periods of this order have also been observed by Rušin and Minorovjech (1991, 1994) in both the green and red (6374 Å) lines.

We note that there are also examples of observations where oscillations have not been detected (see, for example, Schmidt, Wagner and Newkirk 1972; Koutchmy 1975; Vernazza et al. 1975).

1.2.4 Radio and X-ray Observations

There are many reported examples of coronal oscillations using observations of both radio and X-ray emission. The source of these oscillations is likely to be impulsive, for example a solar flare (see Tables 1.6 and 1.7). However, Tapping (1978) and Gaizauskas and Tapping (1980) have reported oscillations without any flare association. The observations are summarised comprehensively in Tables 1.6 and 1.7, which have been updated from Edwin (1984). The information depicted in these tables shows whether the period is constant in time (periodic) or irregular (quasi-periodic). In addition the period of oscillation is given and also the observing wavelength. Finally, the source of the oscillations is given in the final column of each table. We now summarise the main results from Tables 1.6 and 1.7.

Many of the periods are of the order of a few seconds. These periods have been confirmed in a range of wavelengths. For example, following a solar burst, Kaufmann, Rizzo Piazza and Rafaelli (1977) detected periodic oscillations of 4.7 seconds in microwaves. In addition, measuring X-ray emission, Desai et al. (1986) reported a 1.64 second oscillation with constant amplitude. In radio emission Mangeney and Pick (1989) observe quasi-periodic oscillations with periods between 2 and 3 seconds. In addition sub-second oscillations are frequently reported. For example, Li, Messerotti and Zlobec (1987) and Correia and Kaufmann (1987) both report a 0.3 second fast pulsation in X-rays.

Recently McKenzie (1997), using soft X-ray observations from the Yohkoh mission, has

Author	Year	Spectral Region	Intensity Period (s)	Line width Period (s)	Doppler Velocity Period (s)
Billings	1959	5303 Å	None	Wave pattern	None
Noxon	1966	5303 Å	480	None	None
		6374 Å	None	None	None
Lilliequist	1966	5303 Å	490	490	—
		6374 Å	300,150	300,150	—
Curtis et al.	1971	5303 Å	—	500,270 185	—
Chapman et al.	1972	EUV	262	—	—
Schmidt et al.	1972	White light	None	—	—
Liebenberg and Hoffman	1974	5303 Å	360±60	—	—
Koutchmy	1975	White light	None	—	—
Vernazza et al.	1975	EUV	None	—	—
Tsubaki	1977	5303 Å	None	280, 325 (Weak)	280, 315
Egan and Schneeberger	1979	5303 Å	366	366	None
Koutchmy et al.	1981	5303 Å	None	None	43, 80, 300
Antonucci et al.	1984	EUV	117, 141	—	—
Pasachoff and Landman	1984	5303 Å	0.5–2	—	—
Tsubaki et al.	1986	5303 Å	235±2.5	None	None
Pasachoff and Ladd	1987	5303 Å	0.5–4	—	—
Rušin and Minorovjech	1991	5303 Å	7.5, 12, 30–60, 67–95, 222, 312	—	—
		6374 Å	74, 99, 120 222, 296	—	—
Dermendjiev et al.	1992	5303 Å	64, 83, 130 (not significant)	—	—
Rušin and Minorovjech	1994	5303 Å, 6374 Å	5.5–5.7, 7.0–7.5, 10, 12, 30–43, 83, 328	—	—
Singh et al.	1997	Continuum	5.3, 6.1, 8.0, 13.5, 19.5, 56.5	—	—

Table 1.5: Summary of oscillations in coronal emission lines. The table has been adapted and updated from Tsubaki (1988).

Author	Year	P/Q	Period	E.M. Designation	Nature of Source
Young et al.	1961	Q	< 0.3s	UHF	—
Janssens and White	1969	P	Train > 9 pulses of ≈16s preFlare pulse train of ≈23s	UHF μ	trains during and after Flare
Frost	1969	Q	35s	Hard X-ray, μ	Eruptive prominence
Parks and Winckler	1969	P	16s	X-ray, μ, UHF	Flare related
Cribbens and Matthews	1969	Q	6→60s 180→600s	UHF	—
Abrami	1970	Q	1.7→3.1s	VHF	Subflare, Type IV
Rosenberg	1970	P,Q	≈1s, subharmonic ≈3s	VHF	Type IV
McLean et al.	1971	Q	≈1s, 2.5→2.7s between pulses in train of a minute	VHF	Flare 25min earlier, Type IV
Abrami	1972	Q	train of sub-second pulses	VHF	Type IV
Elgaroy and Lyngstad	1972	Q	2→3s	VHF, UHF	Type III
Gotwols	1972	Q	≈0.5s	UHF	Flare 6-10min earlier Type IV
Janssens et al.	1973	P,Q	4,5,6 Spikes separated by 10→20s	X-ray EUV, μ	Some Flare association Type III
Kai and Takayanagi	1973	Q	≈2→5s	VHF	Flare related Type II, IV
McLean and Sheridan	1973	P	4.28±0.1s	VHF	Subflare 7min earlier
Maxwell and Fitzwilliam	1973	Q	1→200s 7→15 min durations	μ	Type IV
Achong	1974	Q	≈4s, 12s subharmonic	HF	—
Anderson and Mahoney	1974	Q	2→20s	Hard X-ray	Flare related
Jakimiec and Jakimiec	1974	Q	200→900s	X-ray	Flare 1hr40 earlier
Cliver et al.	1976	Q	9→74s 130→480s	UHF	Flare related
Kaufmann et al.	1977	P	4.7±0.9s for > 1 hr	μ	Simultaneous solar great burst
Pick and Trottet	1978	Q	0.37s, trains recurring after 1.7 ±0.4s	VHF	Flare related Type IV
Tapping	1978	Q	Trains of ≤ 20 pulses frequency $0.2s^{-1} \rightarrow 15s^{-1}$	VHF	No Flare
Teuber et al.	1978	Q	85s, 256s,	X-ray	Flare related
Praća and Karlický	1979	Q	Bursts of 0.1s	UHF	2-ribbon Flare ≈4hr earlier
Trottet et al.	1979	Q	1 minute	VHF, μ	Eruptive prominence Type IV

Table 1.6: Oscillations reported in X-ray and radio emission, updated from Edwin (1984). In the table we give the paper and the year in which it was published. Next we denote whether the oscillations were periodic (P) or quasi-periodic (Q). The period of oscillation is given in the next column. The observational wavelength and the likely source of the oscillations are given in the final two columns. The electromagnetic designation is as follows: HF : 3 MHz–30 MHz; VHF : 30 MHz–300 MHz; UHF : 300 MHz–3 GHz; μ : 3 GHz–30 GHz; EHF : 30 GHz–300 GHz.

Author	Year	P/Q	Period	E.M. Designation	Nature of Source
Gaizauskas and Tapping	1980	Q	≈2.5s, trains of pulsations over 5 hours	μ	No Flare
Wiehl and Matzler	1980	Q	5s	μ, Hard X-ray	—
Dennis et al.	1981	Q	$\geq$ 8 peaks ≈1s separated by 1→2s	Hard X-ray	Flare related
Orwig et al.	1981	Q	groups of spikes 7→11s between peaks	X-ray Hard X-ray	Flare related
Trottet et al.	1981	Q	1.7±0.5s	VHF	Type IV
Sastry et al.	1981	Q	2→5s	HF, VHF	—
Švestka et al.	1982	Q	13 pulses 20min	X-ray, VHF	Flare 6.5hrs before
Kane et al.	1983	Q	7 peaks with 8s separation	X-ray, μ VHF	Flare related
Kiplinger et al.	1983a	Q	< 1s	Hard X-ray	Flare related
Kiplinger et al.	1983b	Q	recurrent train of 8.2s pulse interval	Hard X-ray, μ γ-ray	Flare related
Takakura et al.	1983	Q	$3s^{-1} \rightarrow 4s^{-1}$	X-ray, μ	Subflare earlier
Benz (See Edwin 1984)	1984	Q	1.1s for ≈29s	UHF	—
Benz (See Roberts et al. 1984)	1984	Q	≈40s	UHF	—
Zodi Vaz and Kaufmann	1984	Q	1.5s over 10min	μ	Solar Burst
Wiehl et al.	1985	Q	1→2s	UHF	Type IV
Elgaroy	1986	Q	0.75s over 2hrs	UHF	Flare related
Aschwanden and Benz	1986	Q	0.4→1.4s	UHF	Flare related
Desai et al.	1986	P	1.64s constant amplitude	Hard X-ray	Flare related
Kosugi and Kiplinger	1986	Q	8s and 16s	μ, Hard X-ray, γ	Flare related
Thomas et al.	1986	P	1.6s amplitude decreasing	Soft X-ray	Flare related
Wells et al.	1986	Q	2→10s	VHF, UHF, μ, X-ray	Flare related
Zodi Vaz et al.	1986	Q	0.29→0.5s	Hard X-ray, UHF, μ, EHF	Flare related
Aurass et al.	1987	Q	0.3→0.4	VHF	Type IV
Wright and Nelson	1987	Q	3min initially, 5min after large flare, 4min towards end	UHF	Flare related
Li et al.	1987	Q	0.3s	UHF	Type IV
Correia and Kaufmann	1987	Q	0.2→0.3s	μ, EHF	—
Harrison	1987	Q	24 minutes over 6 hours	Soft X-ray	Flare related
Mangeney and Pick	1989	Q	Range 1→6s 2→3s common	VHF, UHF	Type III
Švestka et al.	1989	Q	19min	Hard X-ray, μ	Flare related
Zhao et al.	1990	Q	1.4→1.6s	μ	—
Fu et al.	1990	Q	4s	μ	—
Kurths et al.	1991	Q	2.7s, 4.3s	UHF	Flare Related
Zhao et al.	1991	Q	1→6s	VHF, UHF	Type III
Zlobec et al.	1992	Q	11.4s	UHF	Flare 2hrs before Type IV
Aschwanden et al.	1992	Q	8.8 seconds	VHF, UHF	Flare related
Aschwanden et al.	1993	Q	45 pulses 1.6±0.6s	VHF, UHF, Hard X-ray	—
Aschwanden et al.	1994	Q	1→2s	UHF	Flare related
Švestka	1994	Q	20min 50s	X-ray	Flare related
Correia et al.	1995	Q	Sub-second pulses superimposed onto fast 1s pulse	EHF	Flare related
Karlický and Jiricka	1995	Q	0.1→0.5s, 0.7→1.0s 2.8→3.9s, 75→170s	UHF	Subflare
Qin et al.	1996	Q	1.5s superimposed onto 40s oscillation	μ	Flare related
McKenzie	1997	Q	9→62s average 35 seconds	X-ray	Flare related

Table 1.7: Oscillations reported in X-ray and radio emission, updated from Edwin (1984). The table gives the paper and the year of publication. We also denote whether the oscillations were periodic (P) or quasi-periodic (Q). The period of oscillation is given in the next column. The wavelength observed and the source of the oscillations are given in the final two columns. The electromagnetic designation is as follows: HF : 3 MHz–30 MHz; VHF : 30 MHz–300 MHz; UHF : 300 MHz–3 GHz; μ : 3 GHz–30 GHz; EHF : 30 GHz–300 GHz.

performed a systematic search for periodic modulations (of the order of 1 %) in the X-ray brightness of coronal loops. The smallest detectable period in this study is 8 seconds. The short (one second) period oscillations reported (see Tables 1.6 and 1.7) are therefore beyond the resolution of this work. McKenzie finds periods lying in the range from 9 to 62 seconds, with an average of 35 seconds. This is in good agreement with models of ducted magnetoacoustic waves in either coronal loops (see Chapter 2) or current sheets (see Chapters 3 and 4), and may be attributable to the fundamental kink mode. Periods of oscillation τ are found to be consistent with $\tau = 2L/v_A$, where v_A is the Alfvén speed and L the loop length. No evidence for longer periods ($>$ 15 minutes) — which would relate to slow magnetoacoustic waves — is found. In addition, no periodic variations were found in either the density or temperature. McKenzie (1997) suggests the wave motion may not be compressive (Alfvén waves), or the density variation may be below the threshold of the observations.

As shown in Table 1.5 for coronal emission lines, oscillations with longer periods are also found. These periods are detected in observations of both radio and X-ray emission. For example the X-ray measurements of Teuber, Wilson and Henze (1978) showed quasi-periodic oscillations with periods of 85 and 256 seconds. Following the eruption of a prominence, Trottet, Pick and Heyvaerts (1979) detected periods of 1 minute in radio emission. Even longer periods, around 20 minutes, have been reported. In particular, Harrison (1987) reports a 24 minute period over a duration of 6 hours in X-rays. A series of papers by Švestka et al. (1982), Švestka, Fárník, Fontenla and Martin (1989) and Švestka (1994) have found 20 minute modulations, again in the X-ray regime.

Many of the oscillations only last for a few cycles (see, for example, Aschwanden, Benz, Dennis and Gaizauskas 1993; Correia and Kaufmann 1987) whilst other reported oscillations may last for several hours. In particular, Gaizauskas and Tapping (1980) reported the existence of 2.5 second pulsations over a period of 5 hours. Furthermore, Kaufmann, Rizzo Piazza and Rafaelli (1977) detected a periodic modulation of 4.7 seconds lasting for over an hour.

Observational evidence for magnetoacoustic waves in coronal loops is limited. Loughhead, Bray and Wang (1985) investigated the fractional variation (deviation from the mean) of the plasma density, pressure and temperature at eight positions along a coronal loop. The temperature of the loop was found to be approximately constant along its length. Evidence of a wave-like variation in the plasma density and pressure was suggested. The wavelength was approximately half the loop length, some 50 to 60 Mm. Furthermore, the authors suggest the presence of a node at the loop summit.

From this review we conclude that the coronal plasma is able to support oscillations. The periods are diverse ranging from sub-second through to 24 minutes. It is the objective of this thesis to investigate the guiding of magnetoacoustic waves in structured media, and thereby provide a possible explanation for these observations. In the next section we present the governing equations used in this thesis; the equations of magnetohydrodynamics (MHD) are discussed, together with definitions of the important parameters used in our study.

1.3 The MHD Equations

In this section we introduce the fundamental equations which are used to investigate ducted magnetoacoustic waves in the solar corona. We use the magnetohydrodynamic (MHD) equations which are discussed in considerable detail by P.H. Roberts (1967); see also Priest (1982). MHD describes the interaction between the magnetic field and the plasma. In using these equations we have made several assumptions which limit the range of validity of our results. In our work we treat the plasma as a continuum, ignoring the effects of particles. In addition the velocity of the plasma is considered to be non-relativistic. We also assume that the collisions between the particles occur frequently enough to ensure an isotropic plasma pressure. Consequently the temporal and spatial scales of interest must be much larger than the characteristic plasma parameters, such as particle collision times and the mean free path length. In the solar corona, a typical mean free path is 50 km and a characteristic particle collision time is 0.01 seconds. Spitzer (1962) gives the mean free path as $5 \times 10^{-2} T^2/n_e$ km, where T is the temperature in kelvin and n_e is the electron density in cm^{-3}. Typical coronal values of $T = 10^6$ K and $n_e = 10^9$ cm^{-3} determine a mean free path of 50 km. The electron-ion collision time is calculated from $0.266 T^{3/2}/n_e \ln\Lambda$ where $\ln\Lambda = 19.3$ for $T = 10^6$ K and $n_e = 10^9$ cm^{-3} (Priest 1982).

The governing equations are Maxwell's equations and Ohm's law, along with a momentum equation, an equation of state and the conservation of energy and mass. Here we give a brief outline of the equations, illustrating the approximations which are relevant to our area of study.

We begin by stating Maxwell's laws, which may be written in the form:
the *Maxwell-Ampère* law,

$$\nabla \times \mathbf{B} = \mu_o \mathbf{j} + \frac{1}{c^2} \frac{\partial \mathbf{E}}{\partial t} \; ; \tag{1.1}$$

Gauss' law for magnetism (no magnetic monopoles — the solenoidal constraint),

$$\nabla \cdot \mathbf{B} = 0; \tag{1.2}$$

Faraday's law of induction

$$\nabla \times \mathbf{E} = -\frac{\partial \mathbf{B}}{\partial t} \; ; \tag{1.3}$$

and *Gauss'* law for electricity,

$$\nabla \cdot \mathbf{E} = \frac{Q}{\epsilon_0} \; . \tag{1.4}$$

In Equations (1.1)-(1.4) $\mathbf{B}$ is the magnetic (induction) field, $\mathbf{j}$ is the current density, c is the speed of light, $\mathbf{E}$ is the electric field, Q is the charge density, and μ_0 and ϵ_0 are the permeability and permittivity of free space respectively. Note that Maxwell's equations are all *linear*; however the equations of MHD are *non-linear* because of Ohm's law and the equations of fluid mechanics.

In Equation (1.1) we may neglect the term $1/c^2\,(\partial \mathbf{E}/\partial t)$ in the non-relativistic approximation. The argument is as follows. Consider a characteristic plasma length, velocity and time scale given by L_0, V_0 and T_0 respectively; $V_0 = L_0/T_0$. Equation (1.3) determines the magnitude of the electric field as $E_0 \approx B_0 V_0$. The left-hand side of Equation (1.1) has magnitude B_0/L_0 whilst the second term on the right-hand side has magnitude $B_0 V_0/T_0 c^2$. The ratio of the term on the right-hand side to the left-hand side is proportional to V_0/c^2. Therefore, in the non-relativistic approximation ($V_0 \ll c$) the term involving the electric field may be ignored. Equation (1.1) may then be written

$$\nabla \times \mathbf{B} = \mu_o \mathbf{j}\,, \tag{1.5}$$

which determines the current density $\mathbf{j}$ from the magnetic induction $\mathbf{B}$. This is Ampère's law in pre-Maxwellian form.

Ohm's law states that the current density is proportional to the sum of the background electric field ($\mathbf{E}$) and the electric field ($\mathbf{v} \times \mathbf{B}$) induced by the plasma motion ($\mathbf{v}$),

$$\mathbf{j} = \sigma\,(\mathbf{E} + \mathbf{v} \times \mathbf{B})\,, \tag{1.6}$$

where σ is the electrical conductivity. Substituting Equation (1.6) into Equation (1.5) yields the *induction* equation,

$$\frac{\partial \mathbf{B}}{\partial t} = \nabla \times (\mathbf{v} \times \mathbf{B}) + \eta \nabla^2 \mathbf{B}\,, \tag{1.7}$$

where we have used the solenoidal constraint $\nabla \cdot \mathbf{B} = 0$ and assumed that the magnetic diffusivity $\eta = 1/\mu_0 \sigma$ is constant. The induction equation is a fundamental equation of MHD, determining the temporal evolution of the magnetic field. The first term on the right-hand side of Equation (1.7) describes the tendency of the magnetic field to be advected with the plasma motion. The second term describes the decay of the magnetic field due to the diffusivity η. In the solar atmosphere we may generally neglect the $\eta \nabla^2 \mathbf{B}$ term. The ratio

$$R_m = \left| \frac{\nabla \times (\mathbf{v} \times \mathbf{B})}{\eta \nabla^2 \mathbf{B}} \right| \approx \frac{V_0 L_0}{\eta}\,, \tag{1.8}$$

is defined as the magnetic Reynolds number. When $R_m \ll 1$ the temporal behaviour of the field is dominated by diffusion, whereas if $R_m \gg 1$ advective effects are important. In the limit $R_m \to \infty$ the fluid is perfectly conducting. In the large magnetic Reynolds number limit, the frozen-flux theorem states that in a perfectly conducting plasma the magnetic field lines behave as if they move with the plasma (see Priest 1982 for a proof). The magnetic Reynolds number is much greater than unity in most astrophysical applications, since the characteristic length and velocity scales are large. In particular, considering a sunspot, with typical values $\eta = 10^3$ m^2 s^{-1}, $L_0 = 10^4$ km and $V_0 = 1$ km s^{-1}, we obtain $R_m = 10^7$. For $R_m \gg 1$ the induction equation may be written in the reduced form

$$\frac{\partial \mathbf{B}}{\partial t} = \nabla \times (\mathbf{v} \times \mathbf{B})\,. \tag{1.9}$$

The equation of *continuity of mass* is given by

$$\frac{\partial \rho}{\partial t} + \nabla \cdot (\rho \mathbf{v}) = 0 \,, \tag{1.10}$$

and describes the temporal evolution of the plasma mass density due to the plasma motion.

The *momentum* equation is given by

$$\rho \left[\frac{\partial \mathbf{v}}{\partial t} + (\mathbf{v} \cdot \nabla) \mathbf{v} \right] = -\nabla p + (\mathbf{j} \times \mathbf{B}) + \rho \mathbf{g} \,. \tag{1.11}$$

This equation of motion determines the time evolution of the plasma velocity in terms of the forces on the right-hand side of the equation, namely the plasma pressure gradient ($-\nabla p$), the Lorentz force ($\mathbf{j} \times \mathbf{B}$) and the gravitational force ($\rho \mathbf{g}$). The gravitational force is neglected in our treatment.

The *adiabatic energy* equation is given by

$$\left(\frac{\partial}{\partial t} + \mathbf{v} \cdot \nabla \right) p = \frac{\gamma p}{\rho} \left(\frac{\partial}{\partial t} + \mathbf{v} \cdot \nabla \right) \rho \,. \tag{1.12}$$

Finally, the plasma is assumed to satisfy the *ideal gas law*, which states that

$$p = \frac{R}{\tilde{\mu}} \rho T \,, \tag{1.13}$$

where p, ρ and T are the plasma pressure, density and temperature respectively. Here $\tilde{\mu}$ is the mean atomic weight in terms of the proton mass and R is the gas constant. The parameter $\gamma\,(= 5/3)$ denotes the ratio of specific heats.

We now introduce some quantities which will prove useful in our work. We firstly define the sound (c_s) and Alfvén (v_A) speeds,

$$c_s = \sqrt{\frac{\gamma p}{\rho}} \quad \text{and} \quad v_A = \frac{B}{\sqrt{\mu_0 \rho}} \,. \tag{1.14}$$

Here B is the magnitude of the magnetic field. It is convenient to introduce the *plasma beta* (β), which is proportional to the ratio of these speeds. The plasma beta is defined as the ratio of plasma pressure (p) to magnetic pressure $\left(B^2/2\mu_0\right)$,

$$\beta = \frac{2\mu_0 p}{B^2} = \frac{2}{\gamma} \frac{c_s^2}{v_A^2} \,. \tag{1.15}$$

The plasma beta determines whether magnetic effects are dominant ($\beta \ll 1$) or weak ($\beta \gg 1$). For example, in the solar corona with $\gamma = 5/3$, $c_s = 200$ km s^{-1} and $v_A = 2000$ km s^{-1}, we obtain $\beta = 0.012$. Therefore in this region of the solar atmosphere the plasma pressure is much less important than the magnetic pressure. It is usually a good approximation to neglect the effects of plasma pressure; the *low-β approximation* ($\beta = 0$). In photospheric flux tubes, typical values for the sound and Alfvén speeds are 8 and 10 km s^{-1} respectively, giving $\beta = 0.77$. In the photosphere the plasma pressure plays a more important role than in the corona.

Theoretically we may expect the magnetic field to support oscillatory behaviour. To see this we substitute Equation (1.5) into the Lorentz force ($\mathbf{j} \times \mathbf{B}$) to obtain

$$\mathbf{j} \times \mathbf{B} = \frac{1}{\mu_0} (\nabla \times \mathbf{B}) \times \mathbf{B} \, . \tag{1.16}$$

Then, using a vector identity, we obtain

$$\mathbf{j} \times \mathbf{B} = \frac{1}{\mu_0} (\mathbf{B} \cdot \nabla) \mathbf{B} - \nabla \left(\frac{B^2}{2\mu_0} \right) \, . \tag{1.17}$$

Therefore the momentum equation (Equation 1.11) has a term of the form

$$\frac{1}{\mu_0} (\mathbf{B} \cdot \nabla) \mathbf{B} - \nabla \left(p + \frac{B^2}{2\mu_0} \right) \, . \tag{1.18}$$

We see that the $\mathbf{j} \times \mathbf{B}$ force introduces a magnetic pressure $(B^2/2\mu_0)$ which augments the plasma pressure (p). In addition, the $(\mathbf{B} \cdot \nabla)\mathbf{B}/\mu_0$ term corresponds to a magnetic tension. Since each flux tube is frozen into the fluid (when $R_m \gg 1$) magnetic field lines are analogous to a loaded string under tension. If the field lines are displaced, we may expect them to oscillate in a similar way to an elastic string.

1.4 MHD Wave Propagation in the Solar Atmosphere

Having seen that the magnetic field may support oscillations, we now briefly review the work on MHD wave propagation in the solar atmosphere. For a discussion on magnetoacoustic wave propagation in a structured plasma see Roberts (1985, 1991a, 1992) and Edwin (1991, 1992); see also Chapters 2, 3 and 4.

In the absence of a magnetic field acoustic waves are present. These sound waves are isotropic, propagating equally in all directions, driven by the gradient of the gas pressure. A preferential direction of propagation occurs in the presence of a magnetic field. To illustrate this consider the driving forces on the right-hand side of the momentum equation (Equation 1.18), assuming gravitational effects are negligible. The first term of Equation (1.18) represents the *tension*, which is anisotropic. The second term denotes the *pressure*, which is isotropic.

Consider a magnetic field $\mathbf{B} = B_0 (x) \, \hat{\mathbf{e}}_z$. We now apply a perturbation to the ideal MHD equations ($\rho = \rho_0 + \rho_1$) etc., assuming that the equilibrium state is static ($v_0 = 0$). In addition, we take the perturbations to be small ($\rho_1 \ll \rho_0$), ignoring squares of perturbed quantities. The *linearised* MHD equations take the form

$$\frac{\partial \rho_1}{\partial t} + \rho_0 \triangle = 0 \, , \tag{1.19}$$

$$\rho_0 \frac{\partial \mathbf{v}}{\partial t} = -\nabla \left(p_1 + \frac{\mathbf{B_0} \cdot \mathbf{b_1}}{\mu_0} \right) + \frac{1}{\mu_0} (\mathbf{B_0} \cdot \nabla) \mathbf{b_1} + \frac{1}{\mu_0} (\mathbf{b_1} \cdot \nabla) \mathbf{B_0} \, , \tag{1.20}$$

$$\nabla \cdot \mathbf{b_1} = 0 \,, \tag{1.21}$$

$$\frac{\partial \mathbf{b_1}}{\partial t} = \nabla \times (\mathbf{v} \times \mathbf{B_0}) \,, \tag{1.22}$$

$$\frac{\partial p_1}{\partial t} = \frac{\gamma p_0}{\rho_0} \frac{\partial \rho_1}{\partial t} \,. \tag{1.23}$$

In Equations (1.19)-(1.23) the subscripts 0 and 1 denote the equilibrium and perturbed quantities respectively. We have defined $\Delta = \nabla \cdot \mathbf{v}$. The linearised induction equation (Equation 1.22) reduces to

$$\frac{\partial \mathbf{b_1}}{\partial t} = B_0 \frac{\partial \mathbf{v}}{\partial z} - B_0 \Delta \hat{\mathbf{e}}_\mathbf{z} \,. \tag{1.24}$$

Now, differentiating the linearised momentum equation (Equation 1.20) with respect to time yields, after some algebra,

$$\rho_0 \frac{\partial^2 \mathbf{v}}{\partial t^2} = \nabla \left[\rho_0 \left(c_s^2 + v_A^2 \right) \Delta - \rho_0 v_A^2 \Gamma \right] + v_A^2 \left[\rho_0 \frac{\partial^2 \mathbf{v}}{\partial z^2} - \hat{\mathbf{e}}_\mathbf{z} \rho_0 \frac{\partial \Delta}{\partial z} \right] \,, \tag{1.25}$$

where $\Gamma = \partial v_z / \partial z$. We have taken ρ_0, c_s and v_A to be dependent only upon x. Now writing Equation (1.25) in terms of the velocity components yields

$$\rho_0 \left(\frac{\partial^2}{\partial t^2} - v_A^2 \frac{\partial^2}{\partial z^2} \right) v_x = \frac{\partial}{\partial x} \left[\rho_0 \Delta \left(c_s^2 + v_A^2 \right) - v_A^2 \rho_0 \Gamma \right] \,, \tag{1.26}$$

$$\rho_0 \left(\frac{\partial^2}{\partial t^2} - v_A^2 \frac{\partial^2}{\partial z^2} \right) v_y = \frac{\partial}{\partial y} \left[\rho_0 \Delta \left(c_s^2 + v_A^2 \right) - v_A^2 \rho_0 \Gamma \right] \,, \tag{1.27}$$

$$\frac{\partial^2 v_z}{\partial t^2} = c_s^2 \frac{\partial \Delta}{\partial z} \,. \tag{1.28}$$

Note that the z-component is independent of the equilibrium magnetic field $\mathbf{B_0}$. This is not surprising since $\mathbf{j} \times \mathbf{B}$ becomes $\mathbf{j} \times \mathbf{B_0}$ in the linear regime. This is perpendicular to the magnetic field $\mathbf{B_0}$, and so does not directly influence the plasma motion in the direction of $\mathbf{B_0}$.

Now consider Fourier components, such that

$$v_x = \hat{v}_x \left(x \right) \exp i \left(\omega t + k_y y + k_z z \right) \,, \tag{1.29}$$

and similarly for the other parameters. Following some algebra, we obtain the second order ordinary differential equation governing wave propagation in a structured media, where the equilibrium quantities depend only upon the direction perpendicular to the magnetic field (Roberts 1981a),

$$\frac{\mathrm{d}}{\mathrm{d}x} \left[\frac{\rho_0 \left(k_z^2 v_A^2 - \omega^2 \right)}{\left(m^2 + k_y^2 \right)} \frac{\mathrm{d}\hat{v}_x}{\mathrm{d}x} \right] + \rho_0 \left(\omega^2 - k_z^2 v_A^2 \right) \hat{v}_x = 0 \,. \tag{1.30}$$

Here $\hat{v}_x$ is the velocity component normal to the magnetic field, ω is the frequency and k_z is the longitudinal wavenumber. In addition

$$m^2 = \frac{\left(k_z^2 v_A^2 - \omega^2 \right) \left(\omega^2 - k_z^2 c_s^2 \right)}{\left(c_s^2 + v_A^2 \right) \left(\omega^2 - k_z^2 c_T^2 \right)} \quad \text{and} \quad c_T^2 = \frac{c_s^2 v_A^2}{c_s^2 + v_A^2} \,, \tag{1.31}$$

where c_T is the tube speed. The velocity parallel to the magnetic field is given by

$$\hat{v}_z = -\frac{ik_z c_s^2}{(\omega^2 - k_z^2 c_s^2)} \frac{\mathrm{d}\hat{v}_x}{\mathrm{d}x} . \tag{1.32}$$

More specifically, setting $k_y = 0$ so that the propagation vector is in the xz-plane, Equation (1.30) reduces to (Roberts 1981a)

$$\frac{\mathrm{d}}{\mathrm{d}x}\left[\frac{\rho_0 \left(c_s^2 + v_A^2\right)\left(\omega^2 - k_z^2 c_T^2\right)}{\left(\omega^2 - k_z^2 c_s^2\right)} \frac{\mathrm{d}\hat{v}_x}{\mathrm{d}x}\right] + \rho_0 \left(\omega^2 - k_z^2 v_A^2\right) \hat{v}_x = 0 . \tag{1.33}$$

On setting $k_y = 0$ in Equation (1.30) there is an implicit cancellation of a factor of $\left(\omega^2 - k_z^2 v_A^2\right)$. Effectively the Alfvén wave is removed from our governing equation (Equation 1.33). This may also be seen from the original wave equations; see Equations (1.26)-(1.28).

We note briefly that in the incompressible regime ($\gamma \to \infty, c_s \to \infty$) the governing equation (Equation 1.30) reduces to

$$\frac{\mathrm{d}}{\mathrm{d}x}\left[\rho_0 \left(k_z^2 v_A^2 - \omega^2\right) \frac{\mathrm{d}\hat{v}_x}{\mathrm{d}x}\right] - \rho_0 \left(k_y^2 + k_z^2\right)\left(k_z^2 v_A^2 - \omega^2\right) \hat{v}_x = 0 . \tag{1.34}$$

In obtaining Equation (1.30) we have derived equations which determine the plasma pressure perturbation ($\hat{p}_1$), the magnetic pressure perturbation ($\hat{p}_{1m}$) and the total pressure (plasma plus magnetic) perturbation ($\hat{p}_{1T}$),

$$\frac{i\omega}{\rho_0}\hat{p}_1 = -\frac{c_s^2 \omega^2}{(\omega^2 - k_z^2 c_s^2)} \frac{\mathrm{d}\hat{v}_x}{\mathrm{d}x} - \frac{\hat{v}_x}{\rho_0}\frac{\mathrm{d}p}{\mathrm{d}x} , \tag{1.35}$$

$$\frac{i\omega}{\rho_0}\hat{p}_{1m} = -v_A^2 \frac{\mathrm{d}\hat{v}_x}{\mathrm{d}x} - \frac{B}{\mu\rho_0}\left(\frac{\mathrm{d}B}{\mathrm{d}x}\right)\hat{v}_x , \tag{1.36}$$

$$\frac{i\omega}{\rho_0}\hat{p}_{1T} = -\frac{\left(c_s^2 + v_A^2\right)\left(\omega^2 - k_z^2 c_T^2\right)}{\left(\omega^2 - k_z^2 c_s^2\right)} \frac{\mathrm{d}\hat{v}_x}{\mathrm{d}x} . \tag{1.37}$$

The magnetic tension force $\hat{\mathbf{T}}_1$ takes the form

$$\frac{i\omega}{\rho}\hat{\mathbf{T}}_1 = -v_A^2 k_z^2 \hat{v}_x \hat{\mathbf{e}}_\mathbf{x} + \left(\omega^2 - k_z^2 c_s^2\right)\frac{v_A^2}{c_s^2}\hat{v}_z \hat{\mathbf{e}}_\mathbf{z} , \tag{1.38}$$

where

$$\hat{\mathbf{T}}_1 = \frac{1}{\mu_0}\left(\mathbf{B_0}\cdot\nabla\right)\hat{\mathbf{b}}_1 + \frac{1}{\mu_0}\left(\hat{\mathbf{b}}_1\cdot\nabla\right)\mathbf{B_0} , \tag{1.39}$$

and $\hat{\mathbf{b}}_1$ is the perturbed magnetic field.

It also proves convenient for our study to write the governing wave equation in terms of the driving forces, namely $-\nabla\hat{p}_1$, $-\nabla\hat{p}_{1m}$ and $\hat{T}_1$. In component form we obtain

$$-\omega^2 \hat{v}_x = -\frac{i\omega}{\rho_0}\frac{\mathrm{d}\hat{p}_1}{\mathrm{d}x} - \frac{i\omega}{\rho_0}\frac{\mathrm{d}\hat{p}_{1m}}{\mathrm{d}x} + \hat{T}_{1x} , \tag{1.40}$$

$$-\omega^2 \hat{v}_z = -\frac{i\omega}{\rho_0}\frac{\mathrm{d}\hat{p}_1}{\mathrm{d}z} - \frac{i\omega}{\rho_0}\frac{\mathrm{d}\hat{p}_{1m}}{\mathrm{d}z} + \hat{T}_{1z} , \tag{1.41}$$

where the subscripts x and z denote the projections normal and parallel to the applied magnetic field.

To gain an insight into the properties of waves in the solar atmosphere we now consider a uniform medium (the equilibrium does not depend upon x). Taking the divergence of Equation (1.25) yields

$$\frac{\partial^2 \Delta}{\partial t^2} = \left(c_s^2 + v_A^2\right) \nabla^2 \Delta - v_A^2 \nabla \Gamma \,, \tag{1.42}$$

and also taking $\partial/\partial z$ of Equation (1.28) gives

$$\frac{\partial^2 \Gamma}{\partial t^2} = c_s^2 \frac{\partial^2 \Delta}{\partial z^2} \,. \tag{1.43}$$

Equations (1.42) and (1.43) are two coupled equations for the unknown parameters $\Delta \left(\equiv \nabla \cdot \mathbf{v}\right)$ and $\Gamma \left(\equiv \partial v_z/\partial z\right)$.

Upon twice differentiating Equation (1.42) with respect to time, and then applying Equation (1.43) we obtain,

$$\left\{ \frac{\partial^4}{\partial t^4} - \left(c_s^2 + v_A^2\right) \frac{\partial^2}{\partial t^2} \nabla^2 + c_s^2 v_A^2 \frac{\partial^2}{\partial z^2} \nabla^2 \right\} \Delta = 0 \,, \tag{1.44}$$

with the same equation being obtained for Γ. Assuming harmonic time dependence

$$\Delta \left(x, y, z, t\right) = \Delta_0 \exp i \left(\omega t - \mathbf{k} \cdot \mathbf{r}\right) \,, \tag{1.45}$$

Equation (1.44) reduces to

$$\left\{ \omega^4 - \left(c_s^2 + v_A^2\right) \omega^2 k^2 + c_s^2 v_A^2 k_z^2 k^2 \right\} \Delta_0 = 0 \,, \tag{1.46}$$

where $k_z = k \cos \theta$, $\mathbf{k} = \left(k_x, k_y, k_z\right)$ and $k = \left(k_x^2 + k_y^2 + k_z^2\right)^{\frac{1}{2}}$. Here θ is the angle that the direction of propagation $\mathbf{k}$ makes with the equilibrium magnetic field $\mathbf{B_0}$. Equation (1.46) may be satisfied in one of two ways. Firstly we consider the case when Δ_0 is zero, before progressing to the case when the term inside $\{\}$ is zero.

When Δ_0 is zero we may make the following deductions from the linearised MHD equations. There are no plasma density (ρ) or pressure (p) variations; the plasma motion is *incompressible*. Furthermore the z-components of the velocity (v_z) and magnetic field (b_z) perturbations are zero; the magnetic pressure vanishes. In this case the wave equation (Equation 1.25) reduces to

$$\frac{\partial^2 \mathbf{v}}{\partial t^2} = v_A^2 \frac{\partial^2 \mathbf{v}}{\partial z^2} \tag{1.47}$$

which is the one-dimensional wave equation for the *Alfvén* mode, driven by the magnetic tension. The equation is analogous to that governing waves on an elastic string. In Fourier space Equation (1.47) reduces to

$$\omega^2 = k_z^2 v_A^2 \,. \tag{1.48}$$

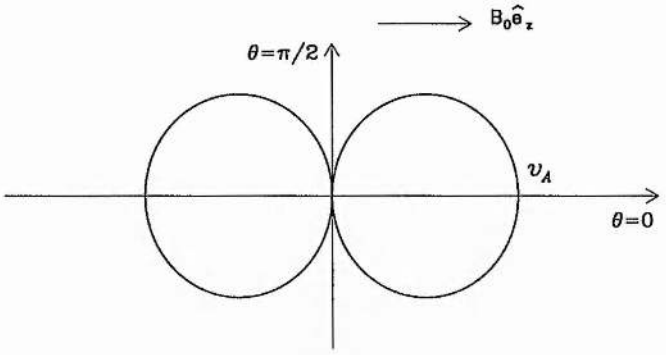

Figure 1.5: The polar diagram for Alfvén wave propagation in a uniform medium (see text). The Alfvén wave is unable to propagate perpendicularly to the magnetic field.

This is the Alfvén wave dispersion relation. The properties of the Alfvén wave may be clearly seen by considering *polar coordinates* (r, θ) if we identify $r \equiv v_{ph}\,(\equiv \omega/k) = v_{ph}\,(\theta)$, where v_{ph} is the phase speed. From Equation (1.48) we obtain $r = v_A \cos\theta$, giving $r = v_A$ at $\theta = 0$, $r = \left(1/\sqrt{2}\right) v_A$ at $\theta = \pi/4$, and $r = 0$ when $\theta = \pi/2$. More specifically, we have the equation of a circle, centre at $(r = \pm v_A/2, \theta = 0)$. See Figure 1.5. Note that perpendicular to the magnetic field $(\theta = \pi/2, k_z = 0)$ the Alfvén wave is unable to propagate.

We now consider the case $\triangle_0 \neq 0$. Fourier transforming we obtain

$$\frac{\omega^2}{k^2} = \frac{1}{2}\left(c_s^2 + v_A^2\right) \pm \frac{1}{2}\left[\left(c_s^2 + v_A^2\right)^2 - 4c_s^2 v_A^2 \cos^2\theta\right]^{\frac{1}{2}} . \tag{1.49}$$

The positive and negative square roots denote the *fast* and *slow* magnetoacoustic waves respectively. These two waves are characterised by different physical properties, which we now summarise.

To illustrate the characteristics of both the fast and slow magnetoacoustic modes we again consider a uniform medium. Therefore, the equations for the perturbed magnetic pressure and plasma pressure simplify because there is no x-dependence in the equilibrium. Furthermore, in a uniform medium we may set $\mathrm{d}v_x/\mathrm{d}x = ik_x v_x$. In this case the x and z-components of the driving forces are given by

$$-\nabla\left(\frac{i\omega}{\rho_0}\hat{p}_1\right)_x = -\frac{k_x^2 c_s^2 \omega^2}{\left(\omega^2 - k_z^2 c_s^2\right)}\hat{v}_x , \tag{1.50}$$

$$-\nabla\left(\frac{i\omega}{\rho_0}\hat{p}_1\right)_z = -\frac{k_x k_z c_s^2 \omega^2}{\left(\omega^2 - k_z^2 c_s^2\right)}\hat{v}_x , \tag{1.51}$$

$$-\nabla\left(\frac{i\omega}{\rho_0}\hat{p}_{1m}\right)_x = -v_A^2 k_x^2 \hat{v}_x , \tag{1.52}$$

$$-\nabla\left(\frac{i\omega}{\rho_0}\hat{p}_{1m}\right)_z = -v_A^2 k_x k_z \hat{v}_x , \tag{1.53}$$

with the tension force determined by

$$\frac{i\omega}{\rho_0}\hat{\mathbf{T}}_1 = -v_A^2 k_z^2 \hat{v}_x \hat{\mathbf{e}}_x + v_A^2 k_x k_z \hat{v}_x \hat{\mathbf{e}}_z \,, \tag{1.54}$$

and the total pressure perturbation by Equation (1.37).

Firstly consider the case when the phase speed is greater than the tube speed ($\omega/k_z > c_T$). This is the fast magnetoacoustic mode. The characteristics of this mode are illustrated in Figure 1.6. The x and z-components of velocity are *in phase*, with $\hat{v}_x > \hat{v}_z$ (see Figure 1.6a). The total pressure (solid line), plasma pressure (dotted line) and magnetic pressure (dashed line) are all *in phase* (Figure 1.6b). In Figure 1.6c the x-components of the driving forces act *in phase*. The tension (solid line) is *in phase* with both the negative gradients of the plasma pressure (dotted line) and the magnetic pressure (dashed line). The z-component of the driving forces show the tension (solid line) acting *out of phase* with both the negative gradient of the plasma pressure and the magnetic pressure (dotted and dashed lines respectively). See Figure 1.6d.

Next we examine the case when $\omega/k_z < c_T$ (Figure 1.7); this is the slow magnetoacoustic wave. The x and z-components of velocity are *out of phase*, with $\hat{v}_z > \hat{v}_x$ (see Figure 1.7a). In Figure 1.7b the total pressure perturbation is *in phase* with the plasma pressure, but *out of phase* with the magnetic pressure. In addition, the x-component of the tension (solid line) is *in phase* with the negative gradient of the magnetic pressure (dashed line), but *out of phase* with the negative gradient of the plasma pressure (dotted line). See Figure 1.7c. In Figure 1.7d the z-component of the tension (solid line) is *in phase* with the negative gradient of the plasma pressure (dotted line), but it acts *out of phase* with the negative gradient of the magnetic pressure (dashed line).

We can also plot the phase speed of the fast and slow magnetoacoustic waves in a polar diagram (Figure 1.8). We set $r \equiv \omega/k$ and then plot r as a function of θ, determined from the dispersion relation (Equation 1.49). The fast magnetoacoustic wave (solid curve) is able to propagate at all angles to the magnetic field. The maximum phase speed $c_f \left[= \left(c_s^2 + v_A^2\right)^{\frac{1}{2}}\right]$ occurs when the wave propagates at right angles to the magnetic field ($\theta = \pi/2$), whereas the minimum phase speed is for parallel propagation ($\theta = 0$). This speed is either v_A or c_s depending on whether $v_A > c_s$ or $c_s > v_A$ respectively. See Figures 1.8a and 1.8b. The slow magnetoacoustic mode (dotted line) is unable to propagate perpendicularly to the magnetic field (zero phase speed). The maximum phase speed occurs for parallel propagation, attaining c_s if $v_A > c_s$ or v_A if $c_s > v_A$.

1.5 Coronal Heating

One of the most puzzling aspects of the Sun is the presence of the hot corona. The coronal plasma is in excess of 10^6 K, 100 times larger than the temperature in the photosphere. The literature on this subject is vast, and here we give only a brief outline of the main theories. Comprehensive reviews may be found in Narain and Ulmschneider (1990, 1996), Hollweg (1990), Browning (1991), Zirker (1993) and Laing (1996).

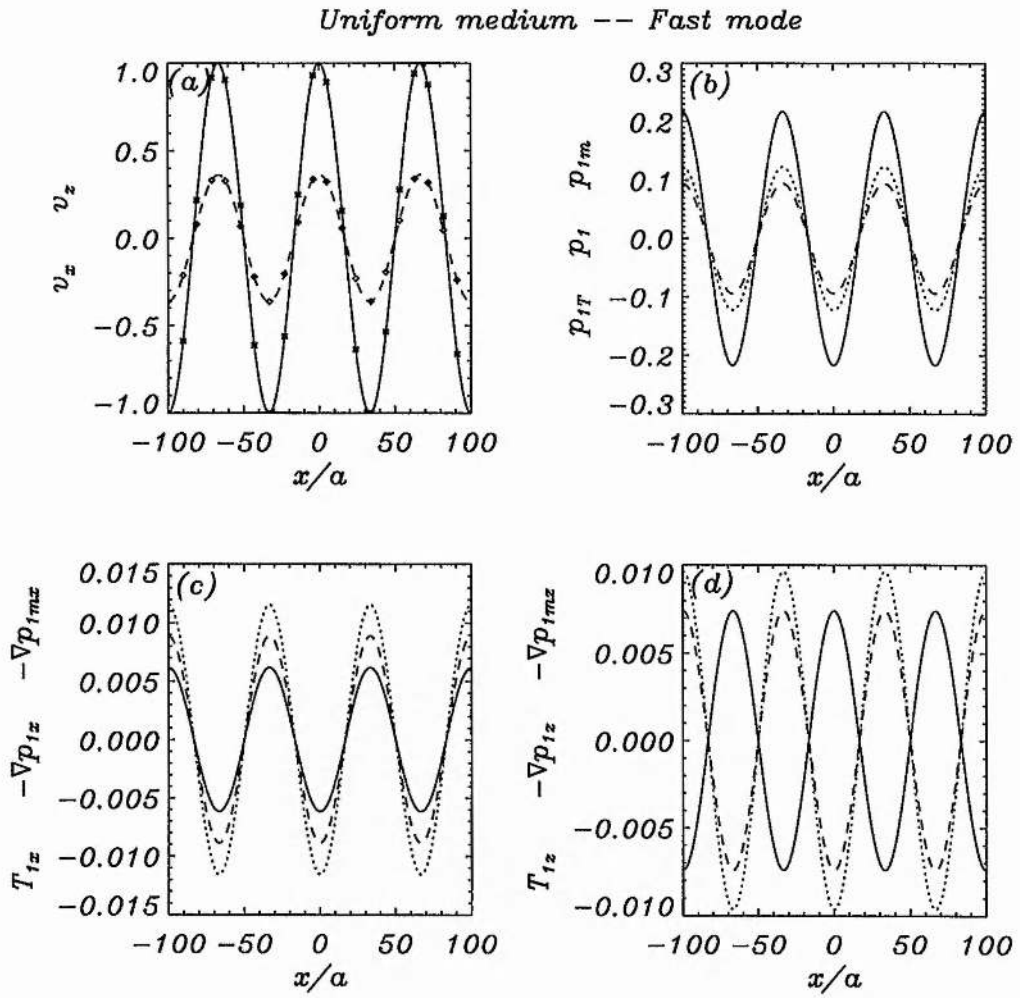

Figure 1.6: The fast magnetoacoustic mode in a uniform, unstructured medium. In (a) we see the x-component of velocity (solid line) is larger in amplitude than the z-component (dashed line), and in phase. The diamonds and asterisks show the sum of the driving forces. In (b) the fast mode is characterised by the total pressure perturbation (solid line) acting in phase with both the plasma (dotted line) and magnetic (dashed line) pressure perturbations. Panel (c) shows the x-components of the driving forces acting in phase; the tension (solid line) is in phase with both the negative gradients of the plasma pressure (dotted line) and magnetic pressure (dashed line). Finally, in (d), the z-component of the driving forces show the tension (solid line) acting out of phase with the negative gradient of both the plasma pressure and magnetic pressure (dotted and dashed lines respectively).

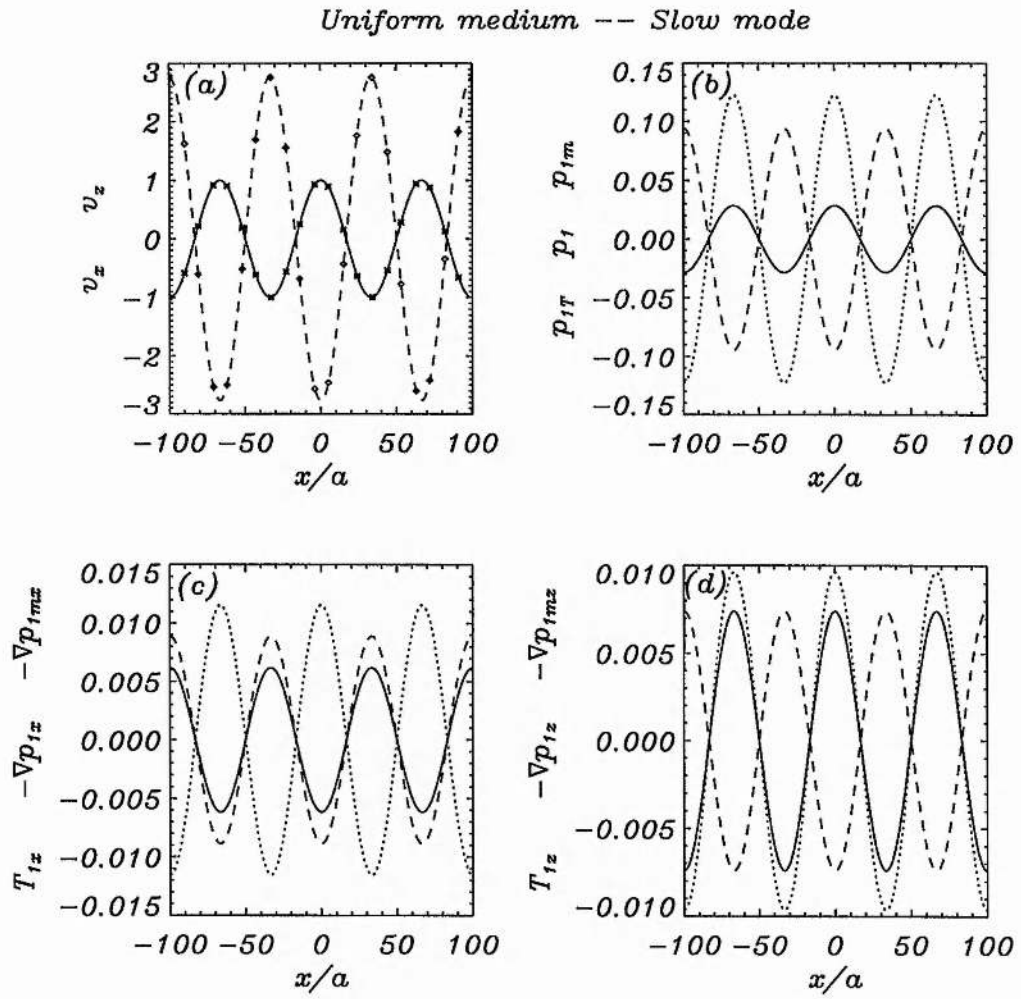

Figure 1.7: The slow magnetoacoustic mode in a uniform medium. In (a) we see that the x-component of velocity (solid line) is smaller in amplitude than the z-component (dashed line), and out of phase. The diamonds and asterisks show the sum of the driving forces. The slow mode is characterised by the total pressure perturbation (solid line) acting in phase with the plasma pressure perturbation (dotted line), but out of phase with the magnetic pressure perturbation (dashed line); see (b). In (c) the x-component of the tension (solid line) is in phase with the negative gradient of the magnetic pressure (dashed line), and out of phase with the negative gradient of the plasma pressure (dotted line). Finally, in (d), the z-component of the tension (solid line) is in phase with the negative gradient of the plasma pressure (dotted line), but it acts out of phase with the negative gradient of the magnetic pressure (dashed line).

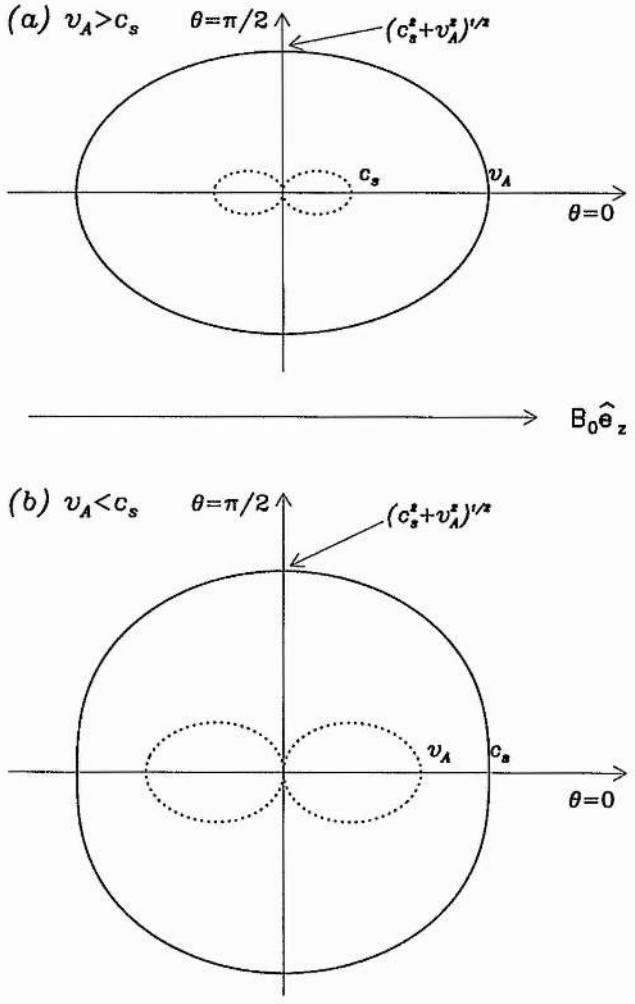

Figure 1.8: The polar diagram for fast and slow magnetoacoustic waves in a uniform medium. In (a) we have the case $v_A > c_s$; specifically we have taken $v_A = 3c_s$. The slow wave (dotted line) is unable to propagate perpendicularly to the field. The fast wave (solid line) has its lowest phase speed (v_A) when propagating parallel to the field ($\theta = 0$). The fastest phase speed $c_f = \left(c_s^2 + v_A^2\right)^{\frac{1}{2}}$ occurs when the wave is propagating at right angles to the field ($\theta = \pi/2$). In (b) we illustrate the case $v_A < c_s$, where we have taken $c_s = 1.5v_A$. Similar results are obtained as in (a), except the roles of the sound and Alfvén speeds are interchanged.

It is natural to believe that the magnetic field plays a role in the heating of the corona. The energy source for heating the coronal plasma originates from the kinetic energy of the photospheric plasma, caused by convective motions. The kinetic energy of the convection is transferred to the coronal field by the footpoint motions. Ionson (1984) and Browning (1991) classify the heating mechanisms on two time scales, namely the photospheric field (τ_v) and the Alfvén transit time (τ_A) across the structure.

Consider first the case when the footpoint motions are slow compared with the Alfvén transit time. The magnetic field becomes twisted and braided and currents are generated because of Ampère's law. These currents can be dissipated and the magnetic energy can be converted into heat. Such heating mechanisms are classified as *Direct Current* (DC). Another DC mechanism is magnetic reconnection, which involves the topological change of the magnetic field and subsequent release of energy.

Suppose, however, that the footpoint motions are fast. In this case both Alfvén and magnetoacoustic waves may be generated. These MHD waves may dissipate their energy and heat the corona. We now give a brief description of two of the main candidates, namely *phase mixing* and *resonant absorption.* Narain and Ulmschneider (1990, 1996) indicate that these dissipation mechanisms are the most likely ways in which an Alfvén wave may convert its energy into heat. These heating mechanisms are denoted by AC (*Alternating Current*).

Alfvén waves that are excited in phase on different magnetic field lines will move out of phase as time increases, since each magnetic surface oscillates with its natural frequency. Consequently large gradients develop across the field lines, generating small length scales and wave damping. This process is called phase mixing (see, for example, Heyvaerts and Priest 1983; Hood, Ireland and Priest 1997).

Resonant absorption involves the excitation of resonant Alfvén waves by magnetoacoustic waves. The condition that resonance occurs is that the frequency of the resonant field line is equal to the frequency of the driver (see, however, Chapter 5). At the resonant field line energy is transferred from the large scale magnetoacoustic wave to the Alfvénic resonance, which is localised along a field line. Small length scales are generated and dissipation is enhanced (Goossens 1994).

In addition, the energy carried by guided magnetoacoustic waves in coronal loops may be converted into heat. For a review and detailed investigation see Laing (1996).

At present, observations are unable to provide information about which mechanism occurs. However the recently launched SoHO mission will hopefully provide some insight.

1.6 The SoHO Mission

The SoHO (Solar and Heliospheric Observatory) satellite, launched on 2 December 1995, is beginning to provide exciting new observations of dramatic events occurring on the Sun. The spacecraft is located at the Lagrangian L_1 point, where the gravitational attraction of the Sun and

the Earth are balanced. Therefore SoHO is able to monitor the Sun continuously. A summary of the latest results from the twelve onboard instruments may be found in Lang (1997). For a more detailed description of the instruments see Domingo, Fleck and Poland (1995) and Volume 162 of the Solar Physics Journal. Here we give a brief outline of each of the experiments, together with some of the highlights obtained so far (Lang 1997). The latest images from the spacecraft may be found on the SoHO home page on the World Wide Web located at http://sohowww.nascom.nasa.gov.

Three of the instruments are related to helioseismology. Oscillations of the solar surface are detected to a resolution of one millimetre per second with the Michelson Doppler Imager (MDI) and GOLF (Global Oscillations at Low Frequencies). In addition VIRGO (Variability of solar IRradiance and Gravity Oscillation) measures intensity changes on the solar surface down to a tiny fraction of the Sun's brightness. An important objective for the GOLF experiment is to detect g modes. These are oscillations where the restoring force is gravity. These experiments will soon have taken enough data to provide important information regarding the density and temperature of the solar interior.

It is a well established result that the photosphere rotates faster at the equator than at higher latitudes. Recently, data taken with the MDI on SoHO has shown that differential rotation occurs throughout the convection zone as well. Furthermore, the differential rotation was found to be zero in the radiative zone (the rotation speed was uniform from pole to pole). Therefore the rotation velocity changes dramatically between the radiative and convective zones. A shear layer in rotation velocity between the two regions exists, which is thought be the source of the magnetic field.

The MDI experiment has also been used in a technique called "time distance helioseismology". Results are obtained which show the motion of the plasma just below the photosphere. Scientists working on this instrument can obtain the three-dimensional interior structure of the Sun. Furthermore, results have shown that concentrated regions of magnetic field arise where the sub-surface plasma flows converge.

The ultraviolet and extreme ultraviolet emission from the Sun is measured by four instruments, namely EIT (Extreme ultraviolet Imaging Telescope), SUMER (Solar Ultraviolet Measurement of Emitted Radiation), CDS (Coronal Diagnostic Spectrometer) and the UVCS (UltraViolet Coronagraph Spectrometer). Preliminary results show enhanced ultraviolet emission in localised bright spots, even at times of low solar activity. The UVCS instrument has examined the spectral emission of hydrogen and the heavily charged oxygen ions. In polar coronal holes the oxygen ions were found to have sixty times the energy of the hydrogen ions. This is in contrast to the equatorial region, where the hydrogen moves faster than the oxygen. This is potentially interesting since oxygen is heavier than hydrogen. A thorough understanding of these results will provide important information about the physical processes occurring.

To examine the higher levels in the solar atmosphere the LASCO (Large Angle Spectroscopic COronagraph) is used. This instrument has provided startling new information regarding coronal mass ejections. These are dynamic events which eject large amounts of plasma into the solar

system. Results show that mass ejections occur within hours of each other on the west and east sides of the Sun; see Figure 1.9. It has been suggested that mass ejection may occur all around the Sun simultaneously.

The Solar Wind ANisotropies (SWAN) instrument measures interstellar hydrogen. The main objective of the instrument is to determine the large scale solar wind proton flux distribution. The CELIAS (Charge, ELement and Isotope Analysis System) instrument measures the abundance of elements and isotopes. This is the first time such observations have been undertaken. The other instruments COSTEP (COmprehensive SupraThermal Energetic Particle) and ERNE (Energetic and Relativistic Nuclei and Electron) have begun to take in-situ measurements of energetic electrons, protons and helium nuclei approaching the Earth. The source of these particles are violent explosions which have been detected with the EIT experiment.

This brief review has shown that SoHO is taking results which will increase our understanding of the processes occurring on the Sun. However, SoHO may not be able to increase our knowledge of short period coronal oscillations. In particular, for the CDS instrument the temporal and spatial resolutions are theoretically 1 second and 2 arcseconds respectively. However, for practical purposes the temporal resolution is of the order 10 seconds. Therefore the high frequency oscillations (of the order of 1 second) are beyond the scope of the experiment. However, long period oscillations may be detected, and some evidence for 15 minute modulations in the coronal plasma has been given by Ireland, Walsh, Harrison and Priest (1997). The EUV and UV instruments may be able to improve greatly our knowledge of the solar corona, and in particular coronal loops.

1.7 Outline of Thesis

As seen from the discussion in this introductory chapter, there are many reported examples of oscillations in the coronal plasma. In this thesis we are concerned with the ducting of magnetoacoustic waves in the solar corona, to provide an explanation for these observations.

This introductory chapter has presented an overview of the properties of the Sun, paying particular attention to the solar corona. The basic equations of ideal magnetohydrodynamics have been given. A review of the oscillatory behaviour observed on the Sun has been presented, and a summary of wave theory in plasmas has been given. Details of the instruments onboard the SoHO spacecraft and the latest results obtained have been summarised.

In Chapter 2 we investigate the guiding of fast magnetoacoustic waves in curved coronal loops. Much of the previous work focussed upon magnetic slabs or cylinders, with curvature effects neglected for mathematical simplicity. In this chapter we relax this assumption.

In Chapters 3 and 4 we examine the ducting of magnetoacoustic waves in a current sheet. Initially in Chapter 3, we determine the dispersion relations and the nature of the modes which may propagate in a current sheet. A comparison with the observations is also made. In Chapter 4 numerical simulations of impulsively generated waves are examined.

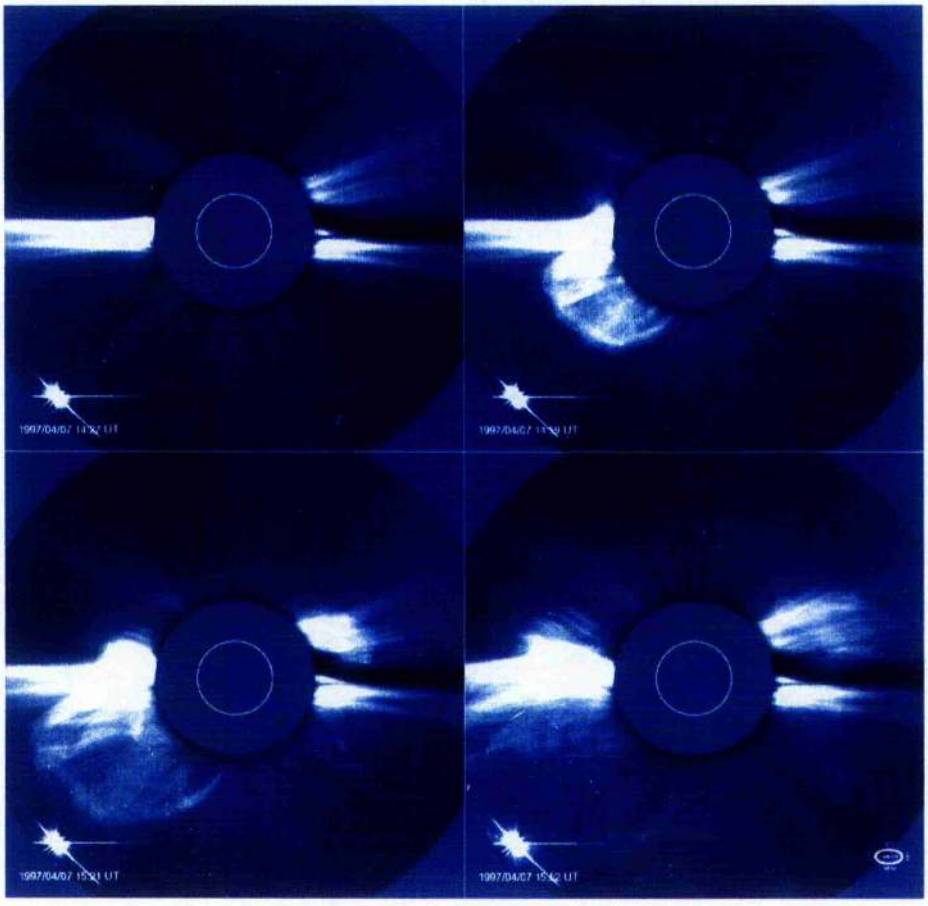

Figure 1.9: Sequence of images recorded by the LASCO c2 coronagraph showing the large coronal mass ejection of 7 April 1997. The first frame shows the corona at time 14:27, just before the eruption. The first stage of the eruption is seen in the upper right-hand corner, at time 14:59. In the fourth image (15:52) one can see a brightening around the entire Sun, instead of just in one direction. Material ejected in this event reached the Earth during the night of 10-11 April. A significant amount of geomagnetic activity was observed in northern regions of the world, reaching as far south as New Hampshire and Montana. Caption and image taken from the LASCO home page on the World Wide Web (http://sohowww.nascom.nasa.gov/gallery/LASCO/index.html).

In Chapter 5 a brief investigation is made into the effect of a random driver in a two-dimensional inhomogeneous cavity. Previous workers have often examined monochromatic driving sources. In this chapter we explore the differences between the random and periodic driving mechanisms.

Chapter 6 is a preliminary investigation into three-dimensional reconnection. In this chapter we are concerned with the three-dimensional magnetic topologies surrounding neutral points. This work is an extension of the two-dimensional cases studied previously.

Finally, in Chapter 7 our conclusions are drawn, and suggestions for further work made.

Chapter 2

Ducted Waves in Coronal Loops: Curvature Effects

2.1 Introduction

Periodic and quasi-periodic oscillations commonly occur in the solar corona with time scales ranging from sub-second to many minutes. Reviews of the observations may be found in Aschwanden (1987) and Tsubaki (1988); see also Tables 1.5, 1.6 and 1.7. Various theoretical models have been proposed to explain these observations and these are reviewed in Aschwanden (1987).

It has been suggested that the detected coronal pulsations may be magnetoacoustic waves trapped in coronal loops (Roberts, Edwin and Benz 1983, 1984) or oscillations within coronal arcades (Oliver, Ballester, Hood and Priest 1994; Oliver, Hood and Priest 1996). Theoretical models for studying magnetoacoustic wave propagation in coronal loops have focussed upon (for physical insight and mathematical simplicity) magnetic slabs or cylinders, ignoring the curvature of a loop. Whilst these models have been successful in explaining the time scales of the pulsations in the solar corona recent observations of X-ray emission, obtained by the Yohkoh satellite (Acton et al. 1992), have emphasised the complex, highly structured nature of the corona. The active region corona consists mainly of dense, curved loops, the transverse dimensions of which are much shorter than the longitudinal ones (Golub 1991). It is natural to believe the curvature of the loops will affect the propagation of the magnetoacoustic modes. It is the purpose of this chapter to investigate the efficiency of wave ducting in curved coronal loops and to investigate how curvature alters wave propagation in such structures.

The format of this chapter is as follows. In Section 2.2 we review the slab or cylinder ducted wave model of Roberts, Edwin and Benz (1983, 1984). In Section 2.3 a comprehensive review of the work undertaken in *curved* dielectric waveguides is presented and in Section 2.4 a review of the previous work on leaky waves in the solar atmosphere is conducted. Our model is described

in Section 2.5 and the results for the kink and sausage modes are given in Sections 2.6 and 2.7 respectively. Our results are discussed and physical explanations given in Section 2.8. Finally our results are summarised in Section 2.9.

2.2 Ducted Wave Model of Roberts, Edwin and Benz (1983, 1984)

In Chapter 1 we noted that periods of a few seconds are commonly reported in the solar corona. Considering a loop of length 2×10^5 km and a typical coronal Alfvén speed of 2000 km s^{-1} gives a characteristic Alfvén time scale of 100 seconds, which is two orders of magnitude greater than the reported time scales in certain observations. Roberts, Edwin and Benz (1983, 1984) suggested this puzzle may be resolved by considering magnetoacoustic wave propagation in a structured media. Their analysis showed that fast magnetoacoustic waves are trapped in regions of low Alfvén speed, typically corresponding to regions of high plasma density. Therefore coronal loops, which typically have a density 3 to 10 times greater than the surrounding plasma (see Table 1.2) may act as waveguides. To illustrate this consider a coronal loop modelled as a dense slab of width $2a$ with plasma density ρ_0, embedded in an environment of density ρ_e ($< \rho_0$). The magnetic field is taken to be uniform and straight $\mathbf{B} = B_0 \hat{\mathbf{e}}_z$, ignoring the effect of curvature (Figure 2.1). The cold plasma approximation is employed (plasma beta equal to zero). The linearised MHD equations lead to the governing wave equation for transverse oscillations $v_x \hat{\mathbf{e}}_x$:

$$\frac{\partial^2 v_x}{\partial t^2} = v_A^2(x) \nabla^2 v_x \,, \tag{2.1}$$

where $v_A(x)$ is the Alfvén speed within the medium and takes the value v_{A0} in the dense slab and v_{Ae} ($> v_{A0}$) in the environment. Equation (2.1) describes fast magnetoacoustic modes; the slow mode is absent in the zero-β approximation. We also take $v_y = 0$ so the Alfvén wave is removed and set $\partial/\partial y \equiv 0$. Assuming v_x takes the form

$$v_x(x,z,t) = U(x) \exp\left[i(\omega t - k_z z)\right] \,, \tag{2.2}$$

the partial differential equation (Equation 2.1) reduces to an ordinary differential equation for the amplitude function $U(x)$,

$$\frac{\mathrm{d}^2 U}{\mathrm{d}^2 x} + \left(\frac{\omega^2}{v_A^2(x)} - k_z^2\right) U = 0 \,. \tag{2.3}$$

Here ω and k_z are the frequency and longitudinal wavenumber respectively.

Inside the dense slab Equation (2.3) possesses a solution of the form,

$$U(x) = \alpha_0 \cos n_0 x + \beta_0 \sin n_0 x \qquad |x| < a \,, \tag{2.4}$$

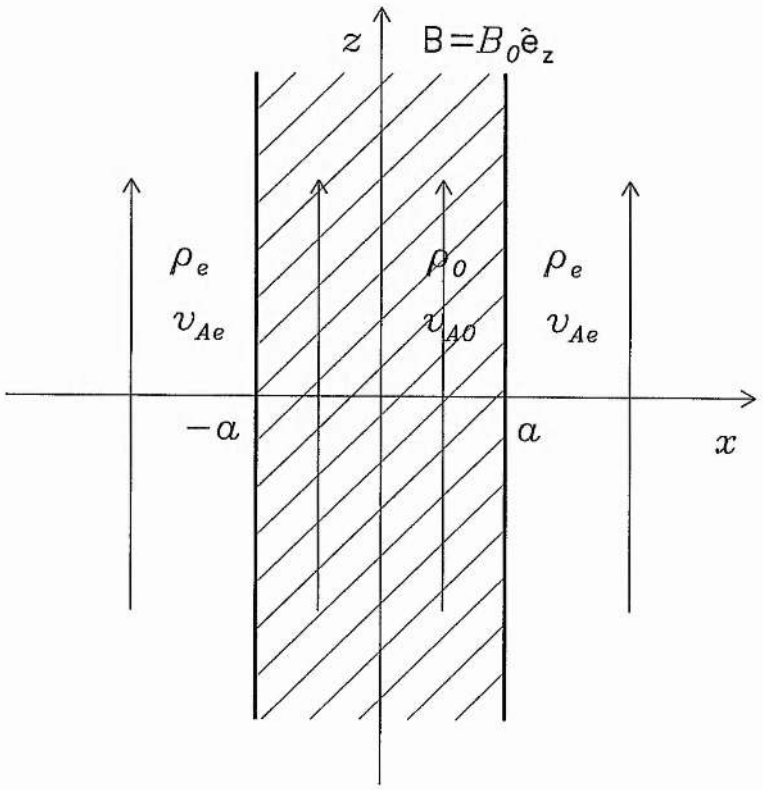

Figure 2.1: The equilibrium for the ducted wave model of Roberts, Edwin and Benz (1983). A slab of width $2a$ and plasma density ρ_0 is embedded in a region of uniform density $\rho_e (< \rho_0)$. Regions of high density (low Alfvén speed) act as waveguides.

where $n_0^2 = (\omega^2/v_{A0}^2) - k_z^2$. The arbitrary constants α_0 and β_0 may be constrained by the boundary conditions at $x = 0$. The *sausage* mode describes waves which disturb the slab symmetrically about $x = 0$, so that $U(x = 0) = 0$; this corresponds to the case $\alpha_0 = 0$ so that $U(x) = \beta_0 \sin n_0 x$ for $|x| < a$. The *kink* mode involves disturbing the axis of the slab and corresponds to the case $\beta_0 = 0$ and so $U(x) = \alpha_0 \cos n_0 x$ for $|x| < a$.

Outside the slab ($|x| > a$) we assume that the velocity decreases exponentially to zero as $|x| \to \infty$. Therefore

$$U(x) = \alpha_e \exp[-m_e(x - a)] \qquad x > a\,, \tag{2.5}$$

$$U(x) = \alpha_e \exp[m_e(x + a)] \qquad x < -a\,, \tag{2.6}$$

where $m_e^2 = k_z^2 - (\omega^2/v_{Ae}^2)$. To satisfy the boundary condition at infinity we require $m_e^2 > 0$, i.e. $\omega^2 < k_z^2 v_{Ae}^2$.

To obtain the dispersion relations we apply the condition that the velocity and the total pressure perturbation are continuous across the boundaries ($x = \pm a$). The resulting dispersion relations are given by

$$\tan n_0 a = \frac{m_e}{n_0} \tag{2.7}$$

for the kink modes ($\mathrm{d}U/\mathrm{d}x = 0$ at $x = 0$) and

$$\tan n_0 a = -\frac{n_0}{m_e} \tag{2.8}$$

for the sausage modes ($U = 0$ at $x = 0$). Roberts et al. (1983, 1984) note the similarity of these dispersion relations with those arising in seismology, oceanography and fibre optics.

A solution of these dispersion relations may be obtained only when $v_{A0} < v_{Ae}$ (i.e. when the slab is denser than the surroundings) and then the phase speed ω/k_z must lie in the range

$$v_{A0} < \frac{\omega}{k_z} < v_{Ae}\,, \tag{2.9}$$

since we must also have $n_0^2 > 0$. We have assumed that ω and k_z are positive. The dispersion curves for a density enhancement of $\rho_0/\rho_e = 5$ are illustrated in Figure 2.2, with kink and sausage modes denoted by dashed and solid lines respectively.

The fundamental kink mode exists for all values of the wavenumber k_z. The period of oscillation of this mode in a slab of length L may be estimated by setting $k_z = n\pi/L$ and taking $\omega/k_z \approx v_{Ae}$, yielding

$$\tau_{kink} = \frac{2L}{n v_{Ae}}\,, \tag{2.10}$$

where $(n - 1)$ is the number of nodes along the structure. This is the period of a kink standing wave in a slab. Taking $L = 10^5$ km and $v_{Ae} = 3000$ km s^{-1} with $n = 1$ (since this is the easiest mode to excite) we obtain a period of about 60 seconds. This is in agreement with the recent observations of Rušin and Minorovjech (1991, 1994); see also Tables 1.5, 1.6 and 1.7.

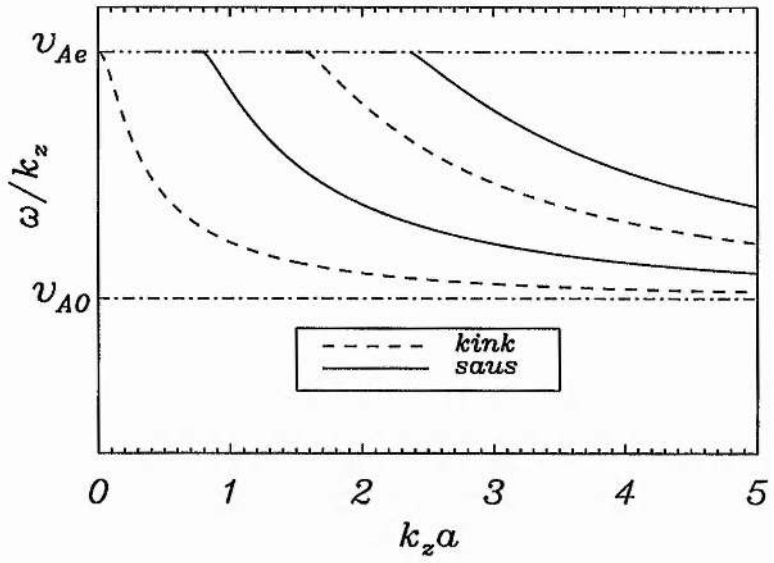

Figure 2.2: The dispersion curves for fast magnetoacoustic body waves in the slab model of Roberts, Edwin and Benz (1983). The density of the loop is five times that of the surrounding medium ($\rho_0/\rho_e = 5$). No slow body modes exist in this case since we have used the cold plasma approximation. The phase speeds (ω/k_z) of the fast magnetoacoustic body modes lie between the interior (v_{A0}) and exterior (v_{Ae}) Alfvén speeds; equilibrium pressure balance in a zero-β plasma requires that $\rho_0 v_{A0}^2 = \rho_e v_{Ae}^2$. Sausage modes are shown as full curves, kink modes as dashed curves. The fundamental kink mode exists for all values of $k_z a$ whereas the sausage mode exists only above a wavenumber threshold. Kink and sausage overtones exist only above wavenumber thresholds.

On the other hand, the fundamental sausage mode only occurs above a wavenumber threshold $k_z > k_z^{crit}$, where

$$k_z^{crit} a = \frac{\pi}{2} \left(\frac{1}{\frac{\rho_0}{\rho_e} - 1} \right)^{\frac{1}{2}} . \tag{2.11}$$

The period of oscillation at the onset of this mode, τ_{saus}, may be estimated by setting $\omega/k_z = v_{Ae}$ at $k_z = k_z^{crit}$ so that

$$\tau_{saus} = \frac{4a}{v_{A0}} \left(1 - \frac{\rho_e}{\rho_0} \right)^{\frac{1}{2}} . \tag{2.12}$$

Considering typical coronal values of $\rho_0/\rho_e = 3$, $a = 1000$ km and $v_{A0} = 2 \times 10^3$ km s^{-1} a period of 1.6 seconds is obtained at the onset of the sausage mode. This compares well with observations by Aschwanden, Benz, Dennis and Gaizauskas (1993), Thomas, Neupert and Thompson (1986) and Desai et al. (1986) amongst others (see Tables 1.6 and 1.7). Roberts, Edwin and Benz (1983, 1984) argue that short period oscillations may be due to loops oscillating in the sausage mode. The short period oscillations in microwaves reported by Zhao, Jin, Fu and Li (1990) have been attributed to propagating waves in a coronal loop. Their results are in good agreement with the theory of impulsively generated waves proposed by Roberts et al. (1983, 1984); see Edwin (1984) for a full discussion of propagating waves. We return to impulsively generated waves in Chapter 4.

The main effect of relaxing the zero-β assumption is to introduce slow body waves, absent when $\beta = 0$. Their phase speed lies between the sound speed and the tube speed of the slab. When β is small these two speeds are close together. To estimate the period of oscillation of a slow mode we may set $\omega/k_z \approx c_{s0}$ and $k_z = n\pi/L$ to give

$$\tau_{slow} = \frac{2L}{nc_{s0}} , \tag{2.13}$$

where c_{s0} is the sound speed in the coronal slab or loop. For $L = 10^5$ km, $c_{s0} = 200$ km s^{-1} and $n = 1$ a period of 16.7 minutes is obtained. This is in reasonable agreement with the observations of Švestka et al. (1982, 1989) and Švestka (1994). These authors have suggested that the 20 minute periods may be due to slow mode oscillations of a coronal loop. Harrison (1987) reports periods of 24 ± 2 minutes over a 6 hour period using soft X-ray measurements and gives the loop length as 2×10^5 km. Using a reasonable value for c_{s0} of 280 km s^{-1} Equation (2.13) gives this observed period. These long period oscillations may be due to slow standing waves in a coronal loop.

We extend the model of Roberts, Edwin and Benz (1983, 1984) by considering the more realistic situation of ducted waves in curved loops, in a potential coronal arcade. To gain an insight into this problem we firstly review the work on wave propagation in curved waveguides. By analogy with the work on trapped waves in curved waveguides (see, for example, Gloge 1972) we gain an insight into magnetoacoustic wave propagation in curved coronal loops (see also Edwin 1984).

2.3 Previous work on curved dielectric waveguides

Wave propagation in curved waveguides has been extensively investigated (see, for example, Marcatili and Miller 1969; Marcatili 1969; Marcatili 1970; Gloge 1972; Snyder and Love 1983; Young 1986). It is found that for dielectric waveguides leaky waves arise due to curvature and power is radiated away from the guide. If the radius of curvature is large (so the straight guide is a good approximation to the curved structure) losses due to the curvature are found to be negligible. As the radius of curvature decreases (so the effect of curvature increases) power is lost rapidly. The energy loss is reduced by increasing the ratio of the refractive index of the guide to that of the surrounding medium. This is equivalent to increasing the density enhancement between a coronal loop and its environment. Also wide guides are found to be more efficient ducts than narrow guides. Waveguides with smoother profiles of refractive index are less efficient and greater energy losses occur than for a step profile. Gloge (1972) and Olshansky (1979) showed that the energy loss in a parabolic profile is twice that of a slab. For smooth profiles part of the wave travels near the edge of the guide where the refractive index is close to the value in the surrounding medium. Wave guiding is therefore less efficient. Considering the propagation of light in optical waveguides Olshansky (1979) and Young (1986) find the radiation loss is dependent upon the mode of oscillation. For modes above a critical mode number all power is immediately lost. Lower order modes are represented by rays inclined with angles much greater than the critical angle (see Section 2.4.3). They correspond to rays that travel along the guide at near grazing incidence. These modes will not suffer significant energy loss unless the bend is sharp (Young 1986). However higher order modes (rays which are incident at angles near the critical angle) will invariably become lossy. Therefore higher harmonics suffer greater energy loss than lower order modes. Young (1986) also suggests that modes which have more power in the outer part of the waveguide will suffer greater loss than modes whose power lies along the axis of the guide. This suggests the sausage mode of a coronal structure will be guided less effectively than the kink mode.

Assuming a coronal loop is analogous to a waveguide, we expect the most efficient guiding of waves in a curved loop to occur under the following conditions:

- low order modes,
- high density enhancements,
- large radius of curvature,
- wide loops.

One effect of curvature is to reduce the angle of incidence. In Section 2.4.3 we shall see that a decrease in the angle of incidence results in an increased leakage. Figure 2.3 shows a ray incident at an angle θ_I just before a bend in a waveguide. After traversing the bend the angle of incidence is less than θ_I; the transmission of wave energy from the guide then increases.

When light is incident upon a curved surface the usual laws of geometrical optics break down. Rays that strike the curved interfaces are partly transmitted and partly reflected even if the

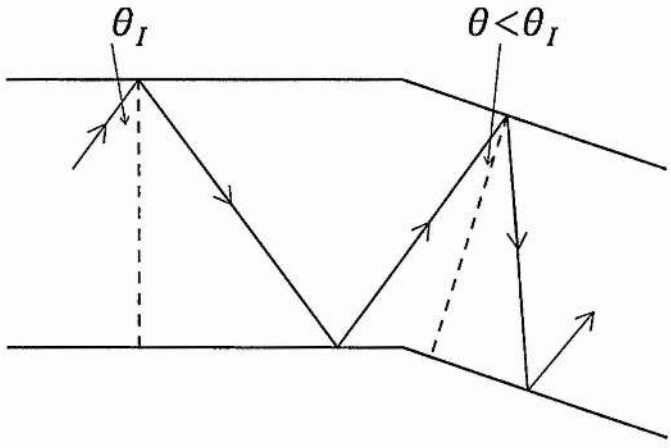

Figure 2.3: A sketch showing how the angle of incidence θ_I decreases due to the effect of curvature. The dashed line represents the normal to the waveguide wall (modified from Young 1986).

angle of incidence exceeds the critical angle. What is the mechanism which causes this? Young (1986) suggests how energy loss may arise in a curved waveguide. The amplitude of the evanescent wave in the environment of the guide decreases with distance. The oscillatory wave within the guide propagates with a certain speed and the evanescent wave must keep pace with this propagating wave. As we move further away from the curved guide the evanescent wave's speed must attain higher values, since it travels a longer distance in the same time. Eventually the speed of the evanescent wave will reach the velocity of light (equivalent to the exterior Alfvén speed in the coronal loop case). At this point the evanescent wave becomes a propagating wave and therefore energy is radiated. Note that in a straight guide the oscillatory and evanescent waves propagate at the same speed.

We may estimate the energy loss in a coronal loop by analogy with the dielectric results of Gloge (1972). Following Edwin (1984) we consider a coronal loop with major radius R, uniform density ρ_0 and Alfvén speed v_{A0} embedded in an environment of density ρ_e and Alfvén speed v_{Ae} (Figure 2.4). The stretching of the loop at the outside of the bend leads to a decrease of the wavenumber k_z. The effective wavenumber is a function of x (the transverse distance into a loop's exterior, measured from its axis). Therefore

$$k_z(x) = k_z(0)\frac{1}{1+\frac{x}{R}}, \tag{2.14}$$

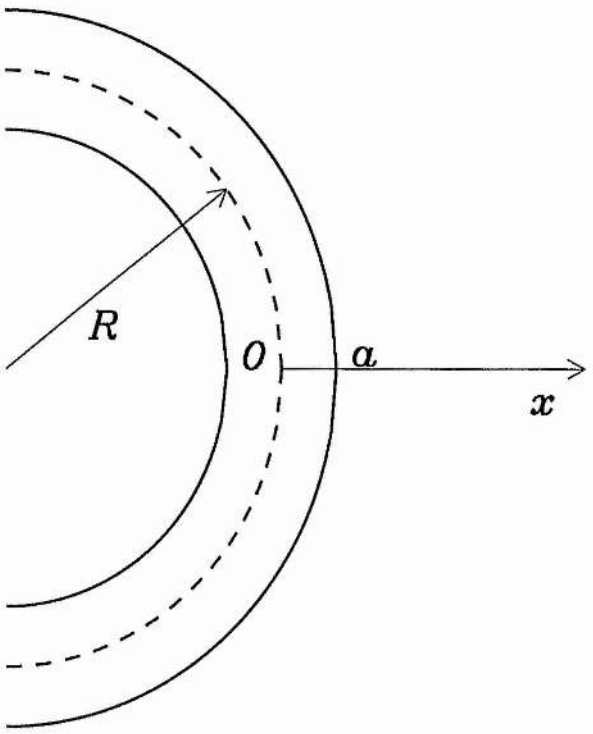

Figure 2.4: A schematic sketch of the curved coronal loop (modified from Gloge 1972). A dense curved coronal loop (ρ_0) is embedded in an environment of density ρ_e ($< \rho_0$). By analogy with dielectric waveguides we may expect waves to leak from coronal loops.

and as $R \to \infty$, $k_z(x) \to k_z(0)$. For a straight loop velocities in the exterior of the loop decrease as

$$\exp\left[-m_e(0)(x-a)\right] , \tag{2.15}$$

where in the cold plasma approximation $m_e^2(0) = k_z^2(0) - \left(\omega^2/v_{Ae}^2\right)$. For a curved loop, where the wavenumber k_z and m_e are now x-dependent, the exterior velocity decreases as

$$\exp\left[-\int_a^x m_e(x)\mathrm{d}x\right] . \tag{2.16}$$

Here $m_e^2(x) = k^2(0)/(1+x/R)^2 - \left(\omega^2/v_{Ae}^2\right)$. To make analytical progress we use the following approximate form of $m_e^2(x)$,

$$m_e^2(x) \approx m_e^2(0) - 2k_z^2(0)\frac{x}{R} , \tag{2.17}$$

obtained by using a binomial expansion. The validity of this approximation requires $x \ll R$.

At a point where $x = x_R$, $m_e(x_R) = 0$. At this location the evanescent wave transforms into an oscillatory wave and energy passing through this point is radiated away. The resulting loss in energy is proportional to the square of the velocity. The constant of proportionality is given by Gloge (1972) as $2m_e^2(0)/k_z(0)$. The energy loss coefficient is therefore given by

$$\alpha = 2\frac{m_e^2(0)}{k_z(0)}\exp\left[-2\int_a^{x_R} m_e(x)\mathrm{d}x\right] . \tag{2.18}$$

Performing the integral in Equation (2.18) yields

$$\alpha = \frac{2}{k_z(0)}\left(k_z^2(0) - \frac{\omega^2}{v_{Ae}^2}\right)\exp\left[-\frac{2R}{3k_z^2(0)}\left(k_z^2(0) - \frac{\omega^2}{v_{Ae}^2} - 2k_z^2(0)\frac{a}{R}\right)^{\frac{3}{2}}\right] , \tag{2.19}$$

upon noting that $m_e(x_R) = 0$. Now assuming $k_z(0)a \approx 1$, $\omega \approx k_z(0)v_{A0}$, and then writing $\rho \equiv v_{Ae}^2/v_{A0}^2 = \rho_0/\rho_e$, Equation (2.19) reduces to

$$\alpha R = 2R^*\left(1 - \frac{1}{\rho}\right)\exp\left[-\frac{2}{3}R^*\left(1 - \frac{1}{\rho} - \frac{2}{R^*}\right)^{\frac{3}{2}}\right] , \tag{2.20}$$

where $R^* = R/a$. The quantity αR is the dimensionless energy loss coefficient.

To estimate αR we use values from Table 1.4. Considering $R/a = 25$ and $\rho = 3$ we obtain $\alpha R = 0.0186$. The effect of curvature is to introduce an energy loss from the guide. Figure 2.5a shows how the energy loss depends upon the radius of curvature for a typical density enhancement of 3. For small R^* leakage is important $\left(\alpha R \approx 10^{-1}\right)$. As R^* increases the energy loss rapidly decreases and for $R^* = 100$ we calculate $\alpha R \approx 10^{-13}$. Therefore guides with a small radius of curvature will be less efficient at guiding waves than waveguides with a large radius; as $R^* \to \infty$, $\alpha R \to 0$. Figure 2.5b illustrates how the energy leakage depends upon the density enhancement for a fixed value of $R^* = 20$. For low density enhancements leakage is considerable (when $\rho = 3, \alpha R \approx 0.1$). As ρ increases the energy loss decreases and tends to a constant value for $\rho \gg 1$ of

$$(\alpha R)_{min} = 2R^*\exp\left[-\frac{2}{3}R^*\left(1 - \frac{2}{R^*}\right)^{\frac{3}{2}}\right] . \tag{2.21}$$

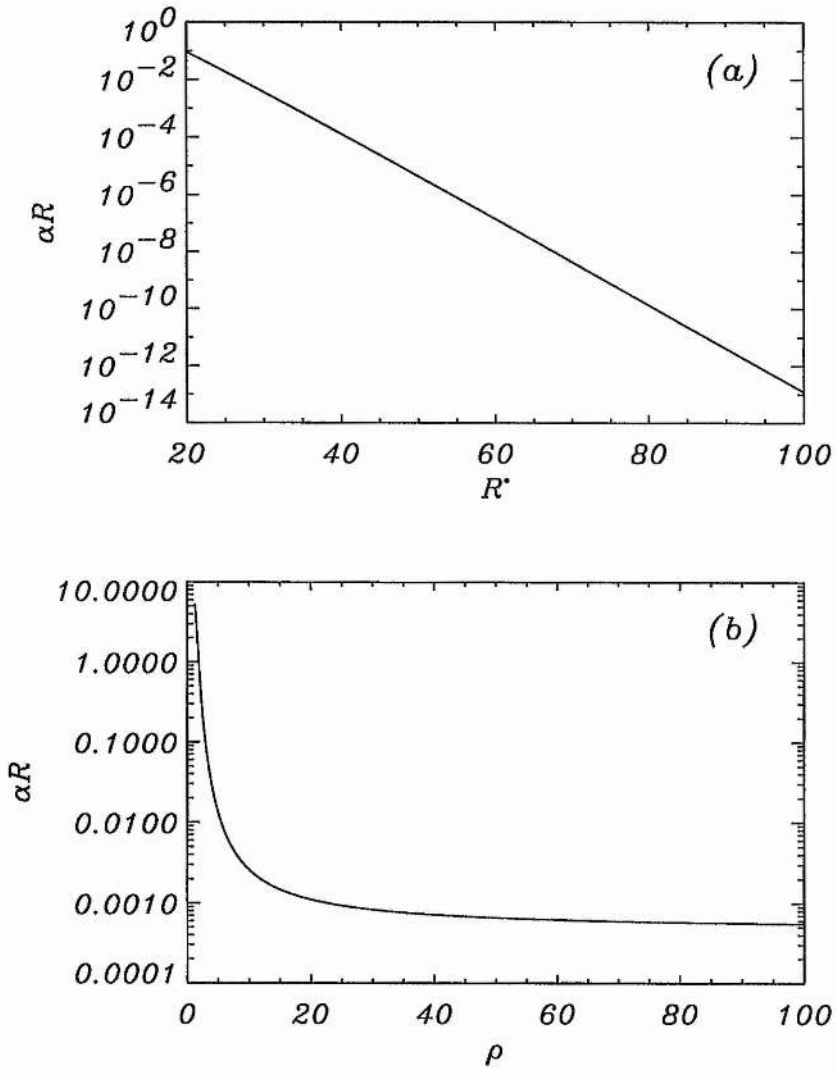

Figure 2.5: The energy loss of a curved coronal loop determined using the waveguide approach of Gloge (1972). In (a) the energy loss is plotted as a function of dimensionless radius of curvature $R^* = R/a$ for a density enhancement of $\rho = \rho_0/\rho_e = 3$. Notice that a low radius of curvature is much more leaky than a high radius. (b) shows that loops with higher density enhancements are more efficient guides. In (b) we have used a fixed value of $R^* = 20$.

This simple estimate, derived from a waveguide approach, has shown that curvature may be an important effect under certain circumstances. We may expect highly curved loops with low density enhancements to be inefficient waveguides. Having seen that the effect of curvature in waveguides is to cause the waves to become leaky we review the previous work examining leaky waves in the solar atmosphere. This gives a vital insight into some of the parameters that affect the efficiency of wave ducting in coronal loops.

2.4 Previous work on leaky waves in the solar atmosphere

Roberts et al. (1984) considered modes that were solely evanescent in the exterior of a loop. For such modes, in a zero-β plasma, the effective transverse wavenumber for a wave of frequency ω and longitudinal wavenumber k_z is $m_e = \left(k_z^2 - \omega^2/v_{Ae}^2\right)^{1/2}$. Modes that are evanescent in the environment of a tube (or slab) are such that $\omega^2 < k_z^2 v_{Ae}^2$, for which m_e is real and positive; no energy leakage from the structure occurs. It is possible also for disturbances to arise that leak into the environment; for such modes m_e^2 is no longer positive. In this section we review the previous work that has been undertaken on leaky waves in the solar atmosphere. In Sections 2.4.1 and 2.4.2 we comprehensively review the work on photospheric flux tubes and coronal loops respectively. The leaky waveguide model of Davila (1985) is reviewed in 2.4.3.

2.4.1 Photospheric Flux Tubes

The numerical simulations of the Huntsville Group (Xiao 1988; Huang 1995; Wu, Xiao, Musielak and Suess 1996) have investigated wave propagation in magnetic slabs and interfaces embedded in both field-free and magnetic environments. These works provide a quantitative investigation into the efficiency of wave ducting. Results show that, under typical conditions, waves which propagate along magnetic structures interact effectively with the environment (i.e. leak energy) and generate acoustic or magnetoacoustic waves. The confinement of waves to the magnetic region was found to be more efficient for a high plasma beta. For $\beta = 1$, 30 % of the total energy leaks from the magnetic region to the surroundings. In addition wider slabs were found to be more effective waveguides than thinner slabs. The authors conclude that energy leakage is always present with up to 62 % of energy lost within 2 wave periods. Therefore for photospheric flux tubes the amount of energy that can be transferred from the photosphere to the chromosphere is reduced. Similar results were reported by Wilson (1981) who examined the leakage of waves from a magnetic tube embedded in a field-free region, through the introduction of complex frequency and wavenumber.

The recent investigation by Ziegler and Ulmschneider (1996) considered the efficiency of wave leakage from a cylindrical flux tube embedded in a field-free environment. For a tube with a plasma beta of 10, it was found that only 7 % of the initial energy leaks into the surrounding medium to create acoustic waves. Lower values of the plasma beta yield greater energy loss. For example

with $\beta = 0.1$ only 57 % of the wave energy is contained within the flux tube. Thin flux tubes were found to be more leaky with up to 80 % of the wave energy leaking into the surrounding plasma. The results of this three-dimensional simulation were found to be in general agreement with the numerical simulations of wave propagation in magnetic slabs embedded in a field-free environment (see Xiao 1988; Huang 1995 and Wu et al. 1996). A comparison between the results of slab and cylindrical geometries suggests that energy leakage from a magnetic slab is greater than from a cylinder. Ziegler and Ulmschneider (1996) conclude that energy leakage is an important process, particularly in low-β plasmas, and therefore should not be ignored.

2.4.2 Coronal Loops

A numerical investigation into magnetoacoustic wave propagation in coronal loops has been undertaken in a series of papers by Murawski and Roberts (1993a-d, 1994). Both standing and propagating, linear and non-linear waves were studied in smoothed slabs of enhanced plasma density, in the cold plasma approximation. The efficiency of wave ducting for different parameters was examined, the leakage arising through the smooth density profile and also the wave adjusting to the loop. Murawski and Roberts (1993a-d) found that the kink mode was more robust than the sausage mode; leakage is small for the asymmetric (kink) oscillations but much larger for the symmetrical (sausage) modes. More energy was lost for loops with smoother profiles of density, lower density enhancements and higher frequencies of oscillation. In addition wave guiding was found to be less efficient for narrow slabs and for modes which are more oscillatory across the loop. The non-linear studies undertaken revealed that small amplitude waves are better guided than large amplitude waves (Murawski and Roberts 1993c).

Considering standing sausage waves (within a loop modelled by a steep profile in plasma density) it was found that 60 % of the initial wave energy was lost from the loop for a density enhancement of 2. For a smoother density profile the energy loss increased up to 80 % within a few Alfvén transit times. For impulsively generated kink waves half of the initial energy was lost for a plasma density enhancement of 5. Decreasing the enhancement to 2 results in a increased leakage of 75 %.

Further simulations by Murawski (1993) and Murawski and Roberts (1994) investigated the wave interaction between two slabs in close proximity (cross-talk). The energy leakage from one slab means that oscillations can enter the second slab and wave trapping can occur. In this case wave propagation is much more complicated. For periodic kink waves oscillating in both slabs there is negligible interaction due to the small leakage of this mode. However for a sausage and kink periodic mode in adjacent slabs the interaction is much stronger (due to the increased leakage of the sausage mode).

The efficiency of the guiding of sausage waves in a dense, cylindrical tube has been numerically investigated by Berghmans, De Bruyne and Goossens (1996). For an impulsive event located

outside the tube only 1 % of the energy of the disturbance was trapped. The coronal loop was unable to capture a significant amount of energy. By contrast, for an impulsive event inside the tube 94 % of the wave energy is trapped for a comparatively low density enhancement of 4. This leakage is significantly smaller than found for the simulations undertaken for coronal slabs (Murawski and Roberts 1993a-d) and photospheric flux tubes (Xiao 1988; Haung 1995 and Wu et al. 1996). The discontinuity in density, the wide tube and the rigid wall boundary conditions may have affected the results. The case of a periodic driver at the base (photosphere) of the loop was also examined. To sustain symmetrical (sausage) oscillations the driving frequency must be greater than a threshold (see Roberts, Edwin and Benz 1983, 1984) otherwise considerable leakage results (Cally 1986).

A comprehensive analytical investigation of non-leaky and leaky oscillations in magnetic flux tubes has been conducted by Cally (1986). Modes of oscillation were found to possess a complex frequency. This corresponds to the wave amplitude decaying in time and radiating energy into the surrounding medium. In particular, for a coronal loop Cally found that the body modes transform into leaky modes below the wavenumber cut-off k_z^{crit}, since the phase speed is in excess of the exterior Alfvén speed. Roberts, Edwin and Benz (1983, 1984) considered only real frequencies and therefore no leaky modes were found.

The investigation of the damping of magnetohydrodynamic waves in flux tubes has also been considered by Meerson, Sasorov and Stepanov (1978). The mechanism that generates the energy loss was the emission of plasma waves into the surrounding medium. In this model sustained oscillations may only occur when this emission is compensated through a resonance effect. The free modes of oscillation, later studied by Edwin and Roberts (1982, 1983) and Roberts, Edwin and Benz (1983, 1984), were ignored. Meerson et al. (1978) found complex frequencies, corresponding to wave energy being emitted by the tube.

Čadež and Okretič (1989) considered the propagation of surface waves along a magnetic slab. Results show the occurrence of surface wave leakage which causes the amplitude of the propagating surface waves to decrease in time.

2.4.3 Leaky wave model of Davila (1985)

Davila (1985) examined the reflection and transmission of MHD waves in both coronal holes and coronal loops. Applying well known results from geometrical optics, the reflection and transmission coefficients can be calculated. This approach provides an insight into some of the parameters which control the efficiency of wave ducting. We now repeat Davila's calculation.

Consider a plane wave, with eigenfunction Ψ, incident from the left on a boundary at $x = 0$ which separates two regions of differing density and Alfvén speed. Regions 1 and 2 are characterised by densities ρ_1 and ρ_2, with the Alfvén speeds given by v_{A1} and v_{A2} respectively. The unperturbed magnetic field is given by $\mathbf{B} = B_0\hat{\mathbf{e}}_z$. See Figure 2.6. Taking the waves to have a temporal variation $\exp(iwt)$ we may write the incident and reflected wavefunctions as (suppressing

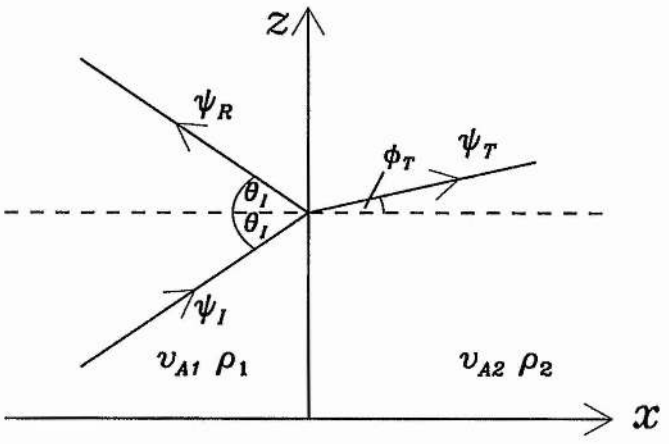

Figure 2.6: A sketch of a wave incident upon a boundary separating two regions of differing density and Alfvén speed in a uniform field. Part of the incident wave is transmitted whilst the remaining wave is reflected.

the common temporal term)

$$\Psi_I = A \exp\left[ik_I \left(z \sin\theta_I + x \cos\theta_I\right)\right] \tag{2.22}$$

and

$$\Psi_R = R \exp\left[ik_I \left(z \sin\theta_I - x \cos\theta_I\right)\right] , \tag{2.23}$$

respectively. The angle of reflection equals the angle of incidence (Snell's Law). Here A is the amplitude of the wave and R is the reflection coefficient. The angle of incidence to the normal is θ_I and the wavenumber in region 1 is k_I. The wavefunction of the transmitted wave is given by

$$\Psi_T = T \exp\left[ik_T \left(z \sin\phi_T + x \cos\phi_T\right)\right] , \tag{2.24}$$

where T is the transmission coefficient, k_T is the wavenumber in region 2 and ϕ_T is the angle of the transmitted wave. This transmitted wave corresponds to a leaky wave whilst the reflected wave denotes a trapped (ducted) mode. To obtain the reflected and transmitted coefficients we impose

that the velocity and total pressure must be continuous across the boundary at $x = 0$,

$$\Psi_I + \Psi_R = \Psi_T \ , \tag{2.25}$$

$$\frac{\partial \Psi_I}{\partial x} + \frac{\partial \Psi_R}{\partial x} = \frac{\partial \Psi_T}{\partial x} \ . \tag{2.26}$$

Substituting Equations (2.22)-(2.24) into Equation (2.25) gives

$$A + R = T \exp\left(iz\left[k_T \sin\phi_T - k_I \sin\theta_I\right]\right) \ . \tag{2.27}$$

On the left-hand side of Equation (2.27) there is no z-dependence which means that we must have $k_T \sin\phi_T = k_I \sin\theta_I$; Snell's Law from optics. Therefore from Equation (2.27) we have $A + R = T$. Now on setting $\omega = k_I v_{A1}$ and $\omega = k_T v_{A2}$ we obtain the relations

$$\frac{k_T}{k_I} = \frac{v_{A1}}{v_{A2}} = \sqrt{\frac{\rho_2}{\rho_1}} = \frac{\sin\theta_I}{\sin\phi_T} \ . \tag{2.28}$$

On substituting Equations (2.22)-(2.24) into Equation (2.26) and using the fact that $A + R = T$ we obtain

$$\frac{k_I \cos\theta_I}{k_T \cos\phi_T} = \frac{A + R}{A - R} \ . \tag{2.29}$$

Now inserting Equation (2.28) into (2.29) gives

$$\frac{R}{A} = \left[\frac{\sqrt{\frac{\rho_1}{\rho_2}}\cos\theta_I - \cos\phi_T}{\sqrt{\frac{\rho_1}{\rho_2}}\cos\theta_I + \cos\phi_T}\right] \ . \tag{2.30}$$

Eliminating the angle ϕ_T in Equation (2.30) by using the fact that $\cos\phi_T = \left[1 - (\rho_1/\rho_2)\sin^2\theta_I\right]^{1/2}$, the reflected energy R^{EN} $(\equiv R^2/A^2)$ is then given by (Davila 1985)

$$R^{EN} = \left(\frac{R}{A}\right)^2 = \left[\frac{\cos\theta_I - \left(\frac{\rho_2}{\rho_1} - \sin^2\theta_I\right)^{\frac{1}{2}}}{\cos\theta_I + \left(\frac{\rho_2}{\rho_1} - \sin^2\theta_I\right)^{\frac{1}{2}}}\right]^2 \ , \tag{2.31}$$

and the transmitted energy is given by $T^{EN} = 1 - R^{EN}$. Note that in our calculation the "sin" and "cos" functions are interchanged with Davila's result; this arises from Davila's definition of the incident angle as $\pi/2 - \theta_I$. There are two cases to consider. Firstly we examine a coronal loop where we take $\rho_1 > \rho_2$ and secondly we model a coronal hole by taking $\rho_1 < \rho_2$.

Coronal Loop: $\rho_1 > \rho_2$

Figure 2.7a shows the reflected intensity R^{EN} plotted against the angle of incidence θ_I for various values of the density enhancement (ρ_1/ρ_2) of the loop. For incident angles above a critical value θ_c, where θ_c is given by

$$\sin^2\theta_c = \frac{\rho_2}{\rho_1} = \frac{v_{A1}^2}{v_{A2}^2} \ , \tag{2.32}$$

the reflection coefficient is equal to one $(R^{EN} = 1)$ and no wave is transmitted $(T^{EN} = 0)$; this represents the fully guided modes of a coronal loop. When $\theta_I < \theta_c$ the wave is only partially reflected, the remaining wave energy being transmitted. The mode has become leaky. As θ_I decreases the reflection coefficient decreases rapidly, reaching a minimum value of

$$R^{EN}_{min} = \left[\frac{1 - \sqrt{\frac{\rho_2}{\rho_1}}}{1 + \sqrt{\frac{\rho_2}{\rho_1}}}\right]^2 \tag{2.33}$$

at $\theta_I = 0$. From Equation (2.33) we see that for high density enhancements (i.e. large ρ_1/ρ_2) the minimum value for the reflected energy attains greater values. Thus coronal loops with high density enhancements are more efficient in guiding the wave energy than loops with lower density enhancements. As the density of the loop and the exterior become equal $(\rho_1 \to \rho_2)$ reflection only occurs for grazing incidence; otherwise for smaller angles all energy is lost from the loop. To summarise, greater losses are expected to occur at smaller angles of incidence. There is no transmitted wave above a critical angle. In addition we may also expect low order modes to suffer less energy loss than higher modes. Lower order modes have larger angles of incidence. That is, they correspond to rays that travel along the guide at nearly grazing incidence and, from Figure 2.7a, energy losses will be small. On the other hand higher order modes have small incident angles and they will be less effectively guided. Therefore higher harmonics (shorter periods) will be selectively lost from waveguides whilst lower order modes are able to propagate more efficiently. High density enhancements are expected to be more effective guides than low density enhancements.

Coronal Hole: $\rho_1 < \rho_2$

For $\rho_1 < \rho_2$ the situation resembles a wave propagating in a coronal hole. The reflected energy R^{EN} as a function of the angle of incidence θ_I is shown in Figure 2.7b. As the angle of incidence approaches $\pi/2$ all wave energy is reflected. Thus a coronal hole may guide waves which propagate at grazing angles of incidence. However for a coronal hole it is not possible to obtain total reflection, as within a coronal loop. The maximum transmission occurs for waves which impinge the boundary head on. As the angle of incidence increases the reflected energy rises (Figure 2.7b). A coronal hole will therefore act as a leaky waveguide. Part of the wave energy will be guided whilst the remaining energy is lost to the surrounding plasma. The numerical treatment of wave propagation in a coronal hole was investigated by Ofman and Davila (1995). A significant proportion of the fast wave energy was found to leak out of the coronal hole. When the fast wave interacts with the boundary the waves undergo partial reflection, the remaining wave energy being lost to the surrounding medium. The results were found to be in good agreement with the analytical treatment of Davila (1985).

In this section we have reviewed the work reported on leaky waves in the solar atmosphere. We now study the leakage from loops arising from the curved geometry of an arcade.

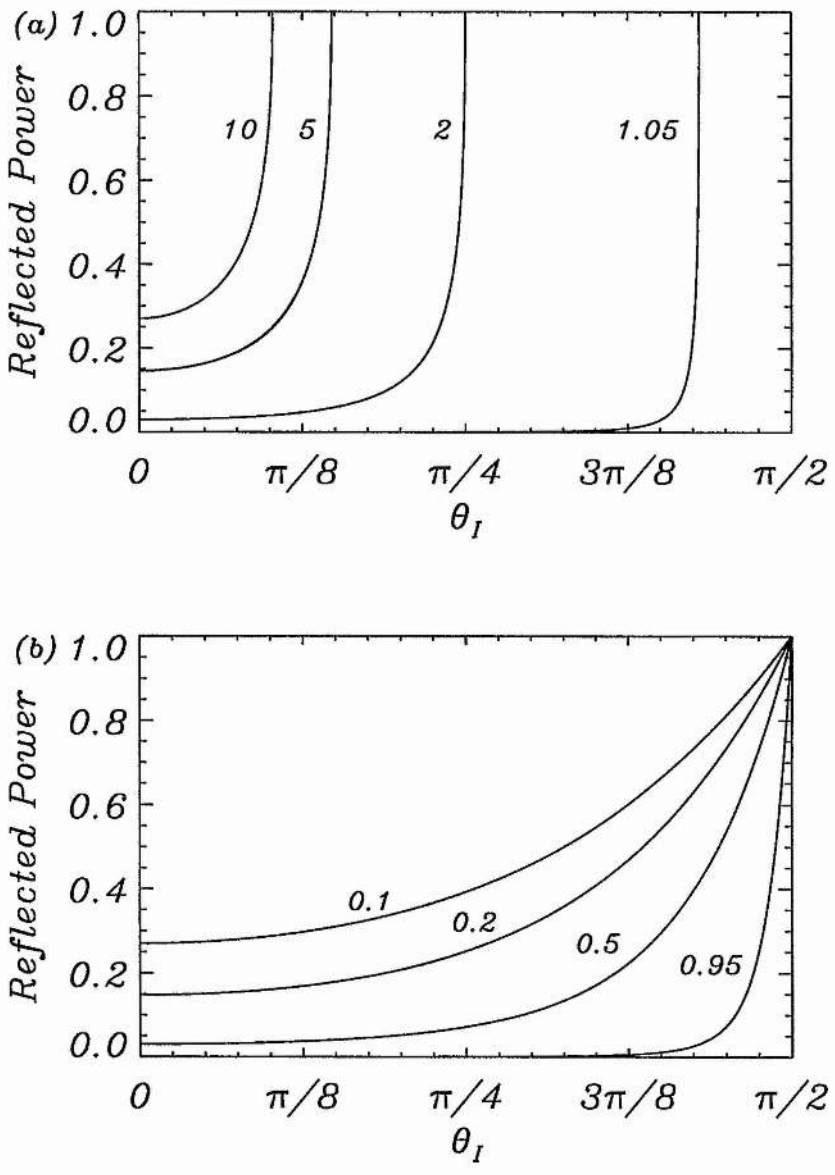

Figure 2.7: The reflected power R^{EN} for (a) a coronal loop and (b) a coronal hole. The numbers next to each curve denote the ratio ρ_1/ρ_2. For case (a) total reflection $\left(R^{EN}=1\right)$ can occur above a critical angle θ_c. For (b) no total reflection occurs. A coronal hole acts as a leaky waveguide.

2.5 Wave Propagation in an Arcade

Having seen that the effect of curvature in dielectric waveguides is to lead to waves which radiate energy away from the guide, we now turn our attention to coronal loops. We investigate how the leakage depends upon the parameters identified in the waveguide work.

2.5.1 The Wave Equation

We consider a two-dimensional (x, z) coronal arcade, which is invariant in the y-direction $(\partial/\partial y \equiv 0)$, modelled as a potential magnetic field satisfying

$$\nabla \times \mathbf{B} = \mathbf{0} \,. \tag{2.34}$$

In using Equation (2.34) we have neglected the plasma pressure and gravity. In the solar corona the sound speed is typically an order of magnitude smaller than the Alfvén speed. The plasma beta is proportional to the squares of these speeds and is therefore much less than one (see Table 1.4). The corona is thus magnetically dominated and it is a reasonable approximation to neglect the plasma pressure term. The magnetic structures that we consider are much smaller than Λ/β, where Λ and β are the pressure scale height and the plasma beta respectively. We may therefore neglect gravity. This makes the problem more tractable.

From the solenoidal constraint $\nabla \cdot \mathbf{B} = 0$ the equilibrium magnetic field $\mathbf{B}$ can be written as

$$\mathbf{B} = \nabla A\,(x, z) \times \hat{\mathbf{e_y}} = \left(-\frac{\partial A}{\partial z}, 0, \frac{\partial A}{\partial x}\right) \,, \tag{2.35}$$

where the magnetic flux function $A\,(x, z)$ satisfies $\nabla^2 A = 0$. The solution for A is obtained by separation of variables, with the condition that A is zero at infinite height and the z-component of the magnetic field is zero at the centre of the arcade. In this configuration the field lines are aligned with the z-axis at $x = \pm L$, with $2L$ being the width of the arcade. The flux function $A\,(x, z)$, which is constant along a field line, is given by

$$A\,(x, z) = B_0 \Lambda_B \cos\left(\frac{x}{\Lambda_B}\right) \exp\left(-\frac{z}{\Lambda_B}\right) \,, \tag{2.36}$$

where B_0 is the magnetic field strength at the base $(z = 0)$ of the corona and $\Lambda_B = 2L/\pi$ is the magnetic scale height. The field components are

$$\begin{aligned} B_x &= B_0 \cos\left(\tfrac{x}{\Lambda_B}\right) \exp\left(-\tfrac{z}{\Lambda_B}\right) \,, \\ B_z &= -B_0 \sin\left(\tfrac{x}{\Lambda_B}\right) \exp\left(-\tfrac{z}{\Lambda_B}\right) \,. \end{aligned} \tag{2.37}$$

The field strength $B = |\mathbf{B}| = B_0 \exp\left(-z/\Lambda_B\right)$. The form of the potential coronal arcade is shown in Figure 2.8.

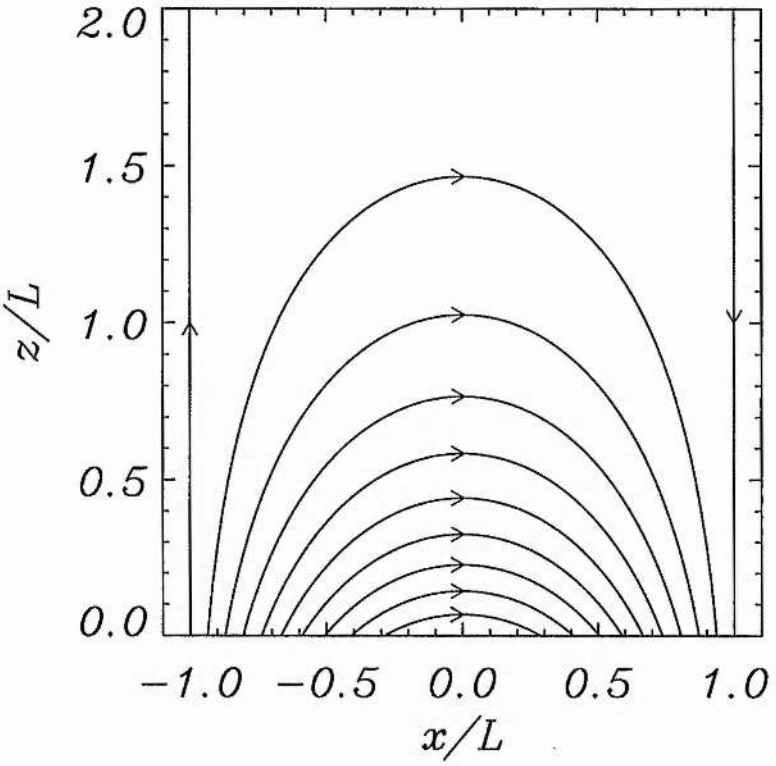

Figure 2.8: The form of the potential arcade in Cartesian coordinates (x, z). The arcade is physically isolated from its surroundings by vertical planes located at $x = \pm L$.

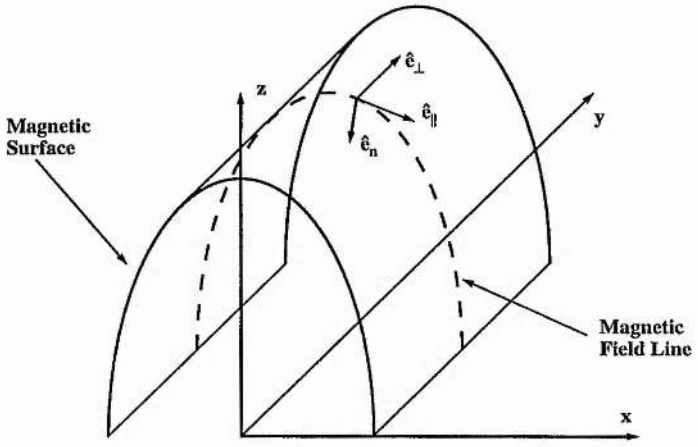

Figure 2.9: The coordinate system used in our model. Vectors $\hat{\mathbf{e}}_\mathbf{n}$, $\hat{\mathbf{e}}_\perp$ and $\hat{\mathbf{e}}_\parallel$ are unit vectors in the directions normal, perpendicular and parallel to the magnetic field respectively. The y-direction is invariant.

Consider the linearised equations of magnetohydrodynamics assuming that the plasma-β is zero (cold plasma) and gravity is negligible. The wave equation for plasma motions $\mathbf{v}$ is

$$\rho_0(x,z)\frac{\partial^2\mathbf{v}}{\partial t^2} = \frac{1}{\mu_0}\{\nabla\times[\nabla\times(\mathbf{v}\times\mathbf{B})]\}\times\mathbf{B}\,, \tag{2.38}$$

where $\rho_0(x,z)$ is the equilibrium plasma density. Equation (2.38) governs the velocity perturbations of fast and Alfvén modes. In the zero-β approximation (the corona is magnetically dominated) there are no motions along the equilibrium magnetic field $\mathbf{B}$ because the only driving force is the $\mathbf{j}\times\mathbf{B}$ force, and the slow mode is absent because we have set the plasma pressure to zero. We ignore the Alfvén mode by setting $v_y = B_y = 0$ so only v_n, the velocity component normal to $\mathbf{B}$, remains. Then, for motions of frequency ω, the wave equation (Equation 2.38) reduces to

$$-\rho_0\omega^2\mathbf{v} = \frac{1}{\mu_0}\nabla^2(\mathbf{v}\cdot\nabla A)\nabla A\,, \tag{2.39}$$

where we have used Equation (2.35). Following Oliver et al. (1993) we consider a local orthogonal coordinate system defined by

$$\hat{\mathbf{e}}_\mathbf{n} = \frac{\nabla A}{|\nabla A|}\,,\quad \hat{\mathbf{e}}_\perp = \hat{\mathbf{e}}_\mathbf{y}\,,\quad \hat{\mathbf{e}}_\parallel = \frac{\mathbf{B}}{|\mathbf{B}|}\,, \tag{2.40}$$

where $\hat{\mathbf{e}}_\mathbf{n}$, $\hat{\mathbf{e}}_\perp$ and $\hat{\mathbf{e}}_\parallel$ are unit vectors in the directions normal, perpendicular and parallel to the magnetic field respectively. The coordinate system is illustrated in Figure 2.9. Thus the normal component of Equation (2.39), which governs the propagation of fast magnetoacoustic waves, is given by

$$-\rho_0\omega^2\mathbf{v}\cdot\nabla A = \frac{B^2}{\mu_0}\nabla^2(\mathbf{v}\cdot\nabla A)\,. \tag{2.41}$$

Introducing the Alfvén speed $v_A(x,z)$ through $v_A^2 = B^2/\mu_0\rho_0$, Equation (2.41) becomes

$$\nabla^2(\mathbf{v}\cdot\nabla\mathbf{A}) + \frac{\omega^2}{v_A^2}(\mathbf{v}\cdot\nabla\mathbf{A}) = 0\,. \tag{2.42}$$

Now $v_n = \mathbf{v}\cdot\hat{\mathbf{e}}_\mathbf{n}$, and from Equation (2.40) we obtain

$$v_n = \frac{\mathbf{v}\cdot\nabla A}{B_0\exp\left(-\frac{z}{\Lambda_B}\right)} = \frac{\mathbf{v}\cdot\nabla A}{B}\,, \tag{2.43}$$

and so Equation (2.42) reduces to

$$\nabla^2(Bv_n) + \frac{\omega^2}{v_A^2}Bv_n = 0\,. \tag{2.44}$$

This equation governs the propagation of fast magnetoacoustic waves in our potential arcade. We note that the parallel component of Equation (2.39) yields $-\rho\omega^2\mathbf{v}\cdot\mathbf{B} = 0$, showing the absence of a slow mode in the low-β approximation.

Since we are neglecting the pressure and gravity terms in the momentum equation we are able to choose the density or Alfvén speed profiles arbitrarily. From the analytical work of Roberts et al. (1983, 1984) it is known that ducted waves occur in regions of low Alfvén speed (high density). A loop is thus modelled as a region contained between two field lines in which a depression in the Alfvén speed occurs. However special care must be taken when defining v_A. Oliver et al. (1993) investigated the normal modes of oscillation of the present magnetic structure for a variety of density profiles and found that whenever the Alfvén speed decreases or remains constant with height the solutions for v_n diverge as $z \to \infty$. We find this property undesirable because it makes the interpretation of the results difficult. To avoid this feature we choose a profile in Alfvén speed $v_A(x,z)$ that exponentially increases with height z both inside and outside the coronal loop; specifically we take

$$v_A(x,z) = \begin{cases} v_{A0}\exp\left(\frac{z}{2\Lambda_B}\right), & A_2 \le A(x,z) \le A_1\,, \\ v_{Ae}\exp\left(\frac{z}{2\Lambda_B}\right), & \text{otherwise}\,. \end{cases} \tag{2.45}$$

Here A_1 and A_2 ($< A_1$) are chosen constant values of the flux function; v_{A0} denotes the Alfvén speed at the base ($z = 0$) of a loop within the arcade and v_{Ae} is the Alfvén speed of the surrounding medium at the base of the loop.

We introduce the parameter $\rho = v_{Ae}^2/v_{A0}^2$, which gives the density enhancement of the loop compared to the surrounding plasma; ρ must be greater than unity in order to have ducted waves in the loop. The Alfvén speed profile for $\rho = 9$ is shown in Figure 2.10. Outside the dense loop the Alfvén speed increases exponentially to ensure a rapidly decreasing velocity for waves outside the loop (Oliver et al. 1993). With this profile any increase in velocity outside the loop must originate from the loop and thus is considered a signature of leaky waves.

2.5.2 Numerical Code and Boundary Conditions

Due to the complexity of the problem the governing wave equation has been solved numerically. The numerical code we employ was developed by Oliver, Hood and Priest (1996) to solve the

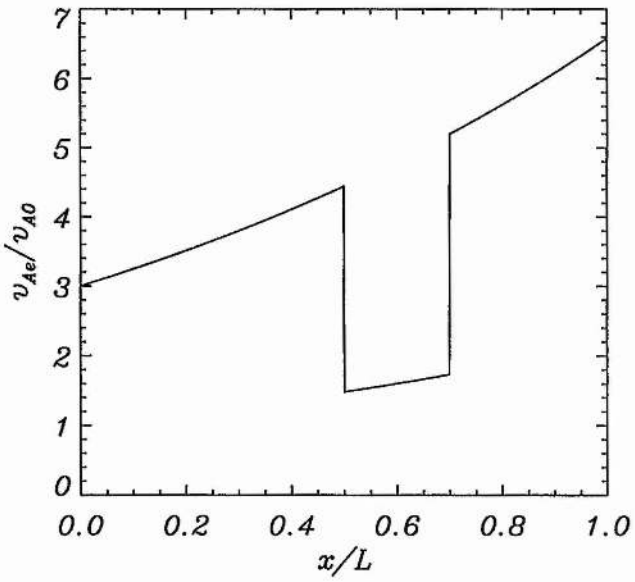

Figure 2.10: The Alfvén speed profile $v_A\,(x=0,z)$ for $\rho = v_{Ae}^2/v_{A0}^2 = 9$. The dense loop (corresponding to a depression in Alfvén speed) is situated between $z/L = 0.5$ and $z/L = 0.7$.

fast and slow mode equations in a two-dimensional equilibrium with no gravity (Appendix C). Oliver et al. (1996) cast these equations as two coupled partial differential equations with non-constant coefficients in which the velocity components normal and parallel to the equilibrium magnetic field (v_n and $v_\parallel$) are the unknowns. The equations were discretised using a finite difference scheme and the resulting algebraic eigenvalue problem was solved by inverse vector iteration, yielding individual eigenvalues ω_d^2, together with v_n on a rectangular grid of points. The eigenvalue ω_d^2 is the dimensionless frequency squared: $\omega_d^2 \equiv (\omega L/v_{A0})^2$. The eigenvalue takes only real values, so any energy leakage observed is attributable to the magnetic geometry. In all our numerical computations we use 60×60 points in our simulation region.

The code provides the capability to modify the coordinate system using a pair of generalised coordinates. For example these coordinates can be the Cartesian coordinates (x,z) with $-1 \leq x/L \leq 1$ and $0 \leq z/L \leq H$. The main drawback of this coordinate system is that it is not possible to consider the full height of the arcade, although one suspects that ducted modes, with exponentially decreasing velocity amplitudes outside the loop, will be obtained with good precision using a reasonable value of H. However in order to investigate the effects of curvature it is convenient to use a flux coordinate system covering the whole arcade (Oliver et al. 1996). In the (χ,ψ)

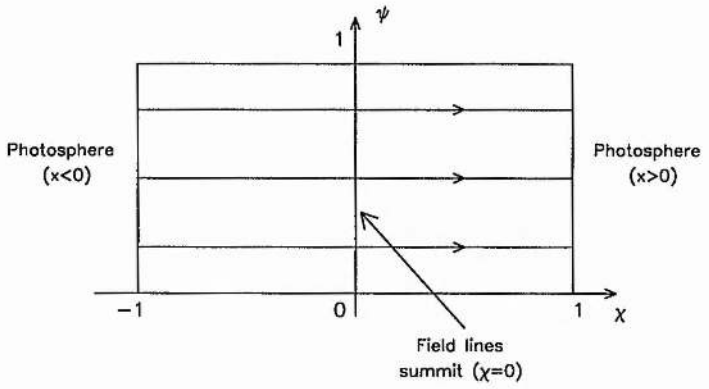

Figure 2.11: A potential coronal arcade in flux coordinates (χ, ψ). Field lines are horizontal, given by $\psi =$ constant. The photosphere is modelled by $\chi = -1\,(x < 0)$ and $\chi = 1\,(x > 0)$. All field lines have length 2.

coordinates the curved loop becomes horizontal. The flux coordinates are given by

$$\begin{aligned} \psi &= \cos\left(\tfrac{x}{\Lambda_B}\right) \exp\left(-\tfrac{z}{\Lambda_B}\right) , \\ \chi &= \left(1-\psi^2\right)^{-\frac{1}{2}} \sin\left(\tfrac{x}{\Lambda_B}\right) \exp\left(-\tfrac{z}{\Lambda_B}\right) , \end{aligned} \tag{2.46}$$

with $0 \leq \psi \leq 1$ and $-1 \leq \chi \leq 1$. Note that ψ is proportional to the flux function A. The potential arcade illustrated in Figure 2.8 in Cartesian coordinates is shown again in Figure 2.11 in flux coordinates. Field lines are now horizontal, given by $\psi =$ constant. The field lines in the (χ, ψ) system all have a length of 2, which is achieved through the normalisation factor $\left(1-\psi^2\right)^{-1/2}$ in Equation (2.46).

The line $\psi = 0$ is the field line in the (x, z) system that originates at $(-L, 0)$, extending up to infinity, and terminating at $(L, 0)$. The photosphere is modelled by $\chi = -1\,(x < 0)$ and $\chi = 1\,(x > 0)$. The line $\psi = 1$ is the point $x = z = 0$. We have assumed that the velocity $\mathbf{v}$ vanishes at the coronal base $z = 0$ ($\chi = \pm 1$ and $\psi = 1$), modelling the line-tying boundary condition at the photosphere (see, for example, Van der Linden, Hood and Goedbloed 1994). The arcade under consideration is taken to be isolated in the sense that no plasma traverses the boundaries at $x = \pm L$ ($\psi = 0$). The trapped waves are unaffected by the boundary condition imposed at $\psi = 0$. However the behaviour of the leaky waves is influenced by the rigid wall. Taking the velocity v_n to be zero at $\pm L$ means any leaky waves are contained within the arcade. Leaky waves will therefore oscillate in a similar manner to the modes studied by Oliver et al. (1993). Of course in practice, no rigid walls exist at the edges of the arcade. Therefore we may expect these waves to propagate away from the loop and possibly to be observable at large heights in the corona. In the optical waveguide context Snyder and Love (1983) suggest that a varying degree of leakage along a waveguide results

in a similar spatial variation of velocity perpendicular to the guide (at a fixed location along the waveguide).

To examine the effects of curvature we focus attention on different loops within our arcade. These loops have different lengths and hence the effect of curvature in each loop is different. For "long" loops the length is much greater than the horizontal distance between the footpoints, whereas for "short" loops the length of the loop is comparable to the distance between the footpoints. Curvature effects are expected to be more important in short loops. Taking $L = 1.5 \times 10^5$ km gives the distance between the footpoints of the loops considered to be of the order 2×10^5 km. In addition, we take $v_{A0} = 1.5 \times 10^3$ km s^{-1} in order to estimate periods of oscillation.

Before investigating the propagation of magnetoacoustic waves in curved coronal loops it is of great importance to examine the accuracy of the code. In the next section we test the numerical code by comparing the numerical results of some simple physical problems with known analytical or numerical solutions.

2.5.3 Checks on the numerical code

Extensive checks on the accuracy of the code have been made, including a comparison with the analytical work of Roberts et al. (1983, 1984) for a straight slab. Excellent agreement has been found. Here we show some examples of the checks undertaken which illustrate the excellent performance of the code.

Uniform field, constant density

The simplest equilibrium we can consider is that of a uniform magnetic field ($\mathbf{B} = B_0\hat{\mathbf{e}}_z$) with constant density (Figure 2.12). We take the plasma beta equal to zero and neglect gravity. The equation governing the perturbations of the fast magnetoacoustic waves is then simply $\partial^2 v_x/\partial t^2 = v_{A0}^2 \nabla^2 v_x$, where v_{A0} is the constant Alfvén speed. This simple model may be thought of as a coronal arcade with length L and height H. We impose that the fast mode velocity v_x is zero on all four sides of the arcade. Since we have neglected curvature the coronal base is located at $z = 0$ and $z = H$. Such an equilibrium is equivalent to standing waves in an elastic membrane with fixed boundaries (Oliver et al. 1993). The plasma is equivalent to the mass of the membrane whilst the elasticity is given by the magnetic field lines. The frequency of oscillation is given by (see, for example, Rayleigh 1945; see also Roberts 1991b),

$$\omega = \pi v_{A0} \left[\left(\frac{n_x}{L} \right)^2 + \left(\frac{n_z}{H} \right)^2 \right]^{\frac{1}{2}}, \tag{2.47}$$

where n_x and n_z are integers describing the mode of oscillation in the x and z-directions respectively.

To check the accuracy of the code we take $H = L$ and 60 grid points in each spatial direction. The comparison between the analytical and numerical results is illustrated in Figure 2.13. We have varied n_z between 1 and 10, whilst fixing n_x to be 1 or 3. The agreement between the

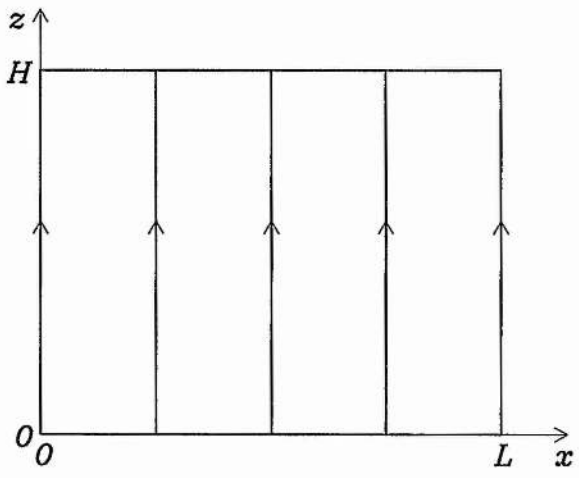

Figure 2.12: The simple equilibrium used to check the accuracy of the code. A uniform field with constant density is used with a plasma beta of zero. The fast mode velocity is zero on all four boundaries. The arcade has length L and height H.

analytical and numerical results is excellent. For low n_z the numerical and analytical results are indistinguishable. As n_z increases the numerical results are slightly less accurate. Increasing the number of grid points for higher order modes improves the accuracy.

This simple model has shown that the numerical code is accurate. We now continue our investigation into the accuracy of the code by considering a more complicated equilibrium.

Uniform field, two-dimensional density profile

A further check on the numerical code is conducted by considering a uniform magnetic field ($\mathbf{B} = B_0 \hat{\mathbf{e}}_z$) and a two-dimensional Alfvén speed profile given by

$$v_A(x,z) = X(x)\,Z(z)\ , \tag{2.48}$$

where

$$X(x) = 1 - \frac{x}{x_0 L}\ , \qquad x_0 = 1.3\ , \tag{2.49}$$

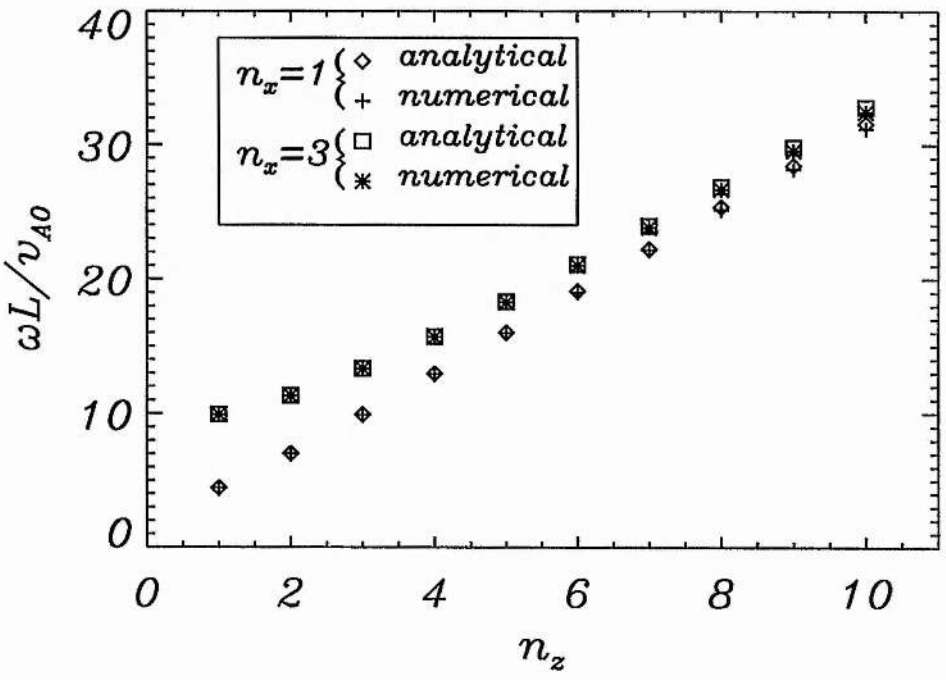

Figure 2.13: A comparison of the numerical and analytical frequencies in a uniform field with constant density. We have fixed n_x and varied n_z. The analytical and numerical frequencies are in excellent agreement.

and

$$Z(z) = \frac{1}{2}\left[3 - \cos\left(\pi\frac{z}{L}\right)\right] , \tag{2.50}$$

with $0 \leq x/L \leq 1$ and $-1 \leq z/L \leq 1$, where L is the width of the cavity. The fast mode velocity is taken to be zero on all four boundaries.

The problem of finding the fast mode eigenfrequencies has recently been considered by Wright and Rickard (1996, private communication) using a different numerical scheme. Wright and Rickard's code excites all the modes of a cavity which lie within the frequency range of a broadband driver. The eigenfrequencies may be found by obtaining a temporal signature of the fast mode velocity in the cavity and then Fourier transforming. Figure 2.14 illustrates the eigenfrequencies calculated by Wright and Rickard; cases (a) and (b) illustrate the symmetric and asymmetric modes respectively. In Figure 2.14c our calculated eigenfrequencies for the lowest 10 modes of oscillation are shown, where we have used 60 grid points in each direction. A comparison of the frequencies determined by the two codes shows an excellent agreement. This shows the code we employ in our work is able to calculate frequencies to a high precision in a two-dimensional density profile. This is an important requirement for our simulations.

Comparison with the slab ducted wave model

Since our work is concerned with trapped waves in curved coronal loops it is of critical importance that the code is able to reproduce the results for the simple slab (Roberts, Edwin and Benz 1983); see also Section 2.2. We consider a uniform magnetic field ($\mathbf{B} = B_0\hat{\mathbf{e}}_z$) in a computational domain $0 \leq x/L \leq 1$ and $0 \leq z/L \leq 1$, where L is the length of the loop. We take the plasma beta to be zero. The density and Alfvén speed in the region outside the loop ($x > a$) are taken to be ρ_e and v_{Ae} respectively. In the region $0 \leq x \leq a$ we take the plasma density and Alfvén speed to be $\rho_0\,(> \rho_e)$ and $v_{A0}\,(< v_{Ae})$ respectively. Here a is the half width of the loop. The fast mode velocity v_x is taken to be zero on all boundaries, except along the line $x = 0$ where we set either v_x or $\mathrm{d}v_x/\mathrm{d}x$ equal to zero depending upon whether we are interested in sausage or kink modes. In all calculations we use 100×100 grid points. It is important to note that since L is finite the wavenumber along the loop k_z may attain discrete values only: $k_z = n\pi/L, \quad n = 1, 2, \ldots$.

We firstly examine the principal ($n = 1$) kink mode with a density enhancement of 9. To check the accuracy we consider a ratio of the length to the half-width of the loop of $L/a = 50$. A comparison between the numerical results and the exact solution of the dispersion relation (Equation 2.7) is shown in Figure 2.15. The agreement between the two approaches is excellent. Roberts et al. (1983) show that the principal kink mode occurs for all values of the wavenumber k_z. This has also been found numerically; no wavenumber threshold exists for the kink mode.

We now consider the sausage mode with $a/L = 0.06$ and a density enhancement of 9. From the analytical work of Roberts et al. (1983) the sausage mode only occurs above a wavenumber

a

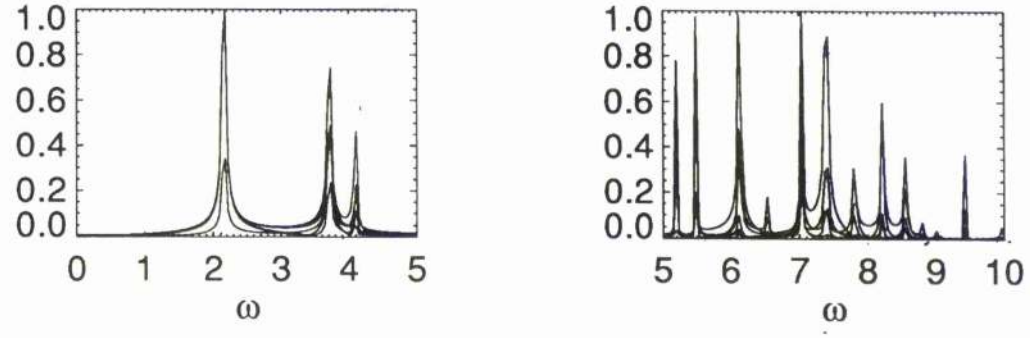

b

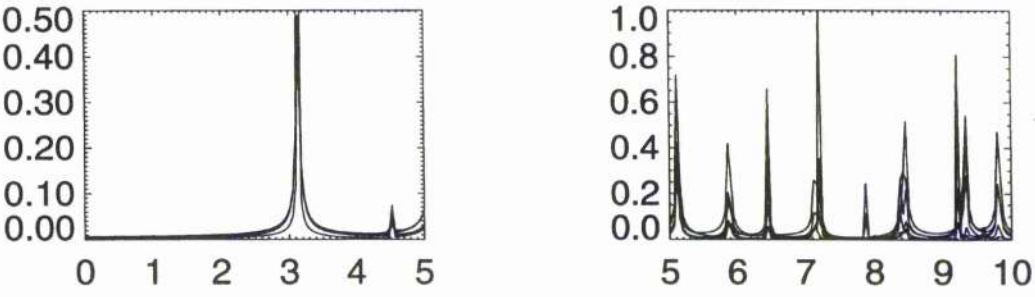

c

Mode	Frequency $\omega L/v_{A0}$
1	2.159
2	3.133
3	3.709
4	4.092
5	4.516
6	5.120
7	5.190
8	5.487
9	5.877
10	6.127

Figure 2.14: A comparison of the results obtained from the numerical code used in our calculations and those from Wright and Rickard's (1996, private communication) code. (a) shows the frequencies obtained by Wright and Rickard for symmetric modes and (b) is for asymmetric modes. The frequencies are in dimensionless units; $\omega L/v_{A0}$. Symmetric and asymmetric modes are defined by an anti-node and node along $z = 0$ respectively. (c) The table shows the frequencies obtained by our code. The frequencies obtained by the two codes are in very good agreement.

threshold given by Equation (2.11). In this case we require $k_z a > 0.555$, with $k_z = n\pi/L$; this means that the first ducted mode occurs at $n = 3$ (n must be an integer). The analytical and numerical results are compared in Figure 2.15.

Once again our numerical results are in accordance with the exact solution of the dispersion relation. In addition the code has been able to locate the wavenumber threshold to high precision. The results are less accurate as k_z increases, but it has been found that increasing the number of grid points results in an improvement in accuracy. We are therefore confident that the numerical code is able to solve the simple slab model to high precision.

Finally we investigate the accuracy of the code for a curved magnetic field.

Potential curved arcade with constant Alfvén speed

We now compare the results obtained from the numerical code with the analytical results of Oliver, Ballester, Hood and Priest (1993), who considered the fast magnetoacoustic modes of a curved magnetic field. The magnetic field is given by Equation (2.37) and is illustrated in Figure 2.8. We take the fast mode velocity to be zero on all four boundaries. The height of the arcade is taken to be equal to its length: $H = L$. Oliver et al. (1993) show that for the case of constant Alfvén speed the eigenfrequencies are given by Equation (2.47); the frequencies in the curved and horizontal field geometries are the same. We use 60 grid points in each spatial direction. We fix n_x to be 1 or 4 and vary n_z between 1 and 10. The numerical results are shown in Figure 2.16 along with the analytical results. Once again the agreement between analytical theory and numerical results using our code is excellent.

Summary

To summarise, the main features of the analytical results of the ducted wave slab model of Roberts et al. (1993, 1994) have been confirmed by the code. The code has also been checked against other analytical results for different equilibria and excellent agreement has been found in all cases. Therefore we are confident that the code can accurately solve the problem of ducted waves in curved loops.

We now present our results for magnetoacoustic wave propagation in curved coronal loops. We begin our investigation by examining the kink mode in Section 2.6, proceeding to the sausage mode in Section 2.7.

2.6 The Kink Mode

Equation (2.44) is solved for various lengths, densities and widths of loops. Ducted modes can be of kink or sausage type. Kink modes produce oscillations of the loop about its central

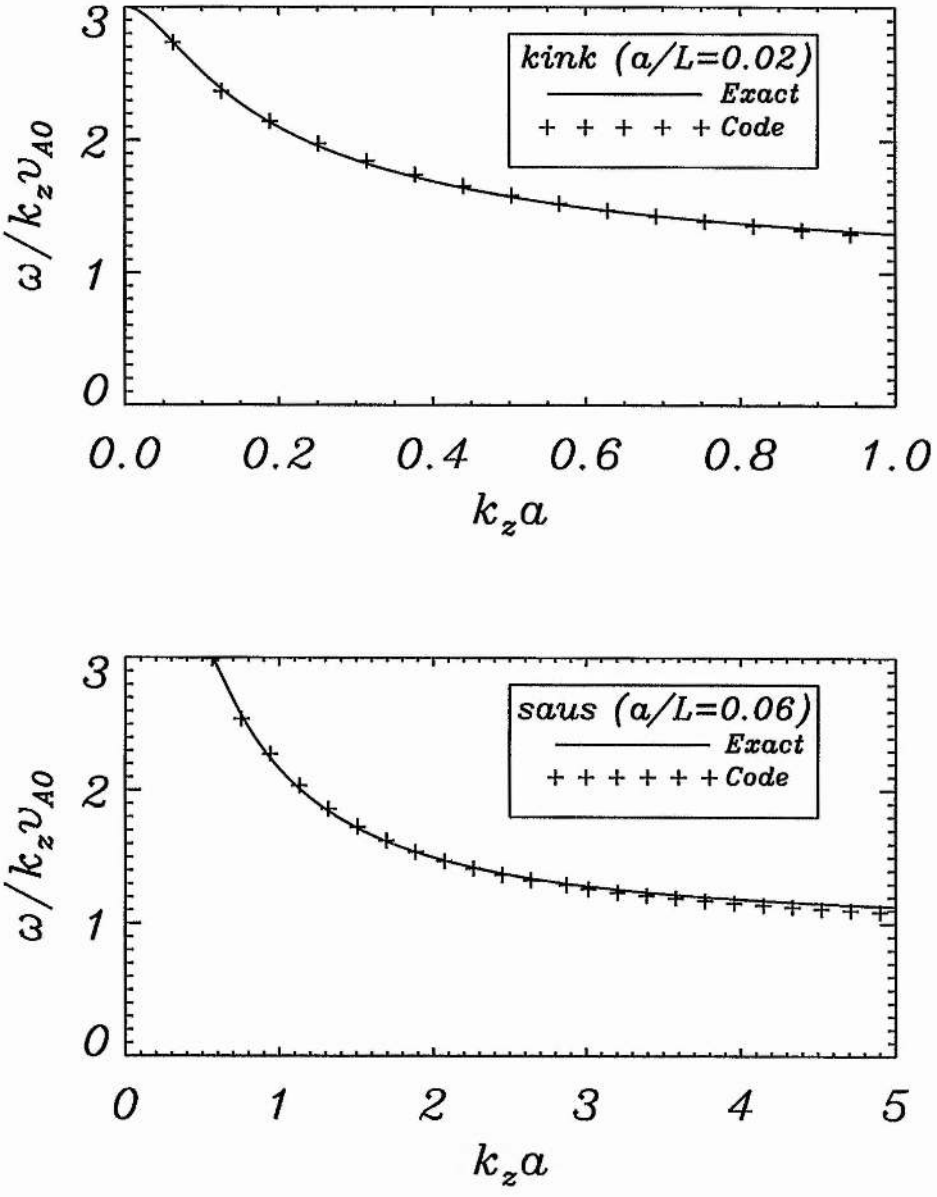

Figure 2.15: A comparison between the results obtained from the numerical code (+) and those obtained from solving the dispersion relations (Equations 2.7 and 2.8) exactly (solid line) for the ducted wave model of Roberts, Edwin and Benz (1983). A density enhancement of 9 has been used. The top and bottom figures illustrate the results for the kink and sausage modes respectively, showing excellent agreement between the code and the dispersion relations.

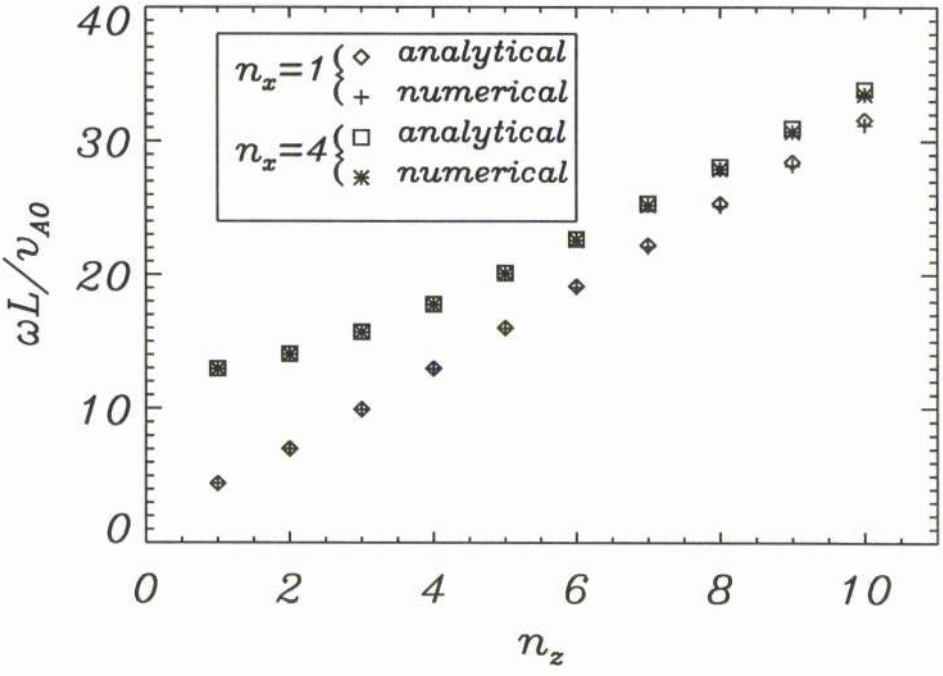

Figure 2.16: A comparison of the numerical and analytical results for a curved potential coronal arcade. The mode number n_z varies between 1 and 10, with n_x fixed to be 1 or 4. Once again the analytical and numerical results are in good agreement.

axis, while the sausage modes give rise to loop motions resembling "heart beats" with the plasma alternately moving away and towards the loop axis; see Figure 2.17.

In the following, the results will be presented as contour plots of $v_n(\chi, \psi)$ in the flux coordinate system. The signature of a mode ducted by the loop will then be a normal velocity component that is maximum in the loop region and decays rapidly to zero outside the loop. Wave leakage from the loop is shown by large oscillatory amplitudes, comparable to the velocity within the loop, occurring outside the loop.

2.6.1 Effect of Frequency

We start by looking at how wave leakage is influenced by the mode frequency. As with the finite slab or cylinder (Roberts et al. 1983, 1984) the line-tied loop has discrete modes because not all values of the wavelength along the loop are allowed. Kink modes present two types of geometry, either *even* or *odd* about the loop summit, characterised by a maximum or vanishing v_n at the top of the loop. When ordered by increasing frequency kink modes are alternately even and odd, the fundamental mode being even, the first harmonic odd, and so on. The geometry of the kink mode is of importance in the ducting of perturbations. To show this we select a loop with conditions appropriate for leakage: a short loop with a moderate density enhancement ($\rho = 5$). Such conditions tend to reduce the ducting of the fast mode.

The velocity v_n of odd modes (zero velocity at the summit of the loop), shown in Figures 2.18b and 2.18d, displays high values inside the loop with a rapid decrease in the surrounding corona, similar to that found in the slab geometry. The wave energy is thus clearly ducted by the high density loop. The results for the even modes (derivative of velocity zero at the top of the loop) are significantly different. Figures 2.18a and 2.18c show high velocity amplitudes in the loop, although a dramatic increase in velocity outside the loop indicates the large leakage associated with these modes. In particular for the second harmonic (Figure 2.18c) we see the wave is clearly ducted at $(\pm 0.5, 0.4)$ whilst the velocity at $(0, 0)$ has leaked from the loop. These results are repeated for higher harmonics although odd modes become more leaky at higher frequencies. Ultimately for very high frequencies the ducted mode is destroyed. The modes described above correspond to the principal kink mode, i.e. with no change in the sign of v_n across the loop. Overtones of this mode have not been considered as they possess very high frequencies and are therefore less likely to be excited.

2.6.2 Length of Loop

To examine the effect of the length of the loop on the trapping of waves by a density enhancement we consider $\rho = 4$ and the third harmonic. Such a small density enhancement makes the loop a poor waveguide for the kink mode, as can be appreciated from Figure 2.19a in which a short loop has been considered. In Figure 2.19a we see wave ducting occurring at $(\pm 0.7, 0.55)$,

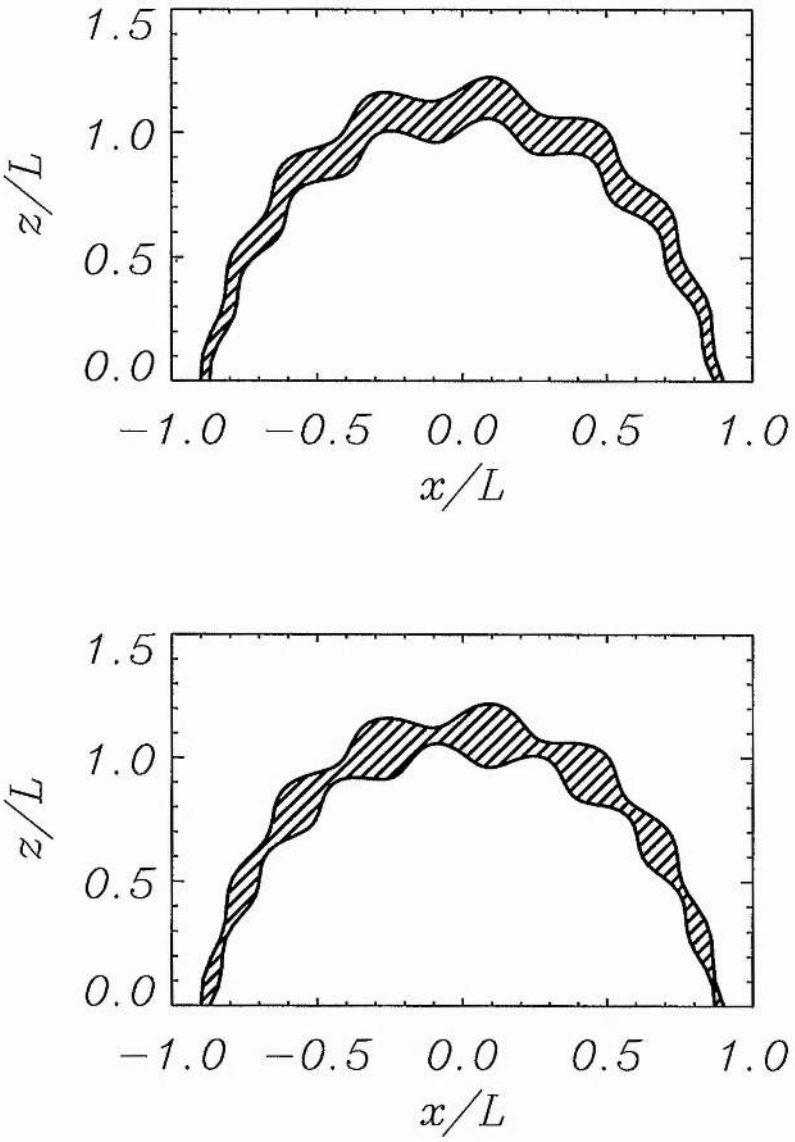

Figure 2.17: Schematic diagram of the fast mode velocity field associated with a kink mode (top panel) and a sausage mode (bottom panel) in curved geometry. The spatial distribution of the velocity needs to be multiplied by a term of the form $\cos\omega t$ to obtain the full temporal evolution. Kink modes give rise to lateral displacements of the loop about its central axis, while sausage modes are characterised by leaving the loop's axis undisturbed and producing converging and diverging plasma motions about the axis.

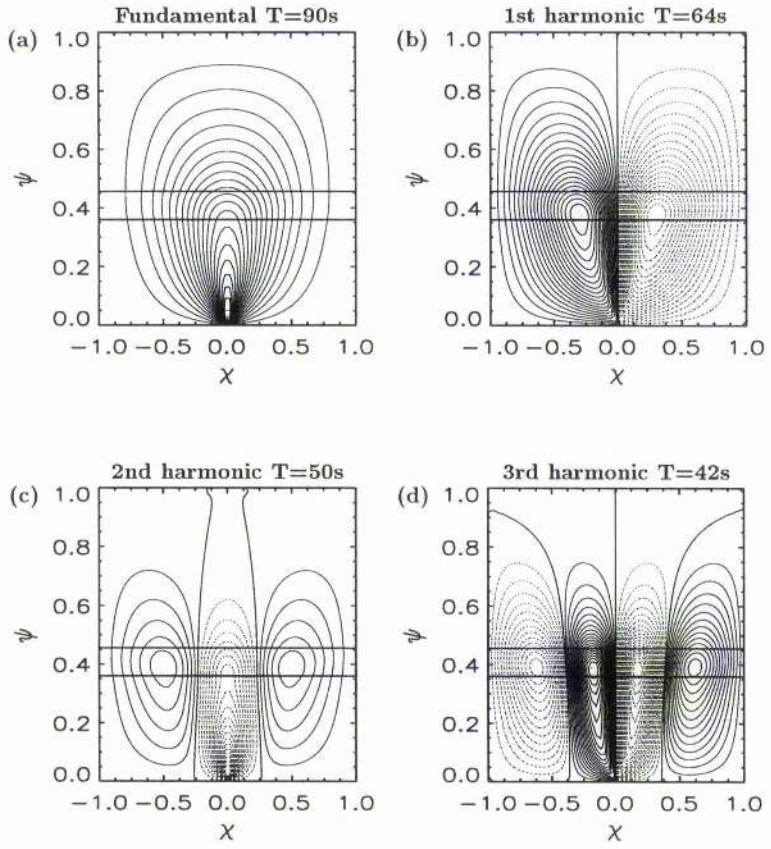

Figure 2.18: Kink mode — The effect of the frequency of oscillation for a short loop, given by $0.36 \leq \psi \leq 0.46$, with a moderate density enhancement ($\rho = 5$). Frequencies are measured in units of v_{A0}/L: $\omega_d \equiv \omega L/v_{A0}$. The motions v_n (in arbitrary units) in the flux coordinate system are displayed as contour plots for the four lowest frequency modes, with (a) $\omega_d = 6.99$ the lowest frequency mode, (b) $\omega_d = 9.82$ is the first harmonic (c) $\omega_d = 11.29$ is the second harmonic and (d) $\omega_d = 14.88$ the third harmonic. The thin solid and dashed lines show contours of constant positive and negative velocity respectively. The two thick horizontal lines show the position of the dense loop. Note the odd modes (cases (b) and (d)) are efficient waveguides with v_n centred in the loop. The even modes (cases (a) and (c)) show increasing velocity outside the loop suggesting leakage. In (c) we see the wave is trapped at $(\pm 0.5, 0.4)$ whilst the velocity peak at $(0, 0)$ has leaked from the loop. Even modes are more leaky than odd modes. Estimated periods $T\,(= 2\pi/\omega)$ of oscillation are given above each figure, taking $L = 1.5 \times 10^5$ km and $v_{A0} = 1.5 \times 10^3$ km s^{-1}.

whilst the two central peaks at $(\pm 0.25, 0.1)$ have clearly leaked from the dense loop. However for a long loop (Figure 2.19b) the mode is ducted. A clear peak in v_n exists within the loop, flanked by two regions of strong velocity decrease suggesting leakage is minimal. These results show that long loops are a more efficient wave trap than short loops.

2.6.3 Density of Loop

We now examine the effect of changing the plasma density ratio on wave leakage. We consider the third harmonic in a short loop for which curvature effects should be most pronounced. The results are illustrated in Figure 2.20. For a density enhancement of $\rho = 5$ (Figure 2.20a) the mode can be considered to be effectively ducted by the loop, with a clear peak in v_n in the loop and an evanescent velocity outside. Decreasing the plasma density ratio to 4.25 (Figure 2.20b) shows the two velocity peaks located at $(\pm 0.5, 0.3)$ have leaked from the loop and the leakage is much larger than in Figure 2.20a. Decreasing the density enhancement further to 4.09 (Figure 2.20c) shows the two central velocity peaks in the loop becoming leaky. Indeed for $\rho = 4.05$ (Figure 2.20d) we see only a small velocity in the loop with a much larger leakage velocity outside. In fact decreasing the density ratio further (not shown) results in the destruction of the mode. These results show that leakage is more significant for low density enhancements (weak slabs) and decreases for high plasma density ratios (strong slabs).

As one can see from the results described in Section 2.6.1 the first and third harmonics are more strongly guided than the second harmonic. The fundamental mode is more leaky than the second harmonic and longer loops or higher densities are needed to achieve efficient guiding of the oscillations.

2.6.4 Width of Loop

To finish our study of the kink mode we look at how the width of the loop changes the nature of the ducted wave. We consider a loop and fix its lower field line (the solid line in Figure 2.21a) but vary the upper field line (to one of the dashed lines in Figure 2.21a). Again, adverse conditions for the guiding of waves are considered. Results are obtained for a density enhancement of 6 and the second harmonic. For the narrowest loop (Figure 2.21b) a ducted wave is observed at $(\pm 0.5, 0.4)$ although leakage is large, especially the central peak. Increasing the width (Figure 2.21b) shows the velocity in the loop is much more pronounced although the central velocity peak is still very leaky. However for the widest loop wave ducting is much more efficient with higher velocities inside the loop region, including the central peak, although leakage is still observed. Increasing the width (Figures 2.21c,d), results in a decrease in leakage. Therefore wide coronal loops are more effective wave traps than narrow ones.

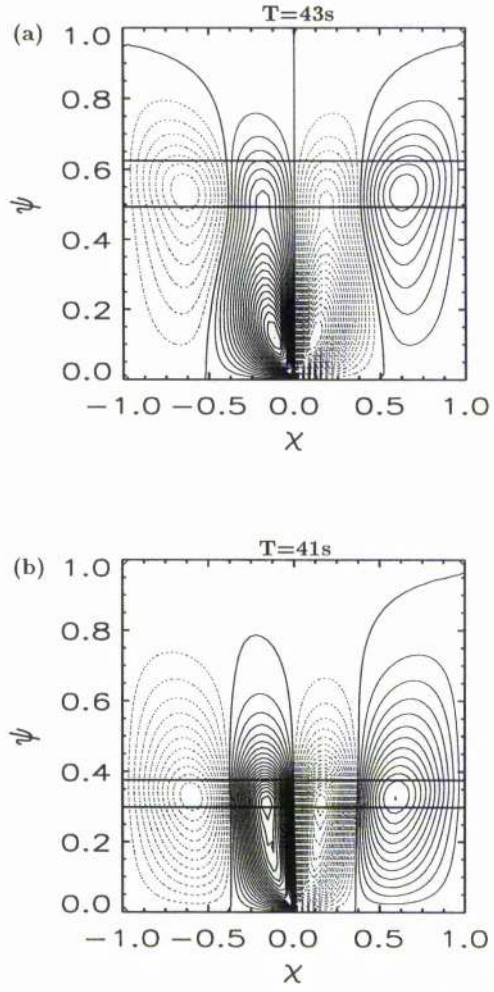

Figure 2.19: Kink mode — The effect of the length of the loop for a density enhancement $\rho = 4$. A flux coordinate contour plot of the normal velocity component v_n for the third harmonic and in (a) a short loop given by $0.49 \leq \psi \leq 0.62$ with frequency $\omega_d = 15.31$, (b) a long loop given by $0.30 \leq \psi \leq 0.39$ with $\omega_d = 11.15$. The ratio of the total length of the loop to the distance between its footpoints is 1.22 in (a) and 1.42 in (b). The longer the loop, the smaller the effect of curvature and the more efficient the wave trapping. Periods of oscillation T for the two cases are given above the figures.

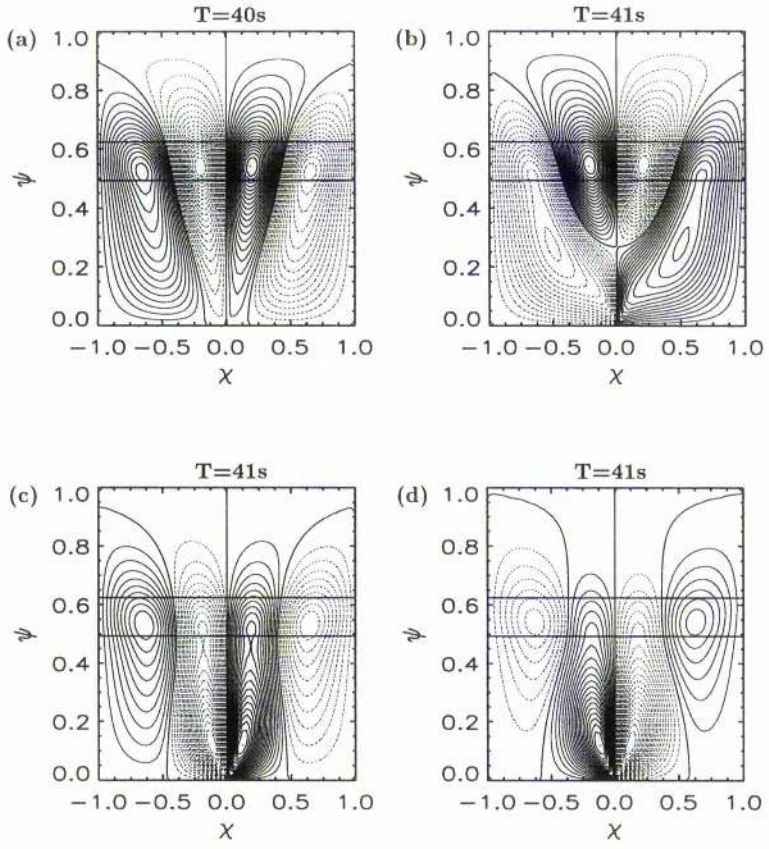

Figure 2.20: Kink mode — The effect of changing the density enhancement of the loop $0.49 \leq \psi \leq 0.62$ for the third harmonic. Contour plots of v_n are shown for (a) $\rho = 5.0$, $\omega_d = 15.76$, (b) $\rho = 4.25$, $\omega_d = 15.35$, (c) $\rho = 4.09$, $\omega_d = 15.37$ and (d) $\rho = 4.05$, $\omega_d = 15.37$. Weak slabs with low plasma density (cases (b), (c) and (d)) are much more leaky than strong, high plasma density slabs (case (a)). Periods of oscillation are given above each figure.

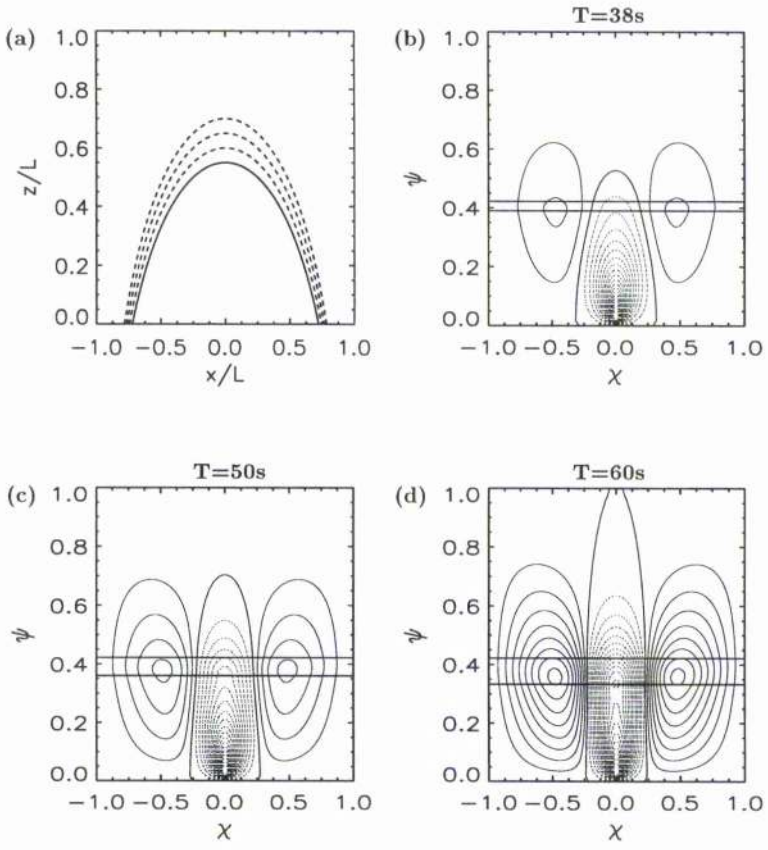

Figure 2.21: Kink mode — The effect of the width of the loop on leakage of the second harmonic in a loop with a density enhancement $\rho = 6$. (a) The three loops considered, shown in (x, z) coordinates, have their boundaries on a fixed field line (lower solid line of loop, $\psi = 0.42$) and one of the three dashed lines. Contour plots of v_n in flux coordinates are shown for (b) a narrow loop $\psi = 0.39$, $\omega_d = 14.11$, (c) an intermediate width loop $\psi = 0.36$, $\omega_d = 12.39$ and (d) a wide loop $\psi = 0.33$, $\omega_d = 10.27$. Wave guiding is much more efficient in wide loops.

2.7 Sausage Mode

The results for the kink and sausage modes turn out to be similar; accordingly we only summarise the main results of the sausage mode.

Whereas in Section 2.6 pure kink waves were found, the sausage mode exists only in a hybrid form: the loops are found to oscillate symmetrically at the top, where the loop is widest, but the lower, narrower parts oscillate asymmetrically.

In agreement with the infinite slab or cylinder cases (Edwin and Roberts 1982, 1983) the sausage mode exists only for wavenumbers above a critical value; in the infinite slab case this is the k^{crit} of Equation (2.11). We refer to the minimum frequency sausage mode as the *critical* mode.

Sausage modes tend to be more leaky than kink modes (sometimes even in long loops or for relatively large values of the density ratio ρ) although the two modes have some features in common. In a similar manner to kink modes, sausage modes have a velocity v_n that is alternately even and odd about the loop summit and, as found in Section 2.6.1, the odd modes appear to be more confined than the even modes. Moreover increasing the frequency tends to produce an increase in leakage. The critical mode produces similar results to the slab geometry and in the loops considered is ducted with minimal leakage. The leakage in other modes depends on their frequency and on whether the normal velocity component is even or odd about the loop summit. As for the kink mode short loops are more leaky than long loops. Also the higher the density ratio the smaller the leakage from the loop. This implies there is a greater energy loss associated with weak loops. We find wave ducting is more efficient in wide loops. This has important consequences since in the slab geometry it is possible to use arbitrarily small values of the slab width $2a$ to obtain short periods (see Equation 2.12). However in a curved geometry this is not possible since leakage increases and ultimately the mode is destroyed.

2.8 Discussion

Our numerical investigation into ducted waves in curved coronal loops has shown that, as in curved waveguides, leaky waves arise in curved magnetic structures. These waves will propagate away from any density enhancement and may be responsible for some of the reported coronal oscillations.

The critical sausage mode exhibits minimal leakage in all the loops considered. Using typical coronal values of $2a = 2 \times 10^3$ km for the width of the loop and an Alfvén speed of $v_{A0} = 1.5 \times 10^3$ km s^{-1} within a loop, we find sausage mode periods of a few seconds, in agreement with the straight slab and cylinder work of Roberts et al. (1983, 1984). Hence the abundantly reported short period oscillations (see Chapter 1) may indeed be due to the critical sausage mode and its low harmonics. Higher sausage harmonics are not likely to be observed in coronal loops because of the large leakage. The fundamental kink mode is found to have periods in the range 40 to 60 seconds, also in agreement with the analytical work of Roberts et al. For shorter loops

(e.g. 2×10^4 km) periods are between 4 and 6 seconds, typical of observed periods. Since the kink mode is less prone to leakage higher harmonics may account for some of the observations. However it is likely that some of the reported periods are not due to oscillations specifically within a loop but to the waves that leak from it.

The extent of the leakage depends upon the length, width and density enhancement of the loop, as well as the mode and frequency of oscillation. Increasing the length, width or plasma density ratio reduces leakage, whilst higher harmonics result in an increase in energy leakage. In addition even harmonics are less confined than odd harmonics and the sausage mode is more affected by the loop curvature than the kink mode and is thus more leaky.

We may offer some physical explanations for these results. Firstly it is worth recalling the numerical results of Murawski and Roberts (1993a-d) who considered ducted waves in a smoothed slab geometry embedded in a uniform field. They found for the sausage mode that waves with low frequency or in wide slabs leak less energy. Additionally the energy leakage is lower for stronger slabs (higher density ratio). Also the kink wave was much more robust than the sausage mode and consequently the sausage mode was more prone to leakage. The energy leakage in a spatially smooth density profile for the kink mode was negligibly small, even for weak slabs. The effectiveness of wave guidance depends upon the Alfvén speed profile — the smoother the profile, the higher the leakage. These results for a straight slab in a uniform field are in good agreement with the results in the curved structure presented here.

For long loops the geometry is less significant and the situation is similar to the slab case. Hence the leakage is less from these loops. Long loops have a length which is much greater than the horizontal distance between the two footpoints. In such loops the effect of curvature is small. In short loops, with length comparable to the horizontal distance between footpoints, curvature is a much more important factor. Short loops have greater curvature and so, by analogy with waveguide theory (Gloge 1972), the larger the effect of curvature the greater the leakage. Hence the smaller the loop the greater the energy loss.

Loops with high plasma density ratio (i.e. strong slabs) act as effective waveguides and leakage from these loops is small. Low density enhancements (i.e. weak slabs) are inefficient wave traps and waves are able to leak more readily. Therefore for high density active regions and flare loops ($\rho > 10$) we may expect leakage to be negligible. For lower density active region loops, say $\rho < 10$, wave ducting will be less efficient.

For high modes of oscillation the waves "feel" the curvature more than lower modes. Hence higher frequencies lead to increased leakage. Therefore it is not possible to consider an arbitrarily high harmonic to explain certain observations. This is a familiar result from waveguide theory where higher harmonics leak more strongly due to the angle of incidence of the wave on the boundary (e.g. Young 1986). In waveguide theory there is a critical mode above which ducted waves will not propagate. This has been considered in curved waveguides by Gloge (1972) and agrees with our numerical results. In addition odd modes with a node at the summit of the loop have a wavelength

which minimises the effect of curvature, thus reducing the leakage.

The sausage mode has its kinetic energy density located near the loop edges, whereas for the kink mode the energy is located in the centre of the loop. Therefore the kink mode is much more robust to curvature and waves are more confined. In addition the sausage mode has a nodal line (zero v_n) in the centre of the loop. Hence curvature effects are stronger since part of the curve is stationary. For the kink mode the entire loop oscillates so curvature is not as strongly felt. Also the velocity is greater at the interface for the sausage mode and it will tend to lose more energy (since energy loss is proportional to the velocity squared).

A similar argument applies for the results concerning the width of the loop. Wide loops have a relatively smaller velocity at the loop interface and thus are less leaky. Narrow loops emphasise the curvature which increases the leakage. The sausage mode was found to guide waves only for sufficiently large loop widths, which puts a lower bound on the period of this mode.

The hybrid nature of the sausage mode can be explained by the non-uniform width of the curved loop. The loops considered have a maximum width at the summit of the loop. From the slab case (Roberts et al. 1983) the sausage mode occurs only above a threshold (Equation 2.11). Hence for a fixed mode (i.e. fixed k_z) this condition may be satisfied where the loop is wide, but not in the narrowest parts of the loop. Where Equation (2.11) is satisfied the loop will oscillate symmetrically; asymmetric oscillations will be observed elsewhere.

Finally it is worth mentioning that photospheric line-tying of field lines has little effect on the ducting properties of loops and only gives rise to discrete modes (as opposed to the continuous dependence of ω on k_z in the case of an infinite slab; see Edwin and Roberts 1982). Therefore the fast mode leakage in the present geometry must be ascribed solely to the curvature of the loop and not to its length.

2.9 Summary

We now summarise the main results of this chapter. We have examined the effect of curvature on fast magnetoacoustic waves in dense coronal loops situated in a potential coronal arcade. The wave equation governing velocity perturbations has been solved numerically ignoring gravity. Due to the curvature of the structure leaky waves arise. The extent of the leakage depends upon the length, width and density enhancement of the loop, as well as the frequency of oscillation and its geometrical nature. The sausage mode is more affected by curvature and is more leaky than the kink mode. An increase in length, width or plasma density reduces the leakage, whilst higher frequencies result in greater energy leakage. Odd modes of oscillation (zero velocity at the loop summit) are more strongly confined than even modes. Modes of oscillation may be destroyed by curvature and above a critical frequency ducted waves cease to exist. The results from our investigation have shown that a curved geometry does play an important role, with magnetoacoustic waves leaking from the loop into the environment. However we have also found that the main results

reported by Roberts, Edwin and Benz (1983, 1984) for a straight slab or cylinder are relevant to the more complicated geometry of a magnetic arcade.

Chapter 3

Ducted Waves in Current Sheets

3.1 Introduction

The investigation in the previous chapter focussed upon ducted waves in curved coronal loops. However current sheets may also act as a guide for waves. This chapter examines in detail the properties of ducted magnetoacoustic waves in a current sheet. The equilibrium magnetic field strength, Alfvén speed and plasma density vary continuously across the structure. The results are applied to sheets both in the solar corona and the Earth's magnetosphere.

The formal definition of a current sheet is given by Priest (1982) as the *non-propagating boundary between two plasmas, with the dominant magnetic field tangential to the boundary.* The special case where the magnetic field reverses in direction from one side of the sheet to the other, becoming zero in the centre, is called a *neutral sheet.* This chapter investigates the magnetoacoustic modes of a neutral sheet.

Ducted waves occur in regions of low Alfvén speed (Edwin and Roberts 1982; Roberts, Edwin and Benz 1984; Murawski and Roberts 1993a,b; Nakariakov and Roberts 1995; Smith, Roberts and Oliver 1997a; Chapter 2). Therefore we may expect wave energy to be localised where the magnetic field is weak, as in a neutral sheet, or where plasma density is high, as within a coronal loop. Hence coronal streamers, which contain both closed dense loops and current sheets, are expected to provide effective wave ducts. The investigation of magnetoacoustic wave propagation in inhomogeneous photospheric flux tubes and coronal loops has been comprehensively studied (see the reviews by Roberts 1985, 1991a, 1992 and Edwin 1991, 1992). A variety of waves may be present in the solar atmosphere — body or surface, fast or slow — their existence and properties depending upon the relative orderings of the Alfvén and sound speeds.

Direct observations of current sheets in the solar atmosphere are not common. Eddy (1973), analysing results from the 1922 solar eclipse, suggests the existence of a coronal neutral sheet which separates regions of opposite magnetic polarity. The width and length of the sheet were

found to be 9 arcseconds ($\approx$ 6.5 Mm) and 4 solar radii (2784 Mm) respectively. Neutral sheets are expected to be present above the helmet structures in coronal streamers and between coronal loop systems of opposite polarity. Current sheets may be formed in one of three ways (Priest 1982): the interaction of topologically distinct regions, the loss of equilibrium of a force-free field, or X-point collapse. In addition, within the Earth's magnetosphere, the nightside central plasma sheet and dayside magnetopause both contain current sheets. We show here that such sheets may support magnetoacoustic waves.

Current sheets are important structures which may guide waves; the damping of these waves may be an important mechanism for coronal heating (see, for example, Cramer 1994; Tirry, Čadež, and Goossens 1997). The study of magnetoacoustic waves in current sheets may also provide valuable insight into the origin of the frequently reported oscillations in the corona (see Chapter 1) and the Earth's magnetosphere (see Anderson 1994 and references therein). Evidence of wave-like motions in solar current sheets is limited, although Aurass and Kliem (1992) associate a Type IV radio burst with activity in a large sheet. These authors suggest that the formation of current filaments by the tearing mode instability may create propagating magnetoacoustic waves. In addition, there have been many recent observations of short period coronal oscillations (Correia and Kaufmann 1987; Zhao et al. 1990; Rušin and Minarovjech 1994; Zlobec et al. 1992), with periods ranging from 0.3 to 12 seconds, which may be associated with oscillating current sheets. There have also been reports of current sheet oscillations in the Earth's magnetotail. Periodicities in the range 3.5 to 5 minutes in the electron flux were reported by Montgomery (1968). Mihalov, Sonett and Colburn (1970) found periods ranging from 0.5 to 15 minutes with peaks at 100 seconds, 4.5 minutes and 8 minutes. Recently, Bauer, Baumjohann and Treumann (1995a) and Bauer, Baumjohann, Treumann, Sckopke and Lühr (1995b) have reported 1–2 minute oscillations in the vicinity of a current sheet where the perturbed plasma and magnetic pressures were out of phase.

In this chapter we investigate in detail the eigenmodes supported by a current sheet. Such an investigation may provide important seismic information about the corona and magnetosphere. We show that a current sheet supports both kink and sausage oscillations. In the sausage mode the current sheet pulsates like a blood vessel with the central axis remaining undisturbed. In the kink mode the central axis moves back and forth during the wave motion. In a simple slab trapped modes may also be characterised as either *body* (oscillatory in the interior) or *surface* (hyperbolic in the interior); see Roberts (1981a,b, 1985, 1991a, 1992), Edwin and Roberts (1982) and Edwin (1991, 1992) for a full discussion. We show here that in a continuously structured medium, three types of trapped mode can exist: *body, surface,* and *hybrid.* The nature of the mode is governed by the phase speed and wavenumber. Hybrid modes contain elements of both body and surface waves. We restrict attention to modes which are evanescent outside the current sheet and therefore ignore any wave leakage; *leaky* modes have been discussed by Cally (1986) and in Chapter 2.

The component of velocity transverse to the sheet can have nodes in two spatial directions, across the sheet width or along the sheet length. Modes with the least number of nodes across

the sheet are referred to as principal modes. Traversing the sheet from one boundary to the other the velocity in the principal kink mode does not change sign, whereas the principal sausage mode changes sign once (at the central axis). Overtones of the kink and sausage modes have a greater number of nodes in the direction perpendicular to the current sheet axis.

For the neutral sheet in the Earth's magnetotail, widths of 3–6 Earth radii ($1R_E = 6400$ km) have been used by Patel (1968), McKenzie (1970) and Edwin, Roberts and Hughes (1986) in theoretical models. Hopcraft and Smith (1985) used a range from 1000 km to 50 000 km, whilst Seboldt (1990) used a sheet thickness of 30 000 km. For our calculations we use current sheet widths of $2a = 1000$ km for solar applications and $2a = R_E$ for the Earth's magnetotail. The constant Alfvén speed in the corona is taken to be 1000 km s^{-1}, whilst in the magnetosphere a value of 500 km s^{-1} is considered (Mihalov et al. 1970). In this chapter we use the standard ideal magnetohydrodynamic (MHD) equations. The mean free path in the solar corona (for temperatures 10^6 K and number densities 10^9 cm^{-3}) is of the order of 50 km whereas the electron gyro-radius is 20 cm for a field of a gauss (Spitzer 1962). Using these values the effective electron collision time is 0.014 seconds. Hence we consider only current sheets with widths greatly in excess of 50 km and time scales much greater than 0.014 seconds to ensure the applicability of MHD. Ideal MHD may only be applied with caution in the Earth's magnetosphere. A discussion on the validity of the use of MHD in the magnetosphere may be found in Schindler and Birn (1978, 1986) and Birn, Hesse and Schindler (1996). The authors suggest that a MHD approach may be justified because the plasma pressure is approximately isotropic within the plasma sheet. In addition, Birn et al. (1996) compare the results of simulations of the magnetotail using MHD, hybrid and particle codes. The results are qualitively similar in each case, suggesting that MHD is a good approximation to the more rigourous particle treatment.

The format of the chapter is as follows. In Section 3.2 we review the previous work undertaken on wave propagation in current sheets, whilst in Section 3.3 the equilibrium and governing wave equation for our model are discussed. In Section 3.4 the numerical procedure for solving the governing equation is described and in Section 3.5 we explain the properties of magnetoacoustic waves in current sheets. Finally, in Section 3.6 our results are summarised and conclusions are drawn.

3.2 Previous work

Several authors have investigated wave propagation in neutral sheets. Here we review this work, firstly examining the special case of an incompressible plasma (Section 3.2.1) and then turning to a compressible plasma (Section 3.2.2). A general review of waves in compressible current sheets has been given recently by Cramer (1995). Our review is similar to that of Cramer, although we have included details of the additional work reported in this field and also of incompressible sheet models.

3.2.1 Incompressible Plasma

The Model of Lau (1979)

The incompressible case is studied by letting $\gamma \to \infty \left(c_s^2 \to \infty\right)$ in Equation (1.31) which gives $m^2 \approx k_z^2$. For $m^2 > 0$ the modes of oscillation are surface waves (see Edwin and Roberts 1982). Body modes require $m^2(x)$ to be negative which is not possible in this case since k_z^2 is always positive. For an incompressible plasma with constant density and a magnetic field profile $\mathbf{B} = B(x)\,\hat{\mathbf{e}}_z$, with field $B(x)$ given by

$$B(x) = \begin{cases} B_e\,, & x > a \\ B_e\,(x/a)\,, & |x| \le a \\ -B_e\,, & x < -a\,, \end{cases} \tag{3.1}$$

the governing wave equation (Equation 1.34) becomes (after taking $k_y = 0$ and $-\omega^2 = \partial^2/\partial t^2$)

$$\left[X^2 + \frac{\partial^2}{\partial \tau^2}\right]\left[\frac{\partial^2 v_x}{\partial X^2} - v_x\right] + 2X\frac{\partial v_x}{\partial X} = 0\,. \tag{3.2}$$

In Equation (3.2) the dimensionless space X and time τ variables are defined by

$$X = k_z x \qquad \tau = \frac{v_{Ae}}{a}t\,, \tag{3.3}$$

where $v_{Ae} = B_e/\sqrt{\mu_0 \rho}$ is the Alfvén speed in the environment of the sheet.

Following Lau (1979), we now Fourier transform in X such that

$$v_x(X,\tau) = \int_{-\infty}^{\infty} u(s,\tau)\,\mathrm{e}^{-iXs}\mathrm{d}s\,, \tag{3.4}$$

with inverse

$$u(s,\tau) = \frac{1}{2\pi}\int_{-\infty}^{\infty} v_x(X,\tau)\,\mathrm{e}^{iXs}\mathrm{d}X\,. \tag{3.5}$$

Then, after some algebra (Appendix D), Equation (3.2) reduces to

$$\frac{\partial^2 u}{\partial \tau^2} = \frac{1}{A}\frac{\partial}{\partial s}\left[A\frac{\partial u}{\partial s}\right]\,, \tag{3.6}$$

with $A \equiv 1 + s^2$. This transformed governing wave equation is identical to that determining the propagation of sound waves in a diverging tube of cross sectional area A (see, for example, Kinsler and Frey 1962; Fletcher and Rossing 1991).

Transient Behaviour

To investigate the transient behaviour of an impulsive event in a current sheet we seek a solution to Equation (3.6) of the form (Lau 1979),

$$u(s,\tau) = f(s)\,\delta(s - s_o + \tau)\,, \tag{3.7}$$

so that the initial impulse is centred on $s = s_o$. Here $\delta(s, \tau)$ is the Dirac delta function. Substitution of Equation (3.7) into the wave equation (Equation 3.6) yields the approximate solution

$$u(s,\tau) = \left[\frac{1+s_o^2}{1+s^2}\right]^{\frac{1}{2}} \delta(s - s_o + \tau) \ . \tag{3.8}$$

This solution does not satisfy the governing equation exactly. There is an error proportional to $1/\left(1+s^2\right)^{5/2}$, which is small for large s. A numerical solution of Equation (3.6) has been obtained by Lau, Davidson and Hui (1980), with similar results to the approximate analytical solution presented here. Substituting Equation (3.8) into (3.4), and using the following property of the delta function,

$$\int_{-\infty}^{\infty} f(x)\,\delta(x)\,\mathrm{d}x = f(0) \ , \tag{3.9}$$

we obtain the velocity of propagating waves in the negative s-direction as

$$v_x = v_o \left[\frac{1+s_o^2}{1+(s_o-\tau)^2}\right]^{\frac{1}{2}} \exp\left[i\left(k_x x + k_z z + k_z x s_o\right)\right] \exp\left[-ik_z x \tau\right] \ . \tag{3.10}$$

We have used the initial condition (Lau 1979)

$$v_x = v_o \exp\left[i\left(k_x x + k_z z + k_z x s_o\right)\right] \ , \tag{3.11}$$

where v_o is constant and s_o represents the initial inclination of the impulse in the xz-plane. The initial condition, according to Equation (3.11), is $u(s,0) = \delta(s - s_o)$ which describes a sound pulse at a distance s along the tube.

Consider the transient behaviour of the wave. Suppose first that s_o is positive. The initial pulse splits into two, generating two pulses which propagate in opposite directions. The pulse which travels in the negative s-direction grows in amplitude as $A^{-1/2}$ ($\approx 1/s$ for large s), so from $s = 20$ to $s = 10$ we expect an amplitude increase of about 2. The numerical results of Lau et al. (1980) show that reflections (scattering) occur in the region about $s = 0$, with the reflected pulse returning to $s \to \infty$, with diminishing amplitude. The transmitted pulse also declines. Equation (3.10) shows that the pulse will grow in amplitude from v_o to a maximum $v_o\sqrt{1+s_o^2}$ in a time $\tau = s_o$.

In Figure 3.1a the amplitude $\mathcal{A}$ of the pulse,

$$\mathcal{A} = v_o \left[\frac{1+s_o^2}{1+(s_o-\tau)^2}\right]^{\frac{1}{2}} \ , \tag{3.12}$$

versus (dimensionless) time is shown for various inclinations ($s_o = 10, 20, 30$) of the initial impulse. As the wave propagates towards $s = 0$ the amplitude of the wave increases, reaching a maximum at $\tau = s_0$, i.e. at a time

$$t = \frac{a s_o}{v_{Ae}} \ . \tag{3.13}$$

For large distances away from s_o the amplitude of the wave tends towards zero. Therefore, impulsively generated surface waves in current sheets show a transient growth up to $\tau = s_o$ and then a

subsequent decrease in amplitude. After a time 2τ the amplitude of the wave has returned to its initial value. The magnitude of the amplitude enhancement is of order s_o.

For an impulse with initial position $s_o < 0$ and wave propagation in the negative s-direction, the wave shows no amplification and the amplitude simply decreases in time (Figure 3.1b). If an initial impulse splits into two, one pulse will show a transient growth and then decay, whilst the other just decays. An impulse in an incompressible plasma current sheet will grow rapidly over a scale of a few Alfvén times. Small amplitude impulses, which may otherwise go undetected, may become large enough to be observable due to this process. Any current carrying incompressible plasma may support the growth and subsequent decay of surface waves. A similar model was presented by Uberoi (1988) to explain oscillations in the Earth's magnetosphere. However the incompressible assumption means that this application is suspect until it is extended into the compressible regime.

Lau (1979) provides the following physical explanation of the transient growth of the pulse. The magnetic perturbations on different field lines will propagate at the local Alfvén speed (which takes different values inside the current sheet). If the magnetic perturbation on one field line approaches the perturbation on another field line, the current associated with the perturbations are aligned in phase. This leads to an amplification of the perturbation.

We extend the work of Lau (1979) by transforming Equation (3.6) into an equation of the Klein-Gordon type. Using the substitution

$$Q(s,\tau) = A^{\frac{1}{2}}(s)\, u(s,\tau) \ , \tag{3.14}$$

Equation (3.6) becomes

$$\frac{\partial^2 Q}{\partial \tau^2} = \frac{\partial^2 Q}{\partial s^2} - \Omega^2 Q \ , \tag{3.15}$$

where

$$\Omega^2 = \left(\frac{A'}{2A}\right)^2 + \left(\frac{A'}{2A}\right)' \equiv \frac{1}{(1+s^2)^2} \tag{3.16}$$

and the dash denotes the derivative with respect to s.

Assuming the following form for Q,

$$Q = \hat{Q}(s)\, \mathrm{e}^{i\omega_d \tau} \ , \tag{3.17}$$

we may write Equation (3.15) in the form

$$\frac{\mathrm{d}\hat{Q}}{\mathrm{d}s^2} + \left[\omega_d^2 - \Omega^2\right] \hat{Q} = 0 \ , \tag{3.18}$$

where $\omega_d = \omega a / v_{Ae}$. For oscillatory solutions we require the frequency of oscillation, ω_d, to be greater than the local cut-off frequency, Ω. For example, at $s = 0$ where $\Omega^2 = 1$ we require $\omega_d > 1$ for oscillatory $\hat{Q}$. Assuming a current sheet half-width of $a = 500$ km and an environment Alfvén speed of 1000 km s^{-1}, a minimum period of oscillation of 3.14 seconds is obtained (cf. Chapter 1).

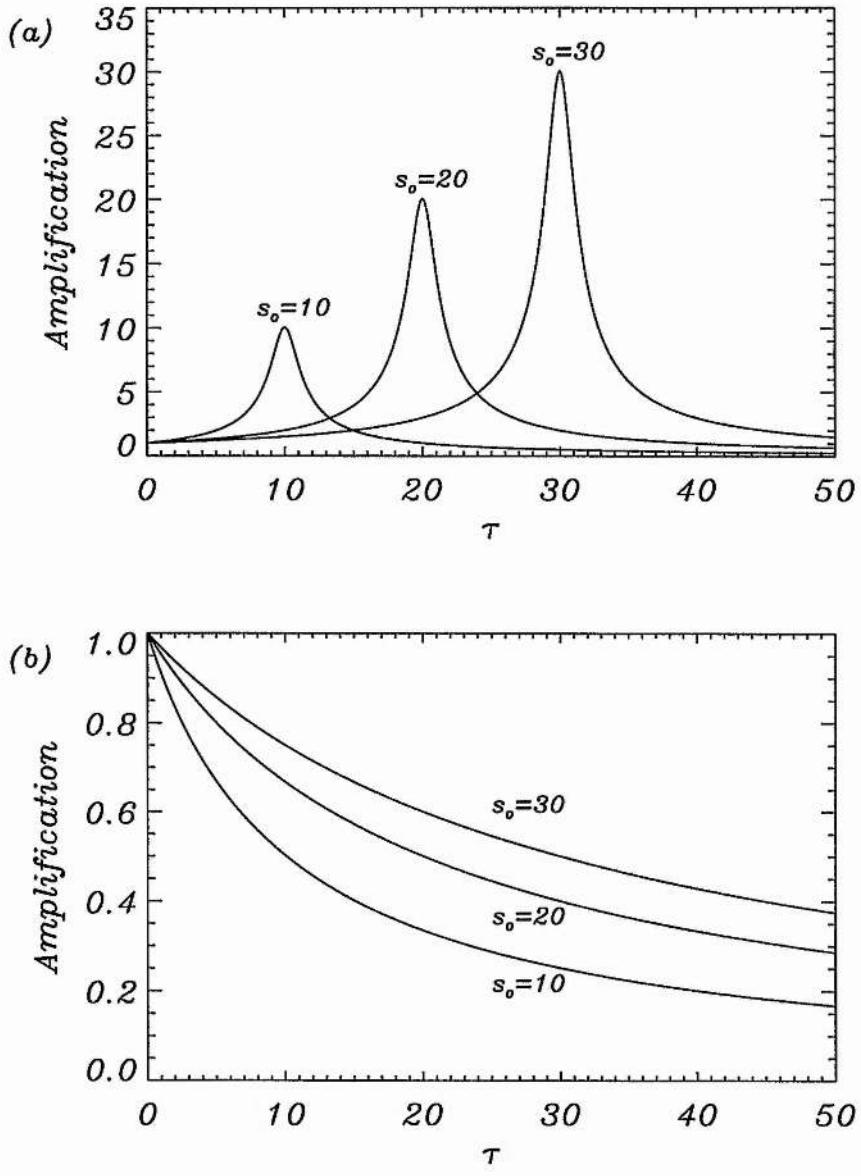

Figure 3.1: (a) A surface wave propagating in an incompressible current sheet undergoes an increase in amplitude (Equation 3.12) ($s_o > 0$ with wave propagation in the negative s-direction). The enhancement in amplitude is approximately given by s_o. (b) The amplitude of a surface wave propagating in the negative s-direction, with $s_o < 0$, decreases with time.

Waves with longer periods will be unable to propagate. Waves are either propagating or evanescent according to whether the frequency of oscillation is greater or less than the local cut-off frequency. Note that if $s \gg 1$ ($\Omega \to 0$) the solution of the wave equation reduces to that of wave propagation in an unstructured medium. A current sheet, especially near the throat ($s = 0$), only allows low period waves to propagate. The sheet acts as a high band pass filter; only high frequency waves are able to propagate and low frequency modes are evanescent.

Model of Bertin and Coppi (1985)

We now briefly describe the results of Bertin and Coppi (1985). In this work a dispersion relation for long wavelength perturbations in an incompressible current sheet was derived. Results show that surface waves may exist in a current sheet. The effect of a current sheet with a finite width is to cause the waves to be dispersive. However, the expansion method for solving the governing wave equation and the lack of consideration of the singularity means the results are suspect.

3.2.2 Compressible Plasma

Infinitely thin current sheets, where the magnetic field has a discontinuous change of direction, have been investigated. Hollweg (1982) examined the case of low frequency oscillations in a low plasma beta equilibrium. Surface waves were found for all angles of rotation of the magnetic field and angles of wave propagation relative to the field. Wessen and Cramer (1991) expanded this work with the inclusion of a finite ion-cyclotron frequency in a low plasma beta equilibrium. They found the surface wave dispersion relation was significantly altered from the low frequency result. The dispersive curves separate into branches through the introduction of the Alfvén resonance and propagation cut-offs. Solutions with frequencies less than, and greater than, the ion-cyclotron frequency were found. The effect of non-zero pressure was investigated by Cramer (1994). Two surface waves (see also Roberts 1981a) were found for some angles of wave propagation relative to the field. In addition stop bands (cut-offs) existed for other angles of propagation. Uberoi and Satya Narayanan (1986) examined the effect of changing the magnetic field direction on surface waves, which existed on a surface separating two plasmas of differing density. They found, for certain angles of rotation of field, no wave propagation occurred. A finite width current sheet was also investigated by Cramer (1994). The sheet was modelled as a field with an arbitrary change of direction through a narrow transition region. The results show that perturbations will be damped through the Alfvén and slow resonances.

Magnetoacoustic waves in a current sheet, where the equilibrium magnetic field changes sign and direction, have been investigated by Hopcraft and Smith (1985, 1986), Seboldt (1990), Tirry, Cadež and Goossens (1997) and Smith, Roberts and Oliver (1997). The equilibrium magnetic field does not rotate but reverses sign in the centre of the sheet. For equilibrium the plasma pressure is a maximum in the centre of the sheet. Hopcraft and Smith (1985) solved the governing wave

equation for a Harris sheet analytically through a small parameter expansion. Although dispersion curves for fast magnetoacoustic waves were presented, the validity of the expansion near the edge of the sheet is uncertain. Further work by Hopcraft and Smith (1986) solved the governing wave equation numerically although no dispersion curves were given. The magnetic field and pressure profiles used by Hopcraft and Smith (1986) were discontinuous at the sheet boundary. Although the sheet was in equilibrium an additional current at the edge of the sheet was generated which may have affected the results. Using the Harris sheet model, Seboldt (1990) investigated the singular solutions of the governing wave equation. This analysis showed that perturbations may be subject to phase mixing. Discrete eigenmodes were also briefly discussed although no detailed analysis of the modes was given. The recent investigation by Tirry, Čadež, and Goossens (1997) explored the damping of surface waves in a Harris profile through the Alfvén resonance; they found only two surface modes existed (the kink and sausage) with the sausage mode undergoing more damping than the kink.

In addition, models of current sheets where the equilibrium magnetic field rotates have been considered by Musielak and Suess (1988, 1989). For a current sheet with finite width they find no normal modes exist. The singularities arising in the governing wave equation suggest the perturbations will be subject to phase mixing. For a sheet of zero width a ducted mode may be supported.

Current Sheet Model of Edwin, Roberts and Hughes (1986)

A slab model of a current sheet was analysed by Edwin, Roberts and Hughes (1986) and Edwin (1992) to explain the generation of Pi2 pulsations in the Earth's plasma sheet. Pi2 pulsations are quasi-periodic oscillations with periods ranging between 40 and 150 seconds, typically lasting for a few cycles (Southwood and Stuart 1980; Singer et al. 1985). The sheet was modelled as an unbounded hot plasma slab, with a narrow field-free region between the anti-parallel fields of the Earth's magnetotail (Figure 3.2). In the magnetic region the cold plasma approximation was used.

The governing wave equation for linear perturbations about an equilibrium, with magnetic field $\mathbf{B} = B(x)\,\hat{\mathbf{e}}_z$, plasma density $\rho(x)$ and plasma pressure $p(x)$ constant in each region under consideration, is (Roberts 1981a)

$$\frac{\mathrm{d}^2 v_x}{\mathrm{d}x^2} - m_i^2 v_x = 0\,, \tag{3.19}$$

where

$$m_i^2 = -n_i^2 = \frac{\left(k_z^2 c_{si}^2 - \omega^2\right)\left(k_z^2 v_{Ai}^2 - \omega^2\right)}{k_z^2 c_{si}^2 v_{Ai}^2 - \left(c_{si}^2 + v_{Ai}^2\right)\omega^2}\,. \tag{3.20}$$

Here the subscript i becomes 0 in the field-free region and e in the magnetic region. The frequency and longitudinal wavenumber are ω and k_z respectively, whilst the sound and Alfvén speeds are denoted by c_{si} and v_{Ai}. The velocity component normal to the magnetic field is v_x. In this chapter we drop the hat notation used in Chapter 1. However all the quantities such as v_x and the perturbed pressures have a $\exp\left[i\left(\omega t - k_z z\right)\right]$ dependence.

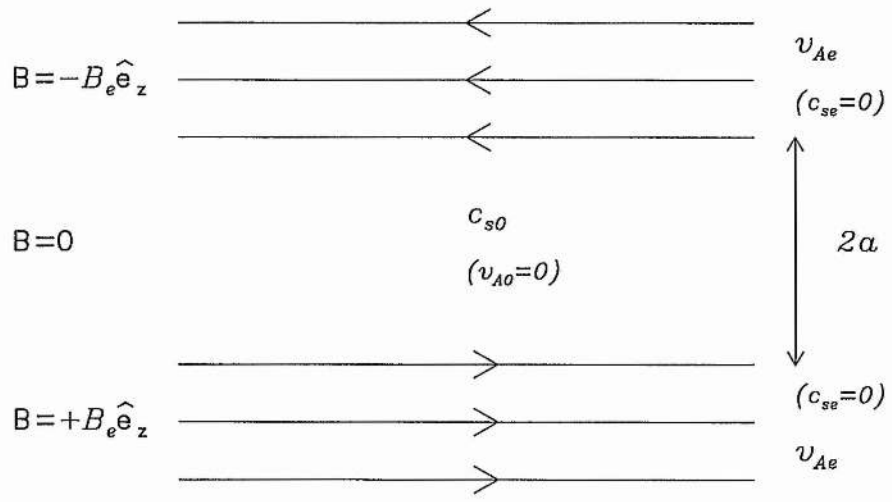

Figure 3.2: The current sheet model of Edwin, Roberts and Hughes (1986). A narrow field-free region of width $2a$ exists between the oppositely directed field of the magnetotail.

For the slab model of Edwin et al. (1986) we have $v_{A0} = 0$, $c_{se} = 0$, $v_{Ae} \neq 0$ and $c_{s0} \neq 0$. Therefore Equation (3.20) reduces to

$$m_0^2 = -n_0^2 = k_z^2 - \frac{\omega^2}{c_{s0}^2} \tag{3.21}$$

and

$$m_e^2 = k_z^2 - \frac{\omega^2}{v_{Ae}^2} \, . \tag{3.22}$$

The general solution of Equation (3.19) for surface waves in the field-free region ($|x| \leq a$) is

$$v_x = \alpha_0 \cosh m_0 x + \beta_0 \sinh m_0 x \; ; \tag{3.23}$$

and for body waves the solution is

$$v_x = \alpha_0 \cos n_0 x + \beta_0 \sin n_0 x \, . \tag{3.24}$$

Body and surface modes are characterised by $n_0^2 > 0$ and $m_0^2 > 0$ respectively. Here α_0 and β_0 are arbitrary constants; $\alpha_0 = 0$ and $\beta_0 = 0$ give sausage ($v_x = 0$ at $x = 0$) and kink modes ($\mathrm{d}v_x/\mathrm{d}x = 0$ at $x = 0$) respectively. Assuming that $v_x \to 0$ as $|x| \to \infty$, the velocity in the magnetic region ($|x| > a$) takes the form,

$$v_x = \alpha_e \exp\left[-m_e \left(x - a\right)\right] \quad x > a \, , \tag{3.25}$$

$$v_x = \beta_e \exp\left[m_e \left(x + a\right)\right] \quad x < -a \, . \tag{3.26}$$

In order to satisfy the boundary condition at $|x| \to \infty$ we require $m_e > 0$. From Equation (3.22) this requires that the phase speed (ω/k_z) is less than the Alfvén speed in the magnetic region (v_{Ae}). Moreover, for the body modes we need $n_0 > 0$. Thus trapped body modes lie in the phase speed range

$$c_{s0} < \frac{\omega}{k_z} < v_{Ae} \,, \tag{3.27}$$

i.e. between the interior sound speed and the exterior Alfvén speed. Similarly, for the surface modes we find the phase speeds must satisfy

$$0 < \frac{\omega}{k_z} < c_{s0} \,. \tag{3.28}$$

To obtain the dispersion relation we match the solutions for the regions $|x| \leq a$ and $|x| > a$ at the sheet boundaries, $x = \pm a$. Taking the velocity component normal to the equilibrium magnetic field, v_x, and the total pressure perturbation, p_T,

$$\frac{i\omega}{\rho_i} p_T = \frac{\left(\omega^2 - k_z^2 v_{Ai}^2\right)}{m_i^2} \frac{\mathrm{d}v_x}{\mathrm{d}x} \tag{3.29}$$

to be continuous across the sheet boundaries, leads to the dispersion relation (Edwin et al. 1986; Edwin 1992)

$$\frac{2c_{s0}^2}{\gamma v_{Ae}^2} \left(k_z^2 v_{Ae}^2 - \omega^2\right) m_0 \left\{ \begin{array}{c} \tanh \\ \coth \end{array} \right\} m_0 a = \omega^2 m_e \tag{3.30}$$

for the surface $\left(m_0^2 > 0\right)$ modes, and

$$\frac{2c_{s0}^2}{\gamma v_{Ae}^2} \left(k_z^2 v_{Ae}^2 - \omega^2\right) n_0 \left\{ \begin{array}{c} -\tan \\ \cot \end{array} \right\} n_0 a = \omega^2 m_e \tag{3.31}$$

for the body $\left(n_0^2 = -m_0^2 > 0\right)$ waves. The "tan" and "tanh" solutions refer to the sausage modes, whereas the "cot" and "coth" terms relate to kink modes; γ is the ratio of specific heats. In deriving the dispersion relation, the calculated density ratio between the magnetic region and field-free region is constrained by the pressure balance condition $p_e + B_e^2/2\mu_0 = p_0$, such that

$$\frac{\rho_e}{\rho_0} = \frac{2c_{s0}^2}{\gamma v_{Ae}^2} \,. \tag{3.32}$$

Both principal kink body and sausage surface modes were found. In the slender sheet approximation $(k_z a \ll 1)$ their phase speeds tended towards the exterior Alfvén and tube speeds respectively. The principal kink body mode transforms to a surface wave when its phase speed falls below the constant sound speed within the sheet. The dimensionless phase speed, $v_{ph} = \omega/k_z v_{Ae}$, of both the sausage and kink surface waves tends towards the same limiting value at short wavelengths $(k_z a \gg 1, \tanh m_0 a, \coth m_0 a \to 1)$, given by

$$v_{ph} = \left[\frac{2\Lambda^2}{(1+\Lambda^2) + \sqrt{1 + 5\Lambda^4 - 2\Lambda^2}} \right]^{\frac{1}{2}} \,, \tag{3.33}$$

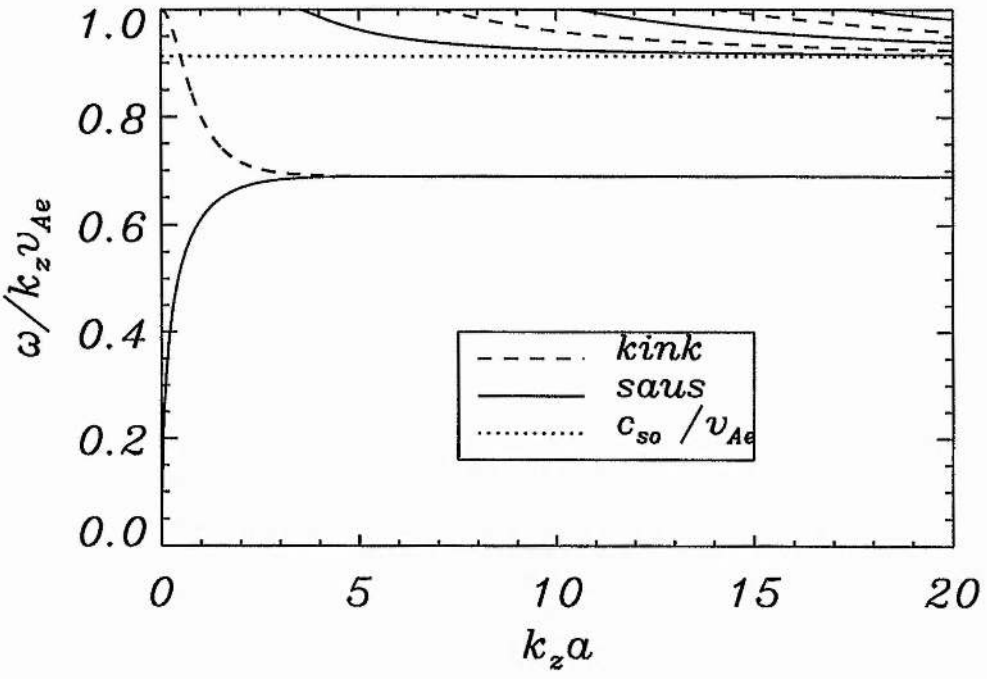

Figure 3.3: The dispersion curves for magnetoacoustic waves in the current sheet model of Edwin et al. (1986), with $\Lambda^2 = \gamma/2$ and $\gamma = 5/3$. The modes are classified as *body* when their phase speed (ω/k_z) lies between c_{s0} and v_{Ae}. Two *surface* modes arise (a kink and sausage). For long wavelength oscillations, the phase speed of the principal kink body and sausage surface modes tend to v_{Ae} and zero respectively. For short wavelengths the phase speeds of both surface modes tend to the same value. Kink and sausage body modes above wavenumber cut-offs also exist, their phase speeds lying between the interior sound speed and exterior Alfvén speed. Notice that here, in the slab model, there is a clear distinction between body and surface modes (cf. Figure 3.7).

where $\Lambda = \gamma v_{Ae}/2c_{s0}$ (see Appendix E). In addition sausage and kink body modes were found above wavenumber cut-offs, occurring at

$$k^{crit}a = \frac{n\pi}{2}\left[\frac{1}{\left(\frac{2\Lambda}{\gamma}\right)^2 - 1}\right]^{\frac{1}{2}}, \tag{3.34}$$

with n an integer. If $\Lambda \to \gamma/2$ (i.e. when the interior sound speed approaches the exterior Alfvén speed) the critical wavenumber tends to infinity, in which case only two surface modes will be able to propagate. The phase speed of the body waves lie between the interior sound speed (c_{s0}) and the exterior Alfvén speed (v_{Ae}). Edwin et al. (1986) and Edwin (1992) suggested that the long period magnetospheric oscillations (see, for example, Anderson 1994) may be due to surface waves, whereas the shorter period Pi2 pulsations may be body waves (see also McKenzie 1970 for a similar model).

Impulsively generated waves in a plasma sheet were found to consist of a well defined wave packet consisting of a periodic phase, followed by quasi-periodic phase and then a decay phase, in good agreement with observations. However an important aspect neglected in this model was the field reversal region. We consider this aspect in detail in this chapter and in Chapter 4, where we discuss propagation in a structured current sheet.

The dispersion diagram resulting from the solution of Equations (3.30) and (3.31) is shown in Figure 3.3 for $\Lambda^2 = \gamma/2$. Kink and sausage modes are denoted by dashed and solid lines respectively. The adiabatic index is $\gamma = 5/3$. Although the dispersive curves are identical to those obtained by Edwin et al. (1986) and Edwin (1992), this figure has been calculated by ourselves using numerical solutions of the dispersion relations.

3.3 Equilibrium and Governing Equations

Having seen the results that arise in the empty slab model of Edwin et al. (1986) we turn now to a detailed investigation of a *structured* current sheet. We suppose that the current sheet has a magnetic field modelled by the Harris (1962) profile. The one-dimensional equilibrium magnetic field $\mathbf{B} = B(x)\,\hat{\mathbf{e}}_z$ is given by

$$\mathbf{B} = B_e \tanh\left(\frac{x}{a}\right)\hat{\mathbf{e}}_z, \tag{3.35}$$

which represents a continuous change of the field strength from B_e at large positive x/a, to $-B_e$ at large negative x/a and passing through zero at $x/a = 0$. Equilibrium demands that the total pressure (plasma plus magnetic) is uniform

$$p(x) + \frac{B^2(x)}{2\mu_0} = constant, \tag{3.36}$$

yielding a plasma pressure $p(x)$ of

$$p(x) = p_0 \mathrm{sech}^2\left(\frac{x}{a}\right), \qquad p_0 = \frac{B_e^2}{2\mu_0}, \tag{3.37}$$

given that $p \to 0$ (cold plasma) as $|x|/a \to \infty$. The plasma density is arbitrary; we assume a density profile $\rho(x)$ of the form (cf. Epstein 1930)

$$\rho(x) = \rho_0 \mathrm{sech}^2\left(\frac{x}{a}\right) + \rho_e \tanh^2\left(\frac{x}{a}\right), \tag{3.38}$$

declining from ρ_0 at $x/a = 0$ to $\rho_e\,(< \rho_0)$ as $|x|/a \to \infty$. Through the ideal gas law ($p \propto \rho T$) the temperature $T(x)$ is not constant. The implied sound speed $c_s(x)$ $\left(= (\gamma p/\rho)^{1/2}\right)$ varies from $c_s(0)$ at the centre of the current sheet to zero in the far environment of the sheet, consistent with our assumption of a cold plasma as $|x| \to \infty$. Specifically, the square of the sound speed $c_s^2(x)$ is given by

$$c_s^2(x) = \frac{c_s^2(0)\,\mathrm{sech}^2\left(\frac{x}{a}\right)}{\frac{\rho_0}{\rho_e}\mathrm{sech}^2\left(\frac{x}{a}\right) + \tanh^2\left(\frac{x}{a}\right)}. \tag{3.39}$$

The square of the Alfvén speed $v_A^2(x)$ $(= B^2/\mu_0\rho)$ is given by

$$v_A^2(x) = \frac{v_{Ae}^2 \tanh^2\left(\frac{x}{a}\right)}{\frac{\rho_0}{\rho_e}\mathrm{sech}^2\left(\frac{x}{a}\right) + \tanh^2\left(\frac{x}{a}\right)}, \tag{3.40}$$

where $v_{Ae}^2 = {B_e}^2/\mu_0\rho_e = 2c_s^2(0)/\gamma$. Thus the Alfvén speed, $v_A(x)$, declines from v_{Ae} in the far environment of the current sheet ($|x|/a \to \infty$) to zero at the centre of the sheet. Figure 3.4 gives plots of these two speeds, together with the tube speed $c_T(x)$ $\left(= c_s v_A/(c_s^2 + v_A^2)^{1/2}\right)$ and the fast speed $c_f(x)$ $\left(= (c_s^2 + v_A^2)^{1/2}\right)$.

Consider the linearised equations of ideal magnetohydrodynamics assuming gravity is negligible. The wave equation for two-dimensional plasma motions,

$$\mathbf{v} = (v_x, 0, v_z)\exp i(\omega t - k_z z), \tag{3.41}$$

in a non-uniform magnetic field $\mathbf{B} = B(x)\,\hat{\mathbf{e}}_z$, where the equilibrium parameters (density and pressure) are dependent upon x, is given by (Roberts 1981a)

$$\frac{\mathrm{d}}{\mathrm{d}x}\left[f(x)\frac{\mathrm{d}v_x}{\mathrm{d}x}\right] + \rho\left(\omega^2 - k_z^2 v_A^2\right)v_x = 0, \tag{3.42}$$

where

$$f = \frac{\rho c_f^2\left(\omega^2 - k_z^2 c_T^2\right)}{\left(\omega^2 - k_z^2 c_s^2\right)}. \tag{3.43}$$

Here v_x is the velocity component normal to the magnetic field, ω is the frequency and k_z is the longitudinal wavenumber along the sheet. The velocity parallel to the magnetic field is given by

$$v_z = -\frac{ik_z c_s^2}{\left(\omega^2 - k_z^2 c_s^2\right)}\frac{\mathrm{d}v_x}{\mathrm{d}x}. \tag{3.44}$$

We only consider motions that are independent of the y-coordinate so that propagation is in the xz-plane.

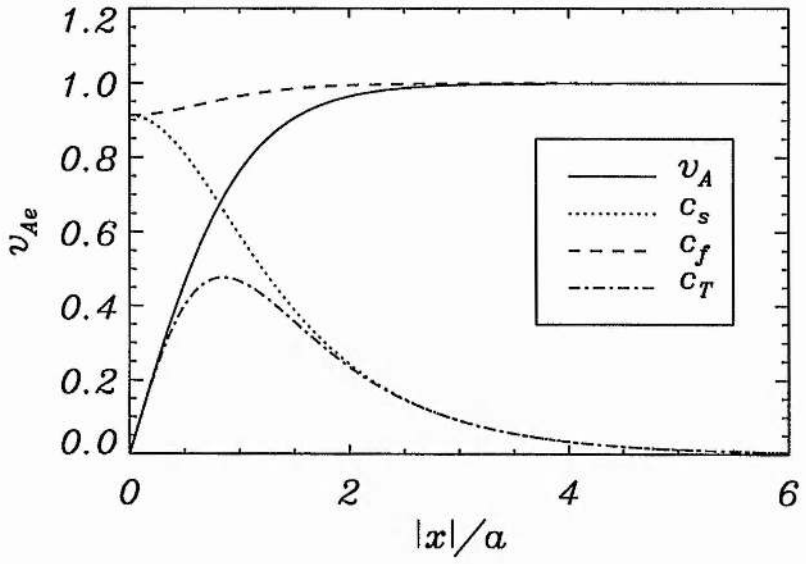

Figure 3.4: A plot of the Alfvén v_A, sound c_s, fast c_f and tube c_T speeds (normalised against v_{Ae}) in a neutral current sheet with uniform density and $\gamma = 5/3$. The region of low Alfvén speed about $x/a = 0$ acts as a duct for magnetoacoustic waves. Note that the fast speed is approximately constant throughout the whole domain. The sound and tube speeds have maxima of $0.9129 v_{Ae}$ and $0.4771 v_{Ae}$ respectively. These speeds are important in determining the nature of the magnetoacoustic waves in a current sheet.

The perturbed plasma (p_1), magnetic ($p_{1m} = \mathbf{B}.\mathbf{b_1}/\mu_0$) and total ($p_T = p_1 + p_{1m}$) pressure perturbations are given by

$$\frac{i\omega}{\rho} p_1 = -\frac{c_s^2\omega^2}{(\omega^2 - k_z^2 c_s^2)} \frac{\mathrm{d}v_x}{\mathrm{d}x} - \frac{v_x}{\rho}\frac{\mathrm{d}p}{\mathrm{d}x} , \tag{3.45}$$

$$\frac{i\omega}{\rho} p_{1m} = -v_A^2 \frac{\mathrm{d}v_x}{\mathrm{d}x} - \frac{B}{\mu_0 \rho}\left(\frac{\mathrm{d}B}{\mathrm{d}x}\right) v_x , \tag{3.46}$$

$$\frac{i\omega}{\rho} p_T = -\frac{c_f^2\left(\omega^2 - k_z^2 c_T^2\right)}{(\omega^2 - k_z^2 c_s^2)} \frac{\mathrm{d}v_x}{\mathrm{d}x} , \tag{3.47}$$

whilst the magnetic tension force $\mathbf{T_1}$ takes the form

$$\frac{i\omega}{\rho}\mathbf{T_1} = -v_A^2 k_z^2 v_x \hat{\mathbf{e}}_\mathbf{x} + \left(\omega^2 - k_z^2 c_s^2\right)\frac{v_A^2}{c_s^2} v_z \hat{\mathbf{e}}_\mathbf{z} , \tag{3.48}$$

where $\mathbf{b_1}$ is the perturbed magnetic field and

$$\mathbf{T_1} = \frac{1}{\mu_0}\left(\mathbf{B}\cdot\nabla\right)\mathbf{b_1} + \frac{1}{\mu_0}\left(\mathbf{b_1}\cdot\nabla\right)\mathbf{B} . \tag{3.49}$$

To investigate the nature of the modes we reduce Equation (3.42) to the canonical form (where the coefficient of the first derivative is equal to zero). Setting $v_x = \phi(x) F(x)$ reduces the governing wave equation to

$$\phi'' + \kappa^2(x)\,\phi = 0 , \qquad \kappa^2 = -m_i^2 - \frac{1}{2}\left(\frac{f'}{f}\right)' - \frac{1}{4}\left(\frac{f'}{f}\right)^2 , \tag{3.50}$$

with m_i^2 given by Equation (3.20) and $F'/F = (-1/2)\,f'/f$, with f given by Equation (3.43). Here the dash denotes a derivative with respect to x. For a uniform medium κ^2 is constant $\left(-m_i^2\right)$; body and surface modes are determined by positive and negative κ^2 respectively. However for a medium which is continuously structured, we define body and surface modes when κ^2 attains positive or negative values respectively, across the whole sheet ($-a < x < a$). In addition hybrid modes occur when $\phi(x)$ possess both positive and negative κ^2 across the width of the sheet.

3.4 Numerical Procedure and Boundary Conditions

We solve Equation (3.42) numerically subject to boundary conditions at the centre of the sheet, so that we have control over the parity of the solution (kink or sausage). At $x = x_{max}$ we take v_x to be zero; the integration range is therefore $[0, x_{max}]$. Lengths and speeds are normalised against the half-width a of the sheet and the Alfvén speed v_{Ae} in the exterior; frequencies are measured in units of v_{Ae}/a. The second order ordinary differential equation (Equation 3.42) is written in terms of two first order equations in the new functions y_1 and y_2,

$$y_1 = f(x)\frac{\mathrm{d}v_x}{\mathrm{d}x} , \qquad y_2 = v_x , \tag{3.51}$$

such that

$$\frac{\mathrm{d}y_1}{\mathrm{d}x} = \rho\left(k_z^2 v_A^2 - \omega^2\right) y_2 , \qquad \frac{\mathrm{d}y_2}{\mathrm{d}x} = \frac{y_1}{f(x)} . \tag{3.52}$$

The boundary conditions at $x/a = 0$ for the kink mode are given by $y_1 = 0$, $y_2 = c$; for the sausage mode by $y_1 = cf\,(0)$ and $y_2 = 0$. The constant c is arbitrary. We impose that v_x is zero at $x = x_{max}$ for both modes.

To obtain a solution of Equation (3.42) we use a fixed value of k_z and integrate the two first order equations (Equation 3.52) using the NAG routine D02BEF. The integration is performed between $x = 0$, where proper initial conditions for y_1 and y_2 are available, and x_{max}, where the condition $v_x = 0$ must be satisfied. A Newton iteration, with NAG routine C05AXF, is done by changing $\omega a/v_{Ae}$ and integrating from $x = 0$ to $x = x_{max}$ until the boundary condition at the second point is satisfied. To ensure convergence and high accuracy x_{max} is reselected for each wavenumber. For long (short) wavelengths the integration range is wide (narrow), in such a way that the frequencies and eigenfunctions are not affected by the boundaries. We do not impose an exponentially decreasing solution. Instead we seek solutions that decay away naturally. This has been found to work well and is more natural than imposing the velocity in a certain range. Hopcraft and Smith (1986) imposed an evanescent solution in the exterior of the sheet by assuming the medium is uniform for $|x|/a > 1.5$. However inspection of Figure 3.4 shows the various speeds varying for larger $|x|/a$ than this value.

To investigate the effect of x_{max} on the dispersion curves we re-examine the slab model of Edwin et al. (1986) discussed in Section 3.2.2. Here we impose that the transversal velocity is zero at $x = x_{max} = H$ (H is at infinity in the model discussed by Edwin et al.). Taking the velocity in the magnetic region to be of the form

$$v_x\,(x) = \alpha_1 \exp\,(-m_e x) + \alpha_2 \exp\,(m_e x)\ , \quad |x| > a\ , \tag{3.53}$$

with $v_x\,(H) = 0$ and α_1, α_2 constants, means the left-hand side of the dispersion relations (Equations 3.30 and 3.31) are multiplied by a factor

$$\mathcal{F} \equiv \left[\frac{1 + \exp\,(-2m_e H)\exp\,(2m_e a)}{1 - \exp\,(-2m_e H)\exp\,(2m_e a)}\right]\ . \tag{3.54}$$

Specifically, the dispersion relations for the slab model embedded with rigid walls at $|x| = H\ (> a)$ are

$$\frac{2\mathcal{F}}{\gamma R^2}\left(k_z^2 v_{Ae}^2 - \omega^2\right) m_0 \left\{ \begin{array}{c} \tanh \\ \coth \end{array} \right\} m_0 a = \omega^2 m_e \tag{3.55}$$

for the surface $(m_0^2 > 0)$ modes, and

$$\frac{2\mathcal{F}}{\gamma R^2}\left(k_z^2 v_{Ae}^2 - \omega^2\right) n_0 \left\{ \begin{array}{c} -\tan \\ \cot \end{array} \right\} n_0 a = \omega^2 m_e \tag{3.56}$$

for the body $(n_0^2 > 0)$ modes. Note that as $H \to \infty$ the dispersion relations reduce to the empty slab model previously discussed.

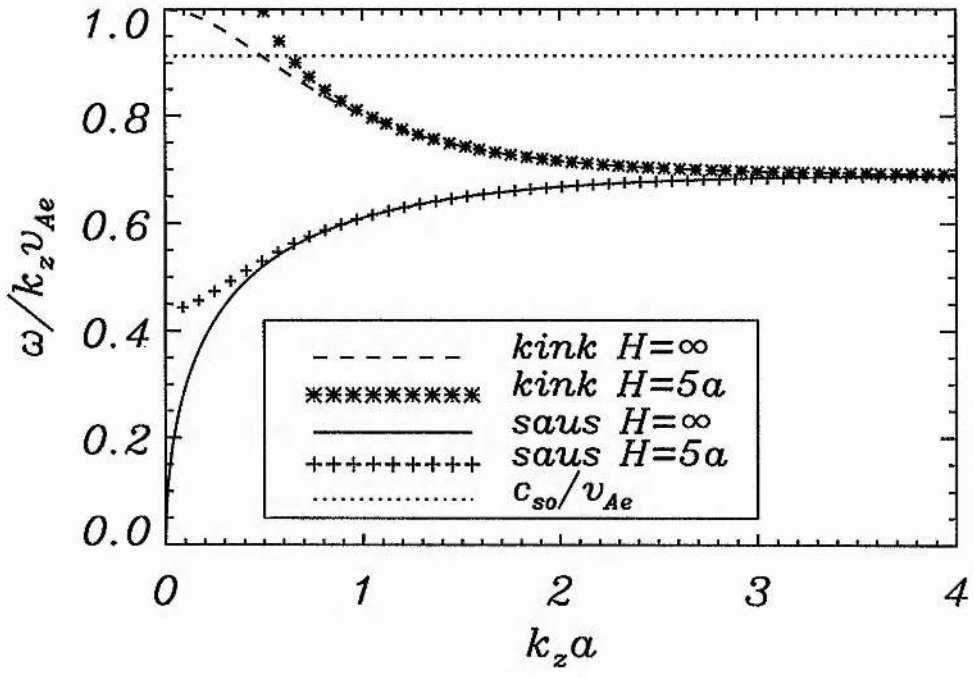

Figure 3.5: The effect of imposing $v_x(H) = 0$ for $H = 5a$ compared with an unbounded domain (where H is at infinity). Modes with long wavelengths (low $k_z a$) are most altered. For short wavelengths the two cases are virtually identical.

Solving the modified dispersion relations (Equations 3.55 and 3.56) shows that by imposing $v_x(H) = 0$ the frequencies and wavenumbers can be significantly altered compared with the infinite domain. In particular, cases with small H and modes with low $k_z a$ are most affected. The dispersion curves for the surface sausage and fundamental kink (body and surface) modes are illustrated in Figure 3.5 for $H = 5a$, allowing a comparison with the results for an unbounded medium (where H is at infinity). Note that only long wavelength modes are affected; above $k_z a = 1$ (i.e. shorter wavelengths) the dispersion curves between the two values of H are indistinguishable.

The fundamental kink mode, which exists above all wavenumbers in the infinite domain, may only propagate above a certain threshold in the finite region. For example for $H = 2a$ the kink mode has a critical wavenumber of $k_z a = 0.97$. As H increases the threshold decreases and ultimately as H approaches ∞ we regain the results of Edwin et al. (1986). Table 3.1 summarises our results. For short wavelengths, regardless of the value of H, the phase speeds attain the same value (since m_e is proportional to k_z and this implies that $\exp(-2m_e H)$ is small for large k_z). This threshold arises from the frequency increase that low $k_z a$ modes encounter when imposing $v_x = 0$ at

H (a)	kink $k_z^{crit}a$	saus $\omega/k_z v_{Ae}$ $(k_z a \to 0)$
2	0.97	0.67
5	0.50	0.41
10	0.34	0.31
25	0.21	0.20
100	0.11	0.10
1000	0.01	0.03
∞	0.00	0.00

Table 3.1: The effect of finite domain H.

H. If the resulting increase in phase speed is in excess of v_{Ae} no solution to the dispersion relation with positive m_e exists. The surface sausage mode exists for all wavenumbers in both the infinite and finite H cases. However the limiting phase speed as $k_z a$ approaches zero is significantly altered by the presence of the boundary at $|x| = H$ (see Table 3.1). The limiting phase speed in the infinite domain is zero as $k_z a$ tends to zero. Imposing $v_x(H) = 0$, however, raises this phase speed. Indeed for $H = 2a$ the phase speed is approximately constant for all wavenumbers. For short wavelength perturbations the dispersion curves for various H are virtually identical.

The body modes, which only occur above a threshold, are affected only slightly by imposing that v_x be zero at H. For example, we find that the fundamental sausage mode has $k_z^{crit}a = 0.35$ (H at infinity) and $k_z^{crit}a = 0.38$ ($H = 2a$). Also, the first harmonic kink mode has critical values of 0.70 and 0.72 for H at infinity and $H = 2a$ respectively. In both cases as $k_z a$ increases the dispersion curves for H at infinity and $H = 5a$ quickly coalesce.

When calculating the dispersion curves for the Harris current sheet x_{max} is selected so that the effects described with finite H are negligible. For modes with $k_z a \ll 1$, x_{max} was set at $100a$. As the wavelengths become shorter the effect of the boundaries are less important and x_{max} is reduced. It is important to note that the introduction of this boundary does not affect the classification of the modes; surface and body modes still exist as distinct entities for both fundamental and harmonic modes.

3.5 Results for a Structured Current Sheet

We turn now to a detailed investigation of the magnetoacoustic modes of a structured current sheet, modelled as a tanh profile (Equation 3.35). We consider two choices of density profile (Equation 3.38), considering first the case of a uniform density (Section 3.5.1). A non-uniform density profile yields similar results which are presented in Section 3.5.2.

3.5.1 Uniform density

The density profile (Equation 3.38) becomes uniform, $\rho(x) = \text{constant}$, in the special case when $\rho_0 = \rho_e$. We begin by looking at the various modes which may propagate in a current sheet. The function κ^2 arising in Equation (3.50) is strongly dependent upon the mode of oscillation (wavenumber and phase speed) and the location along the sheet. We find that *three* types of mode may exist in a continuously structured sheet, compared with two in a simple slab. Modes of oscillation may have $\kappa^2(x) > 0$ or $\kappa^2(x) < 0$ across the entire sheet; these modes are classified as *body* or *surface* respectively. We note, however, that these modes are different from those in a uniform medium where κ^2 is constant. We also find modes where $\kappa^2(x)$ takes both positive and negative values across the sheet; we call these *hybrid* modes. Figure 3.6 shows an example of $\kappa^2(x)$ for a fundamental sausage hybrid mode (solid line) along with the x-component of velocity (dashed line). Firstly, κ^2 varies across the whole domain, being positive in some regions and negative in others. Also, the velocity has maxima where $\kappa^2 > 0$, whereas wave motions are smaller where $\kappa^2 < 0$. The eigenfunction is characterised by the regions of different signs of κ^2; a hybrid mode exists. For harmonics the wave motions are more oscillatory across the sheet, in which case oscillations can occur in regions of both positive and negative κ^2. For all modes we find $\kappa^2 < 0$ for $|x|/a \gg 1$ and solutions are evanescent outside the current sheet.

Figure 3.7 shows the dispersion curves obtained for the case of constant density, $\rho_0 = \rho_e$. Kink and sausage modes are shown as dashed and solid lines respectively. The horizontal dotted line shows the position of the maximum sound speed, c_s^{max} ($\equiv c_s(0)$). Above this line only body and hybrid modes are found. For phase speeds close to the maximum Alfvén speed body modes arise ($\kappa^2 > 0$ for all $|x|/a$ in the structured region). As the phase speeds decrease the body modes transform into hybrid modes (κ^2 attains both positive and negative values). The dot-dashed line shows the maximum value of the tube speed c_T^{max}. Below this value only continuum solutions exist (Rae and Roberts 1982 and references therein; see also Seboldt 1990; Poedts and Goossens 1991; Cramer 1994). Between these two lines both surface and hybrid waves arise. Trapped modes exist only in the phase speed range

$$c_T^{max} < \frac{\omega}{k_z} < v_{Ae} \,. \tag{3.57}$$

The fundamental sausage surface wave (the curve of lowest phase speed in Figure 3.7) is the only mode which exists as a surface wave ($\kappa^2 < 0$ for all $|x|/a$) at all wavenumbers. At long wavelengths ($k_z a \ll 1$) its phase speed falls to the maximum tube speed in the current sheet, $\omega/k_z \to c_T^{max}$ as $k_z a \to 0$. As $k_z a$ increases the phase speed increases, tending to a constant value ($\omega/k_z v_{Ae} = 0.675$) for short wavelengths. It is interesting to note that this limiting value at short wavelengths is close to the value given by the slab model of Edwin et al. (1986). If we set $\Lambda^2 = 2/\gamma$ with $\gamma = 5/3$ in Equation (3.33), as the ratio of maximum Alfvén speed to maximum sound speed, we obtain a phase velocity of 0.689 which compares favourably with the numerical results for the Harris sheet.

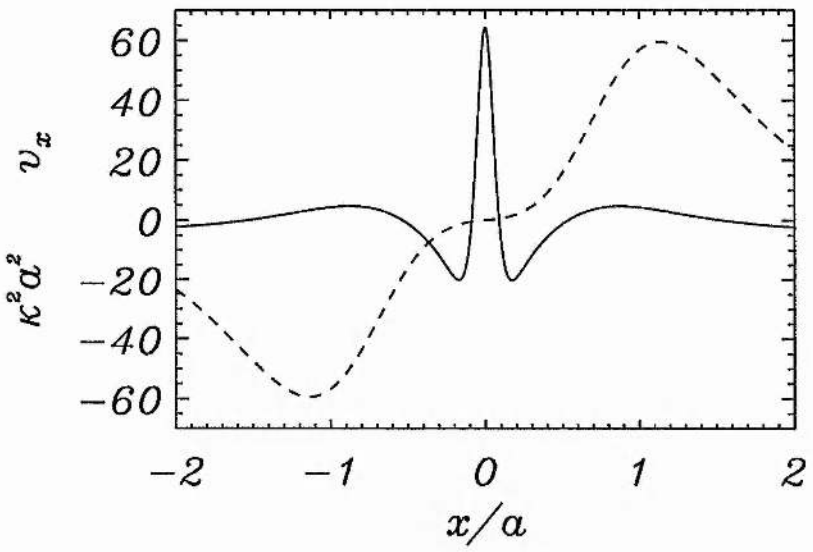

Figure 3.6: The variation of the function $\kappa^2 a^2$ across the uniform density current sheet for the fundamental sausage hybrid mode with wavenumber $k_z a = 5$ and phase speed $\omega/k_z = 0.92 v_{Ae}$ (solid line). The corresponding x-component of velocity (dashed line), scaled so that its maximum value is $v_x = 60$, is also shown. Note that regions of both positive (body type) and negative (surface type) $\kappa^2 a^2$ exist; the mode is hybrid.

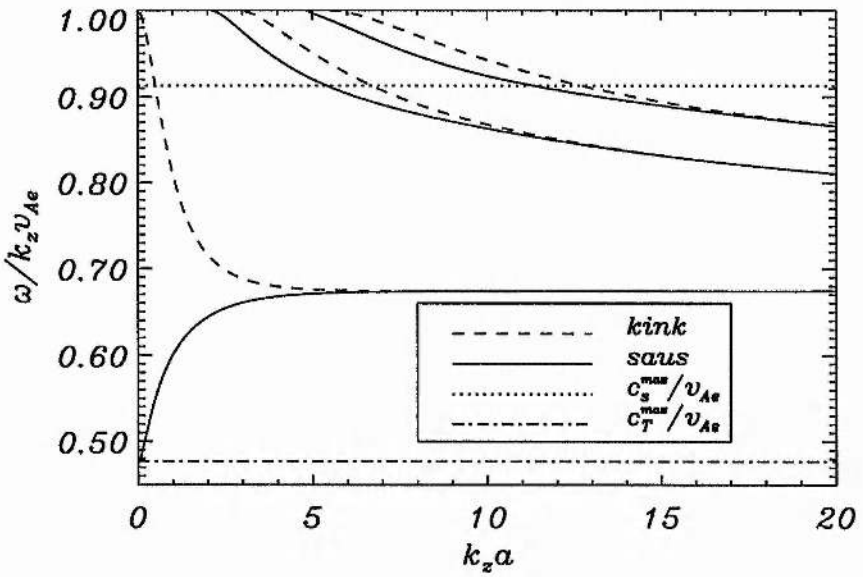

Figure 3.7: The dispersion curves for magnetoacoustic waves in a tanh profile current sheet (Harris neutral sheet) with uniform plasma density. The modes are classified as body when their their phase speed ω/k_z approaches v_{Ae}. A kink and a sausage surface mode arises. For long wavelength oscillations, the phase speed of the principal kink body and sausage surface modes tend to v_{Ae} and c_T^{max} respectively. For short wavelengths the phase speeds of both surface modes tend to the same value. Kink and sausage modes above wavenumber cut-offs also exist; these are body or hybrid depending upon the phase speed. The overtones exist in pairs, their phase speeds merging after the phase speed falls below the maximum sound speed.

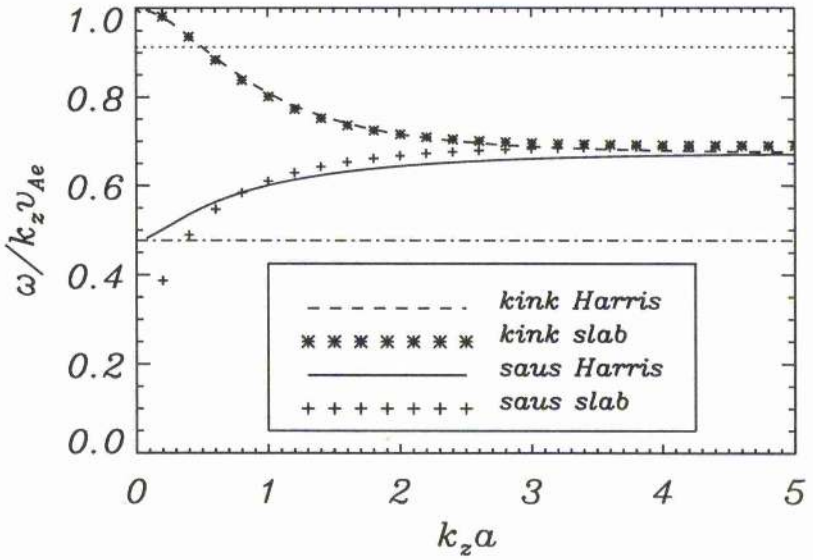

Figure 3.8: A comparison of the fundamental kink and sausage surface modes for the Harris and slab models of a current sheet with uniform plasma density. The agreement between the two models for the kink mode is excellent.

It proves useful to compare the surface sausage and fundamental kink modes for the slab and Harris models (Figure 3.8). The agreement between the dispersive curves for the kink modes is striking. For $k_z a < 3$ the frequencies predicted by the two models are in excellent agreement. The difference between the two curves occurs for large $k_z a$: their limiting ($k_z a \to \infty$) values are different, with $\omega/k_z = 0.675 v_{Ae}$ for the Harris profile and $\omega/k_z = 0.689 v_{Ae}$ for the slab model. The dispersion curves for the sausage surface modes differ more strongly, particularly for $k_z a \ll 1$. This arises because the maximum tube speed in the Harris model is non-zero.

The fundamental kink wave exists for all wavenumbers, although it is a surface wave only for k_z above a threshold. Figure 3.9 illustrates the eigenfunction v_x for the fundamental kink mode. For low $k_z a$ (when $\omega/k_z \approx v_{Ae}$) the kink wave starts off as a body wave and most of the velocity amplitude is concentrated at the centre of the sheet (see Figure 3.9a). As the phase speed decreases the kink mode transforms to a hybrid mode (with κ^2 attaining both positive and negative values). As the phase speed falls below the maximum value of the sound speed the mode transforms into a surface wave, where $\kappa^2 < 0$ across the entire sheet (see Figure 3.9b, where a small "dip" can be observed in the eigenfunction in the centre of the sheet). For larger $k_z a$ this dip becomes more pronounced (Figure 3.9c) and ultimately, for very short wavelengths, there are two peaks in the velocity concentrated near the edge ($x/a \approx \pm 0.9$) of the sheet (Figure 3.9d). The phase speeds

of the kink and sausage waves approach the same limiting value for short wavelengths. For short wavelength perturbations we see that the velocity is concentrated about the sheet boundary, whereas for longer wavelengths, oscillations across the entire sheet may be expected.

In a similar way to the work by Edwin and Roberts (1982), magnetoacoustic modes also exist above wavenumber thresholds (Figure 3.7). At the wavenumber threshold $\left(k_z = k_z^{crit}\right)$ the phase velocity equals the exterior Alfvén speed v_{Ae}. As their phase speeds decrease κ^2 attains both positive and negative values and a hybrid mode forms. The dispersion curve for the fundamental sausage mode, occurring at a critical wavenumber of $k_z^{crit}a = 2.12$, interleaves with the first harmonic kink mode $\left(k_z^{crit}a = 3.06\right)$ when the phase speed falls below the maximum sound speed in the sheet. In addition, the first harmonic sausage mode $\left(k_z^{crit}a = 4.94\right)$ interleaves with the second harmonic kink mode $\left(k_z^{crit}a = 5.50\right)$, and so on. Notice that each merging pair contains a higher overtone kink mode than the sausage. When the "dip" appears in the eigenfunction for the kink mode (Figure 3.9) the number of maxima is the same across the sheet for both kink and sausage modes (although the parity about $x/a = 0$ is different).

Due to the continuous structuring of the sound and Alfvén speed profiles in the current sheet, the phase speeds of these modes do not tend to the maximum value of the sound speed, as in the case studied by Edwin et al. (1986). Instead the phase speeds fall below $c_s\,(0)$; notice how the phase speeds (and therefore frequencies) of these pairs tend to the same value in Figure 3.7, after passing through the maximum value of the sound speed. The phase speed tends to an asymptote which is slightly different for each pair of modes. Each pair tends to a slightly higher phase velocity than the previous pair; for the first pair this is $\omega/k_z = 0.69v_{Ae}$. The value of this asymptote is approximately given by the slab model of Edwin et al. (1986) in the short wavelength limit; see Equation (3.33).

The x and z-components of the velocity are shown in Figure 3.10 for a first harmonic kink hybrid wave. This mode is characterised by two large peaks in v_x at $x/a \approx \pm 0.9$ with $\kappa^2 > 0$ (body modes) plus two smaller peaks at $x/a \approx \pm 0.6$ with $\kappa^2 < 0$ (surface modes) (cf. Figure 3.9). The z-component of velocity shows similar characteristics to v_x but is of opposite parity about $x/a = 0$. The velocity in the inner part of the sheet ($|x|/a < 0.3$) is approximately zero with wave motions concentrated near the edge of the sheet. The amplitudes of the velocity components attain approximately the same value; this is to be expected since the maximum values of the sound and Alfvén speeds are similar. The eigenfunction of the associated sausage hybrid wave (the mode that transformed from the fundamental sausage body) is very similar, the main difference being the parity of the two solutions about the current sheet centre. The oscillation frequencies approach the same value as $k_z a$ increases (Figure 3.7).

It is interesting to note that the coupling between the x and z-components of velocity are different in slab structures and continuously structured media. Consider firstly the slab case. Equation (3.44) shows that when $\mathrm{d}v_x/\mathrm{d}x$ equals zero then iv_z is always zero. However for the Harris profile, we find that when $\mathrm{d}v_x/\mathrm{d}x = 0$ and $\omega/k_z < c_s\,(0)$, iv_z can take both zero and non-

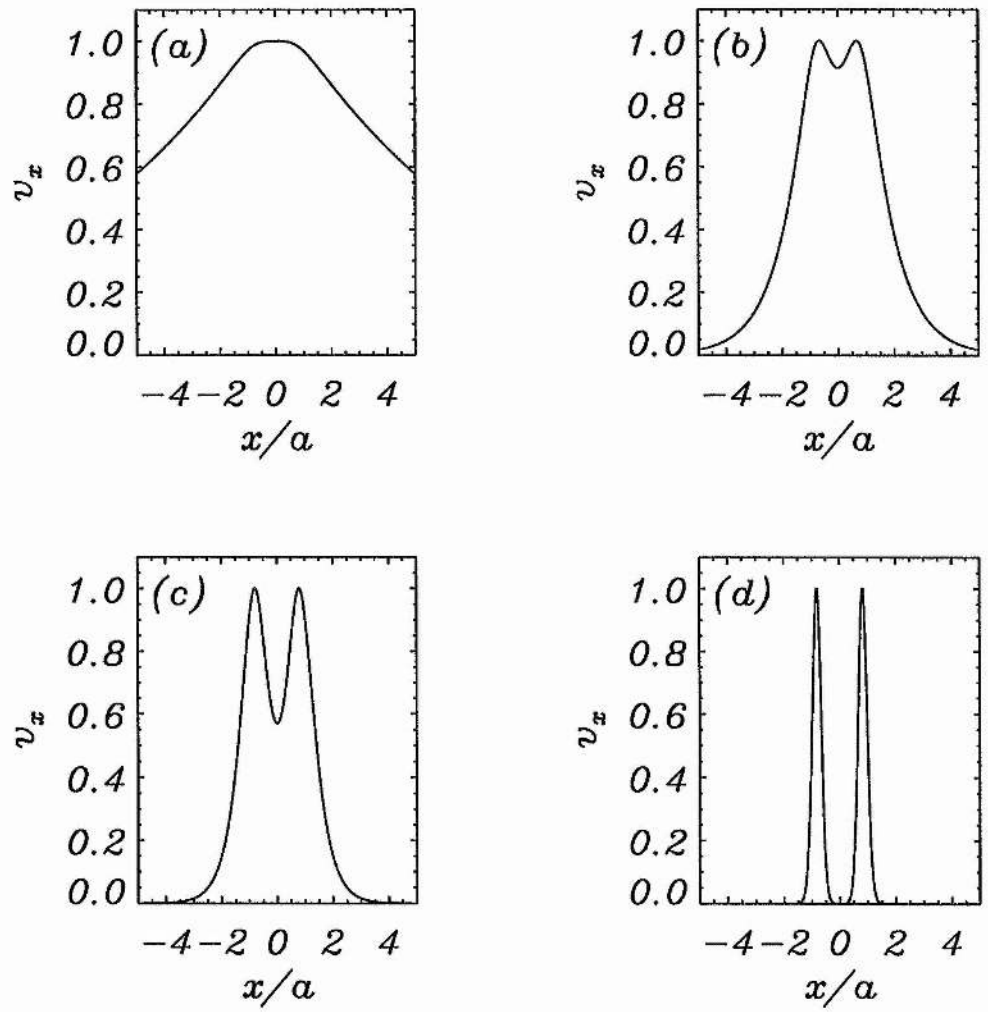

Figure 3.9: The transition from body to surface waves for the principal kink mode with (a) $k_z a = 0.39$, $\omega = 0.37 v_{Ae}/a$ (body), (b) $k_z a = 1.57$, $\omega = 1.177 v_{Ae}/a$, (c) $k_z a = 3.14$, $\omega = 2.167 v_{Ae}/a$ and (d) $k_z a = 27.5$, $\omega = 18.537 v_{Ae}/a$ (surface modes). Notice that as the mode transforms from being body/hybrid (oscillatory in the sheet) to surface a "dip" appears in the eigenfunction around $x = 0$. As $k_z a$ increases the oscillations become more localised about the edge of the sheet.

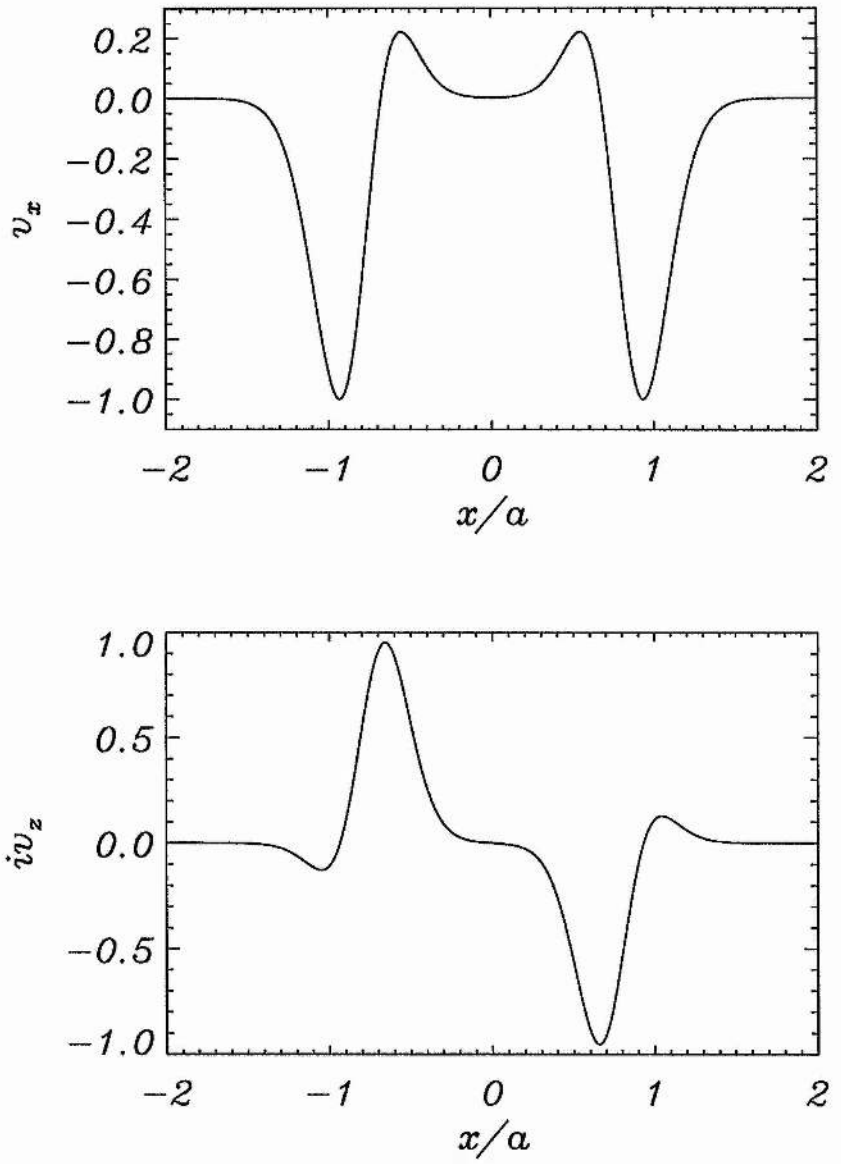

Figure 3.10: An example of a first harmonic kink hybrid mode ($k_z a = 27.5$, $\omega = 21.727 v_{Ae}/a$) showing the v_x and iv_z components of velocity. Two large peaks in the velocity v_x are observed at $x/a \approx \pm 0.9$ (with $\kappa^2 > 0$). In addition two smaller peaks (of opposite parity to the larger peaks) are seen at $x/a \approx \pm 0.6$ (with $\kappa^2 < 0$). Between $-0.3 < x/a < 0.3$ the velocity is almost zero; wave motions are localised in the exterior of the sheet. The situation for iv_z is similar. Two large peaks (of opposite sign) at $x/a \approx \pm 0.65$ are observed, whereas two smaller peaks are present at $x/a \approx \pm 1.1$. The amplitudes of v_x and iv_z are approximately the same.

zero values. This arises from the fact that the phase speed ω/k_z can equal the local sound speed $c_s(x)$ at different locations across the current sheet, since when $\omega/k_z = c_s$ the denominator of Equation (3.44) becomes zero. This poses the question: what happens to the numerator? Consider the mode in Figure 3.10. The phase speed equals the sound speed when $x = \pm 0.55a$. We find that at these locations $\mathrm{d}v_x/\mathrm{d}x = 0$ (i.e. v_x attains a local maximum). Therefore iv_z attains a non-zero value; see Equations (3.42) and (3.44). Hence, peaks in v_x are found at those points where the phase speed equals the local sound speed. At other positions along the sheet where $\mathrm{d}v_x/\mathrm{d}x = 0$ we find $iv_z = 0$ (since $\omega/k_z \neq c_s(x)$). Therefore $iv_z = 0$ if $\mathrm{d}v_x/\mathrm{d}x = 0$ provided $\omega^2 \neq k_z^2 c_s^2$. For phase speeds $\omega/k_z > c_s(0)$, $\mathrm{d}v_x/\mathrm{d}x = 0$ implies that $iv_z = 0$.

We now examine the driving forces (tension and gradients of plasma and magnetic pressure) and the perturbed pressures. This gives some insight into which forces are important in driving wave motions and it affords a comparison with the results of a uniform field, giving us an indication of whether the modes are essentially fast or slow. The linearised MHD equations, leading to the governing wave equation (Equation 3.42), may be written in the form

$$-\omega^2 v_x = -\frac{i\omega}{\rho}\frac{\mathrm{d}p_1}{\mathrm{d}x} - \frac{i\omega}{\rho}\frac{\mathrm{d}p_{1m}}{\mathrm{d}x} + T_{1x}\,, \tag{3.58}$$

$$-\omega^2 v_z = -\frac{i\omega}{\rho}\frac{\mathrm{d}p_1}{\mathrm{d}z} - \frac{i\omega}{\rho}\frac{\mathrm{d}p_{1m}}{\mathrm{d}z} + T_{1z}\,, \tag{3.59}$$

where p_1 and p_{1m} are the plasma and magnetic pressure perturbations, p_T $(= p_1 + p_{1m})$ is the total pressure perturbation, and T_{1x} and T_{1z} are the components of the tension. We first recall the results for a uniform medium, i.e. one in which B, p, ρ (and therefore v_A and c_s) have no x-variation in the region under consideration (see Figures 1.6 and 1.7). From Equations (3.45)-(3.47) we see that if $\omega/k_z < c_T$ the magnetic pressure p_{1m} is out of phase with both the plasma p_1 and total p_T pressure perturbation: $p_{1m}p_1 < 0$ and $p_{1m}p_T < 0$; this is a feature of the *slow* mode. Moreover for this mode the x-projections of the tension force and the velocity are out of phase whereas the z-components are in phase. For $\omega/k_z > c_T$ the total pressure perturbation, plasma pressure and magnetic pressure are all in phase: $p_{1m}p_1 > 0$ and $p_{1m}p_T > 0$; this is a property of the *fast* mode. In addition, for a fast mode in a uniform medium, T_{1x} is out of phase with v_x whilst v_z and T_{1z} are in phase.

The formulae for the total pressure perturbation p_T and the tension force $\mathbf{T_1}$ are the same in both uniform and non-uniform media $(\mathrm{d}p/\mathrm{d}x + B/\mu_0(\mathrm{d}B/\mathrm{d}x) = 0)$. However the perturbed plasma and magnetic pressures are altered by the non-uniformity in pressure and magnetic field; see Equations (3.45) and (3.46). The results show that the magnetoacoustic modes of a Harris current sheet are more difficult to classify than those of a uniform medium, with the non-uniformity playing an important role.

The results for the non-uniform current sheet are illustrated in Figure 3.11 for the principal kink mode of frequency ω=0.67 v_{Ae}/a and wavenumber $k_z = 0.79/a$. Figure 3.11a shows the driving forces in the x-direction $(T_{1x}, -\mathrm{d}p_1/\mathrm{d}x, -\mathrm{d}p_{1m}/\mathrm{d}x)$.

Firstly we consider the x-projection of the driving forces (Figure 3.11a). In the centre

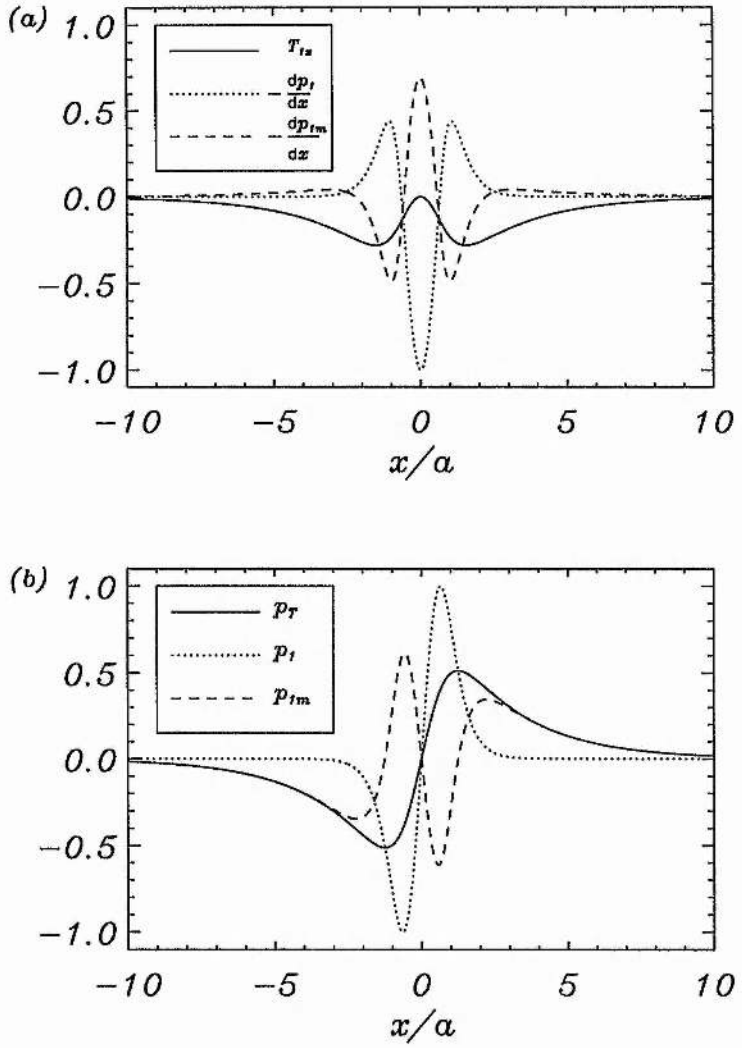

Figure 3.11: (a) The x-component of the driving forces, T_{1x}, $-\mathrm{d}p_1/\mathrm{d}x$ and $-\mathrm{d}p_{1m}/\mathrm{d}x$, for the fundamental kink mode with frequency $\omega = 0.67 v_{Ae}/a$ and wavenumber $k_z = 0.79/a$. The tension forces are very small in the inner part of the sheet ($|x|/a < 1$) and the gradients of plasma and magnetic pressure are in anti-phase. In the outer part of the sheet the gradient of the plasma pressure decays rapidly and the magnetic pressure is the greater force. This mode of oscillation therefore possesses characteristics of both fast and slow modes. (b) The perturbed pressures for the same mode. In the central part of the sheet the magnetic pressure (p_{1m}) is out of phase with both the plasma pressure (p_1) and the total pressure (p_T) perturbations; this is a feature of the slow mode. In the outer part of the current sheet the magnetic and total pressure perturbations are in phase — a fast mode feature.

of the current sheet the gradients of plasma and magnetic pressures are clearly out of phase with $|\mathrm{d}p_1/\mathrm{d}x| > |\mathrm{d}p_{1m}/\mathrm{d}x|$; this is a characteristic of a slow mode. Notice also the gradients of plasma and magnetic pressures are in anti-phase at $|x|/a \approx 1$, where the amplitudes of the driving forces are approximately the same. In the outer part of the current sheet ($|x|/a \geq 1$) the gradient of plasma pressure tends to zero rapidly. In addition, within this region the gradient of magnetic pressure is greater than the gradient of plasma pressure; this is a signature of a fast mode. Thus, as we move away from the centre of the sheet, the mode changes from being slow in character to being fast. This is not surprising since the plasma pressure is maximum (magnetic field minimum) at $x/a = 0$ whereas the situation reverses as we increase $|x|/a$. In other words we are moving from a high plasma beta regime, where we expect slow waves to dominate, to a low beta region, where fast waves are likely to propagate. Therefore it is not possible to classify the mode as globally slow or fast; the mode is locally slow in the inner region and fast in the outer parts of the structure. Furthermore, unlike the uniform case, the non-uniformity in Alfvén speed means the x-projection of tension is not out of phase with the velocity. The Alfvén speed is low in the vicinity of the centre of the sheet and therefore tension forces are small. Similar results are also found for the z-component. The gradients of plasma and magnetic pressures are out of phase around the centre of the sheet. As we move away from the centre the plasma pressure perturbations become less dominant than magnetic pressure perturbations. In the outer part of the configuration the magnetic pressure becomes greater than the plasma pressure.

These points are reinforced by examining the plasma pressure, the magnetic pressure and the total perturbed pressure (Figure 3.11b). Notice that the plasma and total pressures are out of phase with the magnetic pressure around $|x|/a \approx 1$. However, as we increase $|x|/a$ the perturbed plasma pressure decays rapidly and the magnetic pressure and the total pressure are in phase for $|x|/a > 2$. Thus for the principal modes the oscillations within the sheet are essentially slow, whereas the evanescent decaying velocity is predominantly fast.

By contrast, for the overtones of the modes we find that the oscillations within the sheet may possess both fast and slow mode properties. To illustrate this we show the perturbed forces in Figure 3.12 for the first overtone sausage hybrid mode with $\omega = 6.12 v_{Ae}/a$ and $k_z a = 6.28$. Notice that in the inner part of the current sheet the perturbed magnetic pressure is small (since B is small). Consequently the plasma and total pressure perturbations are almost equal for $|x|/a < 0.5$. This suggests that the mode is slow. However the perturbations in the outer part of the sheet are different in character. At $|x|/a \approx 1.0$ the total, plasma and magnetic pressures are almost in phase. Thus both slow and fast type oscillations occur simultaneously in the sheet for the same velocity component. For $|x|/a > 2$ the pressure term is small and the evanescent decaying velocity has the character of the fast mode.

Similar results are found for all modes of oscillation. The tension force in the central part of the sheet is very small, and tension plays an important role only as the Alfvén speed approaches its maximum value. We always see that in the high plasma beta part of the sheet the plasma and

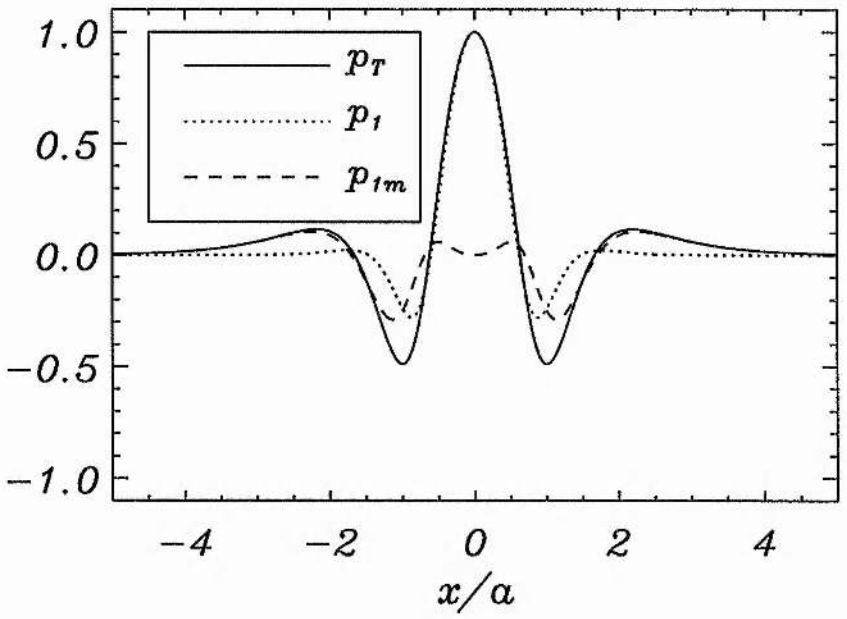

Figure 3.12: A plot of the perturbed pressures for the first harmonic sausage hybrid mode with $\omega = 6.12 v_{Ae}/a$ and $k_z a = 6.28$. In the central part of the current sheet ($|x|/a < 0.5$) the plasma pressure perturbation p_1 dominates over the magnetic pressure perturbation p_{1m} (a slow mode). At $|x|/a = 1$ the plasma and magnetic pressure perturbations are almost in phase with the total pressure perturbation. This is similar to a fast mode. Thus for higher overtones we may expect fast and slow modes to exist simultaneously. For $|x|/a > 2$ the mode is fast since the plasma beta is low in this region.

magnetic pressures are in anti-phase, with the plasma pressure dominating. In the exterior of the sheet the magnetic pressure is greater than the plasma pressure. For all modes considered we see both slow and fast mode characteristics.

It is interesting to note that in the observations of neutral sheet oscillations by Bauer et al. (1995a,b) the plasma and magnetic pressures were in anti-phase, in agreement with our theoretical results.

3.5.2 Epstein density profile

When the plasma density inside the current sheet is no longer equal to the density in the far environment of the sheet, so that $\rho_0 \neq \rho_e$, the profile (Equation 3.38) is the Epstein one. The results for the Epstein profile are similar to those in the uniform density case and so we summarise the main results and illustrate the main differences. We take the plasma density at the centre of the current sheet to be five times larger than the constant density away from the current sheet: $\rho_0/\rho_e = 5$.

The curves in the dispersion diagram are similar to the uniform density case; see Figure 3.13. Both kink and sausage, body, surface and hybrid modes may exist. A current sheet therefore supports a rich spectrum of modes. The sausage surface mode, which again exists for all $k_z a$, has a phase speed equal to the tube speed in the slender current sheet approximation. In the short wavelength limit the phase speed tends to a constant value $\omega/k_z \approx 0.38 v_{Ae}$ for $k_z a \gg 1$. An application of Equation (3.33) gives a phase speed of $0.40 v_{Ae}$. The principal kink mode originates as a body mode ($\omega/k_z \approx v_{Ae}$). As the phase speed decreases the body mode transforms into a hybrid mode. When the phase speed passes through the maximum value of the sound speed the mode changes character and becomes a surface wave. The phase velocity of this mode tends to the same value as the sausage surface wave. In addition, body and hybrid waves exist above wavenumber cut-offs: the fundamental sausage mode has a threshold of $k_z a = 0.63$, first kink overtone 1.10, first sausage overtone 1.65, and the second kink's threshold is at $k_z a = 1.96$. These cut-offs are lower than in the case of uniform density. These body modes, as in the uniform density case, transform into hybrid waves when their phase speed decreases. Again, a sausage and a kink mode interleave when their phase speed falls below the maximum sound speed within the current sheet. Each kink and sausage mode pair tends to a slightly higher value than the previous pair. We see, however, that for the Epstein density profile the phase speed only falls below the maximum sound speed level for much higher values of the wavenumber than in the case of uniform density. For example, for the fundamental body sausage mode the transition occurs at $k_z a \approx 25$, whilst for the uniform density case it is at $k_z a \approx 5$.

The driving forces show a similar form to the uniform density case.

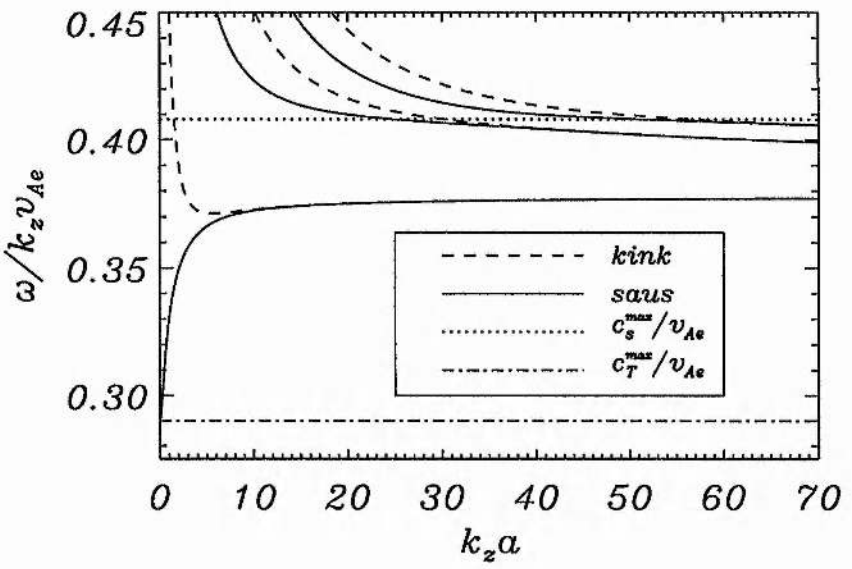

Figure 3.13: The dispersion curves for magnetoacoustic wave propagation in a current sheet with an Epstein density profile (Equation 3.38) with an enhancement of $\rho_0/\rho_e = 5$; $c_s^{max} = 0.408 v_{Ae}$, $c_T^{max} = 0.290 v_{Ae}$. We have only plotted the phase speed over a narrow range. Body and hybrid waves exist in the range $c_s^{max} < \omega/k_z < v_{Ae}$, whilst surface and hybrid waves exist below c_s^{max} and above c_T^{max}. Continuum solutions only exist below c_T^{max}. Modes are classified as either body, surface or hybrid depending upon their phase speed and wavenumber. The modes occur in pairs, the phase speed of each pair merging after they pass through the level c_s^{max}.

3.6 Applications and Conclusion

3.6.1 Application to observations

We now apply our results to some observations. For convenience we use the case of uniform density. For solar applications we consider a constant Alfvén speed in the exterior of the sheet of $v_{Ae} = 1000$ km s^{-1} and a sheet width $2a$ equal to 1000 km. For magnetospheric applications an Alfvén speed of 500 km s^{-1} is used with a sheet width of $2a = R_E$ (= 6400 km). The periods determined using our model are given in Table 3.2. The fundamental surface mode periods are estimated using a value of $k_z a = 0.5$, whilst the periods for the other modes are estimated at the onset of the modes (i.e. at the cut-off value of $k_z a$). For the coronal case periods lie in the range 0.5

Mode	Corona	Magnetosphere
Surface Sausage	12 sec	2.5 min
Fundamental Kink	3.5 sec	1.45 min
Fundamental Sausage	1.5 sec	19 sec
First Harmonic Kink	1.0 sec	13 sec
First Harmonic Sausage	0.5 sec	8 sec

Table 3.2: Estimated periods of ducted waves in current sheets.

to 12 seconds. Interestingly, periods of this order are frequently reported (see Aschwanden 1987 and Section 1.2 for a review of radio and X-ray observations). In particular Zlobec et al. (1992) report a 11.4 second oscillation two hours after a solar flare; we suggest this may be due to surface waves in a current sheet. There are many recent reports of short period oscillations which may also be due to magnetoacoustic waves in current sheets. Pasachoff and Landman (1984) and Pasachoff and Ladd (1987) detected intensity variations of the green coronal line with periods between 0.5 and 4 seconds. Short oscillations are also abundantly reported in radio and X-ray emission. For example, Correia and Kauffman (1987) report oscillations of 0.3 seconds in hard X-rays whilst Zhao et al. (1990) give periods of 1.4 and 1.6 seconds in microwaves; Aschwanden (1994) and Karlický & Jiřička (1995) give further examples of short period coronal oscillations.

For the Earth's magnetosphere our calculations give periods in the range 8 seconds to 2.5 minutes, for the various modes. Therefore the 1–2 minute magnetic field fluctuations of the neutral sheet observed by Bauer et al. (1995a,b) may indeed be due to magnetoacoustic waves propagating in a neutral sheet. Magnetic variations and boundary motions on time scales from a few minutes to several hours have been explained as "flapping" motions of the tail (Mihalov et al. 1970; Hruška and Hruškova 1970; Hones et al. 1971; Russell 1972). Longer periods may be due to surface waves with $k_z a < 0.5$, or for circumstances with lower Alfvén speeds and/or wider sheets.

3.6.2 Summary of results

We have seen that a current sheet may support guided magnetoacoustic waves. The waves are trapped by the inhomogeneity in the magnetic field. Modes may be excited by, say, solar flares, magnetospheric substorms or reconnection events. Once excited the waves may propagate along a current sheet and be the source of reported oscillations in the solar corona and in the Earth's magnetosphere.

A current sheet supports waves which may be body, surface or hybrid. An examination of the driving forces and perturbed pressures shows that no purely fast or slow modes exist in the structure. Observed oscillations have properties of both types of mode. A fundamental sausage surface wave exists for all values of the wavenumber; in the long wavelength limit the phase speed approaches the maximum value of the tube speed in the current sheet. A fundamental kink wave also exists in a current sheet. For long wavelengths (with phase speeds approaching the maximum value of the Alfvén speed in the sheet) the wave is characterised as a body mode ($\kappa^2 > 0$ for all $|x|/a$ in the structured region). As the phase speed decreases κ^2 attains both positive and negative solutions; this is a hybrid mode. For lower phase speeds ($\omega/k_z < c_s^{max}$) the mode changes nature and becomes a surface wave ($\kappa^2 < 0$ for all $|x|/a$ in the inhomogeneous region). For short wavelength oscillations the phase speed of the fundamental kink and sausage surface waves is constant, tending to approximately the value given in the simple slab model of Edwin et al. (1986); see Equation 3.33. Harmonics also exist above wavenumber cut-offs; these may be body or hybrid depending upon the phase speed. The dispersion curves of a pair of kink and sausage modes merge when their phase speeds fall below the maximum sound speed within the sheet (the fundamental sausage mode interleaves with the first overtone kink mode, the first overtone sausage mode with the second kink mode, and so on). The phase speeds of each pair merge after the phase speed passes through the maximum sound speed. The results are similar to those obtained by Edwin et al. (1986) for an unstructured slab. The main difference is that, due to the continuous structuring, body modes transform into hybrid modes for all harmonics. In the slab model of Edwin et al. (1986) body modes were trapped in the phase speed range between the sound speed in the field-free region and the exterior sound speed. In addition the fundamental sausage mode, which in our case tends to c_T^{max} for $k_z a \ll 1$, approaches zero as $k_z a \to 0$; in the slab model the tube speed in the field-free region is zero.

Chapter 4

Impulsively Generated Waves in Current Sheets

4.1 Introduction

Having seen the dispersive form of the magnetoacoustic waves in a current sheet in Chapter 3 it is of interest to examine the group velocity. The group velocity of a mode with dispersion relation $\omega = \omega(k_z)$ is $\partial\omega/\partial k_z$ in the z-direction. Of particular interest is the possible occurrence of a minimum in the group velocity, since this plays a significant role in the behaviour of impulsively generated waves (Roberts, Edwin and Benz 1983, 1984). This chapter investigates the temporal evolution of impulsively generated waves in a structured current sheet through numerical simulations. A comparison with observations both in the solar corona and the Earth's magnetosphere is made.

The format of this chapter is as follows. In Section 4.2 we briefly explain the theory of impulsively generated waves. In Section 4.3 we apply this theory to the current sheets examined in Chapter 3, whilst the results of the numerical simulations are reported in Section 4.4. A comparison with observations of pulsations in the solar corona and the Earth's magnetosphere is made in Section 4.5. Finally our results are summarised, and conclusions drawn, in Section 4.6.

4.2 Impulsively Generated Waves: Theory

Suppose that at a time $t = 0$ an impulse (such as due to a reconnection event or a MHD instability) occurs at a location $z = 0$. This impulse is composed of all frequencies. The wave observable at large distances $z = h$ from the initial impulse evolves on the basis of the group velocity curve, as described in the following (Roberts, Edwin and Benz 1983, 1984); an example of a group velocity curve is shown in Figure 4.1. The event begins with a periodic phase starting at a time $t = h/v_{Ae}$ and consists of low frequency, low amplitude waves; this corresponds to the

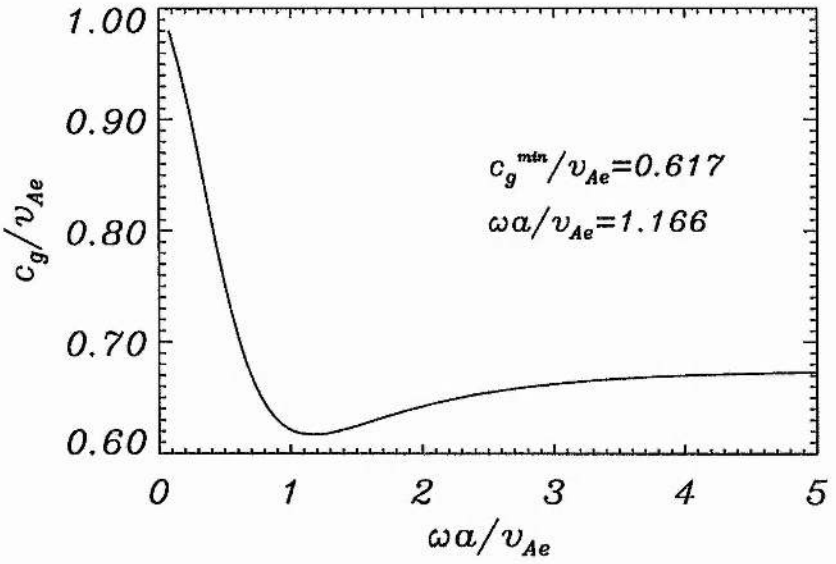

Figure 4.1: The dimensionless group velocity c_g/v_{Ae} plotted as a function of the dimensionless frequency $\omega a/v_{Ae}$ for the principal kink mode in a tanh profile current sheet with uniform density. A minimum in the group velocity occurs ($c_g^{min} = 0.617 v_{Ae}$) for frequency $\omega = 1.166 v_{Ae}/a$. Impulsively generated kink waves will therefore show a wavepacket behaviour similar to that described by Roberts, Edwin and Benz (1983, 1984). Group velocity minima do not exist for the other modes.

left-hand branch of the group velocity curve. The frequency and amplitude of the waves in the periodic phase grow until a time $t = h/c_g^{const}$, where c_g^{const} is the constant group velocity at high frequency. This time marks the onset of the quasi-periodic phase. A train of high frequency waves (from the right-hand branch of the group velocity curve) are superimposed on low frequency waves (from the left-hand side). The amplitude of this phase, in an impulsively excited disturbance, is strongly enhanced due to the superposition of the high and low frequency waves (Pekeris 1948; see also Ewing, Jardetzky and Press 1957). The oscillations are quasi-periodic; the amplitude varying inversely proportionally with the slope of the group velocity curve. During this phase the frequency of the high frequency waves continues to decrease, whilst those of the low frequency waves continue to increase. This occurs up to a time $t = h/c_g^{min}$, where c_g^{min} is the minimum group velocity, when the two frequencies take the same value. This marks the onset of the decay phase. The disturbance then consists of a single frequency ω^{min} and the plasma continues to oscillate with this frequency, although its amplitude decays rapidly. The durations of the periodic and quasi-periodic phases are

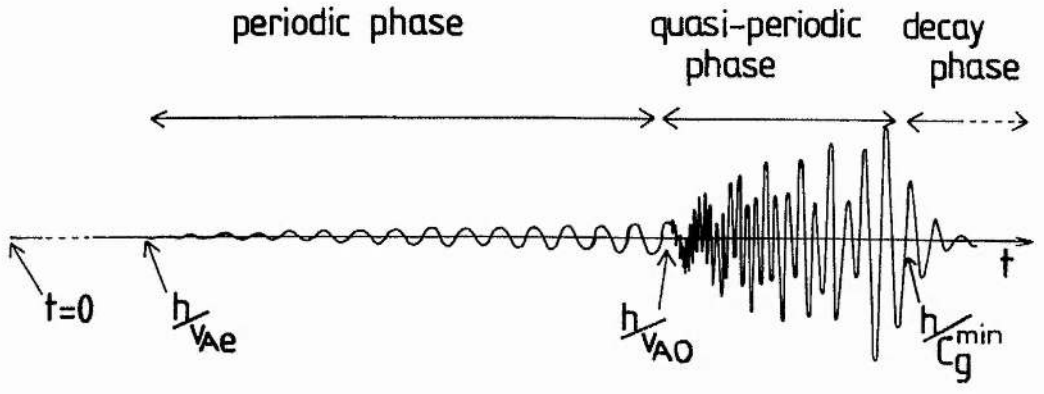

Figure 4.2: The temporal signature of impulsively generated waves in a coronal loop (reproduced from Roberts, Edwin and Benz 1983, 1984). Notice the existence of three distinct phases in the time evolution. In our calculation $v_{A0} \equiv c_g^{const}$.

given by (Roberts et al. 1983, 1984)

$$\tau_{dur}^{P} = h\left[\frac{1}{c_g^{const}} - \frac{1}{v_{Ae}}\right], \qquad \tau_{dur}^{QP} = h\left[\frac{1}{c_g^{min}} - \frac{1}{c_g^{const}}\right]. \tag{4.1}$$

Figure 4.2 reproduces the theoretical prediction of the temporal signature of impulsively generated waves in coronal loops (Roberts, Edwin and Benz 1983, 1984). The authors argue that such a signature is evident in temporal variations of radio, X-ray and coronal emission lines.

4.3 Application of theory to current sheets

The group velocity curve for the principal kink mode is shown in Figure 4.1 for the case of uniform density (Section 3.5.1). Notice the existence of a minimum in the group velocity suggesting that impulsively generated waves in current sheets will possess a temporal signature similar to that displayed in Figure 4.2. The minimum group velocity is $c_g^{min} = 0.617 v_{Ae}$, occurring at a frequency $\omega^{min} = 1.166 v_{Ae}/a$. These values are of importance in the theory of impulsively generated waves (see Roberts, Edwin and Benz 1983, 1984 and Section 4.2). However no minimum in the group velocity exists for the other modes in the uniform density current sheet. For an Epstein density profile we find the group velocities possess minima for all modes except the sausage surface. The value of c_g^{min} is approximately the same for all cases considered; namely $0.316 v_{Ae}$ for the surface kink and approximately $0.356 v_{Ae}$ for all the other modes examined. The minimum frequency equals $0.462 v_{Ae}/a$ and $2.774 v_{Ae}/a$ for the principal and first harmonic kink modes and $1.672 v_{Ae}/a$ and $3.846 v_{Ae}/a$ for the principal and first harmonic body sausage modes. To summarise, impulsively

generated waves in a structured current sheet are expected to show a similar temporal form to that analysed by Roberts et al. (1993, 1984). The absence of a minimum in the group velocity also arises in the work of Nakariakov and Roberts (1995). Considering coronal loops modelled by different density profiles, they found that the Epstein profile was a special case: it had no minimum, whereas other density profiles possessed minima.

As a numerical example consider the principal kink mode for the case of constant density, with the results displayed in Figure 4.1. The minimum group velocity is $c_g^{min} = 0.617 v_{Ae}$ occurring at a minimum frequency of $\omega^{min} = 1.166 v_{Ae}/a$. At high frequency the group velocity approaches $c_g^{const} = 0.675 v_{Ae}$. For solar applications we assume an observational height $h = 10^5$ km above the impulse and an Alfvén speed of 1000 km s^{-1}; then the periodic phase starts 100 seconds after the impulse and lasts for 48 seconds. The quasi-periodic phase has a duration of 13.9 seconds with a minimum period of 2.7 seconds at the end of the phase. For the magnetosphere consider $h = 50$ R_E $(= 3.2 \times 10^5$ km) and an Alfvén speed of 500 km s^{-1}. The periodic phase begins about 10.5 minutes after the impulse and lasts for 5 minutes. The quasi-periodic phase has a duration of 89 seconds with a minimum period of 34 seconds. The decay phase then follows.

The periodic phase is relatively low in amplitude and so may not be observable because of noise or poor resolution. In which case our illustration gives a wavepacket of about 14 seconds duration with a minimum period 2.7 seconds observable in a coronal current sheet. In the magnetospheric sheet the observable quasi-periodic phase would last for about 89 seconds, with a minimum period of 34 seconds. Of course this illustration is for a single pulse initiated at the centre of the sheet. More complicated time signatures may be expected for multiple impulses or pulses that occur away from the centre of the sheet (see the numerical simulations by Murawski and Roberts (1993a,b) for the case of a coronal loop). In our equilibrium a pulse will generate the disturbances described plus a z-component of velocity (v_x and v_z are coupled). Therefore more complicated temporal signatures may result from this coupling.

4.4 Numerical Simulations

A localised impulsive energy source such as a solar flare, a reconnection event, an instability or a magnetic substorm, may generate magnetoacoustic waves within a current sheet. It is the purpose of this section to investigate this phenomenon numerically. The equilibrium magnetic field and plasma pressure profiles are given by Equations (3.35) and (3.37) respectively. The plasma density is taken to be uniform. We again consider the case $\partial/\partial y = 0$ and take $v_y = 0$; this removes the Alfvén wave from our simulations.

Small amplitude perturbations of the equilibrium obey the linearised MHD equations

(Roberts 1981a)

$$\left[\left(\frac{\partial^2}{\partial t^2} - v_A^2\frac{\partial^2}{\partial z^2}\right) - \frac{\partial}{\partial x}\left(c_f^2\frac{\partial}{\partial x}\right)\right] v_x = \frac{\partial}{\partial x}\left(c_s^2\frac{\partial v_z}{\partial z}\right) \tag{4.2}$$

$$\left(\frac{\partial^2}{\partial t^2} - c_s^2\frac{\partial^2}{\partial z^2}\right) v_z = c_s^2\frac{\partial}{\partial z}\left(\frac{\partial v_x}{\partial x}\right) \tag{4.3}$$

where

$$c_s^2 = \frac{\gamma}{2}\frac{v_{Ae}^2}{\cosh^2\left(\frac{x}{a}\right)}\,, \qquad v_A^2 = v_{Ae}^2\tanh^2\left(\frac{x}{a}\right)\,, \tag{4.4}$$

and $c_f^2 = c_s^2 + v_A^2$. The ratio of specific heats γ is taken to be 5/3. Equations (4.2) and (4.3) describe the motions of the x and z-components of velocity, which are coupled. Lengths and speeds are normalised against the half width of the slab (a) and the exterior Alfvén speed (v_{Ae}) respectively.

The time evolution of impulsively generated waves is investigated using a flux corrected transport (FCT) algorithm (Murawski and Goossens 1994). The aim of the algorithm is to minimise numerical errors. For finite difference schemes there are three errors which affect the accuracy of simulations. The first error is numerical diffusion and results from the fact that material which has just entered a cell, and is still near one boundary, becomes smeared over the whole cell. This error is larger for short wavelengths and thus very short wavelengths are removed from the simulations. The second error is dispersive in nature, which means that a wavepacket will disperse in time. The third error is related to the Gibb's phenomenon in Fourier analysis and small ripples appear in the solution. This effect is pronounced near steep gradients and appears because of the truncation of the Fourier spectrum.

The numerical algorithm consists of three stages: transport, diffusion and anti-diffusion. The transport stage (advancing from time t to time $t + \Delta t$) introduces ripples in the solution through numerical errors. In the diffusion stage a strong numerical diffusion is applied to the transported solution to remove these spurious oscillations from it. This transported and diffused solution contains an excess amount of numerical diffusion. This is subsequently compensated for by introducing anti-diffusive fluxes. For full details of the algorithm see Murawski and Goossens (1994).

The boundaries of the simulation box are located at $x/a = \pm 4$ and $z/a = \pm 10$. The computational box is divided into a non-uniform grid of 300 cells in the x-direction and 200 in the z-direction. For all simulations we use free boundary conditions which represent a natural extension of the region outside the computational domain. The proper treatment of the boundary conditions at the edges of the region is a complex aspect of time-dependent numerical simulations. It is not an easy matter to avoid unwanted reflections at the boundaries. To minimise these we stretch the grid near the outflow boundaries and apply damping to the velocity components of the 12 grid points nearest the boundary. This has been found to work well.

Initially, at $t = 0$, we apply an impulse (to excite kink waves) given by

$$v_x\left(x, z, t = 0\right) = \frac{v_{x0}}{\cosh^{14}\left(\frac{x-x_0}{a}\right)\cosh^{14}\left(\frac{z-z_0}{a}\right)}\,, \tag{4.5}$$

where (x_0, z_0) determines the location of the pulse; Equation (4.5) describes a pulse that is strongly concentrated about $x = x_0$, $z = z_0$. We consider only small amplitude perturbations and take $v_{x0} = 0.005 v_{Ae}$ for all simulations. Waves which are trapped by, and leak from, the current sheet are measured at fixed locations $(x/a, z/a) = (0.5, 7)$ and $(-2, 0)$ respectively to obtain the temporal signatures.

4.4.1 Initial Response after Impulse

We consider a single impulse with $x_0 = z_0 = 0$. Initially the pulse disperses in the xz-plane. Some of the wave energy leaks from the current sheet whilst the remaining wave is trapped by the inhomogeneity in the magnetic field. The wave ducting is a consequence of the impulse being reflected by the inhomogeneity in Alfvén speed. The spatial variation of the energy density for the x-component of velocity, $1/2\rho v_x^2$, is illustrated in Figure 4.3 at time $t = 10a/v_{Ae}$. Outwardly propagating (leaky) waves can be seen travelling away from the current sheet. These may be observable wave phenomena in coronal or magnetospheric current sheets. The remaining wave energy is located within the current sheet ($|x|/a < 2$). The impulse generates a pair of surface waves which propagate in opposite directions. The waves have maximum velocity near the edge of the sheet with a dip in the centre. From the dispersive curves (Figure 3.7) we expect the generation of body, hybrid and surface waves. The body and hybrid waves are likely to be observed in the periodic phase, whereas surface waves are probably present in the quasi-periodic phase (see the discussion in Section 4.2).

In addition, due to the coupling of the x and z-components of velocity (see Equations 4.2 and 4.3), the initial impulse in v_x also generates a z-component with comparable amplitudes to v_x. This wave also propagates along the sheet and may be observable. Outside the current sheet region the plasma beta is small and consequently v_z will attain low values in this region. The highest values of v_z will be in the vicinity of the centre of the sheet since the plasma pressure (and also sound speed) is highest there. Therefore a localised energy source, such as a flare or reconnection event, will create propagating waves in a current sheet and also waves which propagate away from the inhomogeneity (leaky waves). Both sets of waves may be observable.

4.4.2 Temporal Signatures

We consider two idealised cases: a single impulse centred on $(x_0/a = 0, z_0/a = 0)$ and two impulses located at $(x/a, z/a) = (2,0)$ and (-4,0). The velocity produced in the time signatures is normalised against the amplitude of the initial impulse v_{x0}. To estimate the periods we take $a = 500$ km and $v_{Ae} = 1000$ km s^{-1}, values representative of the solar corona. The Lomb-Scargle periodogram, in a desired frequency range, is computed using the algorithm of Carbonell and Ballester (1991). The Lomb-Scargle periodogram is a powerful algorithm for the time series analysis of unevenly sampled data. The algorithm of Carbonell and Ballester (1991) allows the search of periodicities in data within a specified time interval (see also Scargle 1982).

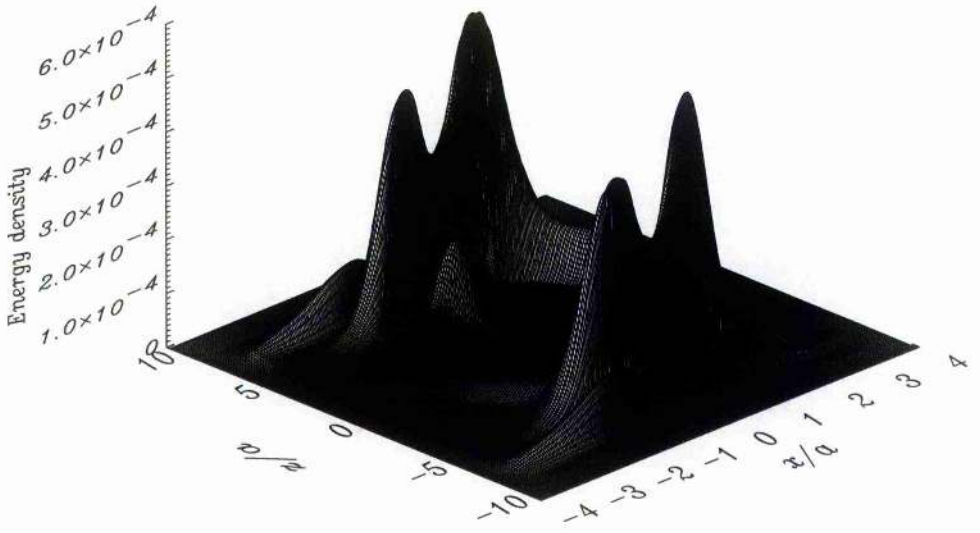

Figure 4.3: A surface plot of the x-component of kinetic energy density $(1/2\rho v_x^2)$ at $t = 10a/v_{Ae}$ for a single impulse applied at $(x_0, z_0) = (0, 0)$. Notice the existence of low amplitude outwardly propagating waves (leaky modes) and high amplitude ducted surface modes. These trapped waves propagate along the current sheet and exhibit a distinctive time signature.

Single Impulse

The results for the time signatures due to the application of a single pulse at $x_0 = z_0 = 0$ applied at time $t = 0$ are presented in Figure 4.4. In Figure 4.4a and 4.4c we show the results of measuring the x and z-components of velocity respectively, at a fixed location in space. We see that the three phases predicted by Roberts et al. (1984) for a coronal loop are also present for a current sheet. The periodic phase is very low in amplitude and is represented by a horizontal line. The quasi-periodic phase begins abruptly and some well defined oscillations can be observed in both components of velocity; finally the oscillations decay. The temporal signature for v_z is longer in duration than the one for v_x. However the largest oscillations in v_z occur through the coupling of v_x and v_z; these are the most likely to be observed. In Figure 4.4b the periodogram of v_x illustrates the periods where power is located. Periods in the range $\tau = 5$–$10a/v_{Ae}$ are obtained with a peak at $\tau = 8.5a/v_{Ae}$ (4.25 seconds). The minimum period is $\tau \approx 5a/v_{Ae}$ (2.5 seconds) which is in broad agreement with the group velocity curve ($\tau = 2\pi a/1.166v_{Ae} = 5.4a/v_{Ae}$). In Figure 4.4d the periodogram of the leaky wave time signature is shown (x-component). Notice that energy is distributed over a broad period range. The maximum power in the leaky waves is seen at $\tau = 3a/v_{Ae}$ (1.5 seconds), whilst significant power is also located between $\tau = 1.5a/v_{Ae}$ (0.75 seconds) and $\tau = 4.5a/v_{Ae}$ (2.25 seconds). Therefore certain reported short period oscillations (see Sections 1.2.3 and 1.2.4) may be due to trapped modes, other oscillations to leaky modes.

We now apply our results to neutral sheet oscillations in the Earth's magnetotail. Bauer et al. (1995a,b) and Mihalov et al. (1970) have measured periods of 1–2 minutes and 100 seconds respectively. Assuming typical magnetospheric values of $v_{Ae} = 500$ km s^{-1} and $a = 6400$ km (radius of the Earth) we obtain, for τ in the range 5–$10a/v_{Ae}$, periods between 1 and 2 minutes. Therefore, these observations may be due to magnetoacoustic waves that have been excited by some impulsive event and then guided by the wave duct.

Multiple Impulse

As an example of a more complicated situation we consider a multiple impulse (Figure 4.5). The time signature of the x-component of velocity (Figure 4.5a) shows the quasi-periodic phase is more oscillatory than that of a single pulse (Figure 4.4a) and a well defined wavepacket can be seen. The power spectrum (Figure 4.4b) shows that the maximum power is located at $\tau = 5.6a/v_{Ae}$ (2.8 seconds). A smaller peak is also seen at $\tau = 3.5a/v_{Ae}$ (1.75 seconds). In Figure 4.5c we see a quasi-periodic oscillation in the z-component of velocity similar to some observations (e.g. Correia and Kaufmann 1987). The leaky wave (v_x) power spectrum (Figure 4.5d) shows that leaky waves have lower periods than trapped waves. The maximum power in the periodogram is at $\tau = 2.5a/v_{Ae}$ (1.25 seconds) whilst significant power is also observed at $\tau = 1.5a/v_{Ae}$ (0.75 seconds), $\tau = 3.75a/v_{Ae}$ (1.875 seconds) and $\tau = 7.5a/v_{Ae}$ (3.75 seconds).

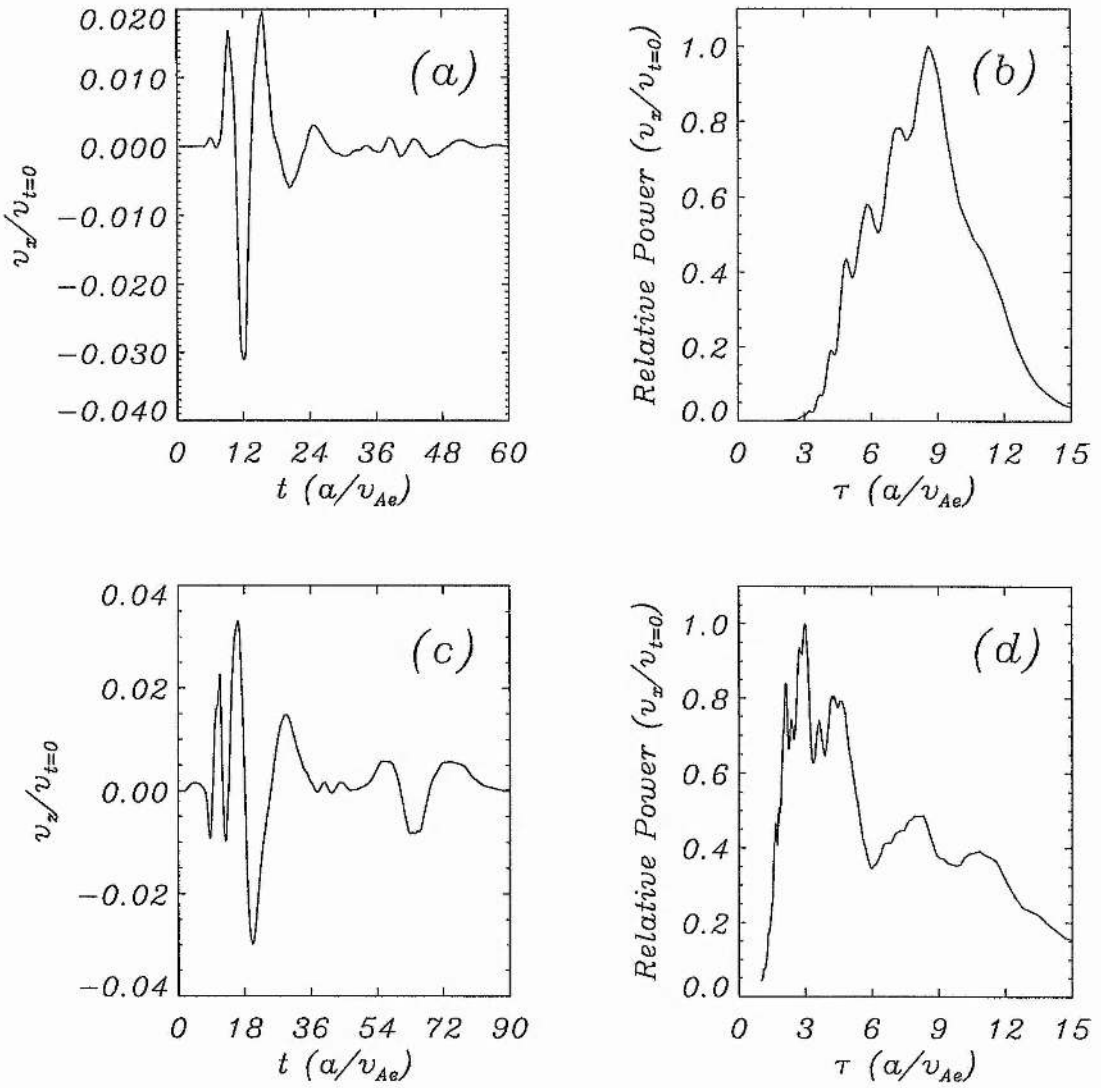

Figure 4.4: Temporal signatures and power spectra resulting from a single impulse applied at $(x_0/a, z_0/a) = (0, 0)$. In (a) the time signature of the x-component of velocity v_x measured at $(x/a, z/a) = (0.5, 7)$ is shown, and in (b) we give the periodogram of v_x. Notice that power exists in a broad range of periods $\tau = 5$–$10a/v_{Ae}$ (2.5–5 seconds). In (c) and (d) the temporal signature for v_z and the periodogram of the leaky waves temporal signature (v_x) are illustrated respectively. The impulsive event generates a distinctive wavepacket behaviour in both velocity components. Notice that significant power exists for short period leaky wave oscillations.

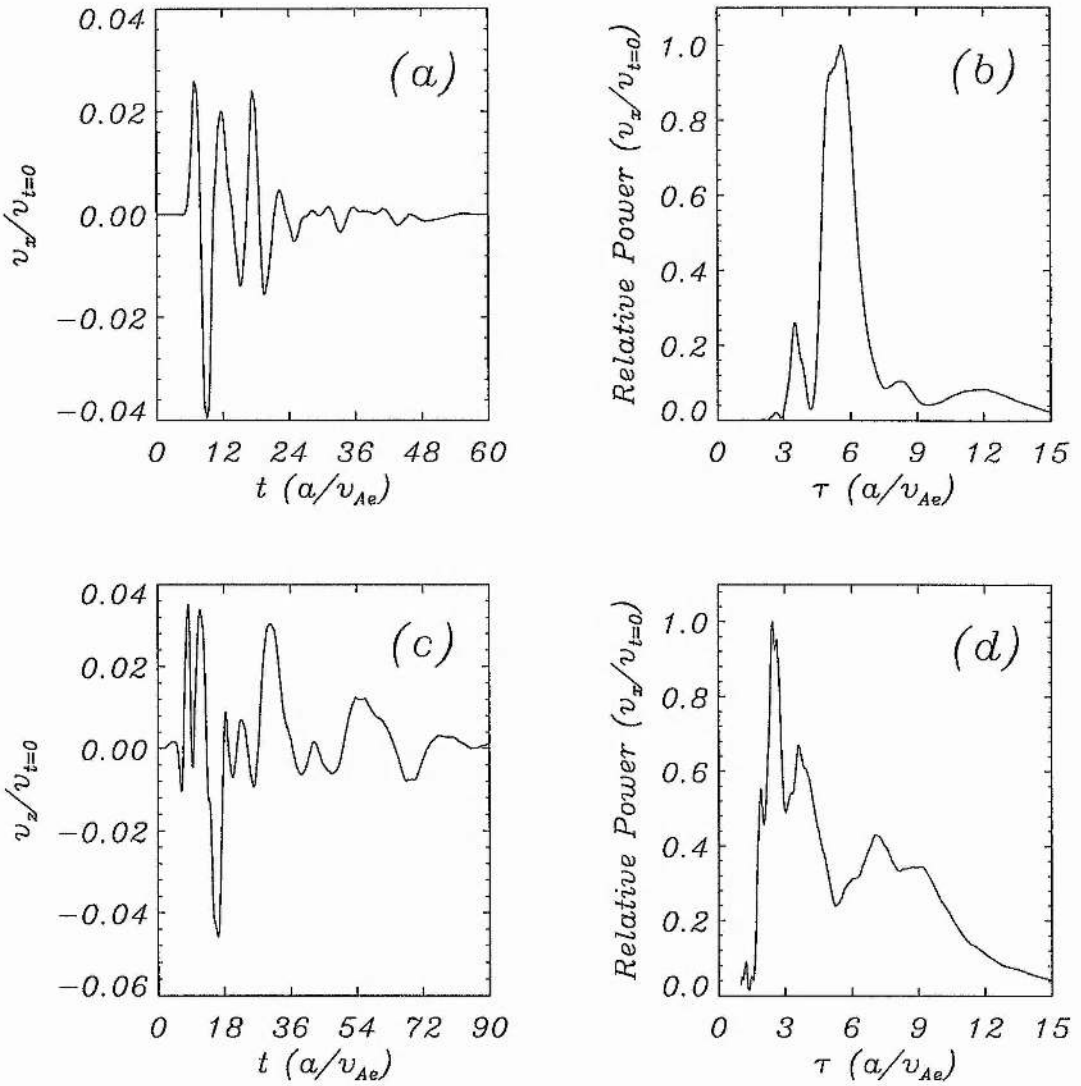

Figure 4.5: Temporal signatures for two impulses applied at $(x_0/a, z_0/a) = (2, 0)$ and (-4, 0) at time $t = 0$. (a) and (c) show the time signatures of the x and z-components of the velocity. Notice that the signatures are more oscillatory than in the case of a single impulse. The periodogram of v_x is shown in (b); power is located at $\tau = 5.6a/v_{Ae}$ and to a lesser extent at $\tau = 3.5a/v_{Ae}$. In Figure (d) the periodogram of the leaky wave (v_x) signature is shown; power is mainly located at $\tau = 2.5a/v_{Ae}$, but there is also significant power at $\tau = 3.75a/v_{Ae}$ (periods of 1.25 and 1.875 seconds respectively). Therefore, short period oscillations may be due to trapped and leaky waves.

4.5 Comparison with Observations

It is interesting to note that similar temporal signatures to our numerical simulations (Figures 4.4 and 4.5) have been observed in both the solar corona and in the Earth's magnetosphere.

For example Correia and Kaufmann (1987) have reported fast pulsations with a similar temporal form to that presented in our simulations. Radio observations at 30 and 90 GHz, following a solar burst, show a striking resemblance to the numerical simulations of impulsively generated waves in current sheets (Section 4.4) and coronal loops (Murawski and Roberts 1993a,b). An extract of Correia and Kaufmann's results is illustrated in Figure 4.6. This comparison between observations and theory suggests that an impulsive event (the solar burst) excites magnetoacoustic waves which are subsequently guided by either a current sheet or coronal loop. Once excited these waves exhibit a similar temporal signature that shown in Figure 4.2.

Furthermore the Pi2 pulsations in the plasma sheet of the Earth's magnetosphere show similar temporal variations to our numerical work. The results of Singer et al. (1985) are shown in Figure 4.7. Initially a low amplitude phase is observed which is followed by a large amplitude quasi-periodic phase. The oscillations decay after a few cycles. This data is in broad agreement with simulations of neutral sheet oscillations.

Finally, the observations of neutral sheet oscillations in the Earth's magnetosphere of Bauer et al. (1995a,b) are illustrated in Figure 4.8. The observations show an irregular period, with the magnetic pressure perturbation p_B out of phase with the plasma pressure p_e and total pressure p_T perturbations (in accordance with Figure 3.11). The oscillations last for a few cycles before decaying which is in good agreement with our simulations. In addition the observations show the three phases predicted by Roberts et al. (1983, 1984).

These examples of oscillations in the solar corona, the plasma sheet and the neutral sheet suggest that some of the reported pulsations in both the corona and magnetosphere may be due to impulsive events. Once generated the magnetoacoustic waves are guided by the inhomogeneity in magnetic field and exhibit a distinctive signature.

4.6 Summary and Conclusion

Impulsively generated waves in neutral sheets have been investigated. For a structured current sheet with a uniform density profile a minimum in the group velocity exists only for the fundamental kink mode, whereas for the Epstein profile minima also exist for other modes. The presence of a minimum in the group velocity plays a significant role in the theory of impulsively generated waves. Roberts, Edwin and Benz (1983, 1984) showed that an impulsive event in a coronal loop generates a distinctive temporal signature consisting of three phases: a low amplitude and low frequency *periodic* phase followed by a large amplitude high frequency *quasi-periodic* phase and finally a *decay* phase. In this chapter we have shown that similar results arise in a structured

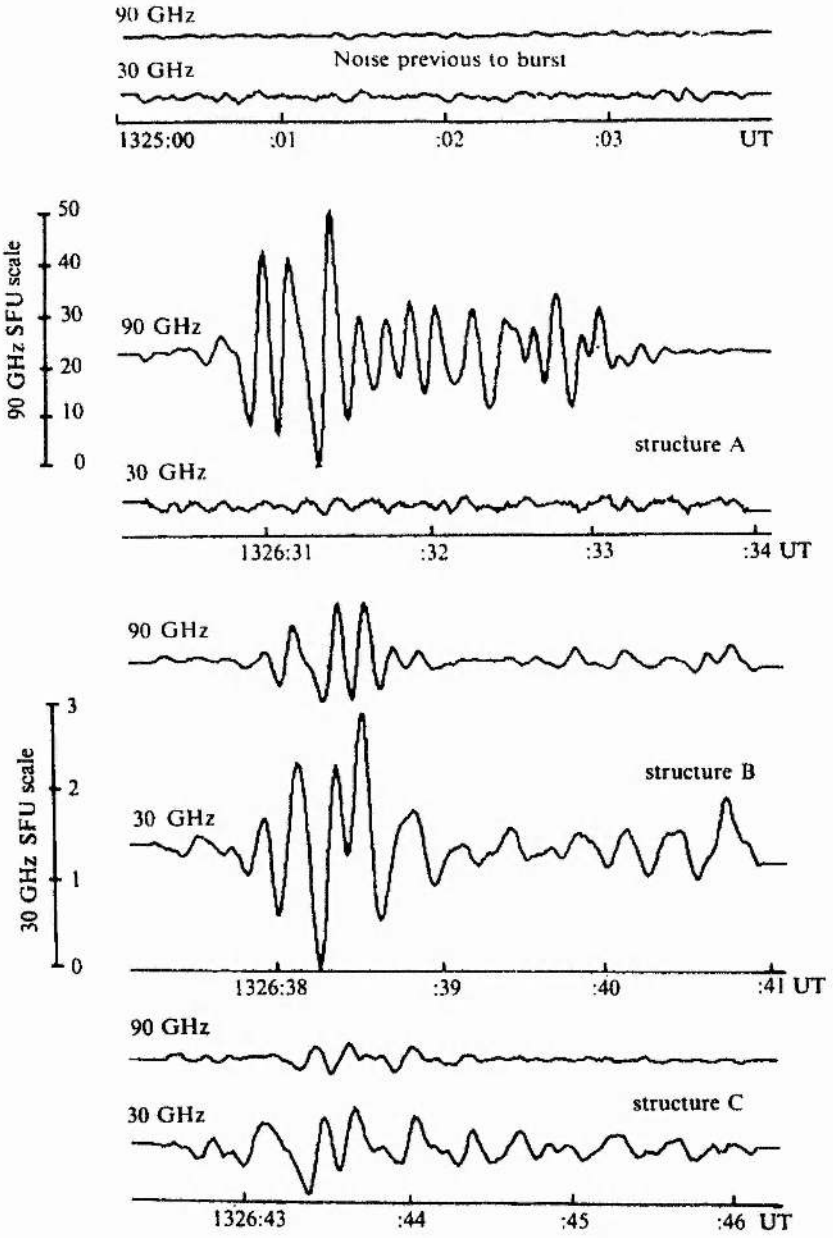

Figure 4.6: Fast pulsations in radio emission in the solar corona from Correia and Kaufmann (1987). Notice the similarity between the observations and the simulations of impulsively generated waves in current sheets (Figures 4.4 and 4.5).

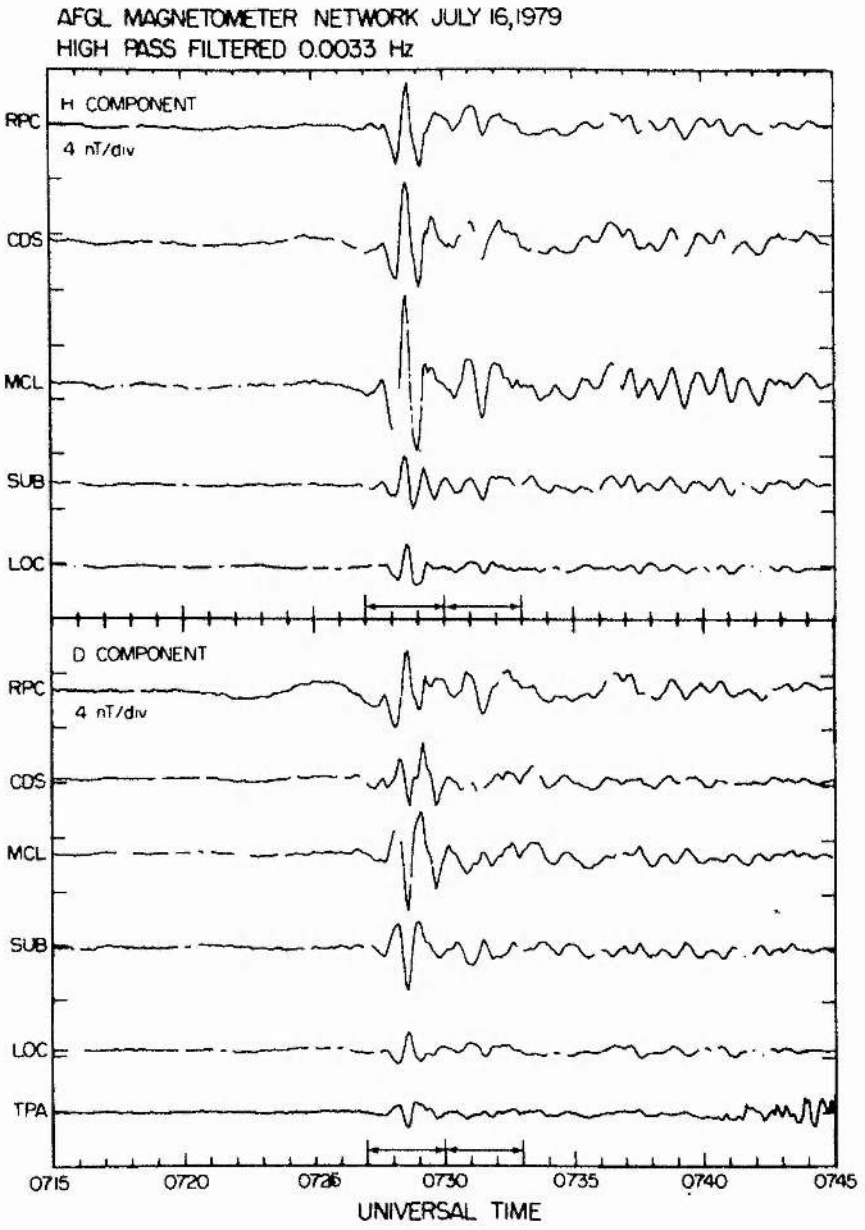

Figure 4.7: An example of Pi2 pulsations recorded by Singer et al. (1986). The agreement between the results and simulations is good.

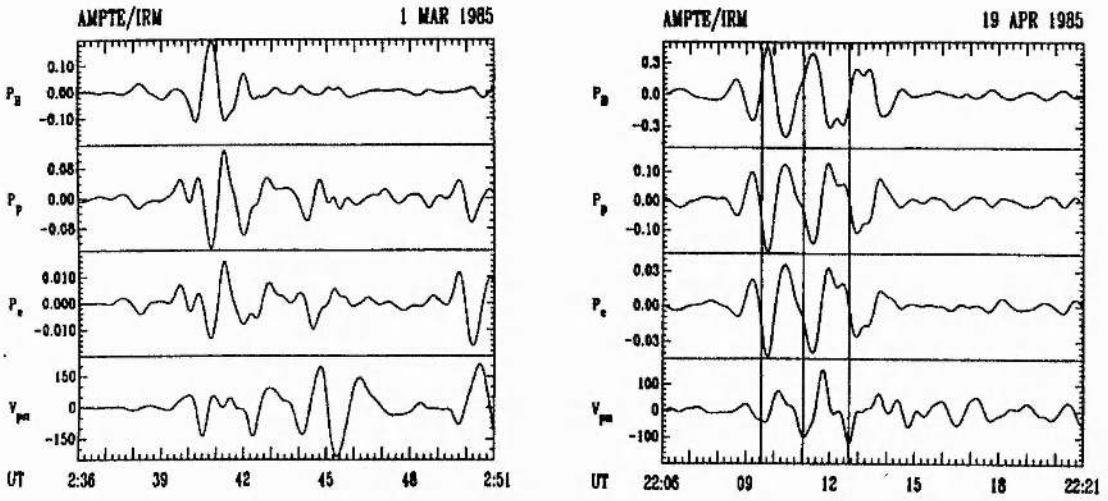

Figure 4.8: An example of neutral sheet oscillations recorded by Bauer et al. (1995a,b).

current sheet. Our numerical results illustrate that if an impulsive event occurs in a current sheet, magnetoacoustic waves will be guided by the inhomogeneity in magnetic field. These waves exhibit a distinctive temporal signature similar to that produced by coronal loops. Leaky waves possess the shortest periods.

An application of Equation (4.1) shows the predicted time scales for impulsively generated waves in the solar corona and Earth's magnetosphere are in good agreement with certain observations. In addition the predicted temporal signatures are in broad accordance with some observed data.

An examination of Figures 4.4 and 4.5 show that an impulse of amplitude v_{x0} generates motions of only 4 % in the velocity. Some of the initial energy of the impulse leaks into the environment whilst the trapped energy is distributed amongst all the various frequencies. In addition the impulse in v_x also generates velocity motions in the z-direction, thus reducing the amplitude of the oscillations. This may suggest that only very energetic events will result in observable wave motions.

In practice we may expect that a flare or reconnection event will not be a single impulse applied in the centre of the current sheet. Instead a series of impulses applied at different times and locations will be more realistic. However the agreement between the observations and numerical results of the time scales and temporal signatures is encouraging.

Chapter 5

A cavity driven by a random boundary displacement

5.1 Introduction

Wave propagation in inhomogeneous plasmas is important not only in the solar atmosphere but also in the Earth's magnetosphere, which provides another excellent example of a structured plasma able to support waves. In Chapter 4 we saw how magnetoacoustic waves in current sheets, both in the solar corona and Earth's magnetosphere, may explain certain of the observed pulsations in these regions. In this chapter we turn our attention to the investigation of the propagation of Ultra-Low-Frequency (ULF) waves in the magnetosphere, paying particular attention to the coupling between the fast and Alfvén modes.

We begin by giving an overview of the magnetosphere. The outer atmosphere of the Sun, the corona, has a temperature of several million degrees kelvin. At such high temperatures the electrons and ions have sufficient energy to escape the Sun's gravitational attraction. This is called the *solar wind*. The Earth's magnetosphere is the region defined by the interaction of the solar wind with the dipole magnetic field of the Earth. It extends from approximately 100 km above the Earth's surface to about 10 R_E ($R_E = 6400$ km) in the sunward direction. In the anti-sunward direction it extends out to several hundred R_E. Since the velocity of the solar wind is greater than the sound and Alfvén speeds a bow shock forms, across which the solar wind flow becomes sub-sonic and gives rise to a turbulent magnetosheath. The magnetopause is the boundary between the magnetospheric and solar wind magnetic fields of the magnetosheath. The magnetotail consists of oppositely directed field separated by a neutral sheet, where the magnetic field passes through zero. Surrounding the neutral sheet is the hot plasma sheet which is 4 to 6 R_E wide. See Mann (1995) for a detailed review of the structure of the Earth's magnetosphere and ULF waves in this region. A schematic sketch of the magnetosphere is shown in Figure 5.1.

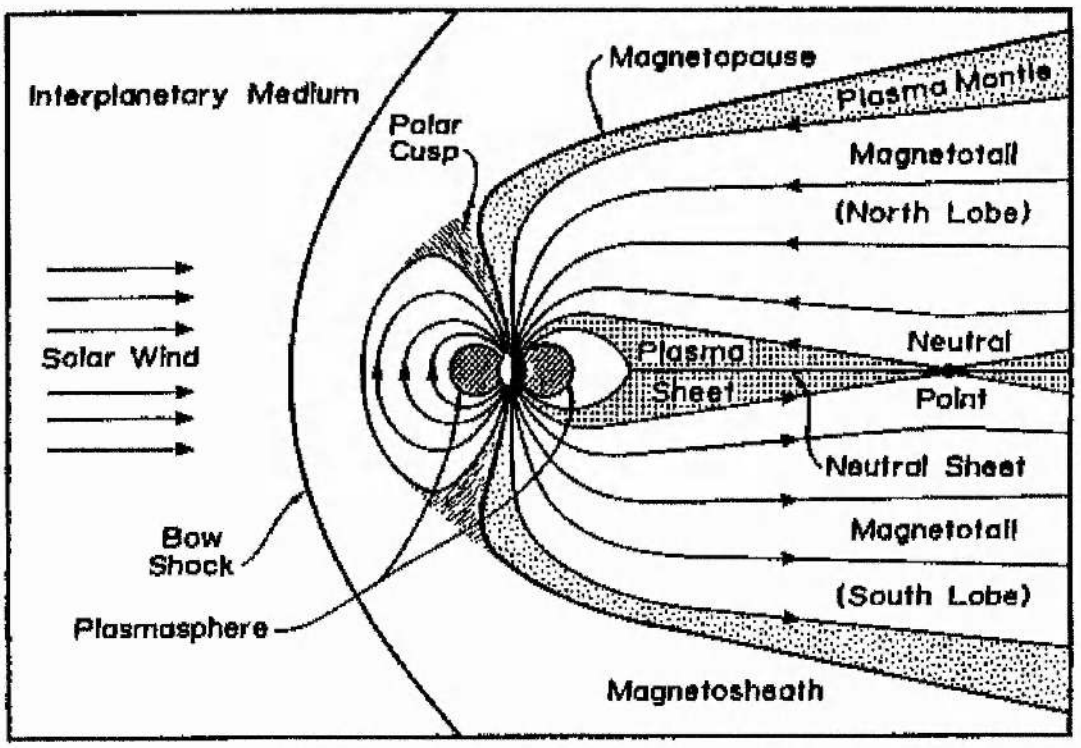

Figure 5.1: A schematic sketch of the Earth's magnetosphere taken from the World Wide Web page http://www-ssc.igpp.ucla.edu/.

ULF waves have frequencies ranging from 1 mHz to 1 Hz (Anderson 1994). Pulsations are classified as either Pc "Pulse continuous" or Pi "Pulse irregular". These refer to waves that are quasi-sinusoidal lasting for a few cycles, or irregular pulsations which are shorter lived.

In this chapter we investigate the coupling between the fast magnetoacoustic and Alfvén modes in a magnetospheric cavity driven by a random boundary displacement. A random driver is a more realistic case than the monochromatic drivers considered by previous workers. For example, the buffeting of the magnetospheric cavity by the magnetosheath is unlikely to result in a monochromatic driving source.

The aim of this chapter is to study ULF waves in the Earth's magnetosphere. To undertake this investigation we use the magnetospheric box model (see, for example, Southwood 1974). The cavity is illustrated in Figure 5.2; its width is L $(0 < x < L)$ and its height is $2L$ $(-L < z < L)$. In this model we take the magnetic pressure to dominate over the plasma pressure; the *cold plasma approximation*. In addition, the magnetic field is assumed to be straight and uniform, and is situated between the Northern and Southern Ionospheres (located at $z = \pm L$). The x and y-axes represent the radial and azimuthal directions respectively. The inhomogeneity in Alfvén speed (and density) is taken to vary in both the x and z-directions, whilst the magnetopause is taken to lie along the $x = L$ field line.

The ionospheric boundaries, located at $z = \pm L$, are assumed to be perfectly reflecting, and therefore the boundary displacement $\boldsymbol{\xi}$ $(z = \pm L)$ is zero. Here $\boldsymbol{\xi} = (\xi_x, \xi_y, 0)$ since ξ_z is zero under the cold plasma approximation. We take the normal component of velocity to the magnetic field (ξ_x) to be zero at $x/L = 0$. This assumes that waves are reflected by a large Alfvén speed gradient along this line. The governing MHD equations are solved by a numerical scheme developed by Wright and Rickard (1995).

We now give some definitions that we use in our work. The Alfvén frequency $\omega_A(\mathbf{r})$ is the natural frequency of an Alfvén wave on a field line. For a cavity which is inhomogeneous $\omega_A(\mathbf{r})$ is constant along a field line, but it varies with position throughout the cavity. The fast magnetoacoustic mode extends throughout the entire cavity and, unlike the Alfvén mode, is not confined to an individual field line; see Section 1.4 for the detailed properties of these modes. The coupling between the fast and Alfvén modes depends upon the wavenumber k_y, with weak coupling arising in the cases when $k_y = 0$ and $k_y \to \infty$.

Wright and Rickard (1995) give two criteria for driving an Alfvén resonance through a random motion. A cavity with an Alfvén speed inhomogeneity in one direction was considered for linear disturbances under the cold plasma approximation. The driver was found to excite the fast eigenmodes which lie within the frequency spectrum of the driver. Therefore, for a fast mode to be excited its frequency must lie within this spectrum. Secondly, for the fast mode to drive an Alfvén resonance the fast mode eigenfrequency must lie within the Alfvén continuum. The principal result from Wright and Rickard (1995) illustrated that Alfvén waves can be resonantly excited even when the cavity is driven by a non-monochromatic source. In this chapter we extend their work by

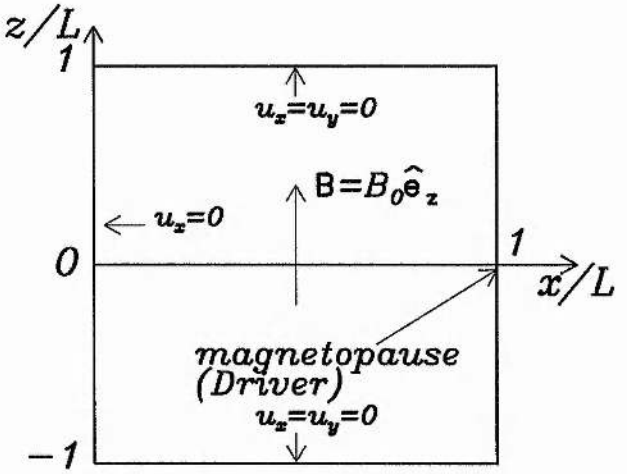

Figure 5.2: A sketch of the MHD cavity used in our simulations. A uniform magnetic field $\mathbf{B} = B_0\hat{\mathbf{e}}_z$ permeates the cavity. The driver is situated along the $x = L$ field line. On the three boundaries $z = \pm L$ and $x/L = 0$ we employ perfectly reflecting boundary conditions for the fast mode ($u_x = 0$). We take u_y equal to zero at $z = \pm L$.

examining randomly driven fast waves in a two-dimensional inhomogeneous cavity.

The format of this chapter is as follows. In Section 5.2 we describe our model and governing equations. In Section 5.3 we give an outline of the numerical scheme for solving the ideal MHD equations and also the algorithm for obtaining a random driving source. Our results are described in Section 5.4. In Section 5.4.1 we calculate the fast mode eigenfrequencies of the cavity and also the upper and lower frequencies of the Alfvén continuum. Section 5.4.2 shows the temporal form of the random driver and its Fourier transform. The response of the cavity to the random driver is discussed in Section 5.4.3, and the coupling between the fast and Alfvén modes is examined in Section 5.4.4. Applications of this work to the seismological study of the magnetosphere are given in Section 5.4.5, and finally our work is summarised in Section 5.5.

5.2 Governing Equations and Equilibrium

The ideal MHD equations governing the small amplitude (linear) velocity ($\mathbf{u} = [u_x, u_y, 0]$) and magnetic field ($\mathbf{b} = [b_x, b_y, b_z]$) perturbations in the low-β approximation are given by

$$\frac{\partial u_x}{\partial t} = \frac{v_A^2}{B_0}\left(\frac{\partial b_x}{\partial z} - \frac{\partial b_z}{\partial x}\right), \tag{5.1}$$

$$\frac{\partial u_y}{\partial t} = \frac{v_A^2}{B_0}\left(\frac{\partial b_y}{\partial z} - \frac{\partial b_z}{\partial y}\right), \tag{5.2}$$

$$\frac{\partial b_x}{\partial t} = B_0 \frac{\partial u_x}{\partial z} , \tag{5.3}$$

$$\frac{\partial b_y}{\partial t} = B_0 \frac{\partial u_y}{\partial z} , \tag{5.4}$$

$$\frac{\partial b_z}{\partial t} = -B_0 \left(\frac{\partial u_x}{\partial x} + \frac{\partial u_y}{\partial y} \right) , \tag{5.5}$$

where the square of the Alfvén speed is given by $v_A^2 = B_0^2/\mu_0\rho$, B_0 is the magnitude of the equilibrium magnetic field and the plasma density is denoted by ρ. We have taken the magnetic field to be uniform; $\mathbf{B} = B_0\hat{\mathbf{e}}_z$. Under the cold plasma approximation the fast and Alfvén modes are present and the slow mode is absent ($u_z = 0$). When the wavenumber k_y is small the fast mode is approximately given by u_x, b_x and b_z, whereas the Alfvén mode is characterised by u_y and b_y (Wright 1992). The Alfvén speed profile $v_A(x,z)$ is assumed to be a separable function: $v_A(x,z)/v_{A0} = X(x)\,Z(z)$. Specifically, we use

$$X(x) = 1 - \frac{x}{1.3L} , \tag{5.6}$$

$$Z(z) = 3 - 2\cos\left(\pi \frac{z}{L}\right) . \tag{5.7}$$

Here v_{A0} is the Alfvén speed at $(x/L = 0, z/L = 0)$ and the cavity width is L. In our work we consider the dimensionless frequency of oscillation, defined to be $\omega L/v_{A0}$. The Alfvén speed profile is plotted in Figure 5.3.

5.3 Numerical Code and Driver

The basis of the numerical code employed in this chapter is described fully by Wright and Rickard (1995). The one-dimensional code was modified to investigate ULF wave propagation in a two-dimensional inhomogeneous cavity (Rickard 1996, private communication). The numerical scheme is Zalesak's (1979) leapfrog-trapezoidal algorithm which is second order in both space and time. The time step was chosen to be 0.05 of the minimum propagation time across a cell. Energy conservation was satisfied to within 1 part in 10^6. Given the velocity and magnetic field perturbation at any time the next state is found by updating $\mathbf{u}$ and $\mathbf{b}$ at every grid point, except where the driver is located along $x = L$. In our numerical work we impose that $u_x = 0$ is zero along $z/L = 0$ so that we are only exciting asymmetric modes. In addition, along the edges of the cavity $x/L = 0$ and $z/L = \pm 1$, we apply perfectly reflecting boundaries ($u_x = 0$), and u_y is set to zero at $z = \pm L$.

The algorithm to obtain the random driving source is described in detail by Wright and Rickard (1995); here we only give a brief outline. A random set of data for the x displacement of the boundary is obtained at discrete times t_n. Two time intervals are specified Δt_1 and $\Delta t_2\,(> \Delta t_1)$. A random number generator gives a value for the boundary displacement between -1 and 1. The time is then determined by $t_n = t_{n-1} + \Delta t$, where the interval Δt is given by either Δt_1 or Δt_2. The probability that Δt_1 is chosen over Δt_2 is taken to be 90 %. If Δt_2 is chosen then the next two time steps are given by Δt_1. A cubic spline is then fitted to the discrete points to give a

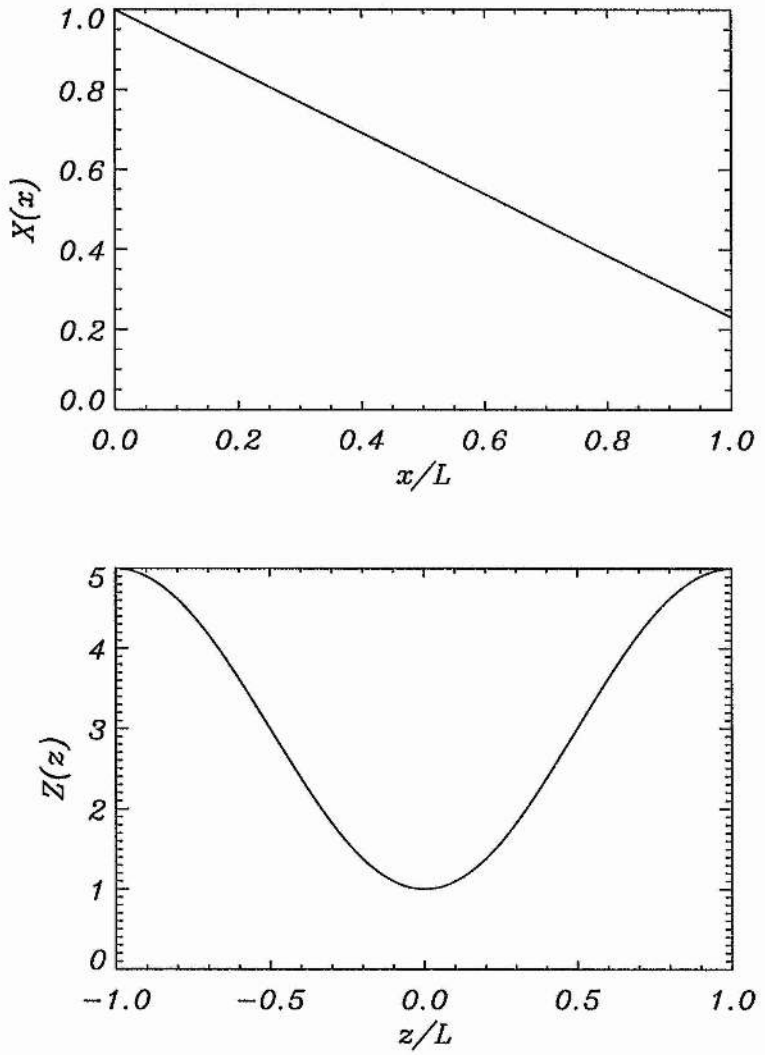

Figure 5.3: A plot of the Alfvén speed profile used in our study. We take the Alfvén speed $v_A(x,z)$ to be a separable function written as $X(x)\,Z(z)$. Specifically we take $X(x) = 1 - (x/1.3L)$ and $Z(z) = 3 - 2\cos(\pi z/L)$.

Mode	$\omega L/v_{A0}$	Symmetry
1	2.520	S
2	4.216	S
3	4.395	A
4	5.869	S
5	6.014	S
6	6.132	A

Table 5.1: The eigenfrequencies and the symmetry of u_x about $z/L = 0$ for the lowest six fast eigenmodes.

continuous expression for the boundary displacement at all times. The x-component of velocity is then obtained by differentiating the continuous function of the boundary displacement. For the simulations undertaken in our work we take $\Delta t_1 = 1$ and $\Delta t_2 = 10$. We measure times in terms of the Alfvén transit time; $t_A = tv_{A0}/L$.

At $t_A = 0$ we impose that both the boundary displacement and the velocity are zero. This removes any transient effects when the boundary motion starts and is achieved by creating a symmetrical set of data points about $t_A = 0$.

5.4 Results of numerical simulations

5.4.1 Calculation of Alfvén continua and fast eigenfrequencies

We now calculate the frequencies associated with both the Alfvén continuum and the fast modes which are of importance for our numerical work. The eigenfrequencies when $k_y \neq 0$ may be estimated by calculating the eigenfrequencies when k_y is set to zero. This is the case when k_y is sufficiently close to zero. This was illustrated by Wright (1992) who finds in the limit of small k_y the decoupled eigenfrequencies ($k_y = 0$) agree with non-zero k_y to within 4 %. Wright (1992) concludes that the fast mode oscillates essentially decoupled for small k_y. Therefore to calculate the eigenfrequencies in our coupled system we take $k_y \ll 1$ and compute the decoupled frequencies.

We begin by examining the fast magnetoacoustic modes. The lowest six modes of oscillation are calculated using the eigenvalue code described in Chapter 2. To obtain these frequencies we set $k_y = 0$ and we use the Alfvén speed profile (Equations 5.6 and 5.7) with a uniform magnetic field $\mathbf{B} = B_0\hat{\mathbf{e}}_z$. Table 5.1 gives the dimensionless frequencies and also denotes whether the modes are symmetric (S) or asymmetric (A) about $z/L = 0$. Asymmetric and symmetric modes are characterised by a node and anti-node in u_x, along $z/L = 0$, respectively. Note that only one asymmetric mode exists (mode 3) in the frequency range $0 < \omega L/v_{A0} < 6$.

We now calculate the upper (ω_+) and lower (ω_-) frequencies of the Alfvén continua and also the position of the resonant field lines for the Alfvén speed profile used in our study. Consider

Harmonic	$\omega_- L/v_{A0}$	$\omega_+ L/v_{A0}$	Fast mode
1	0.5291	2.2928	-
2	1.5834	6.8613	3, 6, ... (A)
3	2.4419	10.5814	1, 2, 4, 5, ... (S)
4	3.2645	14.1462	3, 6, ... (A)
5	4.0765	17.6647	2, 4, 5, ... (S)

Table 5.2: The minimum and maximum frequencies of the first five Alfvén continua. The fast eigenmodes which lie within the Alfvén continuum and share the same symmetry are also given.

the second order ordinary differential equation governing the decoupled ($k_y = 0$) Alfvén wave

$$\frac{\mathrm{d}^2\phi}{\mathrm{d}z^2} + \frac{\omega_A^2(x)}{v_A^2(x,z)}\phi = 0 \,. \tag{5.8}$$

Here ϕ is the Alfvén wave eigenfunction. Writing the Alfvén speed as $v_A(x,z) = X(x)\,Z(z)$, Equation (5.8) becomes

$$\frac{\mathrm{d}^2\phi}{\mathrm{d}z^2} + \frac{\Omega^2}{Z^2}\phi = 0 \,, \tag{5.9}$$

where we have defined $\Omega^2(x) = \omega_A^2/X^2$. Equation (5.9) is solved numerically by applying the boundary conditions $\phi = 0$ at $z = \pm L$. Equation (5.9) determines the eigenvalues Ω_1^2, Ω_2^2, ... of the Alfvén mode. The frequencies of the Alfvén continuum are then calculated by

$$\omega_{Ai}^2(x) = X^2(x)\,\Omega_i^2 \,. \tag{5.10}$$

In addition, to calculate the position of the resonant field lines we set

$$\omega_f^2 = \omega_{Ai}^2 = X^2(x_{ri})\,\Omega_i^2 \,, \tag{5.11}$$

where ω_f is the fast mode eigenfrequency and x_{ri} is the position of the resonant field line.

Table 5.2 gives the frequencies of the first five Alfvén continuum modes (Wright 1996, private communication). The lower ($\omega_- L/v_{A0}$) and upper ($\omega_+ L/v_{A0}$) frequencies of the Alfvén continuum are given. In addition the fast modes from Table 5.1, that have frequencies within each continuum range and possess the same symmetry as the Alfvén mode are given. We also denote whether these modes are symmetric (S) or asymmetric (A).

In our work we suppress symmetric modes by imposing a node in u_x along $z/L = 0$. We notice from Table 5.2 that the third and sixth fast magnetoacoustic modes (which are asymmetric) will couple to both the second and fourth Alfvén harmonics. From Equation (5.11) we calculate that the second and fourth Alfvén harmonics will have frequencies equal to the third fast mode at locations $x_{r2} = 0.467L$ and $x_{r4} = 0.896L$, when driven by the third fast mode with $\omega_f L/v_{A0} = 4.395$. For the sixth fast mode, at a frequency of $\omega_f L/v_{A0} = 6.132$, we find the second and fourth harmonic Alfvén modes will be excited at locations $x_{r2} = 0.138L$ and $x_{r4} = 0.737L$.

5.4.2 Temporal form of random driver

Figure 5.4a shows the random driving velocity $u_x\,(x = L,\ z = 0.15L)$ as a function of tv_{A0}/L. In Figure 5.4b we show the Fourier transform of the velocity in Figure 5.4a. The driver has a broadband frequency spectrum lying in the range $0 < \omega L/v_{A0} < 6$ and there is no preferred driving frequency. The dashed line in Figure 5.4b denotes the frequency of the only asymmetric mode, $\omega_f L/v_{A0} = 4.395$, which exists within the frequency range of the driver. It is important to note that the driver does not favour this eigenfrequency. From Table 5.2 we expect this fast mode to be important in our simulations, along with the second and fourth Alfvén harmonic resonances.

5.4.3 Response of cavity to random driver

In this section we investigate how the cavity responds to the random driving motion. The cavity is randomly driven as described in Section 5.3. We set $k_y L = 0.01$. Figure 5.5a shows the x-component of velocity (u_x) at a fixed point $(x/L = 0.93,\ z/L = 0.45)$ within the cavity as a function of time. The velocity is much more coherent than the driving motion (compare with Figure 5.4a). This is clearly seen by examining the Fourier transform of u_x (Figure 5.5b). The presence of a preferred frequency of oscillation within the cavity is now evident. It is interesting to note that this frequency appears to correspond exactly with the third fast mode eigenfrequency calculated using the code from Chapter 2. Notice that the sixth fast mode frequency, $\omega_f L/v_{A0} = 6.132$, is not excited since it lies outside the frequency range of the driver.

Since $k_y L$ is small, Figure 5.5a essentially gives the temporal variation of the fast magnetoacoustic mode at a fixed location within the cavity. It is evident that the cavity filters the random driving source and frequencies that are not eigenfrequencies of the cavity are suppressed. The cavity oscillates in a quasi-monochromatic fashion, since it is dominated by power in a very narrow frequency range.

The fast eigenmodes in the cavity are excited providing their eigenfrequencies lie within the spectrum of the driver. This is in agreement with the results of Wright and Rickard (1995). This result may be expected by considering physical analogies. Consider, for example, blowing air across an empty bottle or playing a wind instrument. Even though the source of the sound is broadband the instrument or bottle extracts characteristic frequencies.

To summarise, we have driven a cavity with a broadband spectrum $0 < \omega L/v_{A0} < 6$. Within this frequency range we have calculated that one asymmetric frequency exists $(\omega_f L/v_{A0} = 4.395)$. The cavity extracts this eigenfrequency from the driver, suppressing all other frequencies. Having seen that the non-monochromatic driver is able to excite a quasi-monochromatic fast mode, we now examine how this mode may couple to an Alfvén wave.

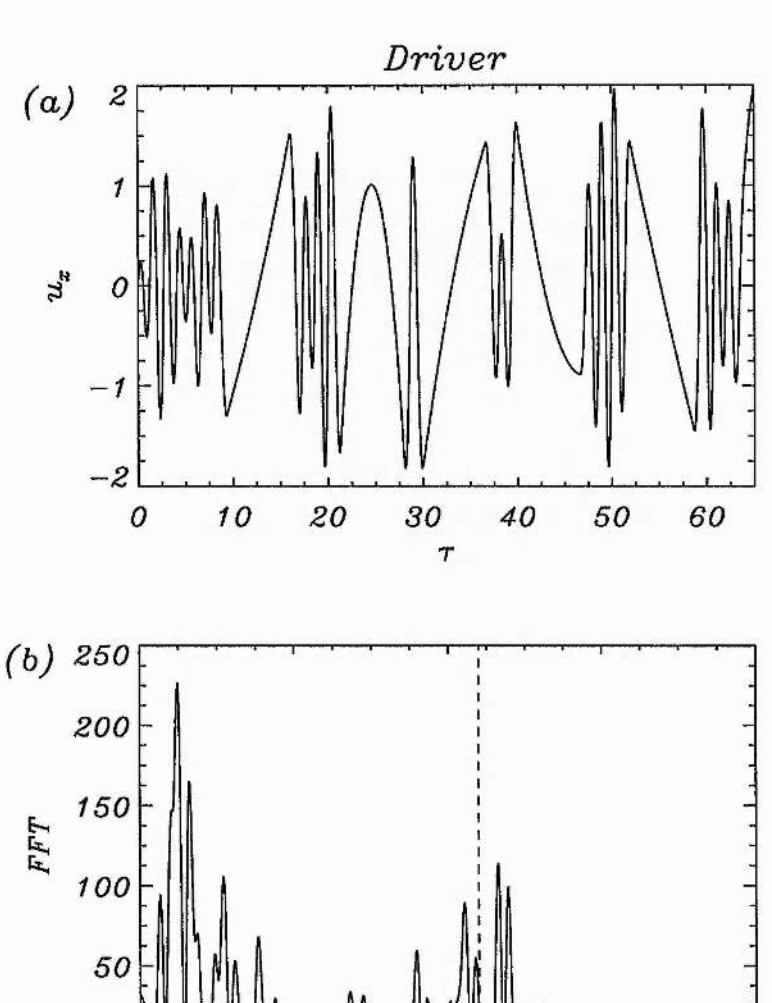

Figure 5.4: In (a) the temporal form of the random driver is depicted and in (b) the Fourier transform of (a) is shown. The velocity u_x is measured at $x = L$, $z = 0.15L$. Notice that the driving source is a broadband spectrum with frequencies lying in the range $0 < \omega L/v_{A0} < 6$. The dashed line denotes the position of the only asymmetric mode which exists within this frequency range. Note that the driver does not favour this frequency.

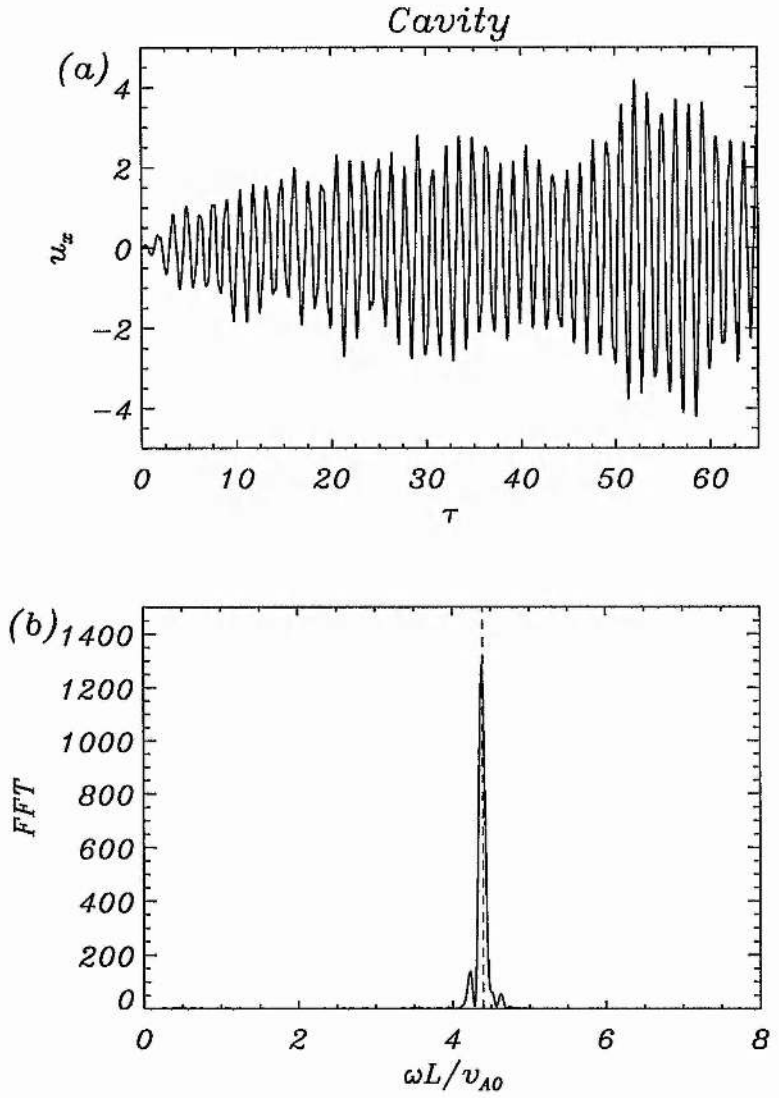

Figure 5.5: In (a) we show the x-component of velocity (corresponding to the fast mode) at the location ($x/L = 0.93$, $z/L = 0.45$) in the cavity. Notice that the oscillation is more coherent than the driving motion (Figure 5.4a). In (b) the Fourier transform of (a) is shown. The dashed line shows the frequency of the first asymmetric mode at a dimensionless frequency of $\omega_f L/v_{A0} = 4.395$. The frequency of the fast mode within the cavity is equal to $\omega_f L/v_{A0}$. The cavity therefore acts as a filter, suppressing frequencies which are not eigenfrequencies of the system, allowing cavity eigenmodes to dominate the solution.

5.4.4 Fast and Alfvén mode coupling

If $k_y = 0$ the fast and Alfvén modes are decoupled, whereas if $k_y \neq 0$ there is coupling between the two modes. The condition for the fast magnetoacoustic mode to drive an Alfvén resonance is that the frequency must lie within the Alfvén continuum. From the Alfvén speed profile we employ, two resonant field lines are expected to exist within the cavity. These correspond to the fast mode eigenfrequency $\omega_f L/v_{A0} = 4.395$, occurring at locations $x_{r2} = 0.467L$ and $x_{r4} = 0.896L$. Here the subscripts 2 and 4 refer to the second and fourth harmonics of the Alfvén mode respectively. The sixth fast mode, with a frequency of $\omega_f L/v_{A0} = 6.132$, is not excited since it lies outside the driving spectrum. Therefore we do not expect this fast mode to drive an Alfvén resonance.

In Figure 5.6 we plot the Alfvén wave energy E_A $(= 0.5\rho u_y^2 + b_y^2/2\mu_0)$ as a function of x/L for $z/L = 0.05$ at two times. Figures 5.6a and 5.6b illustrate E_A at times $t_A = 5$ and $t_A = 20$ respectively. The dashed lines denote the positions of the two predicted resonant field lines at x_{r2} and x_{r4} (assuming a constant fast mode frequency of $\omega_f L/v_{A0} = 4.395$). At low Alfvén times (Figure 5.6a) the Alfvén energy density is broad, although it is primarily located around the resonant field lines. As time increases the resonances becomes much sharper, occurring along the predicted field lines (Figure 5.6b). Therefore the random driving motion can excite a fast eigenmode which can then drive an Alfvén resonance, in much the same way as a monochromatic driver. This is provided that the fast mode frequency lies within the Alfvén continuum.

This result can be confirmed by examining the Alfvén mode eigenfunctions. In Figure 5.7 we show u_y calculated from our time dependent simulations (solid line) for the field lines at x_{r2} and x_{r4}, measured after twenty Alfvén times. In addition we have over plotted the eigenfunction calculated by solving the ordinary differential equation (Equation 5.9) along each resonant field line. It can clearly be seen that the agreement between the time dependent calculation with the random driver and solving the ordinary differential equation for the normal mode is excellent. Therefore, even though a random source is used, the Alfvén wave velocity is essentially identical to the Alfvén wave eigenmode.

To illustrate this in greater detail we plot in Figure 5.8 the difference between the Alfvén wave velocity along each resonant field line, for both a random and constant frequency driving source. The numerical code is re-run, but this time using a monochromatic driver with a frequency $\omega_f L/v_{A0} = 4.395$. We then calculate the difference between u_y along each resonant field line for the two driving mechanisms after twenty Alfvén times, with $k_y L = 0.1$. This is defined to be equal to Δu_y. To calculate the difference between the two drivers the amplitude of u_y is normalised to unity. Figures 5.8a and 5.8b show Δu_{y2} and Δu_{y4} respectively, where the subscripts 2 and 4 denote the second and fourth Alfvén harmonic. The difference between the Alfvén velocity generated by the two drivers is small. In particular, for the second and fourth Alfvén harmonics the maximum differences are 0.0215 and 0.0056 respectively. Therefore a random driving source can generate an Alfvén resonance whose eigenfunction is almost identical to one driven by a monochromatic source.

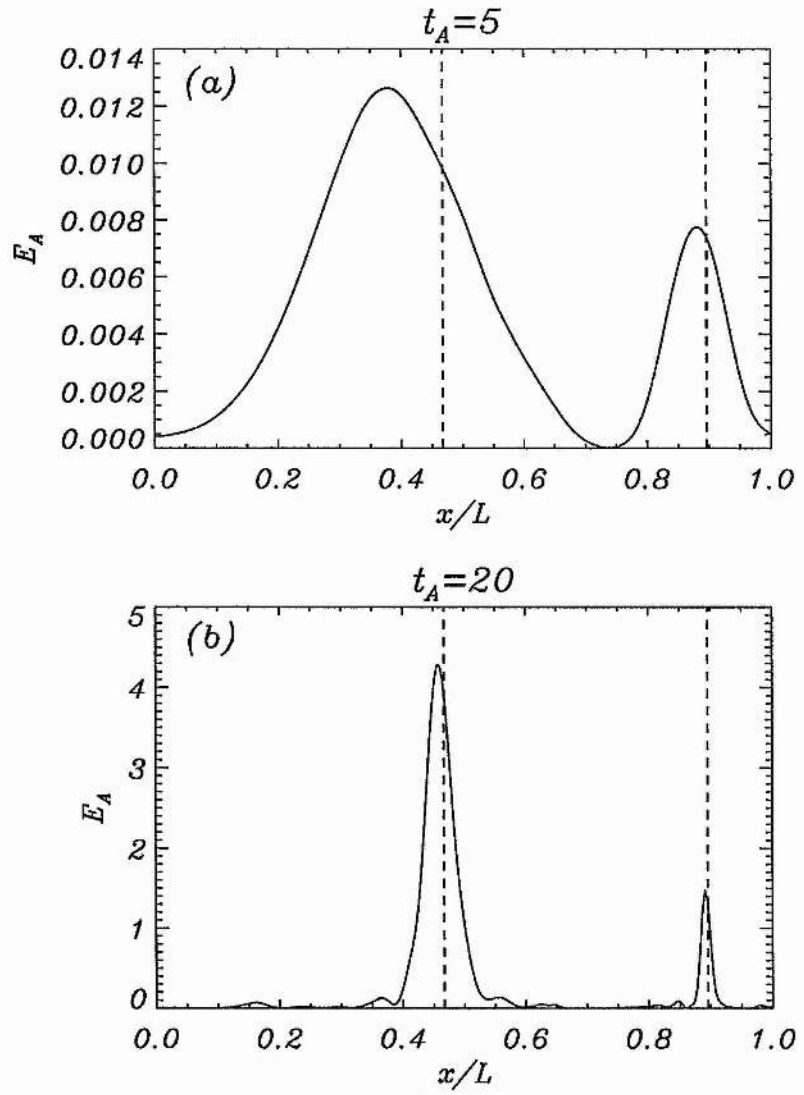

Figure 5.6: The Alfvén energy $E_A\,(=0.5\rho u_y^2+b_y^2/2\mu_0)$ at $z/L=0.05$ at times (a) $t_A=5$ and (b) $t_A=20$, using $k_yL=0.01$. The dashed lines denote the locations of the calculated resonances assuming a monochromatic driver. Notice that as time increases the Alfvén wave energy becomes more localised about the resonant field lines. These are located at $x_{r2}=0.467L$ and $x_{r4}=0.896L$, corresponding to the second and fourth harmonics of the Alfvén mode respectively.

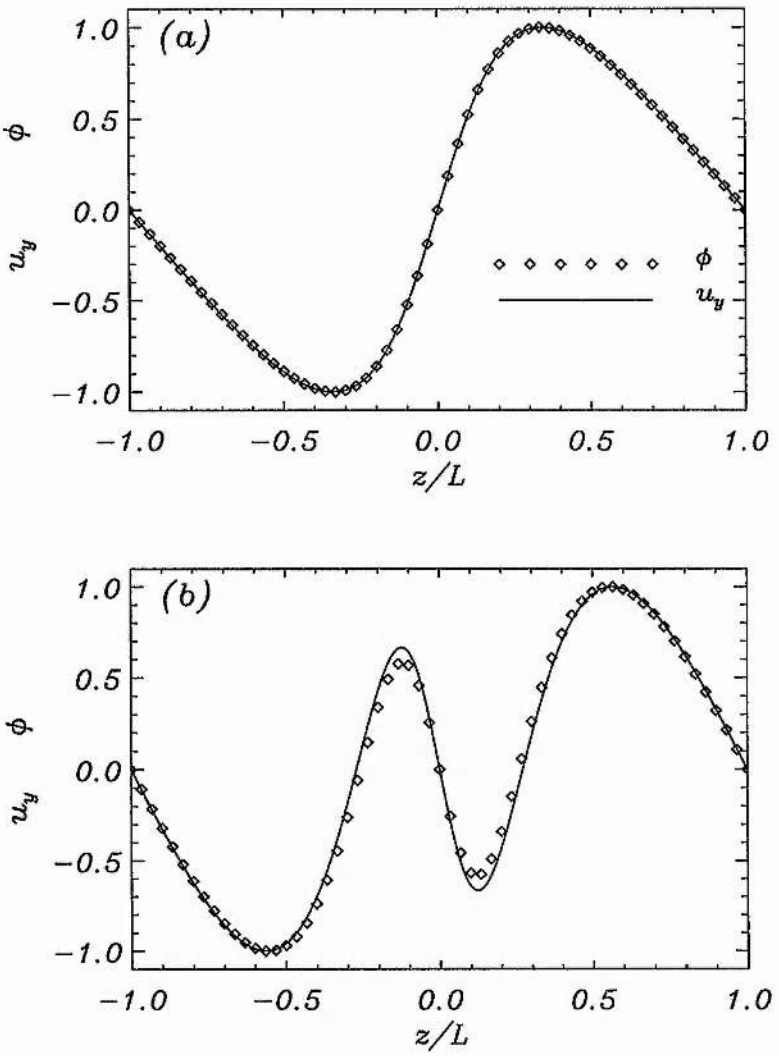

Figure 5.7: The (a) second and (b) fourth harmonics of the Alfvén wave eigenfunction ϕ. The solid line denotes u_y along each resonant field line, calculated from the time dependent code, measured after twenty Alfvén times. The eigenfunction calculated by solving the ordinary differential equation (Equation 5.8) is shown by a diamond symbol. The agreement between the two cases is excellent.

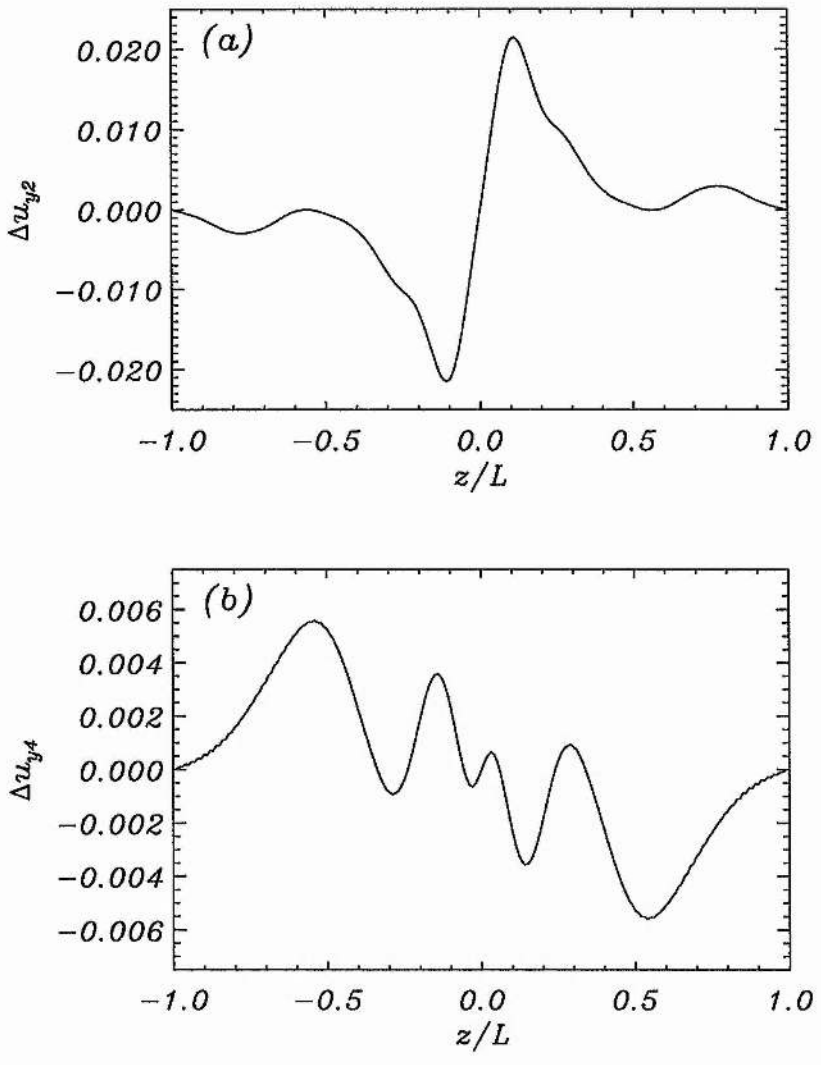

Figure 5.8: In (a) we show the difference Δu_{y2} between the normalised Alfvén wave eigenfunction generated by the monochromatic driver (with a frequency of $\omega_f L/v_{A0} = 4.395$) and the random driver, for the second Alfvén harmonic. Notice that the maximum value of Δu_{y2} is small (≈ 0.02) compared to the amplitude of the eigenfunction (unity). In (b) we show the difference for the fourth harmonic Alfvén mode Δu_{y4} when driven by the constant frequency and random source. Again Δu_{y4} is small. In (a) and (b) we have calculated the difference in u_y along each resonant field line after twenty Alfvén times with $k_y L = 0.1$. The coupling between the Alfvén and fast modes is similar for both driving mechanisms.

5.5 Seismology of the magnetosphere

We now give details about how the work described in this chapter may lead to the seismological study of the magnetosphere. Using analytical results obtained by Wright (1992) we find that the Alfvén energy density ratio between two resonant field lines tends to a constant value for increasing time. The energy density ratio of the two resonant field lines described in Section 5.4.4 is given by Wright (1997, private communication) as

$$\frac{E_{A2}}{E_{A4}} = \frac{X^2(x_{r2})}{X^2(x_{r4})} \left[\frac{\int_{x_{r2}} \phi_r(x_{r2}) \frac{\partial \xi_x}{\partial x} \mathrm{d}z}{\int_{x_{r4}} \phi_r(x_{r4}) \frac{\partial \xi_x}{\partial x} \mathrm{d}z} \right]^2 \frac{\int_{x_{r4}} (\phi_r(x_{r4})/Z)^2 \mathrm{d}z}{\int_{x_{r2}} (\phi_r(x_{r2})/Z)^2 \mathrm{d}z}, \tag{5.12}$$

where the subscripts 2 and 4 denote the second and fourth harmonics respectively. In addition X and Z are the separable functions which determine the Alfvén speed profile, given by Equations (5.6) and (5.7). The function ϕ_r is the Alfvén wave eigenfunction and ξ_x is the fast mode displacement.

In Figure 5.9 we plot the energy ratio as a function of the Alfvén transit time for (a) a random driver, (b) a monochromatic driver, and (c) an impulsive source. In (c) we read in u_x from the eigenvalue code used in Chapter 2 as the initial condition. To obtain u_x we configure the eigenvalue code described in Chapter 2 using $k_y = 0$ with a uniform field $\mathbf{B} = B_0 \hat{\mathbf{e}}_z$ and the Alfvén speed profile given by Equations (5.6) and (5.7). No driver is used in part (c). In Figure 5.9 we use $k_y L = 0.1$. The three cases show that the energy ratio is independent of the driving source. The initial transient stage does exhibit minor differences, but after several Alfvén times all three cases show the energy ratio to be approximately equal to 3.5.

This constant value may also be calculated from Equation (5.12). Inserting the various quantities into this equation we obtain a value of 8.9. Therefore there is a factor of 2.5 separating the numerical results and Equation (5.12). The difference between the numerical and analytical investigations has been examined thoroughly. However the source of this discrepancy has not been found. To conclude, the method described has the potential of providing important diagnostics for the magnetosphere.

5.6 Summary of Results

We have considered a magnetospheric cavity with a two-dimensional profile in Alfvén speed. The cavity has been driven with a non-monochromatic source. Detailed numerical results show that the magnetospheric cavity filters the random signal, and excites only the fast magnetoacoustic modes whose eigenfrequencies lie within the driving spectrum.

These fast modes may also couple to the Alfvén mode, provided $k_y \neq 0$ and their eigenfrequencies lie within the Alfvén continuum. We have shown that the Alfvén mode eigenfunction and the position of the resonant field lines can be calculated to high accuracy by taking the frequency of the driver to be monochromatic.

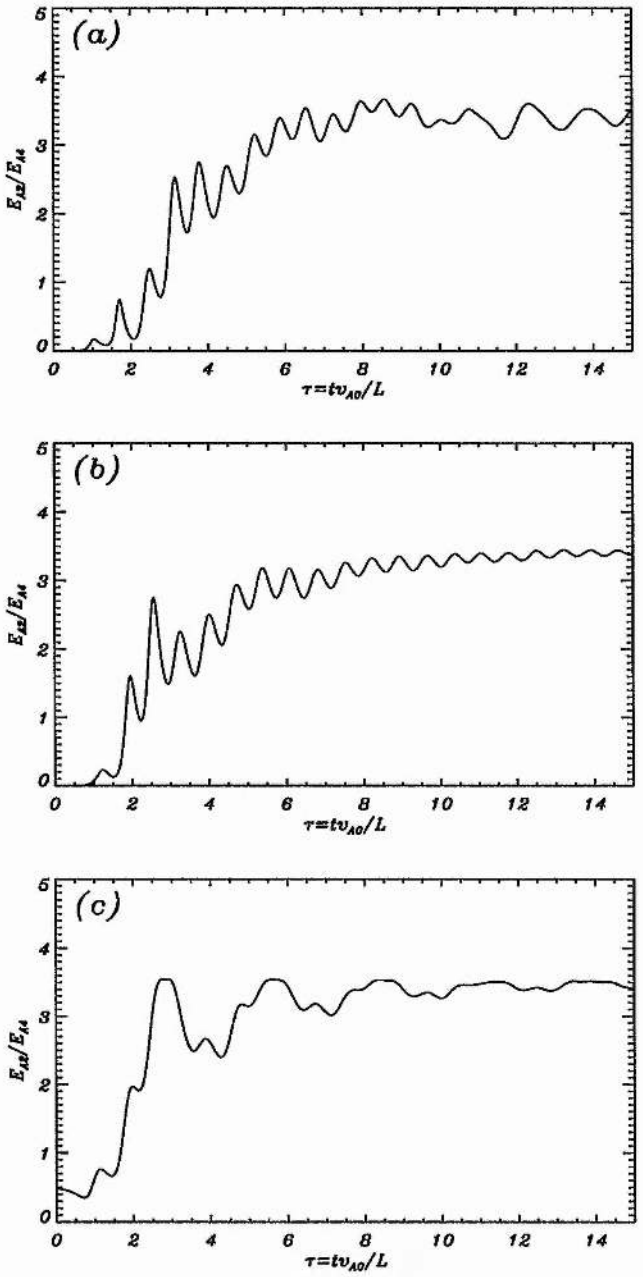

Figure 5.9: The energy ratio of the the Alfvén mode in the two resonant field lines at x_{r2} and x_{r4}. The ratio of the energy of the second harmonic to the fourth harmonic is plotted as a function of the Alfvén transit time. In (a) we use $k_y L = 0.1$ with a random driver. In (b) the same value of $k_y L$ as in (a) is used with a monochromatic driver (constant frequency). In (c) we use u_x obtained from the eigenvalue code (Chapter 2) as the initial condition, again setting $k_y L = 0.1$. In all three cases the energy ratio approaches the same constant value. The energy ratio is therefore independent of the nature of the driving source and depends only on the equilibrium of the cavity.

We have undertaken a preliminary investigation into the seismology of the magnetosphere. The examination of the ratio of energy density in the two resonant field lines potentially offers important seismic information. This ratio tends to a constant value which depends only on the equilibrium and not on the nature of the driving source. An unresolved discrepancy exists between the numerical and analytical results. However, we expect the seismology technique to prove an important diagnostic tool in future studies.

Chapter 6

The Structure of Three-Dimensional Neutral Points

6.1 Introduction

One of the most puzzling aspects of the Sun is the presence of the hot corona. The corona has a temperature of several million degrees kelvin, two orders of magnitude greater than the temperature in the photosphere. Various heating mechanisms have been proposed and comprehensive reviews may be found in Ulmschneider and Narain (1990, 1996), Browning (1991) and Laing (1996). These mechanisms may be broadly classified into two groups, wave heating and reconnection of the magnetic field. In the previous chapters we have concentrated on the guiding of magnetoacoustic waves in the solar corona. In this region of the solar atmosphere we have shown that a wide variety of magnetoacoustic waves may be supported. The damping of these waves may contribute to the heating of the corona. For example the numerical investigation of wave propagation in current sheets by Tirry, Čadež and Goossens (1997) has shown that, through the Alfvén resonance, wave damping may occur. The dissipation of magnetoacoustic waves in coronal loops has also been suggested as a possible source of coronal heating (see, for example, Laing 1996). In this chapter, we turn our attention to heating the corona by the process of magnetic reconnection.

Magnetic reconnection involves the topological change of the magnetic field and the subsequent release of energy. Reconnection plays a central role in many phenomena that occur both in laboratory and astrophysical plasmas. In particular, on the Sun, we expect reconnection to be important in coronal heating, solar flares, X-ray bright points and in the formation of prominences. Over the last twenty years many aspects of two-dimensional reconnection have been extensively studied (see the review by Priest 1997). In two-dimensional reconnection the important regions are those where the magnetic field locally vanishes ($\mathbf{B} = 0$); these are called *neutral points*. The X-type and O-type two-dimensional configurations are well known. Recently the more complex nature of

three-dimensional reconnection has been investigated.

In three dimensions reconnection can occur with or without null points. For example, reconnection in quasi-separatrix layers without neutral points has been proposed by Priest and Démoulin (1995). However analytical studies by Lau and Finn (1990) and Priest and Titov (1996) and also numerical investigations by Galsgaard and Nordlund (1996), have shown the importance of neutral points in three-dimensional reconnection. In this chapter we study three-dimensional neutral points in detail by considering the local magnetic topology occurring around these important regions. This is an important first step in understanding how reconnection may occur in three dimensions.

To find the local magnetic structure about a neutral point we consider the magnetic field in the neighbourhood of a point where the field $\mathbf{B}$ vanishes ($\mathbf{B}$=0). Since the magnetic field is a solution of Maxwell's equations it is reasonable to assume that $\mathbf{B}$ is differentiable, and therefore can be expanded in a Taylor series. If, without loss of generality, we take the neutral point to be situated at the origin and assume that the magnetic field approaches zero linearly, the magnetic field $\mathbf{B}$ near a neutral point may be expressed to lowest order by

$$\mathbf{B} = \mathbf{M}.\mathbf{r} \, . \tag{6.1}$$

Here $\mathbf{M}$ is a matrix with elements $M_{ij} = \partial B_i / \partial x_j$ and $\mathbf{r}$ is the position vector $(x, y, z)^T$. The matrix $\mathbf{M}$ is studied in detail, firstly in two dimensions (Section 6.2) as a preliminary to the three-dimensional work. In Section 6.3 the matrix $\mathbf{M}$ is reduced to its simplest three-dimensional form, and the theory used in calculating the magnetic field configurations is also discussed. Sections 6.4 and 6.5 discuss the potential and non-potential three-dimensional configurations respectively. In Section 6.6 brief consideration is given to the evolution between different neutral point configurations. Section 6.7 discusses recent developments of this work, and finally, in Section 6.8, we conclude this chapter by summarising our results.

6.2 Review of Two-Dimensional Neutral Points

In two dimensions the matrix $\mathbf{M}$, which determines the local magnetic field topology surrounding a neutral point, is given by

$$\mathbf{M} = \begin{bmatrix} a_{11} & a_{12} \\ a_{21} & a_{22} \end{bmatrix} \tag{6.2}$$

where a_{ij} is a *real* constant. The solenoidal constraint $\nabla \cdot \mathbf{B} = 0$ gives $a_{11} = -a_{22}$ and therefore the trace of $\mathbf{M}$ (the sum of the diagonal entries) is zero. With $\mathbf{r} = (X, Y)^T$ the magnetic field may be written in the form

$$\mathbf{B} = (a_{11}X + a_{12}Y, a_{21}X - a_{11}Y) \, . \tag{6.3}$$

The diagonal entries in the matrix are associated with the potential field, so we define $a_{11} = p$. Since the current associated with the neutral point is

$$\mathbf{J} = \frac{1}{\mu_0}(0, 0, a_{21} - a_{12}) \ , \tag{6.4}$$

we may define

$$a_{12} = \frac{1}{2}(q - j_z) \qquad \text{and} \qquad a_{21} = \frac{1}{2}(q + j_z) \ . \tag{6.5}$$

For a current-free (potential) neutral point we have $a_{21} = a_{12} = q/2$. Therefore the parameter q is also associated with the potential field. The magnitude of the current perpendicular to the plane of the null point is given by j_z. The matrix $\mathbf{M}$ may then be written in the form

$$\mathbf{M} = \begin{bmatrix} p & \frac{1}{2}(q - j_z) \\ \frac{1}{2}(q + j_z) & -p \end{bmatrix} \ , \tag{6.6}$$

with the magnetic field given by

$$\mathbf{B} = \left(px + \frac{1}{2}(q - j_z)\, y, \frac{1}{2}(q + j_z)\, x - py \right) \ , \tag{6.7}$$

which satisfies the solenoidal constraint $\nabla \cdot \mathbf{B} = 0$. It proves useful to define a threshold current j_{thresh}, where

$$j_{thresh} = \sqrt{4p^2 + q^2} \ . \tag{6.8}$$

The threshold current only depends on the parameters associated with the potential configurations (p and q).

We now calculate the magnetic flux function A, satisfying

$$B_x = \frac{\partial A}{\partial Y} \qquad \text{and} \qquad B_y = -\frac{\partial A}{\partial X} \ , \tag{6.9}$$

so that $\mathbf{B} = \nabla A \times \hat{\mathbf{e}}_z$. The flux function (which is constant along each field line) is given by

$$A = \frac{1}{4}\left[(q - j_z)\, Y^2 - (q + j_z)\, X^2\right] + pXY \ . \tag{6.10}$$

Here B_x and B_y are the magnetic field components and $\hat{\mathbf{e}}_z$ is a unit vector perpendicular to the plane of the null point. If we now rotate the XY-axes through an angle θ to give xy-axes, using the relations

$$X = x\cos\theta - y\sin\theta \ , \tag{6.11}$$

$$Y = x\sin\theta + y\cos\theta \tag{6.12}$$

in Equation (6.10), we find the flux function becomes

$$A = \frac{1}{4}\left((j_{thresh} - j_z)\, y^2 - (j_{thresh} + j_z)\, x^2\right) \ . \tag{6.13}$$

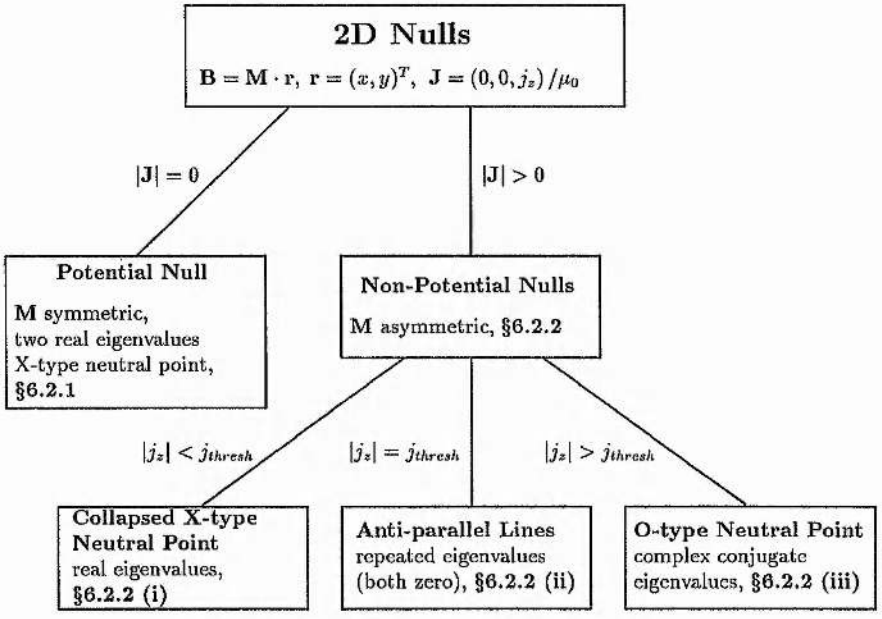

Figure 6.1: Diagram showing the different types of two-dimensional nulls and the relative sizes of j_z (the z-component of current) and j_{thresh} (the threshold current) at which they occur.

Here we have used trigonometric identities and set $\tan 2\theta = -2\,p/q$.

From Equation (6.13) we see that in two dimensions, two parameters j_{thresh} and j_z, govern the local magnetic field configuration about the two-dimensional null point. The nature of the magnetic field is therefore determined by the eigenvalues of the matrix $\mathbf{M}$, which are given by

$$\lambda = \pm\frac{1}{2}\sqrt{j_{thresh}^2 - j_z^2}\ . \tag{6.14}$$

Therefore, depending on whether the current j_z is greater or less than the threshold current (j_{thresh}), the eigenvalues will be real or imaginary, and the magnetic field configuration will vary accordingly.

In the following sub-sections the magnetic field configuration about a two-dimensional null is studied, initially depending on whether it is potential (Section 6.2.1) or non-potential (Section 6.2.2). The non-potential case is sub-divided into cases where the current j_z is less than (Section 6.2.2 (i)), equal to (Section 6.2.2 (ii)), or greater than (Section 6.2.2 (iii)) the threshold current. Figure 6.1 shows the format of this section, summarising the important details of the matrix $\mathbf{M}$, along with the type of neutral point that arises given the nature of the eigenvalues.

6.2.1 Potential Two-Dimensional Neutral Points

In the case of a current-free (potential) two-dimensional null the eigenvalues are given by

$$\lambda = \pm\frac{1}{2}j_{thresh}\ . \tag{6.15}$$

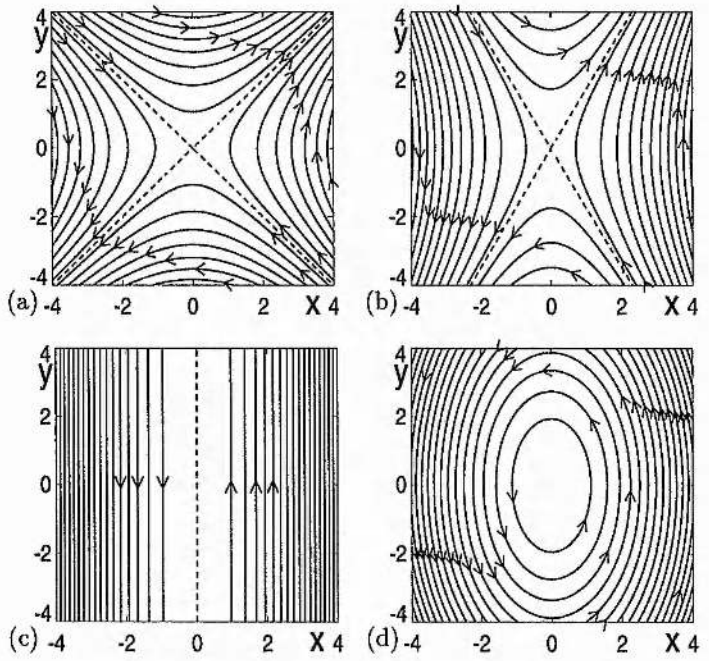

Figure 6.2: The possible two-dimensional magnetic fields surrounding a neutral point situated at the origin ($x = y = 0$). In (a) we have an X-type potential null ($j_z = 0$), whereas in (b) a non-potential ($j_z \neq 0$) X-type null is shown. In (a) and (b) there are two distinct real eigenvalues of the matrix **M**. In (c) we have anti-parallel field lines since both eigenvalues of the matrix are zero. A null line lies along $x = 0$. In (d) the eigenvalues are complex conjugates with the magnetic field consisting of elliptical field lines.

Therefore we have two real, non-zero eigenvalues which are equal in magnitude but opposite in sign. The equation for the flux function (Equation 6.13) consequently becomes

$$A = \frac{j_{thresh}}{4}\left(y^2 - x^2\right) \ . \tag{6.16}$$

The field lines are therefore rectangular hyperbolae (the separatrices intersect at an angle of $\pi/2$). This is an *X-type neutral point* as illustrated in Figure 6.2a. This is the only possible configuration for a potential two-dimensional neutral point.

6.2.2 Non-Potential Two-Dimensional Neutral Points

The non-potential two-dimensional configurations around neutral points are classified with respect to the magnitude of the current perpendicular to the plane of the null point (j_z) and the threshold current (j_{thresh}).

(i) $|j_z| < j_{thresh}$

When $|j_z| < j_{thresh}$ the eigenvalues are real and equal in magnitude, but opposite in sign, and are given by

$$\lambda = \pm \frac{j_{thresh}}{2} . \tag{6.17}$$

From the flux function (Equation 6.13) we see that the field lines are hyperbolae with separatrices that intersect at an angle of

$$2 \tan^{-1} \left(\frac{j_{thresh} + j_z}{j_{thresh} - j_z} \right) . \tag{6.18}$$

The null point formed is therefore a collapsed X-type neutral point as shown in Figure 6.2b. As the current approaches zero the hyperbolae tend to rectangular hyperbolae, reducing to the potential case ($j_z \rightarrow 0$). As the current increases the angle of the separatrices increases.

(ii) $|j_z| = j_{thresh}$

When the perpendicular current equals the threshold current the two eigenvalues are equal, and from Equation (6.14) they are zero ($\lambda = 0$). The flux function $A(x, y)$ reduces so that it depends only on x^2 if $j_{thresh} = j_z$, or y^2 if $j_{thresh} = -j_z$; the magnetic configuration consists of anti-parallel field lines with a null line along the y-axis or x-axis respectively (Figure 6.2c). Notice that this configuration is similar to the current sheet equilibrium in Chapters 3 and 4, where we investigated the guiding of magnetoacoustic waves in these structures.

(iii) $|j_z| > j_{thresh}$

If $|j_z| > j_{thresh}$ the eigenvalues are complex conjugates given by

$$\lambda = \pm \frac{i}{2} \sqrt{j_z^2 - j_{thresh}^2} . \tag{6.19}$$

When $j_{thresh} = 0$ ($p = q = 0$) we find from the flux function (Equation 6.13) that the topology consists of circular magnetic field lines centred around the origin, whereas if $j_{thresh} \neq 0$ the field lines are elliptical (Figure 6.2d).

6.3 Theory of Three-Dimensional Neutral Points

6.3.1 Terminology and Review of Matrix Theory

Having seen the magnetic field configurations about a two-dimensional null point we now consider the possible three-dimensional magnetic structures. Figure 6.3a shows a three-dimensional neutral point formed by a field due to four point sources, two positive and two negative (Parnell, Priest and Golub 1994). If we look closely at the local structure about this null (Figure 6.3b) we

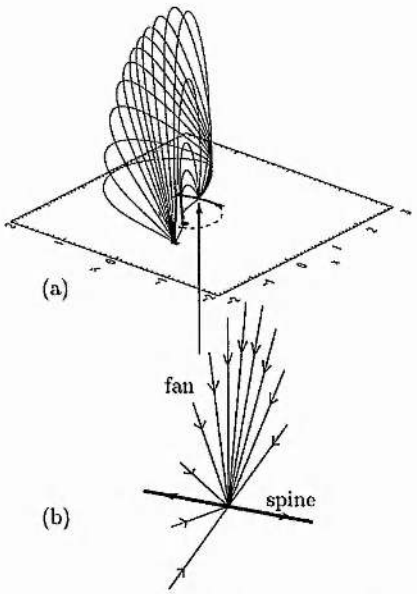

Figure 6.3: (a) A three-dimensional potential magnetic field configuration showing the global magnetic field due to four point sources (shown by asterisks). The diagram is taken from Parnell, Priest and Golub (1994). Two neutral points exist in the $z = 0$ plane. In (b) a schematic enlargement of the local region about one neutral point in (a) is depicted, showing the spine curve (thick solid line) and fan plane (fainter solid line).

find that there are many field lines heading into the neutral point forming a surface (the *fan plane*), but only two field lines leaving the null point (the *spine*). The fan plane and the spine are the two fundamental components (the "skeleton") that make up a neutral point in three dimensions (Priest and Titov 1996).

The fan is a surface made up of field lines which leave, or enter, the null point (Priest and Titov 1996). This plane is the same as Lau and Finn's $\sum$ surface (Lau and Finn 1990). The spine is made up of two field lines that are directed away from the null if the field lines in the fan are directed towards the null and vice-versa (Priest and Titov 1996). These lines are equivalent to Lau and Finn's γ line. Field lines that lie near the null point but do not pass through it form bundles around the spine. These spread out above and below the fan surface.

Mathematically, the linearised magnetic field about a three-dimensional neutral point may be described using Equation (6.1) with a matrix of the form

$$\mathbf{M} = \begin{bmatrix} a_{11} & a_{12} & a_{13} \\ a_{21} & a_{22} & a_{23} \\ a_{31} & a_{32} & a_{33} \end{bmatrix}, \tag{6.20}$$

where a_{ij} is a real constant. The constraint $\nabla \cdot \mathbf{B} = 0$ implies that the trace of $\mathbf{M}$ must be zero,

giving

$$a_{11} + a_{22} + a_{33} = 0 \,. \tag{6.21}$$

This condition also implies that the eigenvalues λ_1, λ_2 and λ_3 associated with the matrix sum to zero. The eigenvectors associated with these eigenvalues are given by $\mathbf{x}_1, \mathbf{x}_2$ and $\mathbf{x}_3$ respectively.

We now give some important results from matrix theory, applying these in our investigation into the three-dimensional magnetic structures surrounding neutral points. The theory is comprehensively discussed by Boyce and DiPrima (1969).

We may write the magnetic field near the neutral point in terms of a position vector $\mathbf{r} = (x, y, z)^T$, where

$$\frac{\mathrm{d}\mathbf{r}(k)}{\mathrm{d}k} = \mathbf{M}.\mathbf{r}(k) = \mathbf{B} \,. \tag{6.22}$$

The position vector is dependent upon an arbitrary parameter k; $\mathbf{r} = \mathbf{r}(k)$.

To find the local three-dimensional magnetic topologies surrounding the neutral point, we solve the homogeneous linear system of equations (Equation 6.22) for a constant matrix $\mathbf{M}$. The nature of the eigenvalues (and corresponding eigenvectors) of the matrix $\mathbf{M}$ determine the nature of the solution to Equation (6.22). There are three possibilities to consider.

(i) All eigenvalues are real and distinct

We begin by examining the case when all three eigenvalues are real and distinct. Therefore in order to solve Equation (6.22) we search for a solution of the form

$$\mathbf{r} = \mathbf{x}\mathrm{e}^{\lambda k} \,, \tag{6.23}$$

where λ is an eigenvalue and $\mathbf{x}$ is a eigenvector, both of which are to be determined. Substituting Equation (6.23) into Equation (6.22) yields

$$(\mathbf{M} - \lambda\mathbf{I})\,\mathbf{x} = 0 \,, \tag{6.24}$$

where $\mathbf{I}$ is the 3×3 identity matrix. Equation (6.24) determines the eigenvectors $\mathbf{x}$ and eigenvalues λ of the matrix $\mathbf{M}$. The vector $\mathbf{r}$, determined by Equation (6.23) is a solution of Equation (6.22), provided λ is an eigenvalue and $\mathbf{x}$ is an eigenvector of $\mathbf{M}$. The eigenvalues λ_1 , λ_2, and λ_3 are given by the roots of the characteristic equation

$$\det|\mathbf{M} - \lambda\mathbf{I}| = 0 \,. \tag{6.25}$$

When all the eigenvectors $\mathbf{x}_i$ associated with each eigenvalue λ_i are real and distinct there exists a linearly independent real eigenvector for each eigenvalue. Therefore the equations of the magnetic field lines are given by

$$\mathbf{r}(k) = A\mathrm{e}^{\lambda_1 k}\mathbf{x}_1 + B\mathrm{e}^{\lambda_2 k}\mathbf{x}_2 + C\mathrm{e}^{\lambda_3 k}\mathbf{x}_3 \,, \tag{6.26}$$

where A, B and C are constant along a magnetic field line. Each field line may therefore be written in terms of the eigenvalues and eigenvectors of the matrix $\mathbf{M}$.

There is always one eigenvalue of opposite sign to the other two, say $\lambda_1, \lambda_2 > 0$ and $\lambda_3 < 0$, since the sum of the three eigenvalues is zero. If we follow a field line towards the neutral point, that is let $k \to -\infty$ in Equation (6.26), we find

$$\mathbf{r}(k) \to C\mathrm{e}^{\lambda_3 k}\mathbf{x}_3 . \tag{6.27}$$

All the field lines that head towards the null lie parallel to the eigenvector $\mathbf{x}_3$. Moving forward along the field lines from the null ($k \to \infty$) we find

$$\mathbf{r}(k) \to A\mathrm{e}^{\lambda_1 k}\mathbf{x}_1 + B\mathrm{e}^{\lambda_2 k}\mathbf{x}_2 . \tag{6.28}$$

Therefore the field lines that leave the null point lie in the plane defined by the eigenvectors $\mathbf{x}_1$ and $\mathbf{x}_2$. Now, comparing this with our geometrical knowledge of a three-dimensional null, we find that the eigenvector $\mathbf{x}_3$ (with eigenvalue λ_3) defines the location of the spine. The fan plane is defined by the eigenvectors $\mathbf{x}_1$ and $\mathbf{x}_2$ (with eigenvalues λ_1 and λ_2 respectively). In addition, we travelled backwards ($k \to -\infty$) along the field lines when $\lambda_3 < 0$. In this case we find that the magnetic field of the spine is directed towards the null, whereas the field lines in the fan emanate radially outwards from the null and are associated with positive eigenvalues.

(ii) Two of the eigenvalues are equal

When two of the eigenvalues are equal it may not be possible to find a linearly independent eigenvector for each eigenvalue. Therefore, in this case, we need to calculate an additional basis vector. This situation is analogous to that of finding solutions of a nth order linear differential equation with constant coefficients. In this case a repeated root of the characteristic equation gives rise to solutions of the form $\mathrm{e}^{\lambda k}$, $k\mathrm{e}^{\lambda k}$ and so on. Suppose that λ is the repeated eigenvalue of the matrix $\mathbf{M}$ with only one linearly independent eigenvector $\mathbf{x}_1$. One solution of Equation (6.22) is given by

$$\mathbf{r} = \mathbf{x}_1\mathrm{e}^{\lambda k} , \tag{6.29}$$

where $\mathbf{x}_1$ satisfies Equation (6.24). The additional basis vector is found to be

$$\mathbf{r}(k) = \mathbf{x}_1 k\mathrm{e}^{\lambda k} + \mathbf{x}_2^*\mathrm{e}^{\lambda k} . \tag{6.30}$$

In this case the associated vectors of the matrix $\mathbf{M}$ are determined by (see, for example, Boyce and DiPrima 1969)

$$\mathbf{M}\mathbf{x}_1 = \lambda\mathbf{x}_1 , \tag{6.31}$$

$$\mathbf{M}\mathbf{x}_2^* = \mathbf{x}_1 + \lambda\mathbf{x}_2^* , \tag{6.32}$$

$$\mathbf{M}\mathbf{x}_3 = -2\lambda\mathbf{x}_3 . \tag{6.33}$$

Therefore upon determining the eigenvector $\mathbf{x}_1$, the basis vector $\mathbf{x}_2^*$ can be calculated. The equation of a field line is given by

$$\mathbf{r}(k) = (A + Bk)\,\mathrm{e}^{\lambda k}\mathbf{x}_1 + B\mathrm{e}^{\lambda k}\mathbf{x}_2^* + C\mathrm{e}^{-2\lambda k}\mathbf{x}_3 \,, \tag{6.34}$$

where A, B and C are all constant along each field line. Taking $\lambda > 0$ and traversing forwards along a field line ($k \to \infty$) we find that

$$\mathbf{r}(k) \to (A + Bk)\,\mathrm{e}^{\lambda k}\mathbf{x}_1 + B\mathrm{e}^{\lambda k}\mathbf{x}_2^* \,. \tag{6.35}$$

The field lines that leave the null point lie in planes defined by $\mathbf{x}_1$ and $\mathbf{x}_2^*$. If, however, we trace backwards along a field line ($k \to -\infty$) then

$$\mathbf{r}(k) \to C\mathrm{e}^{-2\lambda k}\mathbf{x}_3 \,, \tag{6.36}$$

in which case the field lines are parallel to the eigenvector $\mathbf{x}_3$. This corresponds to the spine curve. We find that the fan plane is defined by the vectors which correspond to the repeated eigenvalues. One of these vectors is an eigenvector ($\mathbf{x}_1$), whilst the other ($\mathbf{x}_2^*$) is not. The spine lies in the direction of $\mathbf{x}_3$.

(iii) Two of the eigenvalues occur as a conjugate pair

Finally we discuss the case when two of the eigenvalues (and therefore eigenvectors) are complex. Once again we look for a solution of the form given by Equation (6.23). The complex eigenvalues occur as a conjugate pair since the coefficients of the matrix $\mathbf{M}$ are real. In the situation where we have one real and two complex eigenvalues, say -2η and $\eta \pm i\nu$, the equation of a field line is given by

$$\mathbf{r}(k) = \frac{1}{2}(A + iB)\,\mathrm{e}^{(\eta+i\nu)k}\mathbf{x}_1 + \frac{1}{2}(A - iB)\,\mathrm{e}^{(\eta-i\nu)k}\mathbf{x}_2 + C\mathrm{e}^{-2\eta k}\mathbf{x}_3 \,, \tag{6.37}$$

where A, B and C are all constant along each field line.

The eigenvectors $\mathbf{x}_1$ and $\mathbf{x}_2$ are also a complex conjugate pair. To obtain the basis vectors of the matrix $\mathbf{M}$ we follow Boyce and DiPrima (1969), and write

$$\mathbf{x}_1 = \mathbf{x}_1' + i\mathbf{x}_2' \,, \quad \mathbf{x}_2 = \mathbf{x}_1' - i\mathbf{x}_2' \,, \tag{6.38}$$

which gives

$$\mathbf{x}_1' = \frac{1}{2}(\mathbf{x}_1 + \mathbf{x}_2) \,, \quad \mathbf{x}_2' = -\frac{i}{2}(\mathbf{x}_1 - \mathbf{x}_2) \,. \tag{6.39}$$

The real basis vectors are given by $\mathbf{x}_1'$ and $\mathbf{x}_2'$. Equation (6.37) may then be written in the form

$$\mathbf{r}(k) = R\mathrm{e}^{\eta k}\cos(\Theta + \nu k)\,\mathbf{x}_1' - R\mathrm{e}^{\eta k}\sin(\Theta + \nu k)\,\mathbf{x}_2' + C\mathrm{e}^{-2\eta k}\mathbf{x}_3 \,, \tag{6.40}$$

where R, Θ and C are constant along each field line. We have defined $A + iB = Re^{i\Theta}$. If we take $\eta > 0$, for example, then as $k \to \infty$ Equation (6.40) reduces to

$$\mathbf{r}(k) \to Re^{\eta k} \cos(\Theta + \nu k)\, \mathbf{x}_1' - Re^{\eta k} \sin(\Theta + \nu k)\, \mathbf{x}_2' \,. \tag{6.41}$$

The fan plane is defined by the basis vectors $\mathbf{x}_1'$ and $\mathbf{x}_2'$. An examination of Equation (6.40) shows that field lines in the fan plane will be spirals. The spine lies in the direction of the eigenvector $\mathbf{x}_3$ since as $k \to -\infty$,

$$\mathbf{r}(k) \to Ce^{-2\eta k}\mathbf{x}_3 \,. \tag{6.42}$$

To summarise, for the three cases we have considered the spine lies along the eigenvector of the matrix $\mathbf{M}$ that relates to the eigenvalue whose sign is opposite to that of the real parts of the remaining eigenvalues. The remaining eigenvalues have vectors associated with them which define the fan plane. These vectors may, or may not be, eigenvectors of the matrix $\mathbf{M}$. The vectors which determine the fan plane depend on the nature of the eigenvalues as summarised in Table 6.1.

If the real parts of two of the three eigenvalues are positive, for example $\lambda_1, \lambda_2 > 0\,(\lambda_3 < 0)$, then the neutral point will have field lines that are directed away from the null in the fan. The spine heads into the null along the eigenvector $\mathbf{x}_3$. This type of null is defined as a *positive neutral point.* However, if the real parts of two of the eigenvalues are negative, say $\lambda_1, \lambda_2 < 0\,(\lambda_3 > 0)$, the fan plane will have field lines pointing towards the null, with the spine again lying along the eigenvector $\mathbf{x}_3$ but this time heading away from the null. This type of neutral point is defined as a *negative neutral point* (Priest and Titov 1996).

Neutral points for which field lines in the fan plane approach or emanate from the null in a radial manner are known as *radial nulls*, using the nomenclature of Priest and Titov (1996). If the field lines radiate symmetrically in all directions in the fan plane they are known as *proper nulls*, whereas *improper nulls* are asymmetric. In the latter case the field lines in the fan approach or leave the null aligned preferentially along a line through the null in the fan plane; the *major axis* of the fan. Neutral points with fan plane field lines that approach or leave the neutral point in a spiral are known as *spiral neutral points.*

6.3.2 Reduction of M to its simplest form

In order to examine all the possible configurations of the localised field about the neutral point we reduce the matrix $\mathbf{M}$ to contain the least possible number of free parameters. It is important to remember that the matrix $\mathbf{M}$ determines all the physical characteristics of the magnetic field including, for example, its topology and current. When reducing $\mathbf{M}$ we take this into account, ensuring all the physical properties of the neutral point remain. The matrix $\mathbf{M}$ always has at least one real eigenvalue whose sign is opposite to the real parts of the other two. We therefore choose the local orthogonal coordinate system so that the eigenvector corresponding to this eigenvalue is

Eigenvalues		Associated Vectors
Three real and distinct	-	The eigenvectors $\mathbf{x}_1, \mathbf{x}_2$ and $\mathbf{x}_3$
Two repeated, one distinct	-	The three eigenvectors if they exist or the vectors $\mathbf{x}_1, \mathbf{x}_2^*$ and $\mathbf{x}_3$ which satisfy $\mathbf{M}\mathbf{x}_1 = \lambda\mathbf{x}_1$, $\mathbf{M}\mathbf{x}_2^* = \mathbf{x}_1 + \lambda\mathbf{x}_2^*$ and $\mathbf{M}\mathbf{x}_3 = -2\lambda\mathbf{x}_3$
Two complex conjugate, one real	-	Eigenvectors $\mathbf{x}_1$, $\mathbf{x}_2$ and $\mathbf{x}_3$ give basis vectors $\mathbf{x}_1' = (\mathbf{x}_1 + \mathbf{x}_2)/2$, $\mathbf{x}_2' = -i(\mathbf{x}_1 - \mathbf{x}_2)/2$ and $\mathbf{x}_3$

Table 6.1: Associated vectors that determine the magnetic structure of three-dimensional neutral points.

always aligned in the z-direction, and so consider only cases where the spine is aligned with the z-direction. In addition, the matrix may be reduced further by rotating the xy-plane in such a way that the x-axis lies in the direction of the resultant current in the xy-plane. Finally, by taking a scaling factor from $\mathbf{M}$, the matrix reduces to

$$\mathbf{M} = \begin{bmatrix} 1 & \frac{1}{2}(q - j_\parallel) & 0 \\ \frac{1}{2}(q + j_\parallel) & p & 0 \\ 0 & j_\perp & -(p+1) \end{bmatrix}, \tag{6.43}$$

where $p \geq -1$ and $q^2 \leq j_\parallel^2 + 4p$. The potential part of the configuration is defined by the parameters p and q whilst the current is given by

$$\mathbf{J} = \frac{1}{\mu_0}(j_\perp, 0, j_\parallel) \ . \tag{6.44}$$

Here $j_\parallel$ and $j_\perp$ are the components of current parallel and perpendicular to the spine respectively.

We shall now define a threshold current j_{thresh} which is dependent purely on p and q (the potential field parameters) such that

$$j_{thresh} = \sqrt{(p-1)^2 + q^2} \ . \tag{6.45}$$

The three eigenvalues (λ_1, λ_2 and λ_3) associated with the matrix $\mathbf{M}$ may then be written as

$$\lambda_1 = \frac{p + 1 + \sqrt{j_{thresh}^2 - j_\parallel^2}}{2}, \tag{6.46}$$

$$\lambda_2 = \frac{p + 1 - \sqrt{j_{thresh}^2 - j_\parallel^2}}{2}, \tag{6.47}$$

$$\lambda_3 = -(p+1) \ . \tag{6.48}$$

The constraints $p \geq -1$ and $q^2 \leq j_\parallel^2 + 4p$ ensure that the real parts of λ_1 and λ_2 always have the same sign, whilst λ_3 is of opposite sign. In a similar way to the two-dimensional case, the relative sizes of j_{thresh} and $j_\parallel$ determine the nature of the eigenvalues and consequently the local magnetic configuration around the null point.

When the perpendicular component of current ($j_\perp$) is zero a simple rotation of the matrix $\mathbf{M}$ about the spine (z-axis) reduces it to

$$\mathbf{M} = \begin{bmatrix} 1 & -\frac{1}{2}j_\parallel & 0 \\ \frac{1}{2}j_\parallel & p & 0 \\ 0 & 0 & -(p+1) \end{bmatrix} . \tag{6.49}$$

Therefore throughout this chapter we may assume $q = 0$ in studying configurations where $j_\perp = 0$. Therefore only one potential parameter p is needed to define all the configurations where no component of current exists perpendicular to the spine ($j_\perp = 0$). If a component of perpendicular current exists ($j_\perp \neq 0$) then both potential parameters (p and q) are required. We are excluding the possibility of all the elements of the trace equalling zero since we have taken a scaling factor from the matrix.

6.3.3 Previous Work on Three-Dimensional Neutral Points

We now briefly mention some of the previous work undertaken on three-dimensional neutral points. Cowley (1973) studied a current-free neutral point of the form

$$\mathbf{B} = (\alpha x, \beta y, -(\alpha + \beta)z) , \tag{6.50}$$

where α and β are of the same sign. Here the eigenvalues are α, β and $-(\alpha + \beta)$. Cowley referred to the case $\alpha, \beta > 0$ as Type B, which is a positive radial null point in our nomenclature. Similarly the case $\alpha, \beta < 0$ was referred to as Type A and is a negative radial null point. For $\alpha = \beta$ the neutral point is *proper* (symmetric) whereas for $\alpha \neq \beta$ it is *improper* (asymmetric).

Fukao et al. (1975) studied more general neutral points than Cowley, considering both potential and non-potential configurations. They considered a 3×3 matrix containing 6 parameters. The authors found that when all three eigenvalues are real the null point is radial. When there is one real eigenvalue and two complex conjugate eigenvalues a spiral neutral point arises. They also found that when there is no perpendicular current the spine and fan are perpendicular and the matrix $\mathbf{M}$ is symmetric. Two-dimensional neutral points were also found in special circumstances. These contained either a line of X-points or O-points depending on whether the eigenvalues were real or imaginary respectively.

In this chapter we extend the previous work undertaken by studying the most general form of the matrix $\mathbf{M}$ which defines all the local magnetic field configurations about the null. With our matrix all the magnetic field topologies that can arise are studied using a minimum number of free parameters. Through our study we find that there are extra configurations to those previously reported. In addition, we also explain in detail the effects of the current on the magnetic field.

The structure of this section is illustrated in Figure 6.4. The three-dimensional null point configurations are classified with respect to their current and the eigenvalues of the matrix. In

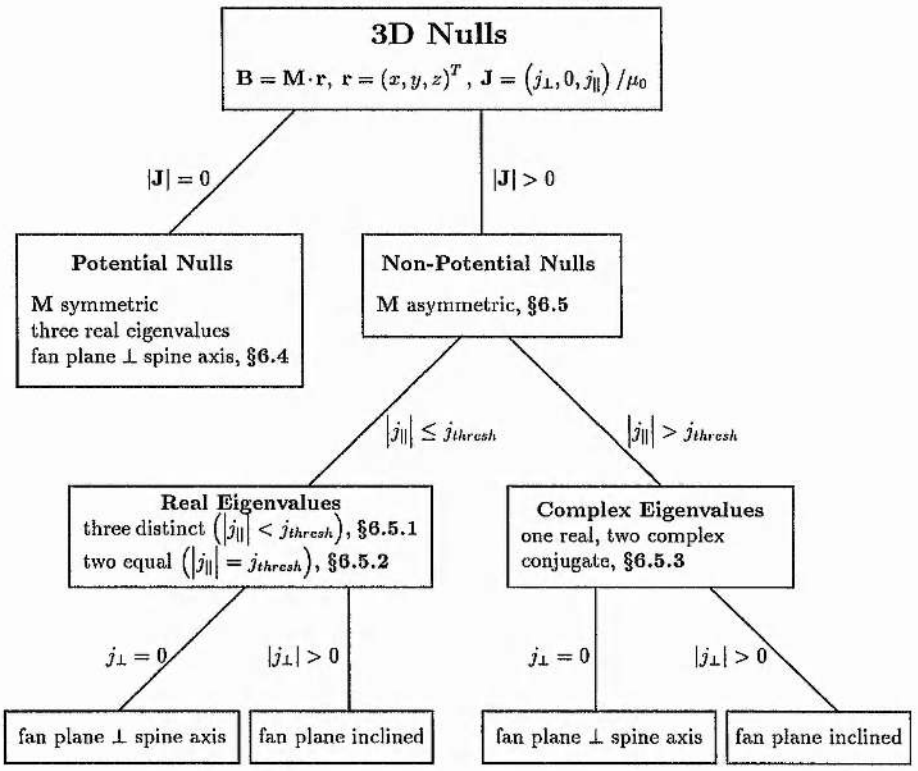

Figure 6.4: Diagram showing the various types of three-dimensional neutral points with respect to the relative sizes of $j_\parallel$ (the component of current parallel to the spine) and j_{thresh} (the threshold current).

Sections 6.4 and 6.5 we investigate the potential and non-potential magnetic field configurations surrounding three-dimensional neutral points.

All the three-dimensional figures are illustrated as follows. The spine is plotted as a solid thick line in the z-direction. The fan plane is shown by the square region enclosed by dashed lines. The fan field lines are depicted by continuous lines. The bundle of field lines around the spine are illustrated by dashed lines and these are only drawn below the fan plane for clarity.

6.4 Three-Dimensional Potential Nulls

The matrix $\mathbf{M}$ representing the linear magnetic field about a potential three-dimensional null may be written in the form

$$\mathbf{M} = \begin{bmatrix} 1 & 0 & 0 \\ 0 & p & 0 \\ 0 & 0 & -(p+1) \end{bmatrix} , \tag{6.51}$$

since we have set both the perpendicular ($j_\perp$) and parallel ($j_\parallel$) components of current to zero. The eigenvalues relating to this matrix are

$$\lambda_1 = 1, \qquad \lambda_2 = p \, , \qquad \lambda_3 = -(p+1) \, . \tag{6.52}$$

We have the constraint that $p \geq 0$ so that the eigenvalue λ_3 (which corresponds to the eigenvector that lies along the z-axis) forms the spine of the neutral point. With $p \geq 0$ λ_1 and λ_2 always have the same sign. The eigenvectors $\mathbf{x}_1$, $\mathbf{x}_2$ and $\mathbf{x}_3$ are given by

$$\mathbf{x}_1 = \begin{pmatrix} 1 \\ 0 \\ 0 \end{pmatrix} , \qquad \mathbf{x}_2 = \begin{pmatrix} 0 \\ 1 \\ 0 \end{pmatrix} , \qquad \mathbf{x}_3 = \begin{pmatrix} 0 \\ 0 \\ 1 \end{pmatrix} . \tag{6.53}$$

As found by Fukao et al. (1975) the fan plane is perpendicular to the spine for a potential magnetic field.

We now consider three situations. We examine the case where all eigenvalues are non-zero and two are equal ($p > 0$, $j_{thresh} = 0$) in Section 6.4.1. Secondly, in Section 6.4.2, the case where one eigenvalue is zero ($p = 0$) is studied, and finally, in Section 6.4.3, we examine the case where all the eigenvalues are non-zero and unequal ($p > 0$, $j_{thresh} > 0$).

6.4.1 $p > 0$, $j_{thresh} = 0$

Assuming $p > 0$ and $j_{thresh} = 0$ means that the only value the parameter p can take is unity. The matrix $\mathbf{M}$ reduces to

$$\mathbf{M} = \begin{bmatrix} 1 & 0 & 0 \\ 0 & 1 & 0 \\ 0 & 0 & -2 \end{bmatrix} , \tag{6.54}$$

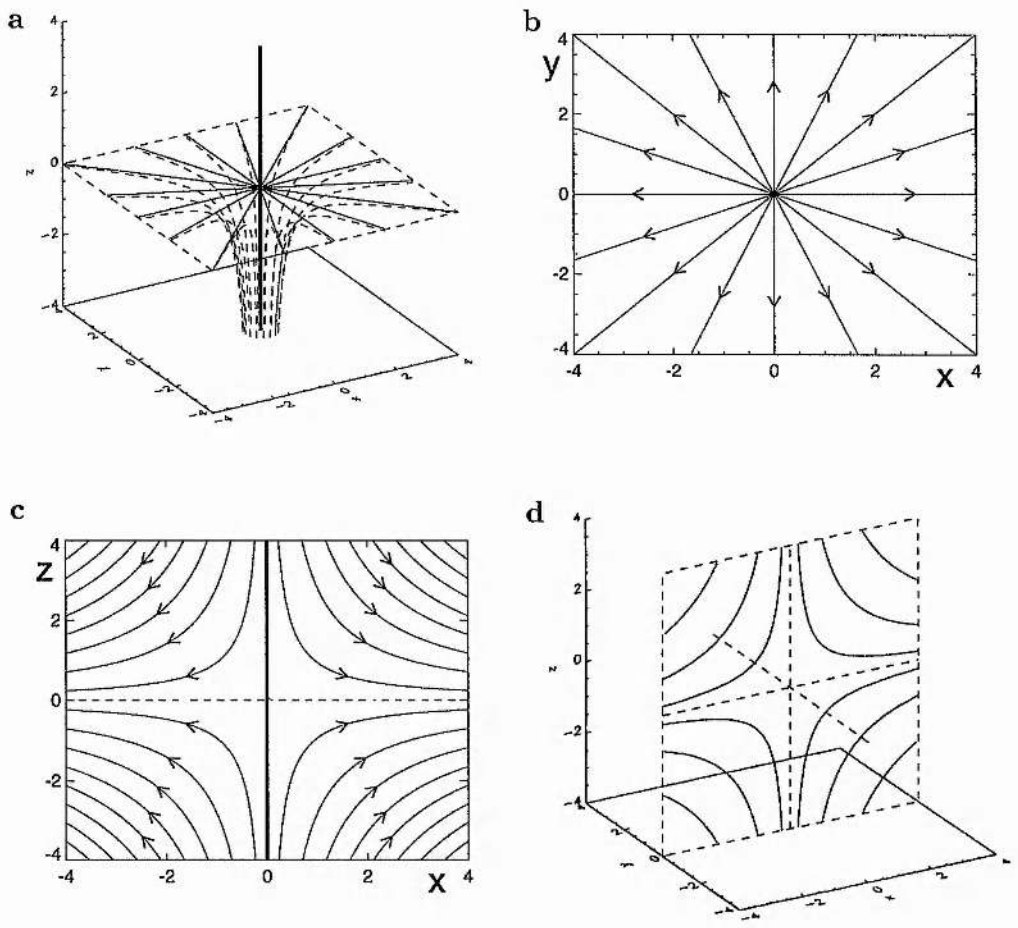

Figure 6.5: The three-dimensional potential proper null ($p = 1$) magnetic field configuration. The three-dimensional structure of the neutral point is shown in (a), whilst in (b) the field lines in the xy-plane (fan plane) are depicted. In (c) the field configuration in the xz-plane is illustrated. When $p = 0$ the three-dimensional field reduces to the two-dimensional X-point field, with a null line along the y-axis as shown in (d).

and the magnetic field is given by $\mathbf{B} = (x, y, -2z)$. We find that two of the eigenvalues are equal. However it is still possible to find the three eigenvectors, given by Equation (6.53). The field associated with this matrix is a positive proper null ($\lambda_1,\ \lambda_2 > 0$) as depicted in Figure 6.5. Since this is the first three-dimensional configuration illustrated in this chapter we draw the full three-dimensional null. This consists of the fan plane, the two spine field lines and also the bundles of field lines approaching the null from below (Figure 6.5a). In Figure 6.5b the field lines in the fan plane (xy-plane) are illustrated and lastly the field lines in the xz-plane are shown (Figure 6.5c).

6.4.2 $p = 0$

When $p = 0$ the matrix $\mathbf{M}$ reduces to

$$\mathbf{M} = \begin{bmatrix} 1 & 0 & 0 \\ 0 & 0 & 0 \\ 0 & 0 & -1 \end{bmatrix}, \tag{6.55}$$

and one of the eigenvalues is zero. The field reduces to a two-dimensional configuration consisting of potential X-points lying in successive xz-planes. A null line is formed along the y-axis (Figure 6.5d). If a scaling factor had not been taken from the matrix the only extra possible field line configuration is the trivial $\mathbf{B} = 0$.

6.4.3 $p > 0,\ j_{thresh} > 0$

All three eigenvalues are non-zero and unequal when $p > 0$ and $j_{thresh} > 0$. In this case improper radial nulls are formed. The field is aligned predominantly in the direction of the eigenvector corresponding to the eigenvalue which has the greater magnitude of the two associated with the fan plane ($\mathbf{x}_1$ and $\mathbf{x}_2$). The field lines rapidly curve so that they run parallel to the x-axis if $0 < p < 1$ and parallel to the y-axis if $p > 1$ (see Figures 6.6a and 6.6b respectively). This can be shown as follows. Considering Equation (6.26) for a field line we find that as $k \to \infty$,

$$\mathbf{r}(k) \to A\mathrm{e}^{k}\hat{\mathbf{e}}_{\mathbf{x}} + B\mathrm{e}^{pk}\hat{\mathbf{e}}_{\mathbf{y}} . \tag{6.56}$$

Now if $0 < p < 1$ then $r(k \to \infty) \approx A\mathrm{e}^{k}\hat{\mathbf{e}}_{\mathbf{x}}$. Therefore the field lines lie in the xy-plane and are aligned along the major axis $y = 0$ (Figure 6.6a). However if $p > 1$ then $r(k \to \infty) \approx B\mathrm{e}^{pk}\hat{\mathbf{e}}_{\mathbf{y}}$ and the major axis of the improper null is the $x = 0$ line (Figure 6.6b).

6.5 Three-Dimensional Non-Potential Nulls

Having considered the possible potential magnetic configurations about a three-dimensional neutral point, we now investigate the non-potential fields that may arise. The matrix $\mathbf{M}$ is now

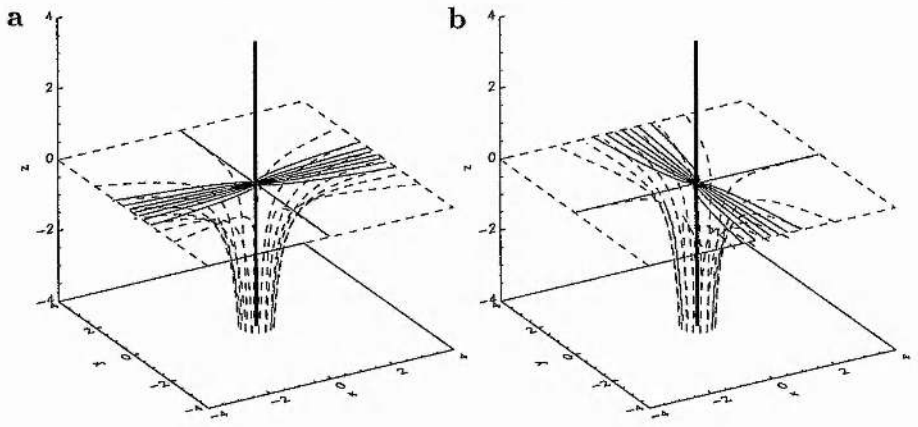

Figure 6.6: The improper (asymmetric) potential null three-dimensional magnetic field configurations ($p \neq 1$) surrounding null points. (a) shows the case when $p < 1$, whilst in (b) we have $p > 1$; the field lines in the fan plane are predominately aligned along the x-axis and y-axis respectively. Specifically, we have used values of $p = 0.5$ and $p = 2$ in (a) and (b) respectively.

asymmetric. The current associated with the field is $\mathbf{J} = (j_\perp, 0, j_\parallel)$, while the eigenvalues of the matrix $\mathbf{M}$ are

$$\lambda_{1,2} = \frac{1}{2}(p+1) \pm \frac{1}{2}\sqrt{j_{thresh}^2 - j_\parallel^2}\,, \tag{6.57}$$

$$\lambda_3 = -(p+1)\,, \tag{6.58}$$

where $p \geq -1$, $(p+1)^2 > j_{thresh}^2 - j_\parallel^2$ and $j_{thresh}^2 = (p-1)^2 + q^2$ as previously defined. These constraints are necessary to ensure that the eigenvalue λ_3 always corresponds to the eigenvector along the spine (i.e. λ_3 has opposite sign to the real parts of λ_1 and λ_2).

6.5.1 $|j_\parallel| < j_{thresh}$

First we investigate the case where the magnitude of the parallel component of current is less than the threshold current. All three eigenvalues are real and distinct, and in addition all three eigenvectors are linearly independent. We now examine the possible field configurations by investigating the effects of (i) the parallel component of current, (ii) the perpendicular component of current and (iii) both components of current.

(i) $j_\perp = 0$ and $j_\parallel \neq 0$

Initially we consider the case where the perpendicular component of current is zero and the parallel component is non-zero. If $j_\perp = 0$ ($q = 0$) and we take $p > -j_\parallel^2/4$ the eigenvectors are

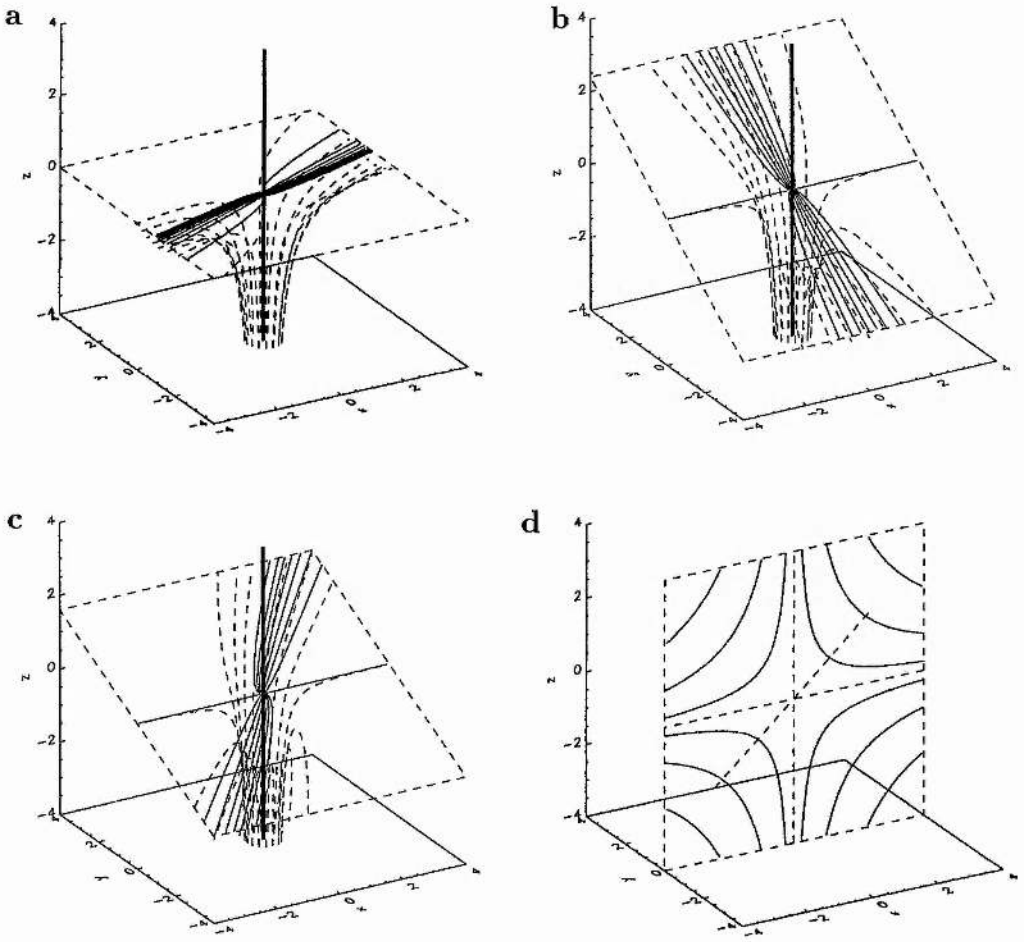

Figure 6.7: The three-dimensional non-potential magnetic field configurations where the component of current parallel to the spine is less than the threshold current $(|j_{\|}| < j_{thresh})$. In cases (a) to (c) we take $p > -j_{\|}^2/4$ and the topologies are three-dimensional. In (a) we have $j_{\|} \neq 0$, $j_{\perp} = 0$, (b) $j_{\|} = 0$, $j_{\perp} \neq 0$ and (c) $j_{\|} \neq 0$, $j_{\perp} \neq 0$. Specifically we have taken the values (a) $p = 0.25$, $j_{\|} = 0.5$, $j_{\perp} = 0$, (b) $p = 2$, $j_{\|} = 0$, $j_{\perp} = 3$ and (c) $p = 2$, $j_{\|} = -1$, $j_{\perp} = 2$, $q = 1$. In (d) the three-dimensional configuration reduces to a two-dimensional field when $p = -j_{\|}^2/4$; $p = 0$, $j_{\|} = 0$, $j_{\perp} = -1$.

found to be

$$\mathbf{x}_{1,2} = \begin{pmatrix} 1 \\ \frac{1-p\mp\sqrt{j_{thresh}^2 - j_\parallel^2}}{j_\parallel} \\ 0 \end{pmatrix}, \qquad \mathbf{x}_3 = \begin{pmatrix} 0 \\ 0 \\ 1 \end{pmatrix}, \tag{6.59}$$

with the corresponding eigenvalues given by Equations (6.57) and (6.58). Hence the fan and spine are perpendicular. We find that as $k \to \infty$ the field lines in the plane of the fan become parallel to the line

$$x = \frac{1-p-\sqrt{j_{thresh}^2 - j_\parallel^2}}{j_\parallel}\, y\,, \tag{6.60}$$

so they form positive *skewed* improper nulls (Figure 6.7a). The topology of this null is different from the potential improper null shown in Figure 6.6. The parallel component of current introduces a preferential direction for the field lines. Mathematically this may be shown by considering the equation for a field line in the plane of the fan

$$\mathbf{r}(k) = Ae^{\lambda_1 k}\mathbf{x}_1 + Be^{\lambda_2 k}\mathbf{x}_2\,. \tag{6.61}$$

Since $p > -1$ and $(p+1)^2 > j_{thresh}^2 - j_\parallel^2$ we have $\lambda_1 > \lambda_2$. Therefore as $k \to \infty$ the dominant term is $Ae^{\lambda_1 k}\mathbf{x}_1$, and so the major axis is defined by the eigenvector $\mathbf{x}_1$.

If $p = -j_\parallel^2/4$ the field reduces to a two-dimensional configuration which consists of collapsed X-points lying in planes defined by $y - (j_\parallel/2)\,x = 0$.

(ii) $j_\perp \neq 0$ and $j_\parallel = 0$

We now examine the case when the parallel component of current is zero $(j_\parallel = 0)$ whilst the perpendicular component is non-zero $(j_\perp \neq 0)$. The eigenvalues for $\mathbf{M}$ become in this case

$$\lambda_{1,2} = \frac{1}{2}\left(p+1 \pm j_{thresh}\right), \qquad \lambda_3 = -(p+1)\,, \tag{6.62}$$

where $p \geq -1$ and $p+1 > j_{thresh}$. The eigenvectors in this case are given by

$$\mathbf{x}_{1,2} = \begin{pmatrix} \frac{-3p^2+3+j_{thresh}^2 \pm 2(p+2)j_{thresh}}{2j_\perp\sqrt{j_{thresh}^2-(p-1)^2}} \\ \frac{3+3p\pm j_{thresh}}{2j_\perp} \\ 1 \end{pmatrix}, \qquad \mathbf{x}_3 = \begin{pmatrix} 0 \\ 0 \\ 1 \end{pmatrix}. \tag{6.63}$$

The fan plane is therefore not perpendicular to the spine when the perpendicular component of current is non-zero. The fan plane is defined by

$$2j_\perp\sqrt{j_{thresh}^2 - (p-1)^2}\,x - 4j_\perp(p+2)\,y + \left(9(p+1)^2 - j_{thresh}^2\right)z = 0\,. \tag{6.64}$$

Note that as $j_\perp$ increases the angle between the fan and spine reduces, so that ultimately $(j_\perp \gg 1)$ the spine lies in the fan plane and the configuration reduces to a two-dimensional case. In addition

from Equation (6.64) we find that the fan rotates about the line in the xy-plane,

$$y = \frac{\sqrt{j_{thresh}^2 - (p-1)^2}}{2(p+2)}\, x = \frac{qx}{2(p+2)}\,. \tag{6.65}$$

Therefore if $q = 0$ the fan tilts about the x-axis, but if $q \neq 0$ the fan twists about the line in the xy-plane described by Equation (6.65). This is a positive improper null with the field lines in the fan orientated predominately along the line

$$z = \frac{-3p^2 + 3 + j_{thresh}^2 + 2(p+2)\, j_{thresh}}{2j_\perp \sqrt{j_{thresh}^2 - (p-1)^2}}\, x + \frac{3 + 3p + j_{thresh}}{2j_\perp}\, y\,, \tag{6.66}$$

which is associated with the eigenvalue λ_1 ($> \lambda_2$). The three-dimensional topology is illustrated in Figure 6.7b. The magnetic configuration is similar to that of the improper potential case ($p \neq 1$) as shown in Figure 6.5b, but now the fan and spine are not perpendicular.

We note that when $p = (j_{thresh} - 1)$ the field reduces to a two-dimensional case with X-points lying in planes defined by

$$\sqrt{p}\, x - y = 0\,. \tag{6.67}$$

The two-dimensional case is illustrated in Figure 6.7d for the case $p = 0$.

(iii) $j_\perp \neq 0$ and $j_\parallel \neq 0$

Finally in this section we investigate the situation where both components of current are non-zero. In this case (when $p > -1$ and $(p+1)^2 > j_{thresh}^2 - j_\parallel^2$) the eigenvalues are defined by Equations (6.57) and (6.58) with corresponding eigenvectors

$$\mathbf{x}_{1,2} = \begin{pmatrix} \frac{-3p^2+3+j_{thresh}^2-j_\parallel^2 \pm 2(p+2)\sqrt{j_{thresh}^2-j_\parallel^2}}{2j_\perp\left(\sqrt{j_{thresh}^2-(p-1)^2}+j_\parallel\right)} \\ \frac{3(p+1)\pm\sqrt{j_{thresh}^2-j_\parallel^2}}{2j_\perp} \\ 1 \end{pmatrix}, \quad \mathbf{x}_3 = \begin{pmatrix} 0 \\ 0 \\ 1 \end{pmatrix}. \tag{6.68}$$

The fan and the spine are not perpendicular because the perpendicular component of current is non-zero. The fan lies in the plane defined by

$$2j_\perp \left(\sqrt{j_{thresh}^2 - (p-1)^2} + j_\parallel\right) x - 4j_\perp (p+2)\, y + \left(9(p+1)^2 - j_{thresh}^2 + j_\parallel^2\right) z = 0\,, \tag{6.69}$$

and the magnetic field lines are illustrated in Figure 6.7c. The field lines lying in the fan plane form a positive skewed null whose major axis is in the direction of the vector $\mathbf{x}_1$ ($\lambda_1 > \lambda_2$). The dominant term in the field line equation for the fan is $Ae^{\lambda_1 k}\mathbf{x}_1$.

The magnetic field reduces to a two-dimensional case consisting of inclined collapsed X-points when $(p+1)^2 = j_{thresh}^2 - j_\parallel^2$. These lie in planes defined by

$$2px - \left(\sqrt{j_\parallel^2 + 4p} - j_\parallel\right) y = 0\,. \tag{6.70}$$

6.5.2 $|j_{\parallel}| = j_{thresh}$

We now examine the possible magnetic field configurations that arise when the magnitude of the parallel component of current equals the threshold current. In the case where $|j_{\parallel}| = j_{thresh}$ we find that two of the eigenvalues are equal. Taking $p \geq -1$ the eigenvalues are given by

$$\lambda_{1,2} = \frac{p+1}{2}, \qquad \lambda_3 = -(p+1) \ . \tag{6.71}$$

We again sub-divide this section by investigating the effects of the two components of current individually and then together.

(i) $j_{\perp} = 0$ and $j_{\parallel} \neq 0$

If $p \geq -1$, $p \neq 1$ and $|j_{\parallel}| = j_{thresh} \neq 0$ we find that the two equal eigenvalues only have one associated eigenvector. To define the plane of the fan we must therefore calculate an additional basis vector $\mathbf{x}_2{}^*$. This is found by solving

$$\mathbf{M}\mathbf{x}_2^* = \mathbf{x}_1 + \lambda \mathbf{x}_2^* \ , \tag{6.72}$$

where λ is the repeated eigenvalue and $\mathbf{x}_1$ is the eigenvector corresponding to this eigenvalue.

Since the perpendicular current is zero we may assume $q = 0$. The vectors which define the fan plane and spine of the null point are therefore calculated to be $(p > -1)$

$$\mathbf{x}_1 = \begin{pmatrix} \frac{1-p}{j_{\parallel}} \\ 1 \\ 0 \end{pmatrix}, \quad \mathbf{x}_2^* = \begin{pmatrix} \frac{3-p}{j_{\parallel}} \\ 1 \\ 0 \end{pmatrix}, \quad \mathbf{x}_3 = \begin{pmatrix} 0 \\ 0 \\ 1 \end{pmatrix} . \tag{6.73}$$

The fan plane is perpendicular to the spine since $j_{\perp} = 0$. In the fan plane there are both straight and curved field lines. The neutral point is therefore a positive *critical spiral* null whose fan field lines gather around the line directed along the eigenvector $\mathbf{x}_1$ (Figure 6.8a). This can be illustrated by considering the equation for a field line in the fan plane,

$$\mathbf{r}(k) = (A + Bk)\, \mathrm{e}^{\lambda k}\mathbf{x}_1 + B\mathrm{e}^{\lambda k}\mathbf{x}_2^* \ . \tag{6.74}$$

The dominant term is $Bk\mathrm{e}^{\lambda k}\mathbf{x}_1$ as $k \to \infty$. This configuration is intermediate between the improper null (Figure 6.6a) and the spiral null (Figure 6.9a). It is important to note that $\mathbf{x}_2^*$ is not an eigenvector.

If $p = -1$ then the neutral point reduces to a two-dimensional non-potential null with anti-parallel field lines (Figure 6.8d).

(ii) $j_{\perp} \neq 0$ and $j_{\parallel} = 0$

If the component of the current parallel to the spine is zero ($j_{\parallel} = j_{thresh} = 0$) then we must have $p = 1$ and $q = 0$ for the spine to be aligned along the z-axis. The eigenvalues are therefore

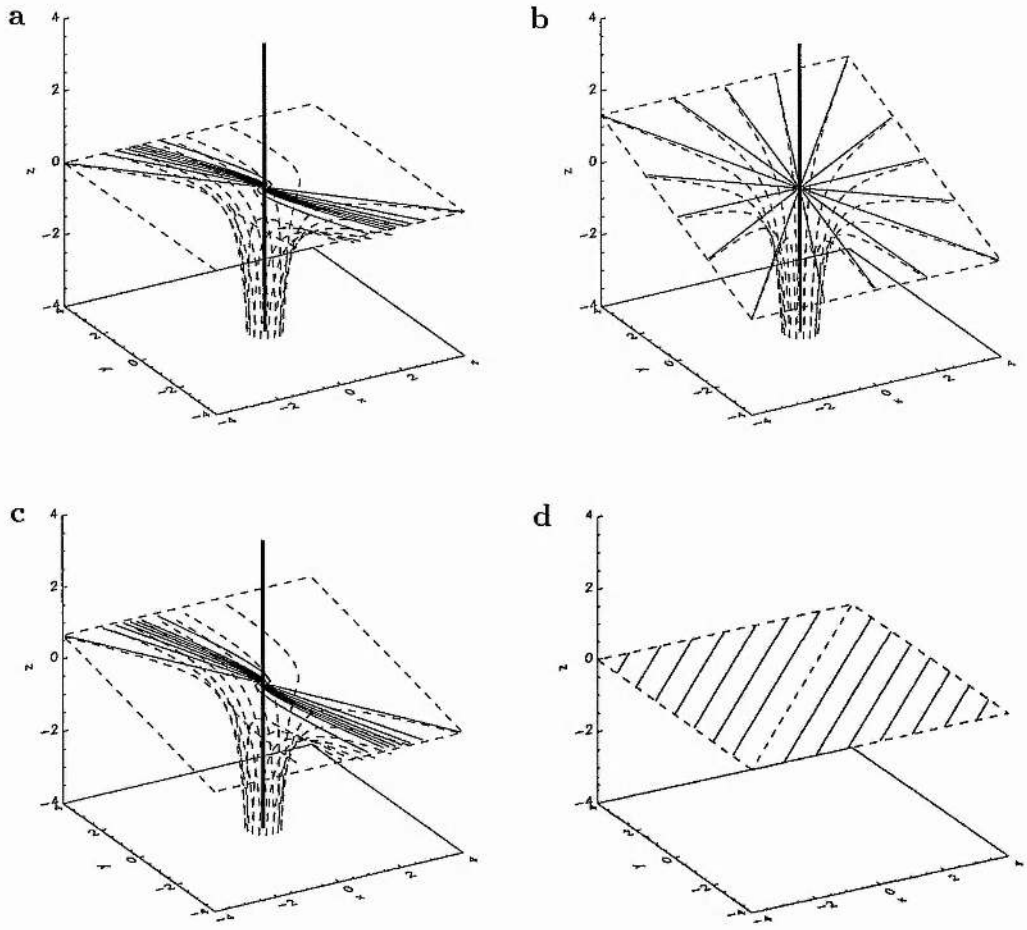

Figure 6.8: The three-dimensional non-potential magnetic field configurations where $(|j_{\parallel}| = j_{thresh})$. In (a) to (c) three-dimensional configurations arise since $p > -1$. In (a) $j_{\parallel} \neq 0$, $j_{\perp} = 0$, (b) $j_{\parallel} = 0$, $j_{\perp} \neq 0$ and (c) $j_{\parallel} \neq 0$, $j_{\perp} \neq 0$. Specifically we take (a) $p = 3$, $j_{\parallel} = 2$, $j_{\perp} = 0$, (b) $p = 1$, $j_{\parallel} = 0$, $j_{\perp} = 1$ and (c) $p = 3$, $j_{\parallel} = 2$, $j_{\perp} = 1$. In (d) the configuration reduces to two dimensions since $p = -1$; we have taken values of $p = -1$, $j_{\parallel} = 2$, $j_{\perp} = 0$.

given by 1, 1, −2. Even though two of the eigenvalues are equal it is possible to find three linearly independent eigenvectors. These are given by

$$\mathbf{x}_1 = \begin{pmatrix} 1 \\ 0 \\ 0 \end{pmatrix}, \qquad \mathbf{x}_2 = \begin{pmatrix} 0 \\ \frac{3}{j_\perp} \\ 1 \end{pmatrix}, \qquad \mathbf{x}_3 = \begin{pmatrix} 0 \\ 0 \\ 1 \end{pmatrix}. \tag{6.75}$$

Therefore, since $j_\perp \neq 0$, the fan does not lie in the xy-plane but in a plane defined by the equation

$$-j_\perp y + 3z = 0\,. \tag{6.76}$$

The field lines lying in the plane of the fan are radial (Figure 6.8b).

(iii) $j_\perp \neq 0$ and $j_\parallel \neq 0$

When both the parallel and perpendicular components of current are non-zero and $p > -1$, but $j_\parallel$ is still equal to the threshold value, we have a repeated eigenvalue. We once again have to look for an additional basis vector, $\mathbf{x}_2^*$. The vectors are found to be

$$\mathbf{x}_1 = \begin{pmatrix} \frac{3(p+1)\left(\sqrt{j_{thresh}^2-(p-1)^2}-j_\parallel\right)}{2j_\perp(p-1)} \\ \frac{3(p+1)}{2j_\perp} \\ 1 \end{pmatrix}, \qquad \mathbf{x}_2^* = \begin{pmatrix} \frac{-3p^2+4p+11}{2j_\perp\left(\sqrt{j_{thresh}^2-(p-1)^2}+j_\parallel\right)} \\ \frac{3p+5}{2j_\perp} \\ 1 \end{pmatrix}, \tag{6.77}$$

$$\mathbf{x}_3 = \begin{pmatrix} 0 \\ 0 \\ 1 \end{pmatrix}. \tag{6.78}$$

In this example a critical spiral forms (Figure 6.8c) whose fan lies in the plane defined by

$$2j_\perp\left(\sqrt{j_{thresh}^2-(p-1)^2}+j_\parallel\right)x - 4j_\perp(p+2)\,y + \left(9(p+1)^2\right)z = 0\,. \tag{6.79}$$

We note briefly that if $p = -1$ then planes are formed containing anti-parallel parabolic field lines.

6.5.3 $|j_\parallel| > j_{thresh}$

When the parallel component of current is greater in magnitude than the threshold current two of the eigenvalues of $\mathbf{M}$ will be a complex conjugate pair, whilst the third eigenvalue is real,

$$\lambda_{1,2} = \frac{p+1}{2} \pm \frac{i}{2}\sqrt{j_\parallel^2 - j_{thresh}^2}\,, \qquad \lambda_3 = -(p+1)\,. \tag{6.80}$$

The eigenvectors relating to the complex eigenvalues will also be a complex conjugate pair. However we have seen in Section 6.3 that if the complex eigenvectors are split up into their real and imaginary parts the resultant basis vectors will define the plane of the fan.

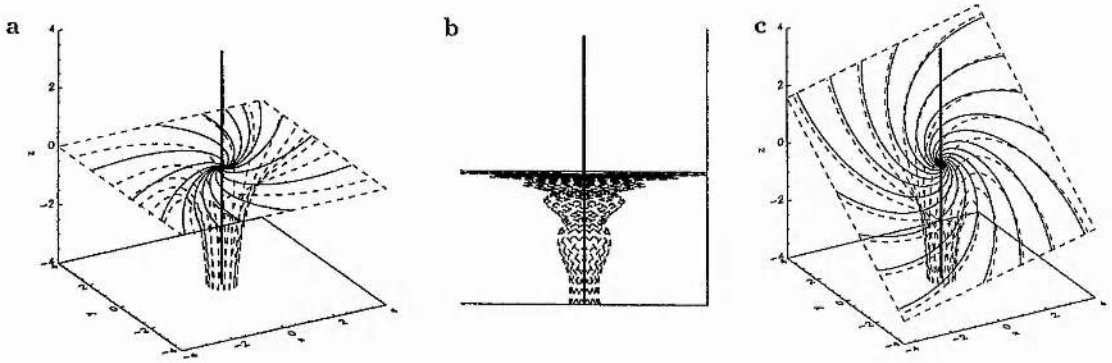

Figure 6.9: Non-potential three-dimensional magnetic field configurations where the component of current parallel to the spine is greater than the threshold current ($|j_\parallel| > j_{thresh}$). In (a) we have illustrated the three-dimensional configuration when $j_\parallel \neq 0$, $j_\perp = 0$. The values $p = 0.5$, $j_\parallel = 1$, $j_\perp = 0$ are used. In (b) the xz-plane is shown, illustrating the spiralling field lines around the spine ($p = -0.5$, $j_\parallel = -4$, $j_\perp = 0$). Finally in (c) we show the effects of both components of current with $p = 1$, $j_\parallel = -2$, $j_\perp = 2$; the fan plane is not perpendicular to the spine.

(i) $j_\perp = 0$ and $j_\parallel \neq 0$

When the perpendicular current is zero ($j_\perp = 0$) the spine is perpendicular to the fan. The basis vectors are given by

$$\mathbf{x}_1' = \begin{pmatrix} \frac{1-p}{j_\parallel} \\ 1 \\ 0 \end{pmatrix}, \qquad \mathbf{x}_2' = \begin{pmatrix} \frac{\sqrt{j_\parallel^2 - j_{thresh}^2}}{j_\parallel} \\ 0 \\ 0 \end{pmatrix}, \qquad \mathbf{x}_3 = \begin{pmatrix} 0 \\ 0 \\ 1 \end{pmatrix}, \tag{6.81}$$

where we have taken $q = 0$ and $p > -1$. The magnetic field lines that lie in the plane of the fan are spirals. Some of the spirals are so weakly coiled that the topology looks more like that of an improper null (Figure 6.9a). The spirals become much tighter for increasing $j_\parallel$ (Parnell et al. 1997). We get proper spirals if $\mathbf{x}_1'$ and $\mathbf{x}_2'$ are perpendicular and improper spirals if they are not. The two basis vectors in the fan plane are only perpendicular when $p = 1$. Therefore, in general, spiral nulls will tend to be of the improper type.

If we look at the equation for a field line,

$$\mathbf{r}(k) = Re^{\eta k}\cos(\Theta + \nu k)\,\mathbf{x}_1' - Re^{\eta k}\sin(\Theta + \nu k)\,\mathbf{x}_2' + Ce^{-2\eta k}\mathbf{x}_3\,, \tag{6.82}$$

then we can see that the field lines are coiled in the $\mathbf{x}_1'$ and $\mathbf{x}_2'$ directions, spiralling first around the spine and then outwards parallel to the fan plane (Figure 6.9b).

When $p = -1$ the field reduces to a two-dimensional null with a null line along the z-axis

and elliptical field lines in successive z = constant planes. These elliptical field lines will become circular only if the matrix has zero entries along the trace.

(ii) $j_\perp \neq 0$ and $j_\parallel \neq 0$

We now consider the case with $j_\perp \neq 0$ and $j_\parallel \neq 0$ since it is not possible to create a spiral null without a component of current parallel to the spine. The basis vectors are defined by $(p > -1)$

$$\mathbf{x}_1' = \begin{pmatrix} \frac{-3p^2+3+j_{thresh}^2-j_\parallel^2}{2j_\perp\left(\sqrt{j_{thresh}^2-(p-1)^2}+j_\parallel\right)} \\ \frac{3(p+1)}{2j_\perp} \\ 1 \end{pmatrix}, \quad \mathbf{x}_2' = \begin{pmatrix} \frac{(p+2)\sqrt{j_\parallel^2-j_{thresh}^2}}{j_\perp\left(\sqrt{j_{thresh}^2-(p-1)^2}+j_\parallel\right)} \\ \frac{\sqrt{j_\parallel^2-j_{thresh}^2}}{2j_\perp} \\ 0 \end{pmatrix}, \tag{6.83}$$

$$\mathbf{x}_3 = \begin{pmatrix} 0 \\ 0 \\ 1 \end{pmatrix}. \tag{6.84}$$

The fan is not perpendicular to the spine and lies in a plane given by

$$2j_\perp\sqrt{j_{thresh}^2-(p-1)^2}+j_\parallel\, x-4j_\perp\,(p+2)\; y+\left(9\,(p+1)^2-j_{thresh}^2+j_\parallel^2\right)\; z=0\,. \tag{6.85}$$

The field lines lying in the plane of the fan are coiled as are the field lines around the spine, illustrated in Figure 6.9c.

The field reduces to a two-dimensional null when $p = -1$ with elliptical field lines in successive planes given by

$$2j_\perp\left(\sqrt{j_{thresh}^2-4}+j_\parallel\right)x-4j_\perp y+\left(j_\parallel^2-j_{thresh}^2\right)z \;=\; 0\;. \tag{6.86}$$

6.6 Evolution of the Magnetic Configurations

In the previous sections we have discussed all the possible configurations that a three-dimensional neutral point may take. The cases we have considered have always had the spine located along the z-axis. We now relax this assumption. It is interesting to consider how the topologies may evolve from one form to another. To do this we consider the variation of the parameter p for a potential magnetic field given by

$$\mathbf{B} = (x, py, -(p+1)\,z)\;, \tag{6.87}$$

where $-\infty \leq p \leq \infty$ (Figure 6.10). Here we find that for $1 \leq p \leq \infty$ we have a positive improper radial null with the spine located along the z-axis. The fan is located in the xy-plane, with the major axis lying along the y-axis. As p approaches unity the null transforms to a proper radial null which then closes down to form an improper null. The major axis is now located along the

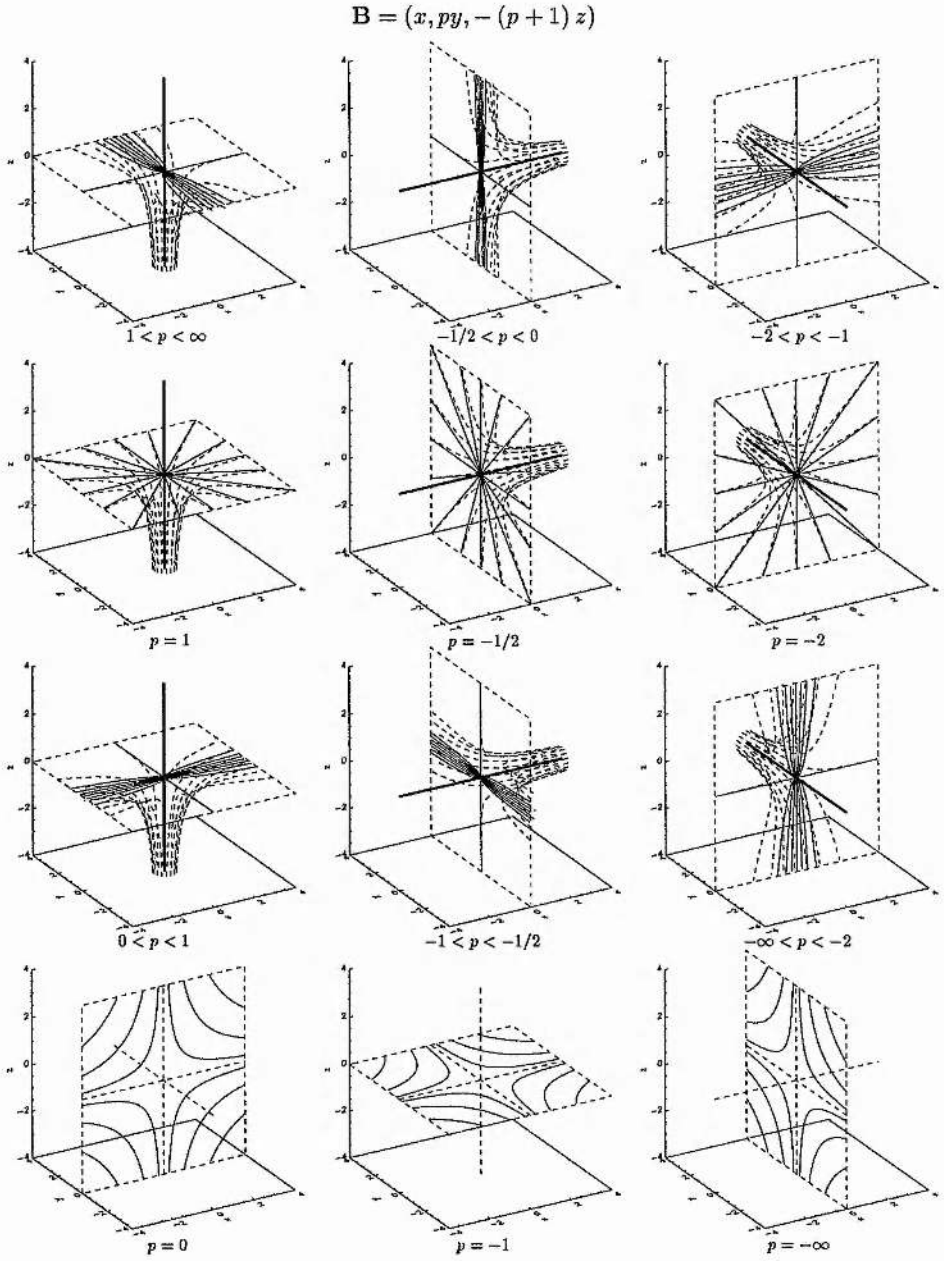

Figure 6.10: The possible topologies of a potential magnetic field surrounding a neutral point due to variation of the parameter p. Both two and three-dimensional configurations may exist depending upon the value of p.

x-axis. As p continues to decrease towards zero the field lines continue to close up until at $p = 0$ the field reduces to a two-dimensional configuration. The y-axis is now a null line with X-points forming in successive xz-planes. For $-1 < p < 0$ the polarity of the null changes so that a negative null point forms. The spine is now aligned along the x-axis whilst the fan is in the yz-plane. The major axis is initially the z-axis but then becomes the y-axis as p approaches -1. When $p = -1$ the three-dimensional configuration reduces to a two-dimensional field with X-points in successive xy-planes. When $-2 < p < -1$ an improper null arises with the fan in the xz-plane and the major axis located along the x-axis. The spine is aligned with the y-axis. Then when $p = -2$ a proper null is formed, with the fan in the xz-plane and the spine located along the y-axis. For $-2 < p < -\infty$ we again have a positive radial null whose fan is in the xz-plane with the spine aligned along the y-axis. The major axis of the fan lies along the x-axis. As $p \rightarrow -\infty$ the field reduces to a two-dimensional X-point configuration in successive yz-planes.

A comprehensive investigation into the variation of all four parameters $(p, q, j_{\parallel}, j_{thresh})$ on potential and non-potential topologies has recently been undertaken by Parnell et al. (1997); see also Section 6.7.

6.7 Recent Developments of the Work

The work described in this chapter was expanded upon by Parnell, Smith, Neukirch and Priest (1996), who classified three-dimensional neutral points in a more comprehensive manner. In this paper it was noted that the eigenvalues obtained from $|\lambda \mathbf{I} - \mathbf{S}| = 0$ for the matrix $\mathbf{S}$ (where $\mathbf{S}$ is the symmetrical part of $\mathbf{M}$) may be written in the form

$$\lambda^3 + a\lambda^2 + b\lambda + c = 0 \,. \tag{6.88}$$

For a divergence-free vector field $a \equiv 0$. The determinant of the matrix $\mathbf{S}$ is $-c$, whilst the discriminant is given by $b^3/27 + c^2/4$. The square root of the discriminant of $\mathbf{S}$ is equal to the threshold current (j_{thresh}) with the same argument applying for two-dimensional neutral points. A similar result may be found in Chong, Perry and Cantwell (1990) who gave a general classification of three-dimensional flow fields in terms of Equation (6.88) for both compressible and non-compressible flows.

From this approach the neutral point can be categorised quickly and easily. The type of null may be obtained from knowledge of the discriminant and the determinant of $\mathbf{M}$, and whether the matrix $\mathbf{M}$ is symmetric or not. See Table II in Parnell et al. (1996) for full details. We now summarise the main results of their approach.

If the matrix $\mathbf{M}$ is symmetric the null point is potential, whereas an asymmetric matrix results in a non-potential null. In addition, if the determinant of the matrix $\mathbf{M}$ is non-zero then a three-dimensional null arises. Furthermore, a positive (negative) null is obtained for negative

(positive) determinant. For the special case when the determinant is zero the structure is two-dimensional. Finally the discriminant of the matrix **M** plays a crucial role in determining the magnetic field topology. When the discriminant is negative the null points are classified as either proper or improper radial nulls (for a potential field) or skewed improper nulls (for a non-potential field). When the discriminant is equal to zero it is possible for a proper radial null (potential) or critical spiral null (non-potential) to arise. Finally for a positive discriminant a spiral null forms which is always non-potential.

Parnell et al. (1996) also briefly considered the topologies that may arise in different geometries such as cylindrical and spherical. However, no new configurations were found.

A comprehensive investigation into the structure and collapse of three-dimensional neutral points was undertaken by Parnell, Neukirch, Smith and Priest (1997). Their work expands the study of the structure of three-dimensional neutral points reported in this chapter. In addition the collapse of a neutral point is investigated.

The effect of the four parameters, identified in this chapter, that define the magnetic field surrounding a null are examined in greater detail. Results show that the perpendicular current ($j_\perp$) causes the fan plane to be inclined to the spine, and when $j_\perp = 0$ the fan and spine are perpendicular. The angle of inclination was investigated for different values of the four parameters. As the current increases the fan and spine close up. The parallel component of current ($j_\parallel$) alters the configuration of the field in a different way, causing the field lines in the fan plane to bend. The two parameters p and q determine the potential structure of the null. In addition these potential parameters can reduce the three-dimensional topology to two dimensions as well as changing positive neutral points to negative points and vice-versa.

An important result found by Parnell et al. (1997) is the existence of three transitional null points. It is possible for a three-dimensional field to reduce to a two-dimensional topology by varying the potential parameters. Parnell et al. (1997) find that the two-dimensional null is the intermediate configuration between positive and negative three-dimensional nulls. The change from a positive to negative null can result in a dramatic change in topology (see Figure 6.10 for a particular example). Another transitional null is the critical spiral which separates spiral and improper null points. The final transitional neutral point is a radial null, which may separate clockwise and anti-clockwise spirals, or improper nulls where the major axis in the fan may change.

Moreover, Parnell et al. (1997) point out that three-dimensional neutral points may collapse when a small perturbation is applied. Solving the linearised MHD equations it was found that the nature of the collapse was dependent upon the initial perturbation. For example, when a current was induced perpendicular to the spine of a potential null the fan plane began to approach the spine. For a perturbed current parallel to the spine the field lines close up in the fan plane. This work, however, requires that energy can propagate into the system and the field lines are not line tied.

	$j_{thresh}^2 - j_\parallel^2$	Eigenvalues	Vectors	Eqn of field lines	Description of null
Potential	—	Three real distinct $\lambda_1, \lambda_2, \lambda_3$	Eigenvectors $\mathbf{x}_1, \mathbf{x}_2, \mathbf{x}_3$	$\mathbf{r}(k) = Ae^{\lambda_1 k}\mathbf{x}_1 + Be^{\lambda_2 k}\mathbf{x}_2 + Ce^{\lambda_3 k}\mathbf{x}_3$	*Radial null*: proper or improper fan $\perp$ spine
Non-potential	> 0	Three real distinct $\lambda_1, \lambda_2, \lambda_3$	Eigenvectors $\mathbf{x}_1, \mathbf{x}_2, \mathbf{x}_3$	$\mathbf{r}(k) = Ae^{\lambda_1 k}\mathbf{x}_1 + Be^{\lambda_2 k}\mathbf{x}_2 + Ce^{\lambda_3 k}\mathbf{x}_3$	*Skewed improper radial null* $j_\perp = 0 \Rightarrow$ fan $\perp$ spine $j_\perp \neq 0 \Rightarrow$ fan $\not\perp$ spine
	$= 0$	Two equal $\lambda, \lambda, -2\lambda$	$j_\parallel = 0 \Rightarrow$ Eigenvectors $\mathbf{x}_1, \mathbf{x}_2, \mathbf{x}_3$	$\mathbf{r}(k) = Ae^{\lambda_1 k}\mathbf{x}_1 + Be^{\lambda_2 k}\mathbf{x}_2 + Ce^{\lambda_3 k}\mathbf{x}_3$	*Radial null* $j_\perp \neq 0 \Rightarrow$ fan $\not\perp$ spine
			$j_\parallel \neq 0 \Rightarrow$ Vectors $\mathbf{x}_1, \mathbf{x}_2^*, \mathbf{x}_3$ which satisfy $M\mathbf{x}_1 = \lambda\mathbf{x}_1$, $M\mathbf{x}_2^* = \mathbf{x}_1 + \lambda\mathbf{x}_2^*$, $M\mathbf{x}_3 = -2\lambda\mathbf{x}_3$	$\mathbf{r}(k) = (A + Bk)e^{\lambda k}\mathbf{x}_1 + Be^{\lambda k}\mathbf{x}_2^* + Ce^{-2\lambda k}\mathbf{x}_3$	*Critical spiral null* $j_\perp = 0 \Rightarrow$ fan $\perp$ spine $j_\perp \neq 0 \Rightarrow$ fan $\not\perp$ spine
	< 0	Two complex conjugate One real $(\eta + i\nu), (\eta - i\nu), -2\eta$	$\mathbf{x}_1' = (\mathbf{x}_1 + \mathbf{x}_2)/2, \mathbf{x}_2' = -i(\mathbf{x}_1 - \mathbf{x}_2)/2$, $\mathbf{x}_3$ where $\mathbf{x}_1$, $\mathbf{x}_2$ and $\mathbf{x}_3$ are eigenvectors	$\mathbf{r}(k) = Re^{\eta k}\cos(\Theta + \nu k)\mathbf{x}_1' - Re^{\eta k}\sin(\Theta + \nu k)\mathbf{x}_2' + Ce^{-2\eta k}\mathbf{x}_3$	*Spiral null*: proper or improper $j_\perp = 0 \Rightarrow$ fan $\perp$ spine $j_\perp \neq 0 \Rightarrow$ fan $\not\perp$ spine

Table 6.2: A summary of the results presented in this chapter. The nature of the eigenvalues and associated vectors, along with the equation of the field lines and a brief description of the null, is given for all the possible three-dimensional configurations.

6.8 Conclusion

In this chapter we have analysed the local linear three-dimensional magnetic structure surrounding a neutral point. The field configurations depend upon four parameters, namely p and q (the potential field parameters), $j_\parallel$ (the parallel component of current) and $j_\perp$ (the perpendicular component of current). The configurations have been classified into cases with no current, current parallel to the spine axis, current perpendicular to the spine axis and current both parallel and perpendicular to the spine axis. The effect of the four free parameters on the system has been examined. A summary of the results is reported in Table 6.2.

For a potential magnetic field one parameter p determines all the possible configurations, which are either proper ($p = 1$) or improper ($p \neq 1$) radial nulls. The spine is also perpendicular to the fan. It is also possible, for particular values of the potential parameter, for the null to reduce to a two-dimensional configuration.

When the current is purely parallel to the spine of the null ($j_\perp = 0$) then just two parameters (p and $j_\parallel$) are required to determine all the possible topologies. However if there is a component of current perpendicular to the spine ($j_\perp \neq 0$) then all four parameters are needed.

To determine the structure of the non-potential magnetic configurations one important parameter is the threshold current (j_{thresh}), which depends only on the potential field parameters. If the absolute value of the spine current ($|j_\parallel|$) is less than the threshold value the neutral points formed are either improper or proper radial nulls. It is also possible to find three linearly independent

eigenvectors of the matrix **M**. When $|j_{\parallel}|$ is equal to j_{thresh} then two of the eigenvalues are equal, in which case it may not be possible to find three distinct eigenvectors of **M** and so an additional basis vector is calculated. The neutral point is either a radial proper null or a critical spiral. Situations where $|j_{\parallel}|$ is greater than j_{thresh} give rise to complex eigenvalues. The field lines lying in the fan plane are of the spiral type. We also find that if the real parts of two of the eigenvalues are greater than zero then the null is positive, with the field lines in the fan leaving the null. If, however, the real parts of two of the eigenvalues are less than zero, a negative null arises and the field lines are directed towards the neutral point.

It is also possible for the three-dimensional nulls to reduce to two-dimensional nulls lying in successive planes containing X-points ($|j_{\parallel}| < j_{thresh}$) or ellipses ($|j_{\parallel}| > j_{thresh}$). If $|j_{\parallel}| = j_{thresh}$ and the perpendicular component of current is zero it is possible for planes to be formed containing anti-parallel field lines for particular values of p. However, if $|j_{\parallel}| = j_{thresh}$ and $j_{\perp} \neq 0$ then successive planes are formed containing anti-parallel parabolic field lines.

Chapter 7

Conclusion

"All our knowledge is but the knowledge of school children. The real nature of things we shall never know, never." Albert Einstein

7.1 Summary of Thesis

This thesis has examined the guiding of magnetoacoustic waves in coronal structures such as loops and current sheets. We have investigated how magnetoacoustic waves may be guided by inhomogeneities both in the magnetic field and the plasma density. The work contained in this thesis is of importance because it attempts to model the observed oscillatory phenomena in terms of structures found in the solar corona, and such a study provides important seismic information about the corona. It may also give an insight into the long standing puzzle of coronal heating. The main conclusions of our study are as follows.

A comprehensive review of coronal oscillations has been presented in the introductory chapter, along with with a detailed summary of coronal loops. The physical characteristics of the other regions of the solar atmosphere are also briefly discussed. The basic equations of ideal MHD are given, and we concluded this chapter with a discussion on the properties of the *Alfvén* mode and the *fast* and *slow* magnetoacoustic modes in a uniform medium.

Chapter 2 was concerned with the guiding of magnetoacoustic waves in *curved* coronal loops. Previous studies have concentrated on dense slabs or cylinders to model coronal loops. Such models are popular because they allow us an insight into the physical processes occurring in the corona. A review of the slab model proposed by Roberts, Edwin and Benz (1983) was presented. We then gave a detailed review of the work undertaken in curved dielectric waveguides. A summary of the previous work on leaky magnetoacoutic waves in the solar atmosphere is then described. Detailed numerical calculations show that the slab model is, in general, a good approximation to the curved loop. The effect of the curvature is to generate wave *leakage* from the loop. The efficiency of wave guiding was investigated for different parameters, namely the loop's length, width, density

enhancement and mode of oscillation. The study found that the fast magnetoacoustic mode was guided more effectively for high density enhancements, high radii of curvature, and wide loops. Moreover, the kink mode was found to be guided better than the sausage mode. Even modes are more leaky than odd modes. Calculated periods of oscillation were in good agreement with the observations.

Chapter 3 considered the guiding of magnetoacoustic waves in a current sheet. Theoretically, coronal loops have often been used to explain the ducting of magnetoacoustic waves in the solar corona. However, in Chapter 3, we have carried out a comprehensive investigation into the propagation of magnetoacoustic waves in a current sheet. Initially we reviewed the slab model considered by Edwin, Roberts and Hughes (1986). A detailed investigation into the type of modes which may propagate in a continuously structured current sheet was undertaken. Typical time scales of oscillation were also examined. A current sheet was found to guide magnetoacoustic waves in a similar way to coronal loops. The cases of constant and non-constant plasma density were considered. It was found that pure fast and slow magnetoacoustic modes do not exist; modes possessed characteristics of both types. Furthermore, body, surface and *hybrid* modes were found, compared with only body and surface modes in the simple slab model. Hybrid modes contained elements of both body and surface modes. Calculated periods of oscillation agreed well with the observations of oscillations in the solar corona and Earth's magnetosphere. It was suggested that certain oscillations may be due to magnetoacoustic waves trapped within current sheets.

Chapter 4 investigated the time evolution of impulsively generated magnetoacoustic waves in current sheets. Minima in the group velocity curves in Chapter 3 were found for certain modes. If a wave is impulsively generated it will exhibit a distinctive temporal signature, as described in Roberts, Edwin and Benz (1983, 1984). Numerical simulations were performed using a flux corrected transport code. Results show that an impulsive event, such as a solar flare, a reconnection site or MHD instability, will generate propagating magnetoacoustic waves. The waves are subsequently guided by the inhomogeneity in the magnetic field. The temporal signatures obtained are in general agreement with observations of both the Sun's corona and the Earth's magnetosphere.

To summarise, the guiding of magnetoacoustic waves in current sheets and coronal loops is an attractive physical process of wide applicability, with results in general agreement with a diversity of observations.

Chapter 5 investigated the effects of randomly driven waves in the Earth's magnetosphere. A magnetospheric cavity was driven by a random boundary displacement containing a broadband spectrum. The driving motion was found to excite quasi-monochromatic fast modes whose eigenfrequencies lie within the spectrum of the driver. In addition these modes will couple to the Alfvén mode provided the wavenumber k_y is non-zero and the fast mode eigenfrequency lies in the Alfvén continuum. The location of the resonant field lines and the Alfvén mode eigenfunctions may be calculated to high accuracy by assuming a monochromatic driver. The ratio of the Alfvén wave energy density in two resonant field lines was found to be constant regardless of the driving mechanism, and

it therefore depends only on the equilibrium of the cavity. Hopefully in the future this will provide important seismic information on the Earth's magnetosphere.

In Chapter 6 we investigated the three-dimensional magnetic topologies surrounding neutral points. This work is a preliminary step in the understanding of three-dimensional reconnection. Results show that the local linear magnetic field surrounding a neutral point is determined by a 3×3 matrix. Both potential and non-potential magnetic field configurations were classified in a systematic manner. Magnetic topologies were classified as either *improper* or *proper*, *skewed* or *spiral*, and *positive* or *negative*, depending on the eigenvalues of the characteristic matrix and the current associated with the null. The three-dimensional fields reduced to the well-known two-dimensional topologies under certain conditions.

7.2 Future Work

We now outline some ideas regarding the future development of the work described in this thesis. In addition, we give details of further projects which may provide greater insight into the propagation of magnetoacoustic waves in the solar corona.

7.2.1 Development of Models Described in Thesis

The models that we have constructed are not able to describe coronal conditions fully, and therefore future work should aim to relax some of the assumptions we have made.

Specifically, we have neglected gravitational stratification in all our models. Although the effects of gravity are likely to be small in the corona (the pressure height is large compared with the height of a typical structure) interesting effects may nonetheless arise. The effect of gravity may be included in both the curved loop and current sheet model.

Furthermore, in Chapter 2 we ignored the effects of plasma pressure in our work on ducted waves in curved coronal loops. Therefore, the effects of finite plasma pressure would provide additional understanding into the nature of wave propagation in the solar corona. However, the complexity of the problem would increase substantially. Both fast and slow magnetoacoustic waves will exist, but they will be coupled. Preliminary work on the propagation of magnetoacoustic waves in curved coronal arcades has been undertaken by Oliver, Hood and Priest (1996), and their results illustrate that strong coupling arises in a curved magnetic field. The numerical code used in Chapter 2 could be modified to undertake such an investigation.

In addition, we have considered a discontinuous density profile in our work on curved loops. In practice however, we may expect the density profile to be smooth, though sharp. It will be interesting to investigate how the efficiency of wave ducting changes with a smooth density profile. Our work has also been undertaken in a Cartesian geometry. In future work, the guiding of magnetoacoustic waves in a cylindrical geometry could be studied. A comparison of the leakage

found in the Cartesian and cylindrical cases could then be made. The inclusion of twisted magnetic fields is another possibility for future study.

In Chapter 4 we examined impulsively generated waves in a current sheet. It may also be worthwhile to consider impulsively generated waves in curved coronal loops. The code implemented in Chapter 4 could be modified to investigate this problem. The temporal signatures of the fast, slow and Alfvén modes within (trapped modes) and outside (leaky modes) a coronal loop may be obtained and compared with the observational data. The effect of parameters such as density, width and the length of the loop can be examined.

In our work on current sheets in Chapter 3 we examined two limiting cases, namely the slab (top hat) and the Harris sheet model. An interesting exercise would be to construct a magnetic field that can vary between these two extremes. A similar task was undertaken by Nakariakov and Roberts (1995) for a coronal loop; they considered a density profile which contained the slab and Epstein profiles as two limiting cases. The proposed current sheet work would investigate, in greater detail, wave guiding in smooth magnetic field profiles.

Our work on current sheets has investigated the types of modes which may propagate, and also the time scales of oscillation. To achieve this we have considered solely parallel propagation ($k_y = 0$). Relaxing this assumption would provide important information about the damping of magnetoacoustic waves and coronal heating. Tirry, Čadež and Goossens (1997) have considered wave damping in current sheets through the Alfvén resonance, although only in the weak damping limit.

In our work we have not been concerned with the problem of coronal heating. Additional work could include dissipative effects (see discussion in Laing 1996). The efficiency of the damping of magnetoacoustic waves could be investigated, for example, by changing the magnetic field strength, plasma density and the mode of oscillation. In addition, the study of resonant absorption in current sheets could offer some interesting results. Resonant absorption occurs when the frequency of the magnetoacoustic wave matches the Alfvén frequency along a particular field line. Within a neutral current sheet a wide range of Alfvén speeds maybe present, ranging from zero to several thousand kilometres per second. Therefore a magnetoacoustic wave propagating in a current sheet is likely to couple to an Alfvén mode. Furthermore, the process of phase mixing in current sheets could be an effective dissipative mechanism because of the wide range of Alfvén speeds present.

7.2.2 Future Theoretical Modelling

An important aspect neglected in our models is the presence of plasma flow. Recently, the effects of flow have been considered both in compressible plasmas (Nakariakov and Roberts 1995) and incompressible plasmas (Mundie 1997). Results show that for sufficiently high flow speeds (twice the Alfvén speed) the Kelvin-Helmholtz instability arises. For typical values in the corona the instability threshold is much larger than the observed flow speeds. However, the effect of flow in

current sheets is potentially an important and interesting area of research. In particular, the Alfvén speed within the central regions of the current sheet is low (for a neutral sheet the Alfvén speed in the centre is zero). Hence, a relatively low flow may be able to excite instabilities, which in turn may excite propagating magnetoacoustic waves. The effects of plasma flow within current sheets has applications both in the solar corona and Earth's magnetosphere.

Future work could also involve the investigation of magnetoacoustic wave interaction between adjacent coronal loops or current sheets. Much of the theoretical work undertaken so far has involved the propagation of magnetoacoustic waves in isolated coronal loops. Recently however, very high resolution (sub-arcsecond) images (November and Koutchmy 1996) suggest that as well as isolated structures, loops are found in close proximity to each other. It will be interesting to see how the presence of one loop (or sheet) influences the wave propagation in a neighbouring loop (or sheet). Preliminary work has been undertaken by Berton and Heyvaerts (1987), who considered a periodic array of slabs, and Murawski (1993) who numerically explored the "cross-talk" interaction between fast magnetoacoustic waves in two slabs. This work could include both analytical and numerical investigations, initially in a low-β plasma. To begin with, for mathematical simplicity, the loops could be modelled as a slab of density enhancement. Further work can then investigate the effect of the loop curvature and finite plasma beta. A comparison with the observations and the implications for coronal heating could be made at each stage of the project.

We note that these suggestions for additional work will increase the complexity of the problem. However, in general, we may expect that the results we have obtained in this thesis are present even in more complicated equilibria.

7.2.3 Use of SoHO observations

The comparison of theoretical results obtained in this thesis with SoHO observations, together with the use of SoHO data in theoretical models, should be an integral part of future research. Only by theorists and observers working together and learning from each others research can any substantial progress be made in the basic understanding of the nature of magnetoacoustic wave propagation in the solar atmosphere. To make progress we need to understand the intrinsic make up of coronal structures, for example loops and current sheets. This requires detailed observational studies of structures yielding information such as their oscillation characteristics, spatial sizes, densities, temperatures and magnetic field strengths. There are a number of proposed observing programs using the CDS (Coronal Diagnostic Spectrometer) and SUMER (Solar Ultraviolet Measurements of Emitted Radiation) instruments on board SoHO which are related to the study of wave propagation in the active region corona.

A study of coronal loops using the CDS instrument will be conducted by Harrison (1996, private communication). Observations will be taken which will provide crucial information about the densities, temperatures and spatial sizes of loops, as well as looking for low frequency oscillations.

Complementary studies using SUMER are proposed by Lemaire (1994) and Mason (1994). Results from such observations could be included in theoretical models to gain important information about the physical processes occurring in the corona.

An investigation of coronal streamers using the CDS has been proposed by Harrison (1995). One of the many matters to be addressed is the physical nature of the current sheet. Accurate information regarding the current sheet will be of paramount importance for future research regarding wave propagation in such structures.

Important information regarding the existence of waves in the solar corona may be provided by studies WAVE (McClements et al. 1995) and BROAD (Harrison and Hassler 1995) using the CDS, and Hassler (1994) using SUMER.

High temporal observations of the solar corona looking specifically for oscillatory phenomena will be made during the 1999 total eclipse (Phillips 1997, private communication). The SECIS (Solar EClipse Imaging System), designed by the Rutherford Appleton Laboratory, provides a temporal resolution of 60 Hz. This ground based instrument will also have high spatial resolution so oscillations within coronal structures can be investigated. The observations will involve measuring the intensity of both the green coronal line (5374 Å) and the 5500 Å continuum. The continuum contains variations in the intensity due to the Earth's atmosphere. To find the excess power due to coronal pulsations the continuum intensity is subtracted from the green coronal line. This experiment has potentially a far superior temporal resolution than instruments onboard SoHO. SECIS will hopefully advance our knowledge of oscillations in the corona, and in particular of oscillations in loops and current sheets.

The solar corona exhibits oscillations with a diversity of periods. In this thesis we have theoretically investigated how magnetoacoustic waves may be trapped within coronal loops and current sheets, as an explanation for the observed oscillatory behaviour. Hopefully this has provided an increased understanding of wave propagation in structured plasmas, and in particular the solar corona. In addition the suggestions for further theoretical studies, as well as the planned higher spatial and temporal observations of the corona from the SECIS instrument, will advance our knowledge of this complicated region of the solar atmosphere even further, and may give clues to the elusive problem of coronal heating.

Appendix A

Spatial Sizes of Coronal Loops

Paper	Length (Mm)	Height (Mm)	Width (Mm)	Observation
Kleczek (1963)	-	50–100 348	3–8 8–12	Green line (5303 Å)
Fisher (1971a)	-	43	5.8–8.7	Green line (5303 Å)
Fisher (1971b)	-	60	-	Green line (5303 Å)
Foukal (1975)	-	-	3–12	EUV
Neupert et al. (1975)	100	20–40	-	EUV
Sheeley et al. (1975)	100	-	-	EUV
Krieger et al. (1976)	-	100 (50 typical)	-	X-ray
McIntosh et al. (1976)	57–490	70–560	-	X-ray
Howard and Švestka (1977)	-	200–260	-	X-ray
Levine and Withbroe (1977)	110	-	-	EUV
Foukal (1978)	40	-	10	EUV
Cheng (1980)	-	-	4.8–6.5	EUV
Kundu and Velasany (1980)	-	-	16–20	Radio
Kundu et al. (1980)	-	-	10–30	Radio
Kundu et al. (1980)	-	5–11	-	EUV
Davis and Krieger (1982)	7–500	-	0.7–30	X-ray
Lang et al. (1982)	40–400	-	-	Radio
McConnell and Kundu (1983)	70	-	-	Radio
Berton and Sakurai (1985)	-	120–130	-	EUV
Stewart et al. (1986)	200	100/290	-	EUV
Haisch et al. (1988)	130	40–60	-	X-ray
Hanaoka et al. (1988)	50–90 -	29–80 29–80	1.5–4.45 5–7	Red line (6374 Å) Green line (5303 Å)
Gary et al. (1990)	22	-	-	Radio
Golub (1991)	1.5–90	-	1.5	X-ray
Acton et al. (1992)	400 18 190	350 10 82	- 4 27	X-ray
Klimchuk et al. (1992)	82	-	7.26–9.1	X-ray
Shimizu et al. (1992)	33	-	7	X-ray
Watanabe et al. (1992)	-	210	-	X-ray
Koutchmy et al. (1993)	-	-	0.726–1.452	White Light
Hiei (1994)	10–200	-	-	X-ray
Porter and Klimchuk (1995)	4.7–33	-	-	X-ray
Krucker et al. (1995)	-	-	18 ± 7	X-ray

Table A.1: Summary of spatial sizes of coronal loops.

Appendix B

Density and Temperatures of Active Regions

Paper	Density ($\times 10^9 cm^{-3}$)	Temp ($\times 10^6 K$)	Observation
Parkinson (1973)	2.0–10.0	2.0–6.0	X-ray
Neupert et al. (1975)	6.7	2.6	EUV/ X-ray
Levine and Withbroe (1977)	1.38–42.6 (FeXV 2.2)	1.4	EUV
McGuire (1977)	3.0	3.0	X-ray
Stewart and Vorpahl (1977)	0.8–2.4	2.0–3.0	X-ray
Švestka et al. (1977)	0.7–1.3	2.1–3.1	X-ray
Foukal (1978)	0.8–2.3	3.0	EUV
Pye et al. (1978)	1.0–6.0	2.6–3.2	X-ray
Cheng (1980)	2.2–3.6	2.0–2.2	EUV
Kundu et al. (1980)	20.0	3.0	EUV
Davis and Krieger (1982)	1.0	2.1	X-ray
Dere (1982)	1.2–3.7	2.0	EUV
Lang et al. (1982)	2.5	2–4	Radio
Gerassimenko et al. (1978)	1.8–2.5	2.2–2.5	X-ray
McConnell and Kundu (1983)	0.5	1.7	Radio
Kundu and Lang (1985)	1.0–10.0	2.0–4.0	Radio
Stewart et al. (1986)	0.19–0.3	2.2	EUV
McKenzie (1987)	2.0–7.9	2.0	X-ray
Webb et al. (1987)	3.4–7.8	1.5–2.5	X-ray
Haisch et al. (1988)	2.0 5.0	4.5 3.8	X-ray
Hanaoka et al. (1988)	0.4–1.5 1.9–7.2	2.0–3.0 2.0–3.0	Green line (5303 Å) Red line (6374 Å)
Gary et al. (1990)	2.4–2.8	2.0	Radio
Shimizu et al. (1992)	4.0	5.3	X-ray
Klimchuk and Gary (1995)	1.5	2.5–5.0	X-ray
Porter and Klimchuk (1995)	1.4	5.7	X-ray
Krucker et al. (1995)	1.5 ± 0.4	2.1 ± 0.1	X-ray

Table B.1: Densities and temperatures of active region loops.

Appendix C

Numerical Scheme for Chapter 2

We wish to solve the equation

$$\nabla^2 (Bv_n) + \frac{\omega^2}{v_A^2} Bv_n = 0 \tag{C.1}$$

numerically in generalised coordinates $\chi(x,z)$ and $\psi(x,z)$. In Equation (C.1) B is the magntitude of the magnetic field, v_n is the component of velocity normal to the field and ω and v_A are the frequency and Alfvén speed respectively. This equation governs the velocity perturbations of the fast magnetoacoustic mode in a potential coronal arcade, with the plasma pressure and gravitational terms being neglected. For full details of the numerical scheme see Oliver, Hood and Priest (1996). Here we only give a brief outline of the numerical method.

Firstly we need to rewrite Equation (C.1) into a form which is more convenient to solve numerically. The unit vectors of the coordinate system are

$$\hat{\mathbf{e}}_\mathbf{n} = \frac{\nabla A}{B}\,, \quad \hat{\mathbf{e}}_\parallel = \frac{\mathbf{B}}{B}\,, \quad \hat{\mathbf{e}}_\perp = \hat{\mathbf{e}}_\mathbf{y}\,, \tag{C.2}$$

where $\hat{\mathbf{e}}_\mathbf{n}$ and $\hat{\mathbf{e}}_\parallel$ are in the direction normal and parallel to the magnetic field respectively. In addition $\hat{\mathbf{e}}_\perp$ is in the direction perpendicular to the field and $A(x,z)$ is the magnetic flux function where $\mathbf{B} = \nabla A \times \hat{\mathbf{e}}_\mathbf{y}$. In addition we take $\partial/\partial y = 0$.

Using Equation (C.2) the gradient of a function $f = f(x,z)$ is given by

$$\nabla f = \frac{1}{B}(\nabla A.\nabla) f \hat{\mathbf{e}}_\mathbf{n} + \frac{1}{B}(\mathbf{B}.\nabla) f \hat{\mathbf{e}}_\parallel\,, \tag{C.3}$$

whilst the divergence of a vector $\mathbf{F}$ is

$$\nabla.\mathbf{F} = \frac{1}{B}(\nabla A.\nabla) f_n - f_n B_a - \frac{1}{B}(\mathbf{B}.\nabla) f_\parallel - f_\parallel B_s\,. \tag{C.4}$$

The Laplacian $\nabla^2 f\,(= \nabla.\nabla f)$ is then obtained from Equations (C.3) and (C.4),

$$\begin{aligned}\nabla^2 f = \frac{1}{B}(\nabla A.\nabla)\left[\frac{1}{B}(\nabla A.\nabla) f\right] &- B_a \frac{1}{B}(\nabla A.\nabla) f \\ &+ \frac{1}{B}(\mathbf{B}.\nabla)\left[\frac{1}{B}(\mathbf{B}.\nabla) f\right] - B_s \frac{1}{B}(\mathbf{B}.\nabla) f\,.\end{aligned} \tag{C.5}$$

Here $B_s = 1/B^2\,(\mathbf{B}.\nabla)\,B$ and $B_a = 1/B^2\,(\nabla A.\nabla)\,B$. In addition f_n and $f_\parallel$ are the normal and parallel components of the vector $\mathbf{F}$.

In Equation (C.1) we need to evaluate $\nabla^2\,(Bv_n)$ so we now set $f = Bv_n$ in Equation (C.5). We obtain, after some algebra and applying various vector identities,

$$\nabla^2\,(Bv_n) = \frac{1}{B}\left[(\nabla A.\nabla)^2\,v_n + (\mathbf{B}.\nabla)^2\,v_n\right] + Bv_n\left[B_{aa} + B_{ss} - 2\left(B_a^2 + B_s^2\right)\right]\,. \tag{C.6}$$

Here $B_{ss} = 1/B^3\,(\mathbf{B}.\nabla)^2\,B$ and $B_{aa} = 1/B^3\,(\nabla A.\nabla)^2\,B$. From Equations (C.1) and (C.6) we obtain

$$\frac{1}{B^2}\left[(\nabla A.\nabla)^2\,v_n + (\mathbf{B}.\nabla)^2\,v_n\right] + v_n\left[B_{aa} + B_{ss} - 2\left(B_a^2 + B_s^2\right)\right] = -\frac{\omega^2}{v_A^2}v_n\,. \tag{C.7}$$

We now write the terms $(\nabla A.\nabla)$ and $(\mathbf{B}.\nabla)$ in a more convenient form for numerical computation. Since our generalised coordinates are χ and ψ we may write the unit vector in the normal direction as $\hat{\mathbf{e}}_\mathbf{n} = (\chi_n, \psi_n)$. Hence

$$\hat{\mathbf{e}}_\mathbf{n}.\nabla = \frac{1}{B}\,(\nabla A.\nabla) = (\chi_a, \psi_a)\,.\left(\frac{\partial}{\partial\chi}, \frac{\partial}{\partial\psi}\right) = \chi_a\frac{\partial}{\partial\chi} + \psi_a\frac{\partial}{\partial\psi}\,, \tag{C.8}$$

and similarly

$$\frac{1}{B}\,(\mathbf{B}.\nabla) = \chi_s\frac{\partial}{\partial\chi} + \psi_s\frac{\partial}{\partial\psi}\,. \tag{C.9}$$

Here $\psi_a = 1/B\,(\nabla A.\nabla)\,\psi$, $\psi_s = 1/B\,(\mathbf{B}.\nabla)\,\psi$, $\chi_a = 1/B\,(\nabla A.\nabla)\,\chi$ and $\chi_s = 1/B\,(\mathbf{B}.\nabla)\,\chi$. Therefore the governing wave equation (Equation C.1) becomes

$$\alpha\frac{\partial^2 v_n}{\partial\psi^2} + \beta\frac{\partial^2 v_n}{\partial\chi\partial\psi} + \gamma\frac{\partial^2 v_n}{\partial\chi^2} + \delta\frac{\partial v_n}{\partial\psi} + \epsilon\frac{\partial v_n}{\partial\chi} + \xi v_n = -\frac{\omega^2}{v_A^2}v_n\,. \tag{C.10}$$

In Equation (C.10) the variables α to ξ are explicitly given by

$$\alpha = \psi_a^2 + \psi_s^2 \tag{C.11}$$

$$\beta = 2\,(\psi_a\chi_a + \psi_s\chi_s) \tag{C.12}$$

$$\gamma = \chi_a^2 + \chi_s^2 \tag{C.13}$$

$$\delta = \psi_{aa} + \psi_{ss} \tag{C.14}$$

$$\epsilon = \chi_{aa} + \chi_{ss} \tag{C.15}$$

$$\xi = B_{aa} + B_{ss} - 2\left(B_a^2 + B_s^2\right)\,, \tag{C.16}$$

where we have defined $\psi_{aa} = 1/B^2\,(\nabla A.\nabla)^2\,\psi$, $\psi_{ss} = 1/B^2\,(\mathbf{B}.\nabla)^2\,\psi$, $\chi_{aa} = 1/B^2\,(\nabla A.\nabla)^2\,\chi$ and $\chi_{ss} = 1/B^2\,(\mathbf{B}.\nabla)^2\,\chi$. A finite difference approximation of the partial differential equation (Equation C.10) is then undertaken. The computational domain is rectangular with sides parallel to the spatial coordinates χ and ψ. In each spatial direction there are N_χ and N_ψ equally spaced grid points. At each grid point the first and second derivatives in Equation (C.10), evaluated at the point $(\chi = i, \psi = j)$, are calculated as follows:

$$\frac{\partial v_n}{\partial\chi} = \frac{v_n^{(i+1,j)} - v_n^{(i-1,j)}}{2h_\chi} + O\left(h_\chi^2\right)\,, \tag{C.17}$$

$$\frac{\partial v_n}{\partial \psi} = \frac{v_n^{(i,j+1)} - v_n^{(i,j-1)}}{2h_\psi} + O\left(h_\psi^2\right) , \tag{C.18}$$

$$\frac{\partial^2 v_n}{\partial \chi^2} = \frac{v_n^{(i+1,j)} - 2v_n^{(i,j)} + v_n^{(i-1,j)}}{h_\chi^2} + O\left(h_\chi^2\right) , \tag{C.19}$$

$$\frac{\partial^2 v_n}{\partial \psi^2} = \frac{v_n^{(i,j+1)} - 2v_n^{(i,j)} + v_n^{(i,j-1)}}{h_\psi^2} + O\left(h_\psi^2\right) . \tag{C.20}$$

In Equations (C.17)-(C.20) h_χ and h_ψ are the uniform grid spacings and $v_n^{(i,j)}$ is the approximation to v_n at the point (χ_i, ψ_j). The mixed derivative takes the form (Oliver et al. 1996)

$$\begin{aligned} \frac{\partial^2 v_n}{\partial \chi \partial \psi} &= \frac{1}{h_\chi h_\psi}\left\{(\phi_2 - \phi_1)\left[v_n^{(i+1,j)} + v_n^{(i,j+1)} + v_n^{(i-1,j)} + v_n^{(i,j-1)}\right]\right. \\ &+ \left.\phi_1\left[v_n^{(i+1,j+1)} + v_n^{(i-1,j-1)}\right] - \phi_2\left[v_n^{(i-1,j+1)} + v_n^{(i+1,j-1)}\right]\right\} \\ &+ O\left[\max\left(h_\chi^2, h_\psi^2\right)\right] , \end{aligned} \tag{C.21}$$

where $\phi_1 + \phi_2 = 1/2$ to ensure the errors in the finite difference scheme are as small as possible.

There are $(N_\chi - 2)(N_\psi - 2)$ interior points and $2(N_\chi + N_\psi - 2)$ unknowns at the boundary. Boundary conditions are needed to eliminate these unknowns. This is achieved by introducing ghost cells outside the computational domain.

The $N_\chi N_\psi$ $(= N)$ grid points are ordered consectively into a vector $\mathbf{U}$ where

$$\mathbf{U} = \left(v_n^1, v_n^2, \ldots, v_n^N\right)^T , \tag{C.22}$$

where v_n^k , $k = 1, 2, \ldots, N$ are the approximations to the eigenfunction v_n at the k^{th} grid point.

The discrete approximation to the partial differential equation (Equation C.10) is now an algebraic eigenvalue problem

$$\mathbf{AU} = \lambda \mathbf{U} \tag{C.23}$$

where $\lambda = \omega^2$. The solution for v_n is achieved by using an inverse vector iteration, with one eigenvector and eigenvalue being calculated at a time. An approximation (λ_0) to the exact eigenvalue (λ) is given. The vector $\lambda_0 \mathbf{U}$ is subtracted from both sides of Equation (C.23), giving

$$(\mathbf{A} - \lambda_0 \mathbf{I})\,\mathbf{U} = \Delta\lambda \mathbf{U} , \tag{C.24}$$

where $\lambda = \lambda_0 + \Delta\lambda$, and $\Delta\lambda$ is the difference between the initial guess and the exact solution. The eigenvector $\mathbf{U}$ and the difference $\Delta\lambda$ are then computed as the iterative solution to the system

$$(\mathbf{A} - \lambda_0 \mathbf{I})\,\mathbf{U}_i = \Delta\lambda_{i-1} \mathbf{U}_{i-1} , \tag{C.25}$$

where $\Delta\lambda_i$ is given by the Rayleigh Quotient

$$\Delta\lambda_i = \frac{\mathbf{U}_i^T (\mathbf{A} - \lambda_0 \mathbf{I})\,\mathbf{U}_i}{\mathbf{U}_i^T \mathbf{U}_i} . \tag{C.26}$$

The vector $\mathbf{U}_0$ is simply filled with random numbers and $\Delta\lambda_0$ is set equal to $\lambda_0 \times 10^{-4}$. The solution $\mathbf{U}_1$ to the linear set of equations (Equation C.24) is computed and the correction $\Delta\lambda_1$ is then obtained from Equation (C.26). The second iteration then proceeds and the iteration continues until a solution converges.

Appendix D

Derivation of the Governing Equation of Lau (1979)

The governing wave equation for plasma motions in an incompressible current sheet (Equation 3.2) may be written in the form

$$X^2\frac{\partial^2 v_x}{\partial X^2}+\frac{\partial^2}{\partial \tau^2}\left(\frac{\partial^2 v_x}{\partial X^2}\right)-\frac{\partial^2 v_x}{\partial \tau^2}-X^2 v_x+2X\frac{\partial v_x}{\partial X}=0\,. \tag{D.1}$$

In Chapter 3 we have also set (Equation 3.4)

$$v_x\left(X,\tau\right)=\int_{-\infty}^{\infty}u\left(s,\tau\right)\mathrm{e}^{-iXs}\mathrm{d}s\,. \tag{D.2}$$

Differentiating Equation (D.2) with respect to X we obtain

$$\frac{\partial v_x}{\partial X}=-i\int_{-\infty}^{\infty}us\mathrm{e}^{-iXs}\mathrm{d}s\,, \tag{D.3}$$

and $\partial/\partial X$ of Equation (D.3) gives

$$\frac{\partial^2 v_x}{\partial X^2}=-\int_{-\infty}^{\infty}us^2\mathrm{e}^{-iXs}\mathrm{d}s\,. \tag{D.4}$$

From Equation (D.1) we need to calculate $X\partial v_x/\partial X$, $X^2 v_x$ and $X^2\partial^2 v_x/\partial X^2$. To evaluate these quantities consider

$$\int_{-\infty}^{\infty}Xw\left(s,\tau\right)\mathrm{e}^{-iXs}\mathrm{d}s\,. \tag{D.5}$$

Taking $w\left(s\right)\to 0$ as $|s|\to\infty$ and integrating by parts, the integral in Equation (D.5) becomes

$$-i\int_{-\infty}^{\infty}\frac{\partial w}{\partial s}\mathrm{e}^{-iXs}\mathrm{d}s\,. \tag{D.6}$$

Now using Equation (D.3) we may write

$$X\frac{\partial v_x}{\partial X} = -i\int_{-\infty}^{\infty} X(us)\,\mathrm{e}^{-iXs}\mathrm{d}s\,. \tag{D.7}$$

Then, upon setting $w(s,\tau)$ in Equation (D.6) equal to us, we obtain

$$X\frac{\partial v_x}{\partial X} = -\int_{-\infty}^{\infty} \frac{\partial(us)}{\partial s}\mathrm{e}^{-iXs}\mathrm{d}s\,. \tag{D.8}$$

Similarly we may write

$$X^2 v_x = \int_{-\infty}^{\infty} X^2 u\mathrm{e}^{-iXs}\mathrm{d}s = X\int_{-\infty}^{\infty} Xu\mathrm{e}^{-iXs}\mathrm{d}s\,. \tag{D.9}$$

Using Equation (D.6) in Equation (D.9) yields

$$X^2 v_x = -i\int_{-\infty}^{\infty} X\frac{\partial u}{\partial s}\mathrm{e}^{-iXs}\mathrm{d}s\,, \tag{D.10}$$

and then applying Equation (D.6) again gives

$$X^2 v_x = -\int_{-\infty}^{\infty} \frac{\partial^2 u}{\partial s^2}\mathrm{e}^{-iXs}\mathrm{d}s\,. \tag{D.11}$$

Finally to calculate $X^2\partial^2 v_x/\partial X^2$ we use Equation (D.4)

$$X^2\frac{\partial^2 v_x}{\partial X^2} = \int_{-\infty}^{\infty} X^2 us^2\mathrm{e}^{-iXs}\mathrm{d}s = -X\int_{-\infty}^{\infty} Xus^2\mathrm{e}^{-iXs}\mathrm{d}s\,. \tag{D.12}$$

An application of Equation (D.6) in Equation (D.12) gives

$$X^2\frac{\partial^2 v_x}{\partial X^2} = i\int_{-\infty}^{\infty} X\frac{\partial\left(us^2\right)}{\partial s}\mathrm{e}^{-iXs}\mathrm{d}s\,, \tag{D.13}$$

and then using Equation (D.6) again gives

$$X^2\frac{\partial^2 v_x}{\partial X^2} = \int_{-\infty}^{\infty} X\frac{\partial^2\left(us^2\right)}{\partial s^2}\mathrm{e}^{-iXs}\mathrm{d}s\,. \tag{D.14}$$

Substituting Equations (D.8), (D.11) and (D.12) into Equation (D.1) gives

$$\left(s^2+1\right)\frac{\partial^2 u}{\partial\tau^2} = \frac{\partial^2}{\partial s^2}\left[\left(s^2+1\right)u\right] - 2\frac{\partial(us)}{\partial s}\,, \tag{D.15}$$

which reduces to the governing equation (Equation 3.6) of Lau (1979)

$$\frac{\partial^2 u}{\partial^2\tau} = \frac{1}{A}\frac{\partial}{\partial s}\left[A\frac{\partial u}{\partial s}\right]\,, \tag{D.16}$$

where $A = s^2+1$.

Appendix E

Edwin et al. (1986) Model: Limiting phase speed as $k_z a \gg 1$

The surface wave dispersion relation (Equation 3.30) in the short wavelength limit reduces to

$$\frac{2c_{s0}^2}{\gamma v_{Ae}^2}\left(k_z^2 v_{Ae}^2 - \omega^2\right) = \omega^2 \frac{m_e a}{m_0 a}\,, \tag{E.1}$$

since as $k_z a \gg 1$ both $\tanh m_0 a$ and $\coth m_0 a$ tend towards one. At short wavelengths the limiting phase speed for kink and sausage modes is the same. Here

$$m_e a = k_z a \left(1 - \frac{\omega^2}{k_z^2 v_{Ae}^2}\right)^{\frac{1}{2}}\,, \tag{E.2}$$

$$m_0 a = k_z a \left(1 - \frac{\omega^2}{k_z^2 c_{s0}^2}\right)^{\frac{1}{2}}\,, \tag{E.3}$$

$$\text{and} \quad n_o a = k_z a \left(\frac{\omega^2}{k_z^2 c_{s0}^2} - 1\right)^{\frac{1}{2}}\,. \tag{E.4}$$

Substitution of Equations (E.2)-(E.4) into Equation (E.1) gives

$$\frac{\omega^2}{k_z^2} = \frac{2}{\gamma} c_{s0}^2 \left(1 - \frac{\omega^2}{k_z^2 v_{Ae}^2}\right)^{\frac{1}{2}} \left(1 - \frac{\omega^2}{k_z^2 c_{s0}^2}\right)^{\frac{1}{2}}\,, \tag{E.5}$$

and then squaring both sides of Equation (E.5) and multiplying through by $\gamma^2 v_{Ae}^2 / 4 c_{s0}^2$ yields

$$\left(\frac{\omega^2}{k_z^2}\right)^2 \left[\frac{\gamma^2}{4}\frac{v_{Ae}^2}{{c_{s0}}^2} - 1\right] + \frac{\omega^2}{k_z^2}\left(v_{Ae}^2 + c_{s0}^2\right) - v_{Ae}^2 c_{s0}^2 = 0\,. \tag{E.6}$$

Equation (E.6) has solution

$$\frac{\omega^2}{k_z^2} = \frac{\left(v_{Ae}^2 + c_{s0}^2\right) \pm \sqrt{\left(v_{Ae}^2 - c_{s0}^2\right)^2 + 4\Lambda^2 v_{Ae}^2 c_{s0}^2}}{2\left(1 - \Lambda^2\right)} \tag{E.7}$$

where $\Lambda = \gamma v_{Ae}/2c_{s0}$. The squaring of Equation (E.5) introduces a spurious solution which satisfies Equation (E.6) but not the original dispersion relation. An examination of the solution (Equation E.7) shows that the positive root must be neglected to ensure $\omega/k_z < c_{s0}$. Multiplying the numerator and denominator of the right-hand side of Equation (E.7) by $\sqrt{(v_{Ae}^2 - c_{s0}^2)^2 + 4\Lambda^2 v_{Ae}^2 c_{s0}^2}$ and disregarding the spurious solution gives,

$$\left(\frac{\omega}{k_z v_{Ae}}\right)^2 = \frac{2c_{s0}^2/v_{Ae}^2}{1 + c_{s0}^2/v_{Ae}^2 + \sqrt{1 + c_{s0}^4/v_{Ae}^4 - 2c_{s0}^2/v_{Ae}^2 + 4\Lambda^2 c_{s0}^2/v_{Ae}^2}} \,. \tag{E.8}$$

For the case $\Lambda^2 = \gamma/2$ this equation reduces to

$$\left(\frac{\omega}{k_z v_{Ae}}\right)^2 = \frac{2\Lambda^2}{1 + \Lambda^2 + \sqrt{1 + 5\Lambda^4 - 2\Lambda^2}} \,. \tag{E.9}$$

References

Abrami, A. : 1970, *Solar Phys.* **11**, 104.

Abrami, A. : 1972, *Nature* **238**, 25.

Achong, A. : 1974, *Solar Phys.* **37**, 477.

Acton, L.W., Tsuneta, S., Ogawara, S., Bentley, R.D., Bruner, M.E., Canfield, R.C., Culhane, J.L., Doscheck, G.A., Hiei, E., Hirayama, T., Hudson, H.S., Kosugi, T., Lang, J., Lemen, J.R., Nishimura, J., Makishima, K., Uchida, Y., and Watanabe, T. : 1992, *Science* **258**, 618.

Anderson, B.J. : 1994, *Solar Wind Sources of Magnetospheric Ultra-Low Frequency Waves*, eds. Engebretson, M.J., Takahashi, K., Scholer, M., Geophysical Monograph **81**, American Geophysical Union, 25.

Allen, C.W. : 1975, *Mon. Not. R. astr. Soc.* **172**, 159.

Anderson, K.A., and Mahoney, W.A. : 1974, *Solar Phys.* **35**, 419.

Antonucci, E., Gabriel, A.H., and Patchett, B.E. : 1984, *Solar Phys.* **93**, 85.

Aschwanden, M.J. : 1987, *Solar Phys.* **111**, 113.

Aschwanden, M.J. : 1994, *Lecture Notes in Physics* **444**, Springer-Verlag, Heidelberg, 13.

Aschwanden, M.J., and Benz, A.O. : 1986, *Astron. Astrophys.* **158**, 102.

Aschwanden, M.J., Bastian, T.S., and Gary, D.E. : 1992, *Bull. American Astron. Soc.* **23(2)**, 1072.

Aschwanden, M.J., Benz, A.O., Dennis, B.R., and Gaizauskas, V. : 1993, *Astrophys. J.* **416**, 857.

Aschwanden, M.J., Benz, A.O., Dennis, B.R., and Kundu, M.R. : 1994, *Astrophys. J. (SS)* **90**, 631.

Aurass, H., Chernov, G.P., Karlický, M., Kurths, J., and Mann, G. : 1987, *Solar Phys.* **112**, 347.

Aurass, H., and Kliem, B. : 1992, *Solar Phys.* **141**, 371.

Bauer, T.M., Baumjohann, W., and Treumann, R.A. : 1995a, *J. Geophys. Res.* **100**, 23737.

Bauer, T.M., Baumjohann, W., Treumann, R.A., Sckopke, N., and Lühr, H. : 1995b, *J. Geophys. Res.*, **100**, 9605.

Beaufumé, P., Coppi, B., and Golub, L. : 1992, *Astrophys. J.* **393**, 396.

Bertin, G., and Coppi, B. : 1985, *Astrophys. J.* **298**, 387.

Berton, R., and Sakurai, T. : 1985, *Solar Phys.* **96**, 93.

Berton, R., and Heyvaerts, J. : 1987, *Solar Phys.* **109**, 201.

Berghmans, D., De Bruyne, P., and Goossens, M. : 1996, *Astrophys. J.* **472**, 398.

Billings, D.E. : 1959, *Astrophys. J.* **130**, 215.

Birn, J., Hesse, M., and Schindler, K. : 1996, *J. Geophys. Res.* **101**, 12939.

Boyce, W.E., and DiPrima, R.C. : 1969, *Elementary Differential Equations and Boundary Value Problems*, 2nd ed., Wiley, New York.

Bray, R.J., Cram, L.E., Durrant, C.J., and Loughhead, R.E. : 1991, *Plasma Loops in the Solar Corona*, Cambridge University Press, Cambridge.

Brosius, J.W., Davila, J.M., Thomas, R.J., and Monsignori-Fossi, B.C. : 1997, *Astrophys. J. (SS)* **106**, 143.

Brosius, J.W., Davila, J.M., Thomas, R.J., Saba, J.L.R., Hara, H., and Monsignori-Fossi, B.C. : 1997, *Astrophys. J.* **477**, 969.

Browning, P.K. : 1991, *Plasma Physics and Controlled Fusion* **33**, 539.

Čadež, V.M., and Okretič, V.K. : 1989, *J. Plasma Phys.* **41**, 23.

Cally, P.S. : 1986, *Solar Phys.* **103**, 277.

Carbonell, M., and Ballester, J.L. : 1991, *Astron. Astrophys.* **249**, 295.

Chapman, R.D., Jordan, S.D., Neupert, W.M., and Thomas, R.J. : 1972, *Astrophys. J.* **174**, L97.

Cheng, C.-C. : 1980, *Astrophys. J.* **238**, 743.

Cheng, C.-C., Smith Jr., J.B., and Tandberg-Hanssen, E. : 1980, *Solar Phys.* **67**, 259.

Chong, M.S., Perry, A.E., and Cantwell, B.J. : 1990, *Phys. Fluids A* **2**, 765.

Cliver, E.W., Hurst, M.D., Wefer, F.L., and Bleiweiss, M.P. : 1976, *Solar Phys.* **48**, 307.

Correia, E., and Kaufmann, P. : 1987, *Solar Phys.* **111**, 143.

Correia, E., Costa, J.E.R., Kaufmann, P., Magun, A., and Herrmann, R. : 1995, *Solar Phys.* **159**, 143.

Cowley, S.W.H. : 1973, *Radio Science* **8**, 903.

Cramer, N.F. : 1994, *J. Plasma Phys.* **51**, 221.

Cramer, N.F. : 1995, *Physica Scripta* **T60**, 185.

Cribbens, A.H., and Matthews, P.A. : 1969, *Nature* **222**, 158.

Curtis, R., Morel, C., and White, O.R. : 1972, *Ann. Report NCAR*, 127.

Davila, J.M. : 1985, *Astrophys. J.* **291**, 328.

Davis, J.M., and Krieger, A.S. : 1982, *Solar Phys.* **80**, 295.

Dennis, B.R., Frost, K.J., and Orwig, L.E. : 1981, *Astrophys. J.* **244**, L167.

Dere, K.P. : 1982, *Solar Phys.* **75**, 189.

Dermendjiev, V.N., Kolarov, G.V., and Mitsev, Ts. A. : 1992, *Solar Phys.* **137**, 199.

Desai, U.D., Kouveliotou, C., Barat, C., Hurley, K., Niel, M., Talon, R., and Vedrenne, G. : 1986, *Rapid Fluctuations in Solar Flares*, eds. Dennis, B.R., Orwig, L.E., Kiplinger, A.L., NASA CP-2449, 63.

Domingo, V., Fleck, B.S , and Poland, A.I. : 1995, *Solar Phys.* **162**, 1.

Doschek, G.A., Strong, K.T., and Tsuneta, S. : 1995, *Astrophys. J.* **440**, 370.

Dulk, G.A., and Gary, D.E. : 1983, *Astron. Astrophys.* **124**, 103.

Dupree, A.K., Huber, M.C.E., Noyes, R.W., Parkinson, W.H., Reeves, E.M., and Withbroe, G.L. :

1973, *Astrophys. J.* **182**, 321.

Eddy, J.A. : 1973, *Solar Phys.* **30**, 385.

Edwin, P.M. : 1984, *PhD Thesis*, University of St Andrews, Scotland.

Edwin, P.M. : 1991, *Ann. Geophysicae* **9**, 188.

Edwin, P.M. : 1992, *Ann. Geophysicae* **10**, 631.

Edwin, P.M., and Roberts, B. : 1982, *Solar Phys.* **76**, 239.

Edwin, P.M., and Roberts, B. : 1983, *Solar Phys.* **88**, 179.

Edwin, P.M., Roberts, B., and Hughes, W.J. : 1986, *Geophys. Res. Lett.* **13**, 373.

Egan, T.F., and Schneeberger, T.J. : 1979, *Solar Phys.* **64**, 223.

Elgaroy, O., and Lyngstad, E. : 1972, *Astron. Astrophys.* **16**, 1.

Elgaroy, O. : 1986, *Solar Phys.* **104**, 43.

Endler, F., and Deubner, F.-L. : 1983, *Astron. Astrophys.* **121**, 291.

Epstein, P.S. : 1930, *Proc. Nat. Acad. Sci.* **16**, 627.

Ewing, W.M., Jardetzky, W.S., and Press, F. : 1957, *Elastic Waves in Layered Media*, McGraw-Hill, New York.

Fisher, R.R. : 1971a, *Solar Phys.* **19**, 436.

Fisher, R.R. : 1971b, *Solar Phys.* **19**, 440.

Fletcher, N.H., and Rossing, T.D. : 1991, *The Physics of Musical Instruments*, Springer-Verlag, New York.

Foukal, P.V. : 1975, *Solar Phys.* **43**, 327.

Foukal, P.V. : 1976, *Astrophys. J.* **210**, 575.

Foukal, P.V. : 1978, *Astrophys. J.* **223**, 1046.

Foukal, P.V., Huber, M.C.E., Noyes, R.W., Reeves, E.M., Schmahl, E.J., Timothy, J.G., Vernazza, J.E., and Withbroe, G.L. : 1974, *Astrophys. J.* **193**, L143.

Frost, K.J. : 1969, *Astrophys. J.* **158**, 159.

Fu, Q-J., Gong, Y-F., Jin, S-Z., and Zhao, R-Y. : 1990, *Solar Phys.* **130**, 161.

Fukao, S., Ugai, M, and Tsuda, T. : 1975, *Rep. Ion. Space Res. Jap.* **29**, 133.

Galsgaard, K., and Nordlund, A. : 1996, *J. Geophys. Res.* **102**, 231.

Gary, D.E., Zirin, H., and Wang, H. : 1990, *Astrophys. J.* **355**, 321.

Gaizauskas, V., and Tapping, K.F. : 1980, *Astrophys. J.* **241**, 804.

Gerassimenko, M., Solodyna, C.V., and Nolte, J.T. : 1978, *Solar Phys.* **57**, 103.

Gloge, D. : 1972, *Applied Optics* **11**, 2506.

Golub, L. : 1991, *Mechanisms of Chromospheric and Coronal Heating*, eds. Ulmschneider, P., and Priest, E.R., Springer-Verlag, Heidelberg, 115.

Goossens, M. : 1994, *Space Science Reviews* **68**, 51.

Gotwols, B.L. : 1972, *Solar Phys.* **25**, 232.

Haisch, B.M., Strong, K.T., Harrison, R.A., and Gary, G.A. : 1988, *Astrophys. J.(SS)* **68**, 371.

Hanaoka, Y., Kurokawa, H., and Saito, S. : 1988, *Publ. Astron. Soc. Japan* **40**, 369.

Harris, E.G. : 1962, *Nuovo Cimento* **23**, 115.

Harrison, R.A. : 1987, *Astron. Astrophys.* **182**, 337.

Harrison, R.A. : 1995, *CDS-SOHO scientific report*, 14-89.

Harrison, R.A., and Hassler, D. : 1995, CDS-SOHO scientific report, 14-19.

Hassler, D. : 1994, *SUMER-SOHO scientific report*, 8-51.

Hiei, E. : 1994, *Space Science Reviews* **70**, 189.

Heyvaerts, J., and Priest, E.R. : 1983, *Astron. Astrophys.* **117**, 220.

Hollweg, J.V. : 1982, *J. Geophys. Res.* **87**, 8065.

Hollweg, J.V. : 1990, *Computer Physics Reports* **12**, 205.

Hones, E.W. Jr., Asbridge, J.R., and Borne, S.J. : 1971, *J. Geophys. Res.* **76**, 4402.

Hood, A.W., Ireland, J., and Priest, E.R. : 1997, *Astron. Astrophys.* **318**, 957.

Hopcraft, K.I., and Smith, P.R. : 1985, *Phys. Letts.* **113A**, 75.

Hopcraft, K.I., and Smith, P.R. : 1986, *Planetary and Space Science* **34**, 1253.

Howard, R., and Švestka, Z.F. : 1977, *Solar Phys.* **54**, 65.

Hruška, A., and Hrušková, J. : 1970, *J. Geophys. Res.* **75**, 2449.

Huang, P. : 1995, *PhD Thesis*, University of Alabama at Huntsville, USA.

Ionson, J.A. : 1984, *Astrophys. J.* **276**, 357.

Ireland, J., Walsh, R.W., Harrison, R.A., and Priest, E.R.: 1997, *Astrophys. J.*, in preparation.

Jakimiec, J., and Jakimiec, M. : 1974, *Astron. Astrophys.* **34**, 415.

Jansenns, T.J., and White III, K.P. : 1969, *Astrophys. J.* **158**, L127.

Jansenns, T.J., White III, K.P., and Broussard, R.M. : 1973, *Solar Phys.* **31**, 207.

Joarder, P.S., and Roberts, B. : 1992, *Astron. Astrophys.* **256**, 264.

Joarder, P.S., and Roberts, B. : 1993, *Astron. Astrophys.* **273**, 642.

Joarder, P.S., Nakariakov, V.M., and Roberts, B. : 1997, *Solar Phys.*, in press.

Kai, K., and Takayanagi, A. : 1973, *Solar Phys.* **29**, 461.

Kane, S.R., Kai, K., Kosugi, T., Enome, S., Landecker, P.B., and McKenzie, D.L. : 1983, *Astrophys. J.* **271**, 376.

Karlický, M., and Jiřička, K. : 1995, *Solar Phys.* **160**, 121.

Kaufmann, P., Rizzo Piazza, L., and Raffaelli, J.C. : 1977, *Solar Phys.* **54**, 179.

Kinsler, L.E., and Frey, A.R. : 1962, *Fundamentals of Acoustics*, John Wiley and Sons, New York.

Kiplinger, A.L., Dennis, B.R., Emslie, A.G., Frost, K.J., and Orwig, L.E. : 1983a, *Astrophys. J.* **265**, L99.

Kiplinger, A.L., Dennis, B.R., Frost, K.J., and Orwig, L.E. : 1983b, *Astrophys. J.* **273**, 783.

Kleczek, J. : 1963, *Publ. Astron. Soc. Pacific* **75**, 9.

Klimchuk, J.A., Lemen, J.R., Feldman, U., Tsuneta, S., and Uchida, Y. : 1992, *Publ. Astron. Soc. Japan* **44**, L181.

Klimchuk, J.A., and Gary, D.E. : 1995, *Astrophys. J.* **448**, 925.

Kosugi, T., and Kiplinger, A.L. : 1986 in *Rapid Fluctuations in Solar Flares*, eds. Dennis, B.R.,

Orwig, L.E., Kiplinger, A.L., NASA CP-2449, 185.

Koutchmy, S. : 1975, *L'Astronomie* **89**, 149.

Koutchmy, S. : 1977, *Solar Phys.* **51**, 399.

Koutchmy, S. : 1981, *Space Science Reviews* **29**, 375.

Koutchmy, S., Bouchard, O., Mouette, J., and Koutchmy, O. : 1993, *Solar Phys.* **148**, 169.

Krieger, A.S., de Feiter, L.D., and Vaiana, G.S. : 1976, *Solar Phys.* **47**, 117.

Krucker, S., Benz, A.O., Aschwanden, M.J., and Bastian, T.S. : 1995, *Solar Phys.* **160**, 151.

Kundu, M.R., Schmahl, E.J., and Gerassimenko, M. : 1980, *Astron. Astrophys.* **82**, 265.

Kundu, M.R., and Velusamy, T. : 1980, *Astrophys. J.* **240**, L63.

Kundu, M.R., and Lang, K.R. : 1985, *Science* **228**, 9.

Kurths, J., Benz, A.O., and Aschwanden, M.J. : 1991, *Astron. Astrophys.* **248**, 270.

Laing, G.B. : 1996, *PhD Thesis*, The Open University, UK.

Lang, K.R. : 1997, *Scientific American*, March, 32.

Lang, K.R., Willson, R.F., and Rayrole, J. : 1982, *Astrophys. J.* **258**, 384.

Lau, Y.T., and Finn, J.M. : 1990, *Astrophys. J.* **350**, 672.

Lau, Y.Y. : 1979, *Phys. Rev. Lett.* **42**, 779.

Lau, Y.Y., Davidson, R.C., and Hui, B. : 1980, *Phys. Fluids* **23**, 1827.

Leblanc, Y. : 1970, *Astron. Astrophys.* **4**, 315.

Leighton, R.B., Noyes, R.W., and Simon, G.W. : 1962, *Astrophys. J.* **135**, 474.

Lemaire, P. : 1994, *SUMER-SOHO scientific report*, 8-33.

Levine, R.H., and Withbroe, G.L. : 1977, *Solar Phys.* **51**, 83.

Li, H-W., Messerotti, M., and Zlobec, P. : 1987, *Solar Phys.* **111**, 137.

Lilliequist, C.C. : 1966, AAS Meeting.

Liebenberg, D.H., and Hoffman, M.M. : 1974, *IAU Symp.* **57**, 485.

Loughhead, R.E., Bray, R.J., and Wang, J.-L. : 1985, *Astrophys. J.* **294**, 697.

Malitson, H.H., and Erickson, W.C. : 1966, *Astrophys. J.* **144**, 337.

Mangeney, A., and Pick, M. : 1989, *Astron. Astrophys.* **224**, 242.

Mann, I.R. : 1995, *PhD Thesis*, University of St Andrews, Scotland.

Marcatili, E.A.J. : 1969, *Bell System Technical Journal* **48**, 2103.

Marcatili, E.A.J. : 1970, *Bell System Technical Journal* **49**, 1645.

Marcatili, E.A.J., and Miller, S.E. : 1969, *Bell System Technical Journal* **48**, 2161.

Mason, H. : 1994, *Talk at Advanced PPARC Summer School in Solar-Terrestrial Physics*, QMW College, London.

Mason, H. : 1994, *SUMER-SOHO scientific report, 8-43.*

Maxwell, A., and Fitzwilliam, J. : 1973, *Astrophys. Lett.* **13**, 237.

McClements, K., Alexander, D., and Harrison, R.A. : 1995, *CDS-SOHO scientific report*, 14-19.

McConnell, D., and Kundu, M.R. : 1983, *Astrophys. J.* **269**, 698.

McGuire, J.P., Tandberg-Hanssen, E., Krall, K.R., Wu, S.T., Smith, J.B., and Speich, D.M. : 1977,

Solar Phys. **52**, 91.

McIntosh, P.S., Krieger, A.S., Nolte, J.T., and Vaiana, G. : 1976, *Solar Phys.* **49**, 57.

McKenzie, D.E. : 1997, *PhD Thesis*, University of Delaware, USA.

McKenzie, D.L. : 1987, *Astrophys. J.* **322**, 512.

McKenzie, J.F. : 1970, *J. Geophys. Res.* **75**, 5331.

McLean, D.J., Sheridan, K.V., Stewart, R.T., and Wild, J.P. : 1971, *Nature* **234**, 140.

McLean, D.J., and Sheridan, K.V. : 1973, *Solar Phys.* **32**, 485.

Meerson, B.I., Sasorov, P.V., and Stepanov, A.V. : 1978, *Solar Phys.* **58**, 165.

Mercier, C., and Rosenberg, H. : 1974, *Solar Phys.* **39**, 193.

Mihalov, J.D., Sonett, C.P., and Colburn, D.S. : 1970, *Cosmic Electrodynamics* **1**, 178.

Montgomery, M.D. : 1968, *J. Geophys. Res.* **73**, 871.

Moore, R., and Rabin, D. : 1985, *Ann. Rev. Astron. Astrophys.* **23**, 239.

Mundie, C.A. : 1997, *PhD Thesis*, University of St Andrews, Scotland.

Murawski, K. : 1993, *Acta Astronomica* **43**, 161.

Murawski, K., and Roberts, B. : 1993a, *Solar Phys.* **143**, 89.

Murawski, K., and Roberts, B. : 1993b, *Solar Phys.* **144**, 101.

Murawski, K., and Roberts, B. : 1993c, *Solar Phys.* **144**, 255.

Murawski, K., and Roberts, B. : 1993d, *Solar Phys.* **145**, 65.

Murawski, K., and Roberts, B. : 1994, *Solar Phys.* **151**, 305.

Murawski, K., and Goossens, M. : 1994, *Astron. Astrophys.* **286**, 943.

Musielak, Z.E., and Suess, S.T. : 1988, *Astrophys. J.* **330**, 456.

Musielak, Z.E., and Suess, S.T. : 1989, *J. Plasma Phys.* **42**, 75.

Nakariakov, V.M., and Roberts, B. : 1995, *Solar Phys.* **159**, 399.

Narain, U., and Ulmschneider, P. : 1990, *Space Science Reviews* **54**, 372.

Narain, U., and Ulmschneider, P. : 1996, *Space Science Reviews* **75**, 453.

Neupert, W.M., Nakagawa, Y., and Rust, D.M. : 1975, *Solar Phys.* **43**, 359.

Newkirk Jr., G. : 1967, *Ann. Rev. Astron. Astrophys.* **5**, 213.

November, L.J., and Koutchmy, S. : 1996, *Astrophys. J.* **466**, 512.

Noxon, J.F. : 1966, *Astrophys. J.* **145**, 400.

Noyes, R.W., Withboe, G.L., and Kirshner, R.P. : 1970, *Solar Phys.* **11**, 388.

Noyes, R.W. : 1971, *Physics of the Solar Corona*, ed. Macris, C.J., D. Reidel, Dordrecht, 192.

Ofman, L., and Davila, J.M. : 1995, *J. Geophys. Res.* **100**, 23413.

Olshansky, R. : 1979, *Rev. Mod. Phys.* **51(2)**, 341.

Oliver, R., Ballester, J.L., Hood, A.W., and Priest, E.R. : 1993, *Astron. Astrophys.* **273**, 647.

Oliver, R., Hood, A.W., and Priest, E.R. : 1996, *Astrophys. J.* **461**, 424.

Orwig, L.E., Frost, K.J., and Dennis, B.R. : 1981, *Astrophys. J.* **244**, L163.

Parkinson, J.H. : 1973, *Solar Phys.* **28**, 487.

Parks, G.K., and Winckler, J.R. : 1969, *Astrophys. J.* **155**, L117.

Parnell, C.E. : 1994, *PhD Thesis*, University of St Andrews, Scotland.

Parnell, C.E., Priest, E.R., and Golub, L. : 1994, *Solar Phys.* **151**, 57.

Parnell, C.E., Smith, J.M., Neukirch, T., and Priest, E.R. : 1996, *Phys. Plasmas* **3**, 759.

Parnell, C.E., Neukirch, T., Smith, J.M., and Priest, E.R. : 1997, *Geophys. Astrophys. Fluid. Dyn.* **84**, 245.

Pasachoff, J.M., and Landman, D.A. : 1984, *Solar Phys.* **90**, 325.

Pasachoff, J.M., and Ladd, E.F. : 1987, *Solar Phys.* **109**, 365.

Patel, V.L. : 1968, *Phys. Lett.* **26A**, 596.

Pekeris, C.L. : 1948, Theory of Propagation of Explosive Sound in Shallow Water, in *Propagation of Sound in the Ocean*, Geol. Soc. Am. Memoir **27**.

Phillips, K.J.H. : 1992, *Guide to the Sun*, Cambridge University Press, Cambridge.

Picat, J.P., Fort, B., Dantel, M., and Leroy, J.L. : 1973, *Astron. Astrophys.* **24**, 259.

Pick, M., and Trottet, G. : 1978, *Solar Phys.* **60**, 353.

Pick, M., Trottet, G., and MacQueen, R.M. : 1979, *Solar Phys.* **63**, 369.

Poedts, S., and Goossens, M. : 1991, *Solar Phys.* **133**, 281.

Porter, L.J., and Klimchuk, J.A. : 1995, *Astrophys. J.* **454**, 499.

Prača, M., and Karlický, M. : 1979, *Bull. Astron. Inst. Czechosl.* **30**, 257.

Priest, E.R. : 1982, *Solar Magnetohydrodynamics*, Reidel, Dordrecht.

Priest, E.R. : 1997, *Phys. Plasmas* **4**, 1945.

Priest, E.R., and Titov, V.S. : 1996, *Phil. Trans. R. Soc. Lond. A*, **354**, 2951.

Priest, E.R., and Démoulin, P. : 1995, *J. Geophys. Res.* **100**, 443.

Pye, J.P., Evans, K.D., Hutcheon, R.J., Gerassimenko, M., Davis, J.M., Krieger, A.S., and Vesecky, J.F. : 1978, *Astron. Astrophys.* **65**, 123.

Qin, Z.H., Li, C.S., Fu, Q.J., and Gao, Z.M. : 1996, *Solar Phys.* **163**, 383.

Rae, I.C., and Roberts, B. : 1982, *Mon. Not. R. astr. Soc.* **201**, 1171.

Rayleigh, Lord : 1945, *Theory of Sound*, Volume 1, Dover, New York, Chapter 9.

Reeves, E.M., Foukal, P.V., Huber, M.C.E., Noyes, R.W., Schmahl, E.J., Timothy, J.G., Vernazza, J.E., and Withbroe, G.L. : 1974, *IAU Symp.* **57**, 497.

Roberts, B. : 1981a, *Solar Phys.* **69**, 27.

Roberts, B. : 1981b, *Solar Phys.* **69**, 39.

Roberts, B. : 1985, *Magnetohydrodynamic Waves in Solar System Magnetic Fields*, ed. Priest, E.R., Reidel, Dordrecht, Chapter 3.

Roberts, B. : 1991a, *Advances in Solar System Magnetohydrodynamics*, eds. Priest, E.R., and Hood, A.W., Cambridge University Press, Cambridge, 105.

Roberts, B. : 1991b, *Geophys. Astrophys. Fluid. Dyn.* **62**, 83.

Roberts, B. : 1992, *Sunspots: Theory and Observations*, eds. Thomas, J.H., and Weiss, N.O., NATO ASI series, Kluwer, 303.

Roberts, B., Edwin, P.M., and Benz, A.O. : 1983, *Nature* **305**, 688.

Roberts, B., Edwin, P.M., and Benz, A.O. : 1984, *Astrophys. J.* **279**, 857.

Roberts, B., and Joarder, P.S. : 1994, *Lecture Notes in Physics* **432**, eds. Belvedère, Rodono, M., and Simnett, G.M., Springer-Verlag, Berlin, 173.

Roberts, P.H. : 1967, *An Introduction to Magnetohydrodynamics*, Longmans, London.

Rosenberg, H. : 1970, *Astron. Astrophys.* **9**, 159.

Rušin, V., and Minarovjech, M. : 1991, *Mechanisms of Chromospheric and Coronal Heating*, eds. P. Ulmscheider and E.R. Priest, Springer-Verlag, Heidelberg, 30.

Rušin, V., and Minarovjech, M. : 1994, *IAU Colloq.* **144**, 487.

Russell, C.T. : 1972, *Planetary and Space Science* **20**, 1541.

Sastry, Ch. V., Krishan, V., and Subramanian, K.R. : 1981, *J. Astrophys. Astron.* **2**, 59.

Scargle, J.D. : 1982, *Astrophys. J.* **263**, 835.

Schindler, K., and Birn, J. : 1978, *Physics Reports* **47**, 109.

Schindler, K., and Birn, J. : 1986, *Space Science Reviews* **44**, 307.

Schmidt, H.U., Wagner, W.J., and Newkirk, G. : 1972, *Bull. American Astron. Soc.* **8**, 390.

Seboldt, W. : 1990, *J. Geophys. Res.* **95**, 10471.

Sheeley Jr., N.R., Bohlin, J.D., Brueckner, G.E., Purcell, J.D., Scherrer, V., and Tousey, R. : 1975, *Solar Phys.* **40**, 103.

Sheeley Jr., N.R. : 1980, *Solar Phys.* **66**, 79.

Shimizu, T., Tsuneta, S., Acton, L.W., Lemen, J.R., and Uchida, Y. : 1992, *Publ. Astron. Soc. Japan* **44**, L147.

Singer, H.J., Hughes, W.J., Gelpi, C., and Ledley, B.G. : 1985, *J. Geophys. Res.*, **90**, 9583.

Singh, J., Cowsik, R., Raveendran, A.V., Bagare, S.P., Saxena, A.K., Sundararaman, K., Krishan, V., Naidu, N., Samson, J.P.A., and Gabriel, F. : 1997, *Solar Phys.* **170**, 235.

Smith, J.M., Roberts, B., and Oliver, R. : 1997a, *Astron. Astrophys.* **317**, 752.

Smith, J.M., Roberts, B., and Oliver, R. : 1997b, *Astron. Astrophys.*, in press.

Smith, J.M., Roberts, B., and Murawski, K. : 1997, in preparation.

Smith, J.M., Wright, A.N., and Rickard, G. : 1997, in preparation.

Snyder, A.W., and Love, J.D. : 1983, *Optical Waveguide Theory*, Chapman and Hall, London, 495.

Southwood, D.J. : 1974, *Planetary and Space Science* **22**, 483.

Southwood, D.J., and Stuart, W.F. : 1980, in *Dynamics of the Magnetosphere:* Proceedings of the A.G.U. Chapman conference on Magnetospheric Substorms and Related Plasma Processes, ed. Akasofu, S.-I, Reidel, Dordrecht, 341.

Spitzer, L. : 1962, *Physics of Fully Ionized Gases*, Interscience, Wiley and Sons, New York.

Stewart, R.T. : 1974, *IAU Symp.* **57**, 161.

Stewart, R.T. : 1976, *Solar Phys.* **50**, 437.

Stewart, R.T., and Vorpahl, J. : 1977, *Solar Phys.* **55**, 111.

Stewart, R.T., Brueckner, G.E., and Dere, K.P. : 1986, *Solar Phys.* **106**, 107.

Švestka, Z.F. : 1994, *Solar Phys.* **152**, 505.

Švestka, Z.F., Krieger, A.S., Chase, R.C., and Howard, R. : 1977, *Solar Phys.* **52**, 69.

Švestka, Z.F., Dennis, B.R., Pick, M., Raoult, A., Rapley, C.G., Stewart, R.T., and Woodgate, B.E. : 1982, *Solar Phys.* **80**, 143.

Švestka, Z.F., Fárník, F., Fontenla, J.M., and Martin, S.F. : 1989, *Solar Phys.* **123**, 317.

Švestka, Z.F., Fárník, F., Hudson, H.S., Uchida, Y., Hick, P., and Lemen, J.R.: 1995, *Solar Phys.* **161**, 331.

Takakura, T., Kaufmann, P., Costa, J.E.R., Degaonkar, S.S., Ohki, K., and Nitta, N. : 1983, *Nature* **302**, 317.

Tapping, K.F. : 1978, *Solar Phys.* **59**, 145.

Teuber, D.L., Wilson, R.M., and Henze Jr., W. : 1978, *Astron. Astrophys.* **65**, 229.

Thomas, R.J., Neupert, W.M., and Thompson, W.T. : 1986 in *Rapid Fluctuations in Solar Flares*, eds. Dennis, B.R., Orwig, L.E., Kiplinger, A.L., NASA CP-2449, 299.

Tirry, W., Čadež, V.M., and Goossens, M. : 1997, *Astron. Astrophys.*, in press.

Trottet, G., Pick, M., and Heyvaerts, J. : 1979, *Astron. Astrophys.* **79**, 164.

Trottet, G., Kerdraon, A., Benz, A.O., and Treumann, R. : 1981, *Astron. Astrophys.* **93**, 129.

Tsubaki, T. : 1977, *Solar Phys.* **51**, 121.

Tsubaki, T., Saito, Y., Suematsu, Y., and Nakagomi, Y. : 1986, *Publ. Astron. Soc. Japan* **38**, 251.

Tsubaki, T. : 1988, in *Solar and Stellar Coronal Structures and Dynamics*, ed. Altrock, R.C., NSO, Sunspot NM, 140.

Uberoi, C. : 1988, *J. Geophys. Res.* **93**, 7595.

Uberoi, C., and Satya Narayana, A. : 1986, *Plasma Physics and Controlled Fusion* **28**, 1635.

Ulrich, R.K. : 1970, *Astrophys. J.* **162**, 993.

Van der Linden, R.A.M., Hood, A.W., and Goedbloed, J.P. : 1994, *Solar Phys.* **154**, 69.

Vernazza, J.E., Foukal, P.V., Huber, M.C.E., Noyes, R.W., Reeves, E.M., Schmahl, E.J., Timothy, J.G., and Withbroe, G.L. : 1975, *Astrophys. J.* **199**, L123.

Watanabe, T., Kozuka, Y., Ohyama, M., Kojima, M., Yamaguchi, K., Watari, S-I, Tsuneta, S., Joselyn, J.A., Harvey, K.L., Acton, L.W., and Klimchuk, J.A. : 1992, *Publ. Astron. Soc. Japan* **44**, L199.

Webb, D.F., Holman, G.D., Davis, J.M., Kundu, M.R., and Shevgaonkar, R.K. : 1987, *Astrophys. J.* **315**, 716.

Wells, G.D., Hausman, B.A., Kroehl, H.W. : 1986, *Rapid Fluctuations in Solar Flares*, eds. Dennis, B.R., Orwig, L.E., Kiplinger, A.L., NASA CP-2449, 215.

Wessen, K.P, and Cramer, N.F. : 1991, *J. Plasma Phys.* **45**, 389.

White, O.R., and Athay, R.G. : 1979, *Astrophys. J. (SS)* **39**, 317.

Wiehl, H.J., and Mätzler, C. : 1980, *Astron. Astrophys.* **82**, 93.

Wiehl, H.J., Benz, A.O., and Aschwanden, M.J. : 1985, *Solar Phys.* **95**, 167.

Wilson, P.R. : 1981, *Astrophys. J.* **251**, 756.

Wright, A.N. : 1992, *J. Geophys. Res.* **97**, 6429.

Wright, A.N., and Rickard, G.J. : 1995, *Astrophys. J.* **444**, 458.

Wright, C.S., and Nelson, G.J. : 1987, *Solar Phys.* **111**, 385.

Wu, S.T., Xiao, Y.C., Musielak, Z.E., and Suess, S.T. : 1996, *Solar Phys.* **163**, 291.

Xiao, Y.C. : 1989, *PhD Thesis*, University of Alabama at Huntsville, USA.

Young, C.W., Spencer, C.L., Moreton, G.E., and Roberts, J.A. : 1961, *Astrophys. J.* **133**, 243.

Young, M. : 1986, *Optics and Lasers*, 3rd ed., Springer-Verlag, Heidelberg, 212.

Zalesak, S.T. : 1979, *J. Comput. Phys.* **31**, 335.

Zhao, R-Y., Jin, S-Z., Fu, Q-J., and Li, X-C. : 1990, *Solar Phys.* **130**, 151.

Zhao, R-Y., Mangeney, A., and Pick, M. : 1991, *Astron. Astrophys.* **241**, 183.

Ziegler, U., and Ulmschneider, P. : 1996, *Astron. Astrophys.*, in press.

Zirin, H. : 1988, in *Astrophysics of the Sun*, Cambridge University Press, Cambridge.

Zirker, J.B. : 1993, *Solar Phys.* **148**, 43.

Zlobec, P., Messerotti, M., Dulk, G.A., and Kucera, T. : 1992, *Solar Phys.* **141**, 165.

Zodi Vaz, A.M., Kaufmann, P., and Zirin, H. : 1984, *Solar Phys.* **92**, 283.

Zodi Vaz, A.M., Kaufmann, P., Correia, E., Costa, J.E.R., Takakura, T., Cliver, E.W., and Tapping, K.F. : 1986, *Rapid Fluctuations in Solar Flares*, eds. Dennis, B.R., Orwig, L.E., Kiplinger, A.L., NASA CP-2449, 171.